The Optics and Photonics of Two-Dimensional Nanomaterials

Stephen Adrian O’Brien

Trinity College Dublin
Coláiste na Tríonóide, Baile Átha Cliath
The University of Dublin

Supervisors:

Prof. John Donegan

Prof. David McCloskey

A thesis submitted in fulfilment of the requirements
for the degree of Doctor of Philosophy

2020

Declaration

I declare that this thesis has not been submitted as an exercise for a degree at this or any other university and it is entirely my own work.

I agree to deposit this thesis in the University’s open access institutional repository or allow the library to do so on my behalf, subject to Irish Copyright Legislation and Trinity College Library conditions of use and acknowledgement.

X

Stephen O'Brien

Abstract

In this work, by using a broadspectrum angle-resolved absorption technique, we studied enhanced absorption from multi-layered materials with near-zero dielectric permittivity in the near-infrared. These materials, known as epsilon (ε)-near-zero (ENZ) materials, are known to exhibit novel physics, including perfect absorption. We demonstrate, both theoretically and experimentally, the excitation of two plasmon modes in indium tin oxide thin-films, a bulk plasmon mode, know as the “Ferrell – Berreman mode” and a long-range surface plasmon polariton mode known as the “non-radiative ENZ mode”. These modes result in significant absorption from deeply subwavelength ITO thin-films of thickness 127 nm which is enhanced from a value of 52.5% to values >95% by depositing a 10 nm layer of Pt on the ITO layer as a backing. We observed this near-perfect absorption (NPA) from exciting both modes and studied the dependence of the absorption on the thickness of the Pt backing layer. We observed an asymptotic increase in the absorption maximum with increased Pt backing thickness. Furthermore, we numerically and analytically studied the excitation of these modes, with and without a backing of various metals and of various thicknesses. We found that any common metal can be used to achieved near-perfect absorption by depositing on ITO and exciting these plasmon modes, however the thickness at which the maximum absorption can be achieved is dependent on the complex refractive index and the skin depth of each metal. We also found that there is a maximum in the non-radiative ENZ mode absorption when the metal backing is sufficiently thin so as to allow the excitation of an insulator – metal – insulator (IMI) mode, where two long-range surface plasmons, on the upper and lower surfaces of the metal, are coupled together with the ENZ mode to result in near-perfect absorption.

Finally, we studied the suitability of high aspect ratio two-dimensional (2D) nanoflakes of hexagonal boron nitride (h-BN) produced by Liquid Phase Exfoliation (LPE) as a 2D material to deposit on our ITO – Pt structures. As these nanoflakes are produced in aqueous suspensions and tend to form high-scattering surfaces when deposited on solid substrates, we characterised the scattering from these nanoflakes in aqueous suspension using a diffuse scattering intensity path-length resolved technique. We considered several models to describe the scattering from these highly anisotropic nanoflakes and found that the Two-Stream Approximation to the Radiative Transfer Equation best described the scattering form such flakes. Furthermore, we devised an in-situ technique to estimate the lateral size of these particles by direct comparison with polystyrene (PS) nanospheres of similar diameter. However, we found that these nanoflakes are not suitable for coupling with ENZ materials as the highly irregular size and shape led to a dominance of scattering in the optical response.

Acknowledgements

I’d like to start by acknowledging my PhD supervisors, Prof. John Donegan and Prof. David McCloskey for their encouragement, support and mentorship throughout my PhD journey. I would also like to thank my friends and colleagues from the Photonics Group who provided me with interesting discussion, ideas, and friendship. A PhD is a difficulty journey and a good team is essential. In particular, I would like to thank Brian Jennings, Chuan Zhong, William Abbott, Guarav Jain, Michael Wallace, Robert McKenna, Jorge García, Kenny Wu, Naveen Balla, Simon Corbett, Chris Murray and every other person who I’ve worked with in the past four years.

I would also like to thank several collaborators who have helped me with some of the work presented in this thesis. Thanks to Prof. Johnny Coleman, Dr. Andrew Harvey, and Aideen Griffin who provided me with some of the samples used in this work. Big thanks to Chris Smith, Karsten Fletscher and Matthew Wells are also necessary for their help, both experimentally and for valuable discussion.

On a more personal note, thanks to my parents, Patrick and Margaret O’Brien, for all the support over the years of study, for all the science/physics books and toys that they bought for me as a child, and for always encouraging my interest in science, all of which inevitably led me to where I am now.

An aspect of science and academia that I have always loved is being surrounded by an international community of skilled and lovely people with whom I have become great friends. To Jane O’Reilly and Stephen Porter with whom I’ve had the pleasure of being both a student and a colleague, thank you for your kindness, your openness, and always making me feel like I belong somewhere. Thanks to Katarzyna Siewierska for the crazy nights out and helping me through some very stressful periods. To Katya Zibrek, James Creel, and Karaca, thank you for the afterwork pints and giving me a lovely social group.

To my oldest friend from home, Zoë Lawlor, thank you for always being there for me, for being a constant in my life and always reminding me who I am. To my friend Nico Crescini, thanks for always being my connection to the real world, for your delicious tiramisu, and for always being there for me and all the great times we’ve spent together.

Il y a aussi une personne qui me fait toujours sourire, quelqu’un de très important et spécial dans ma vie, Romina Charifou. Pour tous les soirs qu’on passait ensemble chez toi, pour tous les conseils que tu m’as donnés, pour toutes les blagues sombres qu’on a partagées, et d’être la personne sympathique, chaleureuse, et incroyable que tu es, merci.

Ao meu pastel, João, my favourite chemist, thanks for being a passable friend over the past few years. I suppose there are worst people I could have been stuck with. I can’t imagine how the last few years would have been if it weren’t for your daily inappropriate memes, your constant sassiness, and the tales of your late night antics (and subsequent mornings on Baggot Street!). Thanks for always being there, for your advice, and your massive charisma, uniqueness, nerve, and talent. Eu te amo, paizinho!

Y por fin, hay una persona más a quien quería dar muchas gracias. A mi pareja, Enzo Muñoa Silva. Gracias a ti por aguantarme durante este tiempo tan difícil. Gracias por siempre darme tu

sonrisa, tus consejos y tu amor. Sin ti, no sé cómo sería mi vida, y no lo quiero imaginar tampoco. No hay palabras para describir lo importante que eres en mi vida. ¡Te quiero mucho, guapo!

Publications

- **S A O’Brien**, A Harvey, A Griffin, T Donnelly, D Mulcahy, J N Coleman, J F Donegan and D McCloskey, “Light scattering and random lasing in aqueous suspensions of hexagonal boron nitride nanoflakes,” Nanotechnology, vol. 28, no. 47, p. 47LT02, 2017.

Poster Presentations

- **Stephen A. O’Brien**, Frank Bello, Niall McEvoy, David McCloskey and John F. Donegan, “Epsilon Near Zero Metamaterials, ” Photonics Ireland, Cork, 2017.

- **Stephen A. O’Brien**, Frank Bello, Lisanne Peters, Niall McEvoy, John F. Donegan, and David McCloskey, “Pursuit of ENZ Response in 2D Thin Films,” XXV International Summer School Nicolás Cabrera, Miraflores de la Sierra, Madrid, Spain, 2018.

- **Stephen A. O’Brien**, Frank Bello, Lisanne Peters, Niall McEvoy, David McCloskey, and John F. Donegan, “Near Perfect Absorption in Epsilon-Near-Zero Thin Films”, META 2019, Lisbon, Portugal, 2019.

List of Abbreviations

ENZ	Epsilon (ε) Near Zero
MNZ	Mu (μ) Near Zero
EMNZ	Epsilon (ε) & Mu (μ) Near Zero
NPA	Near-Perfect Absorption
PA	Perfect Absorption
TE	Transverse Electric
TM	Transverse Magnetic
AFM	Atomic Force Microscopy
TEM	Transmission Electron Microscopy
SPP	Surface Plasmon Polariton
FB	Ferrell – Berreman
TMM / T-Matrix	Transfer Matrix Method
FEM	Finite Element Method
h-BN	Hexagonal Boron Nitride
PS	Polystyrene
SLS	Single Light Scattering
DLS	Dynamic Light Scattering
LPE	Liquid Phase Exfoliation
sccm	Standard Cubic Centimetres per Minute
PVD	Physical Vapour Deposition
TO	Transverse Optic
LO	Longitudinal Optic
TCO	Transparent Conducting Oxide
TMDC	Transition Metal Dichalcogenide
ITO	Indium Tin Oxide
IZO	Indium Zinc Oxide
QCM	Quartz Crystal Monitor
NIR	Near-Infrared

List of Figures

- Figure 7.19 (a – d) Monte Carlo method simulations for light scattering through turbid suspensions of PS microspheres of various diameters and (e – h) experimental (solid lines) and simulated (dashed lines) normalised diffuse scattered intensities as a function of path length for the various PS nanosphere suspensions.
- Figure 7.20 Schematic diagram of the angle-resolved single scattering setup.
- Figure 7.21 Scattered light intensity as a function of angle for (a) h-BN nanoflakes and (b) PS nanospheres of diameter 400 nm for co-polarized incidence and collection, h-BN nanoflakes (c) and 400 nm PS nanospheres (d) for cross polarized incidence and collection, and relative depolarisation for h-BN (e) and PS nanospheres (f). The specified concentrations are multiples of the initial stock concentration which was unknown.
- Figure 7.22 (a) PL spectrum for increasing incident pump energy. Peak forming at 587nm (b) Light-Light curve showing onset of lasing with threshold at pump energy of 0.8 mJ.
- Figure 8.1 2D schematic of the Cr – ITO – Pt multilayer structure. Absorption from the structure was considered in the case of an air superstrate (a) and a glass superstrate (b).
- Figure 8.2 Broad spectrum angle-resolved absorption from a Cr (10 nm) – ITO (127 nm) – Pt (10 nm) multilayer structure excited from (a) an air superstrate and (b) a glass superstrate.
- Figure 8.3 Absorption profile as a function of wavelength from a Cr (10 nm) – ITO (127 nm) – Pt (10 nm) multilayer structure at normal incidence (a) and oblique incidence (b).
- Figure 8.4 Broad spectrum angle-resolved absorption from a Cr (10 nm) – Glass (127 nm) – Pt (10 nm) multilayer structure excited from (a) an air superstrate and (b) a glass superstrate.
- Figure 8.5 Absorption profile as a function of wavelength from a Cr (10 nm) – Glass (127 nm) – Pt (10 nm) multilayer structure at normal incidence (a) and oblique incidence (b).
- Figure 8.6 An estimation of the required carrier concentration needed to achieve an ENZ wavelength in the 600 nm – 2000 nm spectral range.
- Figure 8.7 2D schematic of the structure studied by Feigenbaum *et al.* for the generation of ITO with an ENZ wavelength at visible frequencies. By applying an applied voltage in the 0 – 2.5 V range, significant concentration of charge carriers could be setup in the depletion layer leading to an increased localised carrier concentration and a visible range ENZ wavelength.
- Figure 8.8 (a) Carrier concentration as a function of applied voltage for the depletion layer of the Au – ITO – SiO_2 – Au structure studied by Feigenbaum et al. and (b) the resulting plasma frequency (black) and ENZ wavelength (red) for the depletion region.
- Figure 8.9 Broadspectrum angle-resolved absorption for (a) a 127 nm ITO with a plasma frequency, $\omega_p = 6.00$ rad fs^{-1}, and (b) a 127 nm ITO with a plasma frequency, $\omega_p = 6.00$ rad fs^{-1} and a 10 nm Pt backing. Both the Ferrell – Berreman mode, below 41° and the non-radiative ENZ mode, above 41° are clearly visible below 600 nm.
- Figure 8.10 A comparison of (a) the Ferrell – Berreman mode absorption and (b) the non-radiative ENZ mode absorption from a 127 nm ITO with a plasma frequency, $\omega_p = 6.00$ rad fs^{-1} with (red) and without (black) a 10 nm Pt backing layer.
- Figure 8.11 Schematic of the waveguide structure considered by Engheta et al. demonstrating the coupling between two dipoles in (a) a standard linear waveguide, and (b) two waveguides

List of Tables

Table of Contents

“*An experiment is a question*
which science poses to Nature,
and a measurement is the
recording of Nature’s answer.”

Max Planck

Chapter 1: Introduction and Motivation

1.1 Introduction

Photonics is field of physics concerned with light, its fundamental properties, its propagation, detection, generation and manipulation [1][2]. While the term "photonics" originated in the 1960s with the invention of the laser [3][4][5] and later the invention of laser diodes in the 1970s as well as optical fibres which formed the basis of the telecommunications industry, the foundation of the field is based more generally in optics. The foundations of optics itself can be traced back to antiquity, particularly the development of the first lenses by the Egyptians and Mesopotamians. This was later followed by the theories of vision of the great Greek philosophers such as Ptolemy and the development of geometric optics [6]. In fact, the word "optics" comes from the ancient Greek word "ὀπτικά" which translates as "appearance" or "look". In the centuries that followed, further advancements in optics were made by Islamic scholars such as Ibn Sahl, Ibn al-Haytham, Avicenna, and Alhazen on the focusing of light with curved mirrors, the refraction of light, and even positing that the speed of light is finite [7]. For centuries following this and throughout the Renaissance period in Europe, significant discoveries were made regarding the wave nature of light, its basic properties, and behaviours such as the mathematical description of refraction devised by Willebrord Snellius in 1621, now known as Snell's Law [8]. During this historic period, René Descartes outlined the laws of reflection, Sir Isaac Newton demonstrated his Theory of Colour and the phenomenon of dispersion, and diffraction was described by Francesco Maria Grimaldi in his 1665 posthumous publication [9]. It was then Thomas Young in 1803 who demonstrated the wave nature of light using his famous double slit interferometer [10]. Up until the 19th century, optics was largely concerned with light itself and its properties, however in 1839 at the age of 19, Edmund Becquerel produced the first photovoltaic cell by coating platinum electrodes with either silver bromide or silver chloride [11]. Upon illumination a voltage was setup across these electrodes and a current was detected passing through them, thus providing the first ever demonstration of the photovoltaic effect. This was, perhaps, the first discovery that laid the foundation of photonics as a field of its own. In 1865, James Clerk Maxwell published his four famous equations of electromagnetism in his book "A Dynamical Theory of Electromagnetic Fields." [12] These equations formed the basis of our understanding of light as an electromagnetic wave and paved the way for a century of great discoveries. In 1905, Albert Einstein demonstrated, via his work on the photoelectric effect, that light is not just a wave, but also comes in discrete packets of energy or "quanta" for which he later won the Nobel Prize in physics [13]. This not only revolutionised our understanding of light, but also created the entirely new and enigmatic field of quantum theory. Throughout the 20th century, further advancements were made such as stimulated emission in 1917, the first practical photovoltaic cell by Fuller and Pearson of Bell Labs in 1954 [14], the development of the semiconductor laser in 1962 [15], the development of optical fibres for transmitting signals in 1966 [16], the charge coupled device (CCD) based digital camera in 1975 [17], and the first transatlantic fibre cable in 1988 [18]. Indeed, the focus of much research on light shifted from the study of light itself to the design and fabrication of devices that allow us to manipulate its interaction with materials for own purposes and application, now known as photonics.

Photonics encompasses a range of fields from telecommunications [19], laser manufacturing [20], environmental photonics [21], chemical sensing [22][23], biochemical sensing [24], and even medical diagnostics [25][26]. It also encompasses a range of classical, modern, and quantum physics from classical linear and opto-mechanics to electro-optics and quantum optics. However, photonics does not only help us to build new technology but also allows us to understand the very fundamental nature of materials at the macroscopic, microscopic, and nanometre scales. From techniques such as spectroscopic ellipsometry we can determine the optical constants of a material and the propagation of light within that material [27][28]; from rotational-vibrational spectroscopy in the infrared we can determine the vibrational and rotational states of molecules [29][30]; from x-ray spectroscopy we determine the arrangement, density, and lattice constants of atoms in a material [31], and from UV spectroscopy we can determine the bandgaps of many materials [32]. Indeed, photonics has not only become a field for manufacturing new technology but has become an important and vital technique to understanding the world around us and the materials of which it is composed. In this work, we employ photonics to understand the nature and behaviour of materials and use our understanding to design and fabricate structures with unique optical properties.

1.2 The 2D Revolution

For decades, like much of physics, photonics was isolated to studying bulk materials, however that all changed with the isolation of graphene from graphite in 2004 [33]. This was the first ever reported two-dimensional (2D) material and ever since then a whole range of 2D materials have now become readily available in research labs. Much research has been carried out into the properties of graphene and particularly into the optical and photonic properties of graphene [34][35][36][37]. Graphene has been demonstrated to exhibit saturable absorption [38][39] and the nonlinear Kerr effect [40][41] and has even been used to produce a graphene-based Bragg grating [42][43]. However, graphene is not the only 2D material that has become available and certainly not the only thin film material that has been produced. With the development of extremely precise deposition techniques such as atomic layer deposition (ALD) [44], ion sputtering [45], direct current (DC) and radio frequency (RF) magnetron sputtering [46], chemical vapour deposition [47], molecular beam epitaxy (MBE) [48], and pulsed laser deposition (PLD) [49] the production of extremely thin films has become possible. The density of states (DoS) of graphene matches quite precisely with the DoS which would be expected of a truly 2D material [50]. Thus, it is important that we correctly define what we consider in this work to be a 2D material. While in materials science and chemistry, a “2D material” is typically considered to be monolayer think material such as graphene, in this work, we consider any thin film which is sufficiently smaller than the wavelength of incident light and exhibits unique optical properties different from the bulk material as a result of this, to be a 2D material. In this work, we particularly study nanometre thick flakes of hexagonal boron nitride, and thin layers (< 150 nm) of indium tin oxide (ITO).

1.3 Epsilon-Near-Zero (ENZ) 2D Nanomaterials

A particular phenomenon that is studied in photonics is absorption of light. Significant research, both theoretical and experimental, has been carried out on the achievement of near-perfect and perfect absorption in 2D and thin-film materials [51][52][53][54]. The achievement of such a feat would have a strong impact on future technologies such as solar cells [55], anti-reflective coatings [56], and near-field transducers. A set of materials which is expected to exhibit significantly high absorption are epsilon-near-zero (ENZ) materials. An ENZ material is a material with a dielectric permittivity, ε close to zero, or more specifically, a material with a zero-real component of the dielectric permittivity and a reasonably small imaginary component [57][58]. The dielectric permittivity is an important parameter in photonics as it tells us how an electric field is affected by the medium in which it’s propagating [59]. The effects of permittivity on the wave dynamics in a material has been well understood for quite some time, however, the case where $\varepsilon \approx 0$ has been surprisingly neglected, possibly due to difficulty involved in measuring such effects in bulk materials. However, with the ability to deposit thin films and 2D materials, the study of ENZ effects in naturally occurring ENZ materials is now possible, and particularly the ability to produce multi-layered structures with unique topologies that combine to form effective ENZ materials are not only possible but have been experimentally demonstrated. Much of the unique physics surrounding these materials is a result of spatial confinement of electric field in these ultra-thin materials. Such materials have been theoretically and experimentally demonstrated to host unusual physical effects such as super-coupling [60], infinite phase velocities [61], static electric fields [62], reduced group velocities [63], perfect reflection [64], near-perfect absorption (NPA) [65], and even confinement of light [66]. These materials have been a topic of intense study in recent years by researchers such as Nader Engheta [67], Andrea Alù [68], and Salvatore Campione [69]. Much work has been carried out on their unique physics and their potential implementation in photonic devices. The unique physics of such materials will be discussed in further detail in Chapter 4. One such ENZ material that is readily available is ITO which for extremely thin films can achieve enhanced absorption as a result of its ENZ behaviour. This ENZ behaviour is a direct result of the confinement of electric fields in deeply-subwavelength films of ITO and presents promising prospects in future technology. However, this enhanced absorption is confined to a small spectral region about the ENZ wavelength. Thus, the achievement of broadband absorption from such materials is highly desired to allow these materials to be used in a range of optical devices, such as detectors, anti-reflective coatings, etc. In this work we demonstrate the achievement of near-perfect absorption in various ITO thin-films with Pt metal backings of thicknesses less than 25 nm. While NPA has previously been achieved in ITO films with a Pt backing > 100 nm [69], we demonstrate that the same effect can be achieved using a range of different metals and with backing thicknesses significantly thinner than ever previously considered. Furthermore, we provide the first study of ENZ-based NPA for various metal backings. The ability to achieve such NPA in such thin films makes the ITO – Metal structures in this research potential candidates for thermally stable alternative to gold-based near-field transducers in heat-assisted magnetic recording (HAMR) technology which are subject to thermal degradation with CW laser irradiation [70][71].

1.4 Liquid Phase Exfoliation of 2D Nanoflakes

A recently developed and unique method of synthesising 2D nanomaterials is Liquid Phase Exfoliation (LPE) which is a top-down method for synthesising stable dispersions of monolayer nanoflakes by high-shear mixing, sonication and size-selection via centrifugation [72]. This technique is readily used to produce a variety of 2D nanoflakes in dispersion by the Coleman Group in Trinity College Dublin. Of particular interest to this research are nanoflakes of hexagonal boron nitride (h-BN) nanoflakes [73]. These nanoflakes are highly interesting because they have a high refractive index which could make them useful in multi-layered structures, particularly for coupling to ENZ materials such as ITO due to the large mismatch of the refractive indices. However, one drawback of these nanoflakes is that they typically form rather rough surfaces when deposited on solid substrates and films and thus scatter light rather strongly. We aimed to examine the suitability of these 2D particles for coupling to such ENZ structures. However, in order to understand how these nanoflakes would behave in solid multi-layered structures it is first necessary to understand how they scatter light in solution and to find a theory that described this scattering process well. While scattering theory has existed for centuries and has been well understood since the mid-19th century from the works of physicists such as Mie, Rayleigh, and Tyndall, it's important to note that scattering theory is only well defined and well understood for homogenous spheres [74][75]. Scattering is particularly easy when dealing with such spheres as a sphere is the only geometric structure which can be perfectly defined by a single parameter, the radius, R. However, with the advent of highly anisotropic 2D nanomaterials such as h-BN nanoflakes, developing a scattering theory and understanding how these materials scatter light is a difficult challenge, particularly because such flakes require at least three dimensional parameters to be defined, the length, l, the width, w, and the thickness, t, all of which vary over each flake. In this work we set out to study the scattering behaviour of such 2D flakes. We found that the scattering from such films is highly irregular and cannot be easily and fully modelled from current existing scattering theories [76]. The irregular nature of the nanoflakes are not really suitable when making multi-layered nanoscale optical structures, as scattering of light dominate the optical response.

This thesis will begin by laying the foundation for the modelling of ITO and the physics of plasmons in Chapter 2 by describing the Drude model and the free electron gas. These models will then be applied to characterise the optical properties of commercial ITO films in Chapter 3. Chapter 4 will focus on experimental verification of ENZ mode excitation in ITO thin films and the achievement of NPA. In Chapter 5 we will discuss the fabrication of thin-film ITO for ENZ applications via various methods and present a recipe for producing high-quality ITO with ENZ behaviour in the near-infrared. Chapter 6 will present computational modelling of NPA via the excitation of the Ferrell-Berreman plasmon mode in ITO thin-films backed by various metals. Chapter 7 will then examine the scattering from high-refractive index two-dimensional boron nitride nanoflakes and examine their suitability for depositing on ENZ materials. Finally, Chapter 8 will give a summary of proposed future work as well as potential applications for this research.

References

[1] C. Yeh, *"Applied Photonics,"* Appl. Photonics, pp. 1-337, Jan 2012.

[2] R. S. Quimby, *"Photonics and Lasers,"* Wiley Online Library, 2006.

[3] L. Garwin and T. Lincoln, *"A Century of Nature: Twenty-One Discoveries that Changed Science and the World,"* University of Chicago Press, 2010.

[4] R. N. Hall, G. E. Fenner, J. D. Kingsley, T. J. Soltys, and R. O. Carlson, “Coherent light emission from GaAs junctions,” *Phys. Rev. Lett.*, vol. 9, no. 9, p. 366, 1962.

[5] M. I. Nathan, W. P. Dumke, G. Burns, F. H. Dill Jr, and G. Lasher, “Stimulated emission of radiation from GaAs p-n junctions,” *Appl. Phys. Lett.*, vol. 1, no. 3, pp. 62–64, 1962.

[6] A. M. Smith, "*Ptolemy and the Foundations of Ancient Mathematical Optics: A Source Based Guided Study*," vol. 83. American Philosophical Society, 1999.

[7] A. I. Sabra, “Ibn al-Haytham’s criticisms of Ptolemy’s Optics,” *J. Hist. Philos.*, vol. 4, no. 2, pp. 145–149, 1966.

[8] J. A. Vollgraff, “Snellius’ notes on the reflection and refraction of rays,” *Osiris*, vol. 1, pp. 718–725, 1936.

[9] A. I. Sabra and A. al-H. Sabra, "*Theories of Light: From Descartes to Newton*." CUP Archive, 1981.

[10] A. Rubinowicz, “Thomas Young and the theory of diffraction,” *Nature*, vol. 180, no. 4578, pp. 160–162, 1957.

[11] A. E. Becquerel, “The photovoltaic effect,” *Comptes Rendus*, vol. 9, p. 145, 1839.

[12] J. C. Maxwell, "*The Scientific Letters and Papers of James Clerk Maxwell: 1846-1862*," vol. 1. CUP Archive, 1990.

[13] S. Klassen, *“The photoelectric effect: Reconstructing the story for the physics classroom.”* Springer, 2011.

[14] D. M. Chapin, C. S. Fuller, and G. L. Pearson, “A new silicon p-n junction photocell for converting solar radiation into electrical power,” *J. Appl. Phys.*, vol. 25, no. 5, pp. 676–677, 1954.

[15] J. J. Coleman, “The development of the semiconductor laser diode after the first demonstration in 1962,” *Semicond. Sci. Technol.*, vol. 27, no. 9, p. 90207, 2012.

[16] M. Börner, “Mehrstufiges übertragungssystem für in Pulscodemodulation dargestellte Nachrichten,” *Schutzr. DE1254513*, 1967.

[17] N. Bilton, “Bits Pics: Kodak’s 1975 Model Digital Camera’,” *Blog New York Times*, 2010.

[18] S. Abbott, “Review of 20 years of undersea optical fiber transmission system development and deployment since TAT-8,” in *2008 34th European Conference on Optical Communication*, 2008, pp. 1–4.

[19] K. Yamada *et al.*, “High-performance silicon photonics technology for telecommunications applications,” *Sci. Technol. Adv. Mater.*, vol. 15, no. 2, p. 24603, 2014.

[20] E. R. H. Fuchs, E. J. Bruce, R. J. Ram, and R. E. Kirchain, “Process-based cost modeling of photonics manufacture: the cost competitiveness of monolithic integration of a 1550-nm DFB laser and an electroabsorptive modulator on an InP platform,” *J. Light. Technol.*, vol. 24, no. 8, pp. 3175–3186, 2006.

[21] J. Lundberg *et al.*, “Light tracking through ice and water—Scattering and absorption in

heterogeneous media with Photonics," *Nucl. Instruments Methods Phys. Res. Sect. A Accel. Spectrometers, Detect. Assoc. Equip.*, vol. 581, no. 3, pp. 619–631, 2007.

[22] C. Fenzl, T. Hirsch, and O. S. Wolfbeis, "Photonic crystals for chemical sensing and biosensing," *Angew. Chemie Int. Ed.*, vol. 53, no. 13, pp. 3318–3335, 2014.

[23] A. Di Falco, L. O'faolain, and T. F. Krauss, "Chemical sensing in slotted photonic crystal heterostructure cavities," *Appl. Phys. Lett.*, vol. 94, no. 6, p. 63503, 2009.

[24] L. Rindorf, J. B. Jensen, M. Dufva, L. H. Pedersen, P. E. Høiby, and O. Bang, "Photonic crystal fiber long-period gratings for biochemical sensing," *Opt. Express*, vol. 14, no. 18, pp. 8224–8231, 2006.

[25] V. V. Tuchin and V. Tuchin, "Tissue optics: light scattering methods and instruments for medical diagnosis," 2007.

[26] T. Vo-Dinh, "*Biomedical Photonics Handbook: Biomedical Diagnostics*." CRC press, 2014.

[27] G. E. Jellison Jr, L. A. Boatner, J. D. Budai, B.-S. Jeong, and D. P. Norton, "Spectroscopic ellipsometry of thin film and bulk anatase (TiO 2)," *J. Appl. Phys.*, vol. 93, no. 12, pp. 9537–9541, 2003.

[28] R. A. Synowicki, "Spectroscopic ellipsometry characterization of indium tin oxide film microstructure and optical constants," *Thin Solid Films*, vol. 313, pp. 394–397, 1998.

[29] S. Krimm and J. Bandekar, "Vibrational spectroscopy and conformation of peptides, polypeptides, and proteins," in *Advances in protein chemistry*, vol. 38, Elsevier, 1986, pp. 181–364.

[30] B. C. Stipe, M. A. Rezaei, and W. Ho, "Single-molecule vibrational spectroscopy and microscopy," *Science (80-.).*, vol. 280, no. 5370, pp. 1732–1735, 1998.

[31] M. Chen *et al.*, "X-ray photoelectron spectroscopy and auger electron spectroscopy studies of Al-doped ZnO films," *Appl. Surf. Sci.*, vol. 158, no. 1–2, pp. 134–140, 2000.

[32] R. Kumar *et al.*, "Study of optical band gap and carbonaceous clusters in swift heavy ion irradiated polymers with UV–Vis spectroscopy," *Nucl. Instruments Methods Phys. Res. Sect. B Beam Interact. With Mater. Atoms*, vol. 266, no. 8, pp. 1788–1792, 2008.

[33] K. S. Novoselov *et al.*, "Electric Field Effect in Atomically Thin Carbon Films," *Science (80-.).*, vol. 306, no. 5696, pp. 666 LP – 669, Oct. 2004.

[34] F. Bonaccorso, Z. Sun, T. Hasan, and A. C. Ferrari, "Graphene photonics and

optoelectronics," *Nat Phot.*, vol. 4, no. 9, pp. 611–622, 2010.

[35] Y. Cai, J. Zhu, and Q. H. Liu, "Tunable enhanced optical absorption of graphene using plasmonic perfect absorbers," *Appl. Phys. Lett.*, vol. 106, no. 4, p. 43105, 2015.

[36] Y. Zhang *et al.*, "Direct observation of a widely tunable bandgap in bilayer graphene," *Nature*, vol. 459, no. 7248, p. 820, 2009.

[37] Z. H. Ni, T. Yu, Y. H. Lu, Y. Y. Wang, Y. P. Feng, and Z. X. Shen, "Uniaxial strain on graphene: Raman spectroscopy study and band-gap opening," *ACS Nano*, vol. 2, no. 11, pp. 2301–2305, 2008.

[38] Q. Bao *et al.*, "Atomic-layer graphene as a saturable absorber for ultrafast pulsed lasers," *Adv. Funct. Mater.*, vol. 19, no. 19, pp. 3077–3083, 2009.

[39] J.-L. Xu, X.-L. Li, Y.-Z. Wu, X.-P. Hao, J.-L. He, and K.-J. Yang, "Graphene saturable absorber mirror for ultra-fast-pulse solid-state laser," *Opt. Lett.*, vol. 36, no. 10, pp. 1948–1950, 2011.

[40] E. Dremetsika *et al.*, "Measuring the nonlinear refractive index of graphene using the optical Kerr effect method," *Opt. Lett.*, vol. 41, no. 14, pp. 3281–3284, 2016.

[41] N. Vermeulen *et al.*, "Negative Kerr nonlinearity of graphene as seen via chirped-pulse-pumped self-phase modulation," *Phys. Rev. Appl.*, vol. 6, no. 4, p. 44006, 2016.

[42] J. Capmany, D. Domenech, and P. Muñoz, "Silicon graphene Bragg gratings," *Opt. Express*, vol. 22, no. 5, pp. 5283–5290, 2014.

[43] Y. Wu *et al.*, "Graphene-coated microfiber Bragg grating for high-sensitivity gas sensing," *Opt. Lett.*, vol. 39, no. 5, pp. 1235–1237, 2014.

[44] S. M. George, "Atomic layer deposition: an overview," *Chem. Rev.*, vol. 110, no. 1, pp. 111–131, 2009.

[45] U. Valbusa, C. Boragno, and F. B. De Mongeot, "Nanostructuring surfaces by ion sputtering," *J. Phys. Condens. Matter*, vol. 14, no. 35, p. 8153, 2002.

[46] F. Kurdesau, G. Khripunov, A. F. da Cunha, M. Kaelin, and A. N. Tiwari, "Comparative study of ITO layers deposited by DC and RF magnetron sputtering at room temperature," *J. Non. Cryst. Solids*, vol. 352, no. 9, pp. 1466–1470, 2006.

[47] K. L. Choy, "Chemical vapour deposition of coatings," *Prog. Mater. Sci.*, vol. 48, no. 2, pp. 57–170, 2003.

[48] A. Y. Cho and J. R. Arthur, "Molecular beam epitaxy," *Prog. solid state Chem.*, vol. 10,

pp. 157–191, 1975.

[49] R. Eason, *Pulsed laser deposition of thin films: applications-led growth of functional materials*. John Wiley & Sons, 2007.

[50] L. A. Ponomarenko *et al.*, “Density of States and Zero Landau Level Probed through Capacitance of Graphene,” *Phys. Rev. Lett.*, vol. 105, no. 13, p. 136801, Sep. 2010.

[51] J. Yoon, T. Y. Kim, W. Kim, Y. C. Jun, and C. K. Hwangbo, “Tunable Epsilon-Near-Zero ITO Thin Films and Broadband Perfect Absorption in the Near-Infrared,” in *Optical Interference Coatings 2016*, 2016, p. MD.7.

[52] S. Campione, I. Kim, D. De Ceglia, G. A. Keeler, and T. S. Luk, “Experimental verification of epsilon-near-zero plasmon polariton modes in degenerately doped semiconductor nanolayers,” *Opt. Express*, vol. 24, no. 16, pp. 18782–18789, 2016.

[53] J. Yoon, M. Zhou, M. A. Badsha, T. Y. Kim, Y. C. Jun, and C. K. Hwangbo, “Broadband Epsilon-Near-Zero Perfect Absorption in the Near-Infrared,” *Sci. Rep.*, vol. 5, p. 12788, 2015.

[54] L. J. Krayer, J. Kim, “Near-perfect absorption throughout the visible using ultra-thin metal films on index-near-zero substrates,” vol. 9, no. 1, pp. 330–338, 2019.

[55] Z. Tan *et al.*, “High-Performance Inverted Polymer Solar Cells with Solution-Processed Titanium Chelate as Electron-Collecting Layer on ITO Electrode,” *Adv. Mater.*, vol. 24, no. 11, pp. 1476–1481, 2012.

[56] W.-F. Wu and B.-S. Chiou, “Mechanical and optical properties of ITO films with anti-reflective and anti-wear coatings,” *Appl. Surf. Sci.*, vol. 115, no. 1, pp. 96–102, 1997.

[57] R. Maas, J. Parsons, N. Engheta, and A. Polman, “Experimental realization of an epsilon-near-zero metamaterial at visible wavelengths,” *Nat Phot.*, vol. 7, no. 11, pp. 907–912, 2013.

[58] N. Engheta, A. Alù, M. G. Silveirinha, A. Salandrino, and J. Li, “DNG, SNG, ENZ and MNZ metamaterials and their potential applications,” in *MELECON 2006-2006 IEEE Mediterranean Electrotechnical Conference*, 2006, pp. 258–261.

[59] H. Lobato-Morales, D. V. B. Murthy, A. Corona-Chavez, J. L. Olvera-Cervantes, J. Martinez-Brito, and L. G. Guerrero-Ojeda, “Permittivity Measurements at Microwave Frequencies Using Epsilon-Near-Zero (ENZ) Tunnel Structure,” *IEEE Trans. Microw. Theory Tech.*, vol. 59, no. 7, pp. 1863–1868, 2011.

[60] A. M. Mahmoud, I. Liberal, and N. Engheta, “Dipole-dipole interactions mediated by

epsilon-and-mu-near-zero waveguide supercoupling [Invited],” *Opt. Mater. Express*, vol. 7, no. 2, p. 415, 2017.

[61] Y. Li *et al.*, “On-chip zero-index metamaterials,” *Nat Phot.*, vol. 9, no. 11, pp. 738–742, 2015.

[62] A. M. Mahmoud and N. Engheta, “Wave–matter interactions in epsilon-and-mu-near-zero structures,” *Nat Commun*, vol. 5, 2014.

[63] F. Bello, A. F. Page, A. Pusch, J. M. Hamm, J. F. Donegan, and O. Hess, “Combining ε-Near-Zero Behavior and Stopped Light Energy Bands for Ultra-Low Reflection and Reduced Dispersion of Slow Light,” *Sci. Rep.*, vol. 7, no. 1, p. 8702, 2017.

[64] J. Luo, P. Xu, L. Gao, Y. Lai, and H. Chen, “Manipulate the Transmissions Using Index-Near-Zero or Epsilon-Near-Zero Metamaterials with Coated Defects,” *Plasmonics*, vol. 7, no. 2, pp. 353–358, 2012.

[65] T. Y. Kim, M. A. Badsha, J. Yoon, S. Y. Lee, Y. C. Jun, and C. K. Hwangbo, “General Strategy for Broadband Coherent Perfect Absorption and Multi-wavelength All-optical Switching Based on Epsilon-Near-Zero Multilayer Films,” *Sci. Rep.*, vol. 6, 2016.

[66] I. Liberal and N. Engheta, “Zero-Index Platforms: Where Light Defies Geometry,” vol. 2016. OSA, Optics & Photonics News, 2017.

[67] I. Liberal, A. M. Mahmoud, Y. Li, B. Edwards, and N. Engheta, “Photonic doping of epsilon-near-zero media (Submitted).”

[68] N. Kinsey, C. DeVault, J. Kim, M. Ferrera, V. M. Shalaev, and A. Boltasseva, “Epsilon-near-zero Al-doped ZnO for ultrafast switching at telecom wavelengths,” *Optica*, 2015.

[69] T. S. Luk *et al.*, “Enhanced third harmonic generation from the epsilon-near-zero modes of ultrathin films,” *Appl. Phys. Lett.*, vol. 106, no. 15, 2015.

[70] A. Datta and X. Xu, “Infrared Near-Field Transducer for Heat-Assisted Magnetic Recording,” *IEEE Trans. Magn.*, vol. 53, no. 12, pp. 1–5, 2017.

[71] W. M. Abbott *et al.*, “Solid state dewetting of thin plasmonic films under focused cw-laser irradiation,” *Acta Mater.*, vol. 145, pp. 210–219, 2018.

[72] V. Nicolosi, M. Chhowalla, M. G Kanatzidis, M. S Strano, and J. Coleman, "*Liquid Exfoliation of Layered Materials*," vol. 340. 2013.

[73] J. N. Coleman *et al.*, “Two-Dimensional Nanosheets Produced by Liquid Exfoliation of Layered Materials,” *Science (80-.).*, vol. 331, no. 6017, pp. 568 LP – 571, Feb. 2011.

[74] H. C. Hulst and H. C. van de Hulst, "*Light Scattering by Small Particles*." Dover Publications, 1981.

[75] C. F. Bohren and D. R. Huffman*, "Absorption and Scattering of Light by Small Particles."* Wiley, 2008.

[76] S A O’Brien and A Harvey and A Griffin and T Donnelly and D Mulcahy and J N Coleman and J F Donegan and D McCloskey, “Light scattering and random lasing in aqueous suspensions of hexagonal boron nitride nanoflakes,” *Nanotechnology*, vol. 28, no. 47, p. 47LT02, 2017.

Chapter 2: The Free Electron Gas, Bulk Plasmons and Surface Plasmon Polaritons

2.1 Introduction

In solid-state physics, materials can be neatly classified based on the energy separation between the valence and conduction bands. The valence band is the uppermost occupied energy state of a material in which electrons sit and the conduction band is the lowermost unoccupied state to which electrons can be promoted for cases of semiconductors and insulators while in metals the band is occupied [1]. It is convenient to separate materials into three categories, insulators which have a very large energy gap between their bands, semiconductors which have a small gap between bands, and metals which have an overlap between their valence and conduction band as represented in Figure 2.1. The case of metals is particularly interesting because no additional energy is needed to promote an electron to the conduction band of a metal due to the overlap between these bands, and thus electrons are free to conduct and move about the surface of the metal [2].

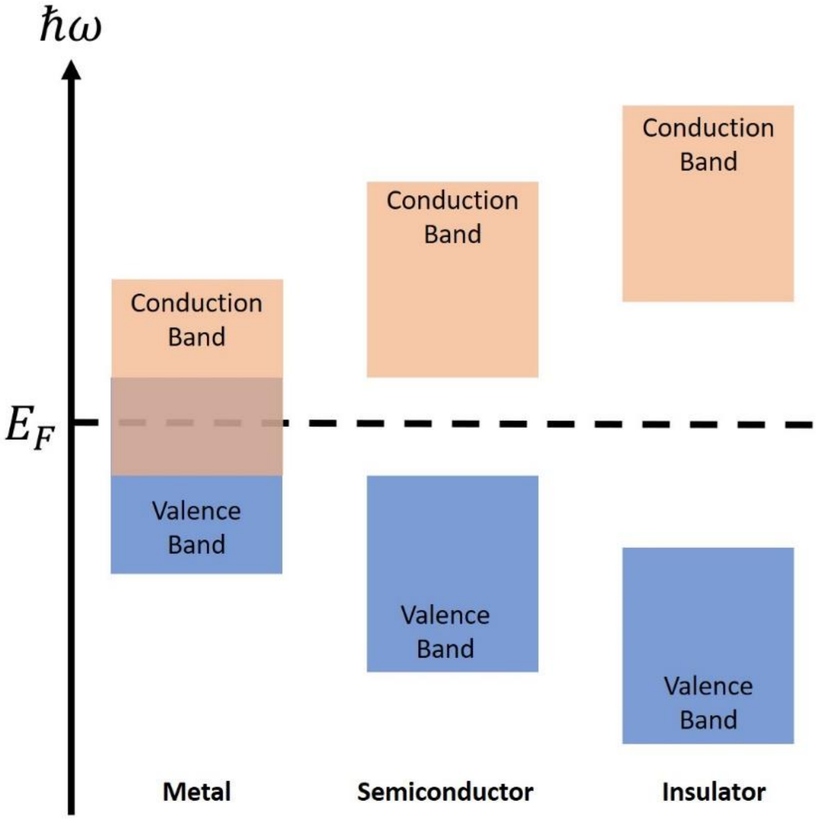

Figure 2.1 Schematic representation of the bands of a metal, semiconductor, and an insulator. The dashed line at an energy value of E_F is the Fermi level.

The freedom of electrons to conduct in a metal means that we can consider a metal to be a sea or gas of negative electrons moving about positive fixed ions. This gas of charged electrons in dynamic equilibrium is also known as a plasma [3]. The charged particles in this plasma are constantly in motion and this can lead to local charge fluctuations in the plasma. If a small region of excess charge forms due to a fluctuation, the charges in that volume will be repelled by the surrounding charges. The velocity acquired by these charges can cause them to overshoot their original position and they are then pulled back in the opposite direction. The result is an oscillation of the plasma, known as a plasma oscillation [4]. Such plasma oscillations occur in metals [5], doped semiconductors [6], and transparent conducting oxides (TCOs) [7]. Consider an oscillating electric field incident on a metal nanoparticle as depicted in Figure 2.2. The presence of the external electric field causes motion of the electrons in the nanoparticle leading to a separation of charges on either side of the nanoparticle. As the electric field oscillates, the electrons follow the field leading to a quantised oscillation of charge called a plasmon which oscillates at the plasma frequency, ω_p. A plasmon is a quasiparticle and is a quanta of plasma oscillation analogous to a phonon which is the quanta of a mechanical lattice vibration.

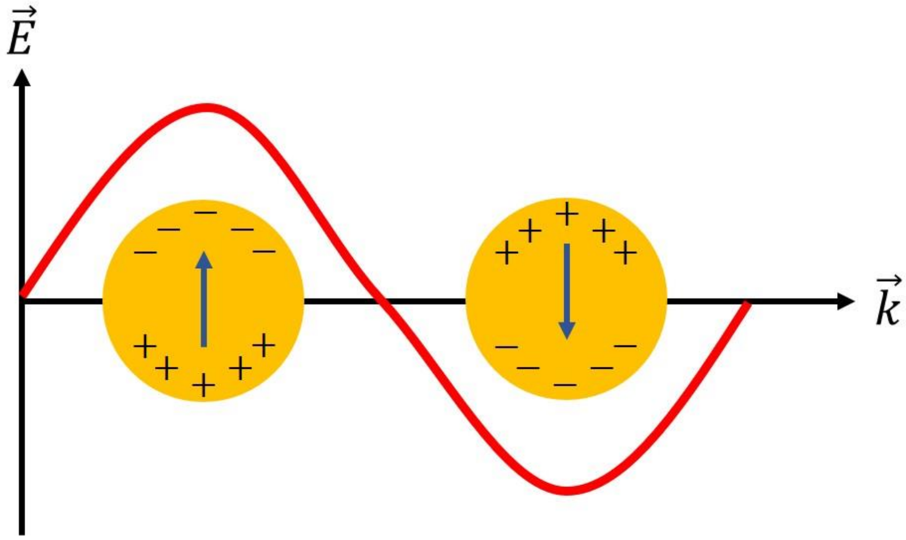

Figure 2.2 Representative diagram of a plasmon on spherical metal particles.

These discrete plasma oscillations create a hybrid particle plasma at optical frequencies resulting in a quasiparticle known as a plasmon polariton [8]. The field of plasmonic has led to the use of plasmons in various technologies and potential future technologies such as molecular sensing [9], plasmon based amplifiers [10][11], high-resolution lithography [12] and microscopy [13], full-colour holograms [14], and even cosmetics [15]. However, in order to understand plasmons, we must first understand the free-electron gas, and specifically the Drude Free-Electron Model.

2.2 The Drude Free-Electron Model for Dielectric Dispersion

The Drude model is a simple model to describe the motion of charge carriers in a metallic conductor. The model is founded on the principles of Boltzmann's kinetic theory for gases [16][17][18] with three added assumptions [3]. These assumptions are:

i. There exists a scattering time, τ such that the probability of scattering within a time interval dt is given by $\frac{d\tau}{\tau}$. The scattering time is a phenomenological parameter and can be described as the average time between scattering events.

ii. The momentum, $\overrightarrow{p_e}$ of an electron returns to zero after a scattering event with the stationary nucleus. While this is a crude assumption that would appear to violate the conservation of momentum, it works in the case of this model because if we take the mean momentum over a period of time, this is equivalent to averaging the momenta over all directions, i.e. $\langle\overrightarrow{p_e}\rangle = 0$.

iii. The electrons respond to external forces between scattering events, such as applied electric or magnetic fields in accordance with a Lorentz force, $\vec{F} = e(\vec{E} + \vec{v} \times \vec{B})$ [19][20].

Despite the simplicity of the model, it works extremely well at describing the motion of electrons in a metal. The oscillatory behaviour of electrons to an applied electric field can be considered as a harmonic oscillator. We start by equating the forces exerted on a charged particle, i.e.

$$m\vec{a} = \vec{F}_E + \vec{F}_d + \vec{F}_r \tag{1}$$

Where m is the electron mass, $\vec{a}$ is the total acceleration, $\vec{F}_E$, $\vec{F}_d$, and $\vec{F}_r$ are the force of the local E-field, the damping force, and restorative force respectively.

$$m\frac{d^2\vec{r}}{dt^2} + m\gamma\frac{d\vec{r}}{dt} + C\vec{r} = -e\vec{E}e^{-i\omega t} \tag{2}$$

Here $\gamma = \frac{1}{\tau}$ is the scattering rate and is the damping coefficient in the second term. While τ is the average time between scattering events, γ is the average number of scattering events that occur in one second. The constant C in the third restorative force term is zero for free electrons, i.e. the electrons in the metal experience no restoring force [4]. The value of this parameter C distinguishes the Lorentz oscillator model from the Drude model. If C is non-zero there is a restoring force and it is the Lorentz model, if $C = 0$ there is no restoring force and it is the Drude model. Given that the velocity is given by $\vec{v} = \frac{d\vec{r}}{dt}$ and the current density, $\vec{J}$ is defined by $\vec{J} = -Ne\vec{v}$ we can rewrite Equation 2 as

$$\frac{d\vec{J}}{dt} + \gamma\vec{J} = \left(\frac{Ne^2}{m}\right)\vec{E} \tag{3}$$

and assuming $\vec{J} = \vec{J}_0 e^{-i\omega t}$ and $\vec{E} = \vec{E}_0 e^{-i\omega t}$ we obtain

$$\frac{d}{dt}\left(\vec{J}_0 e^{-i\omega t}\right) + \gamma\vec{J}_0 e^{-i\omega t} = -i\omega\vec{J}_0 e^{-i\omega t} + \gamma\vec{J}_0 e^{-i\omega t} = \left(\frac{Ne^2}{m}\right)\vec{E}_0 e^{-i\omega t} \tag{4}$$

Multiplying across by ($e^{+i\omega t}$) yields

$$(-i\omega + \gamma)\vec{J} = \left(\frac{Ne^2}{m}\right)\vec{E}. \tag{5}$$

For static fields, $\omega = 0$:

$$\vec{J} = \left(\frac{Ne^2}{m\gamma}\right)\vec{E} = \sigma\vec{E} \tag{6}$$

where $\sigma = \frac{Ne^2}{m\gamma}$ is the static conductivity [21]. For an oscillating applied field, $\omega \neq 0$:

$$\vec{J} = \left(\frac{\sigma}{1 - \frac{i\omega}{\gamma}}\right)\vec{E} = \sigma_\omega\vec{E} \tag{7}$$

where σ_ω is the dynamic conductivity [22]. For low frequencies $\left(\frac{\omega}{\gamma} \ll 1\right)$, σ_ω is purely real and the electrons follow the applied electric field. As the frequency of the applied field increases, a phase lag is introduced due to the inertia of the electrons and σ_ω becomes complex [23]. For high frequencies $\left(\frac{\omega}{\gamma} \gg 1\right)$, the electrons oscillate out of phase by $\frac{\pi}{2}$ and σ_ω becomes purely imaginary. To relate this to the optical properties of a material we now examine Maxwell's equation for the electric field:

$$\nabla^2\vec{E} = \frac{1}{c}\frac{\partial^2\vec{E}}{\partial t^2} + \frac{1}{\varepsilon_0 c^2}\frac{\partial\vec{J}}{\partial t} \tag{8}$$

Substituting Equation 7 into Equation 8 gives

$$\nabla^2\vec{E} = \frac{1}{c^2}\frac{\partial^2\vec{E}}{\partial t} + \frac{1}{\varepsilon_0 c^2}\left(\frac{\sigma}{1 - \frac{i\omega}{\gamma}}\right)\frac{\partial\vec{E}}{\partial t} \tag{9}$$

where c is the vacuum speed of light, and ε_0 is permittivity of free space. This equation has solutions of the form $\vec{E} = \overrightarrow{E_0} e^{i(\vec{k}\cdot\vec{r} - \omega t)}$ where $k^2 = \frac{\omega^2}{c^2} + i\left(\frac{\sigma\omega\mu_0}{1 - \frac{i\omega}{\gamma}}\right)$, $c^2 = \frac{1}{\varepsilon_0\mu_0}$, and μ_0 is the magnetic permeability of free space. The wavevector k^2 can be represented as

$$k^2 = \frac{\omega^2}{c^2} + i\left(\frac{\sigma\omega\mu_0}{1 - \frac{i\omega}{\gamma}}\right) \cong i\sigma\omega\mu_0 = e^{i\frac{\pi}{2}}\sigma\omega\mu_0 \tag{10a}$$

$$\tilde{k} \cong \sqrt{e^{i\frac{\pi}{2}}\sigma\omega\mu_0} = e^{i\frac{\pi}{4}}\sqrt{\sigma\omega\mu_0} \tag{10b}$$

where $\tilde{k}$ now denotes the complex wavevector and is further simplified to

$$\tilde{k} = \left(\cos\frac{\pi}{2} + i\sin\frac{\pi}{4}\right)\sqrt{\sigma\omega\mu_0} = (1 + i)\sqrt{\frac{\sigma\omega\mu_0}{2}} \tag{11a}$$

$$k_R = k_I = \sqrt{\frac{\sigma\omega\mu_0}{2}} \tag{11b}$$

k_R and k_I are the real imaginary components of the complex wavevector. We can now represent this in terms of the real and imaginary components of the complex refractive index, n_R and n_L.

$$n_R = \left(\frac{c}{\omega}\right)k_R = \sqrt{\frac{\sigma c^2\mu_0}{2\omega}} = \sqrt{\frac{\sigma}{2\omega\varepsilon_0}} = n_I \tag{12}$$

The equation for a wave propagating in the +z-direction in a metal is given by

$$\vec{E} = \vec{E}_0 e^{-k_I z} e^{i(k_R \cdot z - \omega t)} = \vec{E}_0 e^{-\frac{z}{\sigma}} e^{i(k_R \cdot z - \omega t)} \tag{13}$$

and the skin depth [24], δ is

$$\delta = \frac{1}{k_I} = \sqrt{\frac{2}{\sigma\omega\mu_0}} = \sqrt{\frac{2\varepsilon_0 c^2}{\sigma\omega}} \tag{14}$$

Leading on from Equation 12 we can relate this to the refractive index

$$\begin{aligned} n^2 = \frac{c^2}{\omega^2}k^2 &= 1 + i\left(\frac{\sigma c^2\mu_0}{\omega\left(1 - i\frac{\omega}{\gamma}\right)}\right) \\ &= 1 + i\left(\frac{i\gamma}{i\gamma}\right)\left(\frac{\sigma c^2\mu_0}{\omega\left(1 - i\frac{\omega}{\gamma}\right)}\right) \\ &= 1 - \frac{\gamma\sigma c^2\mu_0}{\omega^2 + i\omega\gamma}. \end{aligned} \tag{15}$$

We now introduce a term, ω_p, the plasma frequency which is the frequency at which there is a collective oscillation of the charge density.

$$\omega_p^2 = \gamma\sigma c^2\mu_0 = \gamma\left(\frac{Ne^2}{m\gamma}\right)c^2\mu_0 = \frac{Ne^2}{m\varepsilon_0} \tag{16}$$

Thus, the dielectric permittivity, $\tilde{\varepsilon} = \tilde{n}^2$is given by

$$\tilde{\varepsilon}(\omega) = \tilde{n}^2(\omega) = 1 - \frac{\omega_p^2}{\omega(\omega + i\gamma)} \tag{17}$$

wDfhere the tilde diacritics signify that the parameters are complex, i.e. having both a real and imaginary component. For very high frequencies such that $\omega \gg \omega_p$, $\tilde{\varepsilon}(\omega)$ approaches unity, however in reality at higher frequencies, the function $\tilde{\varepsilon}(\omega)$ approached a specified value, ε_∞ known as the high-frequency permittivity limit [25]. Thus, a more precise expression for the dielectric dispersion is

$$\tilde{\varepsilon}(\omega) = \varepsilon_\infty - \frac{\omega_p^2}{\omega(\omega + i\gamma)} \tag{18}$$

When the electrons in the plasma are displaced from the uniform background of ions, the electric field builds up so as to restore the electrons back to their equilibrium positions, however the inertia of the electrons causes them to overshoot the equilibrium position and thus they oscillate around this position at the plasma frequency, ω_p. The plasma wavelength, λ_p is thus

$$\lambda_p = \ 2\pi c\left(\frac{Ne^2}{m\varepsilon_0}\right)^{-\frac{1}{2}} \tag{19}$$

Above λ_p the metal is opaque and highly reflective, but below λ_p the metal is transparent. While this model was originally devised to explain electrodynamics in metals, the model also works surprisingly well for other materials, such as transparent conducting oxides (TCOs). One such TCO that this model is readily applied to with great success is indium tin oxide (ITO). In this research, the Drude model is used to model the dielectric permittivity dispersion of ITO. Of particular interest to this research is the ENZ frequency, ω_{ENZ} which is the frequency at which the real component of the dielectric permittivity is zero. An expression for this parameter can be derived by considering Equation 18 separated into its real and imaginary components, i.e.

$$\tilde{\varepsilon}(\omega) = \varepsilon_\infty - \frac{\omega_p^2}{\omega^2 + \gamma^2} + i\frac{\omega_p^2\gamma}{\omega(\omega^2 + \gamma^2)} \tag{20}$$

Considering just the real component of the permittivity at the frequency, ω_{ENZ} at which this component is zero, we get

$$\varepsilon_\infty - \frac{\omega_p^2}{\omega_{ENZ}^2 + \gamma^2} = 0 \tag{21a}$$

$$\varepsilon_{\infty}\left(\omega_{\mathrm{ENZ}}^{2}+\gamma^{2}\right)=\omega_{\mathrm{p}}^{2} \tag{21b}$$

and hence [26]

$$\omega_{\mathrm{ENZ}}=\sqrt{\frac{\omega_{\mathrm{p}}^{2}}{\varepsilon_{\infty}}-\gamma^{2}} \tag{22}$$

where ω_{ENZ} is the wavelength at which the real component of the dielectric permittivity is zero.

2.3 Dispersion Relation for Bulk Plasmons and Surface Plasmon Polaritons

As mentioned above, a plasmon is the quasiparticle associated with the collective quantised oscillation of the charge density of a polar dielectric material. There are two types of plasmons: bulk plasmon polaritons and surface plasmon polaritons. In this section, we will derive the expression for the dispersion relation of both these plasmons [27][28][29].

2.3.1 Bulk Plasmons

We start by consider a conductive volume, V enclosed by a surface, S. Due to conservation of charge, any net flow of current into or out of the volume must be balanced by a change in the total charge density inside the surface, i.e.

$$\oint_{\mathrm{S}}\vec{\mathrm{j}}\cdot\mathrm{dS}=-\frac{\partial}{\partial\mathrm{t}}\int_{\mathrm{V}}\rho\mathrm{dV} \tag{23}$$

where $\vec{\mathrm{j}}$ is the current density, dS is the surface element, ρ is the charge density, and dV is the volume element. Applying the divergence theorem, i.e.

$$\int_{\mathrm{S}}\vec{\mathrm{j}}\cdot\mathrm{dS}=\int_{\mathrm{V}}\nabla\cdot\vec{\mathrm{j}}\mathrm{dV} \tag{24}$$

to Equation 23, we get that

$$\int_{\mathrm{V}}\nabla\cdot\vec{\mathrm{j}}\mathrm{dV}=-\int_{\mathrm{V}}\frac{\partial\rho}{\partial\mathrm{t}}\mathrm{dV} \tag{25}$$

and since the volume over which we are integrating is arbitrary, we can thus simplify this expression to

$$\nabla\cdot\vec{\mathrm{j}}=-\frac{\partial\rho}{\partial\mathrm{t}} \tag{26}$$

which is known as the charge continuity equation. In this derivation, we consider the collective motion of free electrons relative to the positive ions of the lattice which are considered to be fixed and motionless. Hence, only the charge density of electrons need be considered as the positive ions, being stationary, do not generate current. Equation 26 thus becomes

$$\nabla \cdot \vec{j} = -\frac{\partial \rho_e}{\partial t} \tag{27}$$

where ρ_e now denotes the charge density of electrons. Then considering Gauss' Law, i.e.

$$\nabla \cdot \vec{E} = \frac{\rho_e}{\varepsilon_0} \tag{28}$$

where ε_0 is the dielectric permittivity of free space; rearranging this to find an expression for ρ_e and substituting into Equation 26 we get

$$\nabla \cdot \left(\vec{j} + \varepsilon_0 \frac{\partial \vec{E}}{\partial t} \right) = 0 \tag{29}$$

i.e. a vector in terms of current density and local electric field whose divergence is zero. Mathematically, any vector whose divergence is zero can be rewritten as the curl of another vector which can be demonstrated by considering Maxwell's fourth equation

$$\nabla \times \vec{B} = \mu_0 \vec{j} + \frac{1}{c^2} \frac{\partial \vec{E}}{\partial t} \tag{30}$$

we can thus relate Equation 29 and Equation 30 as

$$\vec{j} + \varepsilon_0 \frac{\partial \vec{E}}{\partial t} = \frac{1}{\mu_0} \nabla \times \vec{B}. \tag{31}$$

Now, taking the time derivative of both sides and applying Maxwell's third equation, i.e.

$$\nabla \times \vec{E} = -\frac{\partial \vec{B}}{\partial t} \tag{32}$$

we obtain

$$\frac{\partial \vec{j}}{\partial t} + \varepsilon_0 \frac{\partial^2 \vec{E}}{\partial t^2} = -\frac{1}{\mu_0} \nabla \times \left(\nabla \times \vec{E} \right). \tag{33}$$

The electrons thus move in response to a local electric field according to their equation of motion

$$m \frac{d\vec{v}}{dt} = -e\vec{E} \tag{34}$$

where m is the electron mass, $\vec{v}$ is the velocity, and e is the charge of an electron. Taking the definition of the current density in terms of the carrier concentration, N

$$\vec{j} = -Ne\vec{v} \tag{35}$$

and taking its time derivative

$$\frac{\partial \vec{j}}{\partial t} = -Ne \frac{d\vec{v}}{dt} \tag{36}$$

we can now substitute the expression for $\frac{d\vec{v}}{dt}$ in Equation 34 to obtain

$$\frac{\partial \vec{J}}{\partial t} = -\frac{Ne^2}{m}\vec{E}\,. \tag{37}$$

This can then be substituted into Equation 33 to yield the equation of a harmonic oscillator.

$$-\frac{Ne^2}{m}\vec{E} + \varepsilon_0 \frac{\partial^2 \vec{E}}{\partial t^2} = -\frac{1}{\mu_0}\nabla \times (\nabla \times \vec{E}) \tag{38}$$

Using the definition of the plasma frequency from Section 2.2,

$$\omega_p = \sqrt{\frac{Ne^2}{m\varepsilon_0}} \tag{39}$$

and the fact that the speed of light in a vacuum is given by $\frac{1}{\varepsilon_0 \mu_0}$, Equation 38 can be simplified to

$$\frac{\partial^2 \vec{E}}{\partial t^2} - \omega_p^2 \vec{E} = -c^2 \nabla \times (\nabla \times \vec{E}) \tag{40}$$

which is the equation of a harmonic oscillator with natural resonant frequency of ω_p. It is now useful to consider the electric field as being composed of two components, a transverse component, $\vec{E}_t$ and longitudinal component $\vec{E}_l$, where $\vec{E} = \vec{E}_t + \vec{E}_l$ and

$$\nabla \cdot \vec{E}_t = 0 \tag{41a}$$

$$\nabla \times \vec{E}_l = 0. \tag{42b}$$

Substituting into Equation 40 gives

$$\frac{\partial^2 \vec{E}_t}{\partial t^2} + \omega_p^2 \vec{E}_t - c^2 \nabla^2 \vec{E}_t = -\left(\frac{\partial^2 \vec{E}_l}{\partial t} + \omega_p^2 \vec{E}_l\right) \tag{43}$$

and thus, we are left with 2 individual equations of motion, one for each component of the electric field:

$$\frac{\partial^2 \vec{E}_t}{\partial t^2} + \omega_p^2 \vec{E}_t - c^2 \nabla^2 \vec{E}_t = 0 \tag{44a}$$

$$\frac{\partial^2 \vec{E}_l}{\partial t^2} + \omega_p^2 \vec{E}_l = 0 \tag{44b}$$

Here we search for temporal and spatially varying solution to Equations 44a and 44b of the form $e^{i(k \cdot r - \omega t)}$. The solution to the Equation 43 and the transverse component of the electric field is

$$\omega^2 = \omega_p^2 + c^2 k^2 \tag{45}$$

and therefore, no propagating solutions with $\omega < \omega_p$ exist because the waves are reflected by the plasma. This is the reasons why metals are reflective below their plasma frequency, and transparent above. For the longitudinal case, Equation 45 has a dispersionless solution independent of the wavevector, k, i.e.

$$\omega = \omega_p \tag{46}$$

And thus, the medium can support longitudinal waves at the plasma frequency. These oscillations are a direct result of a zero valued relative permittivity, $\varepsilon_r = 0$. Consider once more Gauss' Law and the definition of the displacement field, $\vec{D} = \varepsilon_0 \varepsilon_r \vec{E}$, we get

$$\nabla \cdot \vec{D} = \nabla \cdot \left(\varepsilon_0 \varepsilon_r \vec{E}\right) \tag{47}$$

If $\varepsilon_r \neq 0$ then we have that $\nabla \cdot \vec{E} = 0$ which is the normal case for transverse EM waves in which the electric field is normal to the direction of wave propagation. However, if $\varepsilon_r = 0$, then Equation 47 can be satisfied by waves that have $\nabla \cdot \vec{E} \neq 0$, i.e. longitudinal waves. Thus, a dielectric can support longitudinal waves that satisfy the condition that $\varepsilon(\omega) = 0$. These longitudinal plasma oscillations behave as harmonic oscillators with natural resonant frequencies of ω_p.

However, it's important to note that while this derivation is classical, and the harmonic oscillator can take any energy, in reality the energy of the oscillator is quantised and can only take values that are multiples of Planck's reduced constant times the plasma frequency, $\hbar\omega_p$.

2.3.2 Surface Plasmon Polaritons (SPPs)

To derive the expression for the dispersion relation of an SPP we must solve Maxwell's equations for the electric, $\vec{E_i}$ and magnetic, $\vec{H_i}$ fields

$$\nabla \cdot \varepsilon_i \vec{E} = 0 \tag{48a}$$

$$\nabla \cdot \vec{H} = 0 \tag{48b}$$

$$\nabla \times \vec{E} = -\mu_0 \frac{\partial \vec{H}}{\partial t} \tag{48c}$$

$$\nabla \times \vec{H} = -\varepsilon_i \frac{\partial \vec{E}}{\partial t} \tag{48d}$$

where the subscript, i denotes the medium and the equations are subject to the boundary conditions

Dielectric Side $$\vec{H}_d = \left(0, \vec{H}_{y_d} 0\right) e^{i(k_{x_d} x + k_{z_d} z - \omega t)} \tag{49a}$$

$z > 0$: $$\vec{E}_d = \left(\vec{E}_{x_d}, 0, \vec{E}_{z_d}\right)e^{i(k_{x_d}x + k_{z_d}z - \omega t)} \tag{49b}$$

Metal Side $$\vec{H}_m = \left(0, \vec{H}_{y_m} 0\right)e^{i(k_{x_m}x + k_{z_m}z - \omega t)} \tag{49c}$$

$z < 0$: $$\vec{E}_m = \left(\vec{E}_{x_m}, 0, \vec{E}_{z_m}\right)e^{i(k_{x_m}x + k_{z_m}z - \omega t)} \tag{49d}$$

where $z = 0$ is the boundary between the dielectric and metal. At the boundary, the $\vec{E}_x$, $\vec{H}_y$, and $\vec{D}_z = \varepsilon_i \vec{E}_{z_i}$ fields must all be continuous, i.e. at $z = 0$

$$\vec{E}_{x_d} = \vec{E}_{x_m} \tag{50a}$$

$$\vec{H}_{y_d} = \vec{H}_{y_m} \tag{50b}$$

$$\varepsilon_d \vec{E}_{z_d} = \varepsilon_m \vec{E}_{z_m} \tag{50c}$$

Replacing the d and m with j to represent any given layer, the magnetic curl equation is then calculated.

$$\begin{aligned} \nabla \times \vec{H}_j = \varepsilon_j \frac{\partial \vec{E}}{\partial t} &= \left(\frac{\partial \vec{H}_{z_j}}{\partial t} - \frac{\partial \vec{H}_{y_j}}{\partial t}, \frac{\partial \vec{H}_{x_j}}{\partial t} - \frac{\partial \vec{H}_{z_j}}{\partial t}, \frac{\partial \vec{H}_{y_j}}{\partial t} - \frac{\partial \vec{H}_{x_j}}{\partial t}\right) \\ &= \left(-ik_{z_j}\vec{H}_{y_j}, 0, ik_{x_j}\vec{H}_{y_j}\right) = \left(-i\omega\varepsilon_j \vec{E}_{x_j}, 0, -i\omega\varepsilon_j \vec{E}_{z_j}\right) \end{aligned} \tag{51}$$

Comparing both sides and dividing across by common parameters gives

$$k_{z_j}\vec{H}_{y_j} = \omega\varepsilon_j \vec{E}_{x_j} \tag{52}$$

and thus, the electric and magnetic fields in the metal and dielectric can be related as

$$k_{z_d}\vec{H}_{y_d} = \omega\varepsilon_d \vec{E}_{x_d} \tag{53a}$$

$$k_{z_m}\vec{H}_{y_m} = \omega\varepsilon_m \vec{E}_{x_m} \tag{53b}$$

Since the transverse components of the electric and magnetic fields must be continuous at the boundary, such that $\vec{H}_{y_d} = \vec{H}_{y_m}$ and $\vec{E}_{x_d} = \vec{E}_{x_m}$, these equations can thus be related,

$$\frac{k_{z_d}}{\varepsilon_d}\vec{H}_{y_d} = \frac{k_{z_m}}{\varepsilon_m}\vec{H}_{y_m} \tag{54}$$

giving the condition for a surface plasmon to exist, i.e.

$$\frac{k_{z_d}}{\varepsilon_d} = \frac{k_{z_m}}{\varepsilon_m} \tag{55}$$

and $\mathrm{k}_{\mathrm{x}_\mathrm{d}} = \mathrm{k}_{\mathrm{x}_\mathrm{m}} = \mathrm{k}_\mathrm{x}$. For any electromagnetic wave $\mathrm{k}^2 = \varepsilon_\mathrm{j}\left(\frac{\omega}{\mathrm{c}}\right)^2 = \mathrm{k}_{\mathrm{x}_\mathrm{j}}^2 + \mathrm{k}_{\mathrm{z}_\mathrm{j}}^2$ thus for a surface plasmon polariton we obtain an expression for the SPP mode dispersion in both the metal and dielectric

$$\mathrm{k}_{\mathrm{SPP}} = \mathrm{k}_{\mathrm{x}_j} = \frac{\omega}{\mathrm{c}}\sqrt{\frac{\varepsilon_\mathrm{d}\varepsilon_\mathrm{m}}{\varepsilon_\mathrm{d}+\varepsilon_\mathrm{m}}} \tag{56}$$

Where $k_x = k\sin\theta$ is the x-component of the k-vector and θ is the incident angle. It is important to note that both

$$\mathrm{k}_\mathrm{x} = \mathrm{k}_\mathrm{x}' + \mathrm{i}\mathrm{k}_\mathrm{x}'' \tag{57}$$

and

$$\mathrm{k}_{\mathrm{z}_j} = \mathrm{k}_{\mathrm{z}_j}' + \mathrm{i}\mathrm{k}_{\mathrm{z}_j}'' = \pm\sqrt{\varepsilon_j\left(\frac{\omega}{\mathrm{c}}\right)^2 - \mathrm{k}_\mathrm{x}^2} \tag{58}$$

are complex numbers and for bound SPP modes $\mathrm{k}_{\mathrm{z}_\mathrm{j}}$ must be purely imaginary, i.e. $\varepsilon_\mathrm{d} + \varepsilon_\mathrm{m} < 0$ and hence $|\mathrm{k}_\mathrm{x}| > \sqrt{\varepsilon_\mathrm{j}}\left(\frac{\omega}{\mathrm{c}}\right)$. k_x' must be real and $\varepsilon_\mathrm{m}' < -\varepsilon_\mathrm{d}$. Figure 2.3 shows a representative schematic of an SPP and Figure 2.4 shows a representative graph of non-radiative and bound plasmon modes.

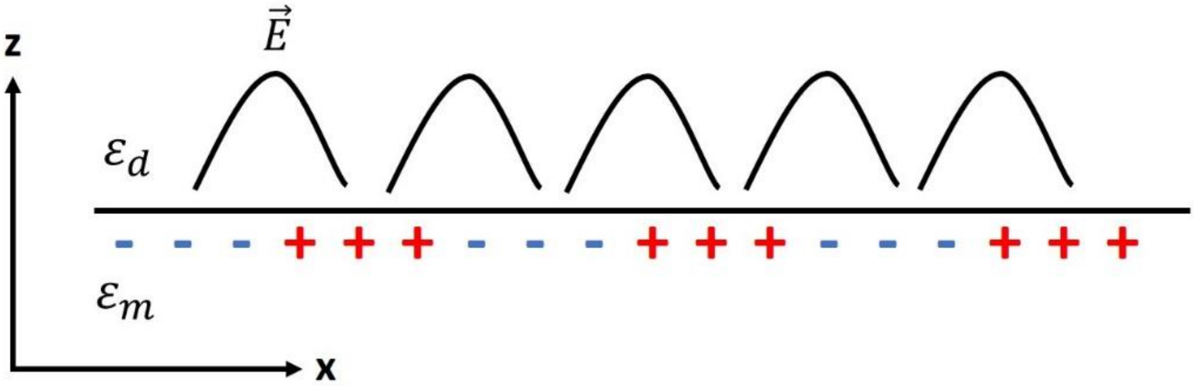

Figure 2.3 Schematic demonstrating the propagation of a surface plasmon polariton at the interface between a metal and a dielectric.

Figure 2.4 compares the dispersion of a bulk plasmon as derived in the previous section and a surface plasmon polariton. Considering the bulk plasmon dispersion again, for frequencies below ω_p, light is reflected, thus there are only evanescent fields in the medium and no propagating modes. For $\omega > \omega_\mathrm{p}$ the dispersion is given by

$$\omega(\mathrm{k}) = \sqrt{\omega_\mathrm{p}^2 + \mathrm{c}^2\mathrm{k}^2} \tag{59}$$

which follows an asymptotic to the free space light line $\omega = \mathrm{ck}$. However, for an SPP the light line for the dielectric is given by

$$\omega = \frac{\mathrm{ck_x}}{\sqrt{\varepsilon_\mathrm{d}}} \tag{60}$$

where ε_d is the permittivity of the dielectric. As shown in Figure 2.4, there are three frequency regions. The first of these is when $0 < \omega < \frac{\omega_\mathrm{p}}{\sqrt{1+\varepsilon_\mathrm{d}}}$ in which ε_m and $(\varepsilon_\mathrm{m} + \varepsilon_\mathrm{d})$ are both negative and thus the wavevector, $\mathrm{k_x}$, is real. At low frequencies $|\varepsilon_\mathrm{m}|$ is large and thus the dispersion curve approaches the light line. The second is when $\frac{\omega_\mathrm{p}}{\sqrt{1+\varepsilon_\mathrm{d}}} < \omega < \omega_\mathrm{p}$ in which ε_m, but $(\varepsilon_\mathrm{m} + \varepsilon_\mathrm{d})$ is positive. This results in an imaginary $\mathrm{k_x}$ and thus there are no propagating modes. The final frequency region to consider is when $\omega > \omega_\mathrm{p}$ in which ε_m and $(\varepsilon_\mathrm{m} + \varepsilon_\mathrm{d})$ are both positive and real solutions for $\mathrm{k_x}$ can be found. At high frequencies, ε_m approaches unity and the dispersion tends towards the limit of $\omega = \frac{\mathrm{ck_x}\sqrt{1+\varepsilon_\mathrm{d}}}{\varepsilon_\mathrm{d}}$. In the first frequency region, the group velocity is zero for large $\mathrm{k_x}$ and $\mathrm{k_x}$ approaches infinity in the limit when $(\varepsilon_\mathrm{m} + \varepsilon_\mathrm{d})$ approaches zero. Thus, by solving the expression

$$\varepsilon_\mathrm{m}(\omega) = -\varepsilon_\mathrm{d} \tag{61}$$

we can find an expression for the surface plasmon frequency, ω_sp for an undamped plasma

$$\omega_\mathrm{sp} = \frac{\omega_\mathrm{p}}{\sqrt{1+\varepsilon_\mathrm{d}}} \tag{62}$$

as shown in Figure 2.4.

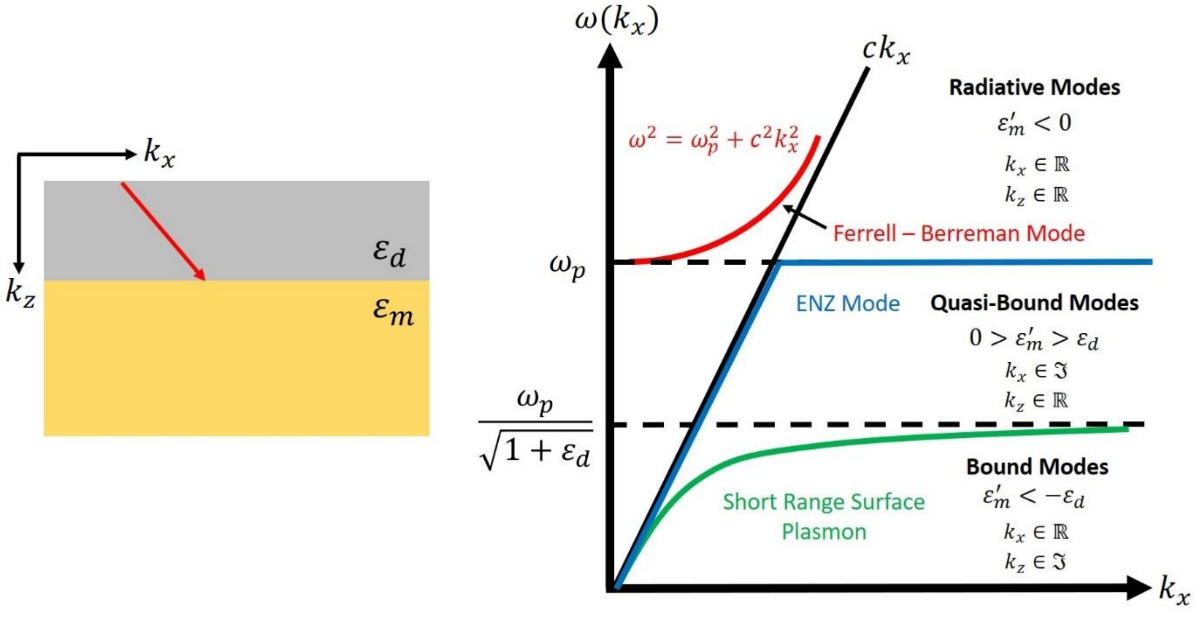

Figure 2.4 Representative figure of the radiative, quasi-bound, and bound plasmon modes in a metal-dielectric structure. The mode lying to the left of the light line and above the plasma frequency, ω_p is a

bulk plasmon mode. The bound mode below $\frac{\omega_p}{\sqrt{1+\varepsilon_d}}$ and to the right of the light line is a bound surface plasmon polariton mode and the modes lying between these two values are long-range surface plasmon modes.

The spatial extent of the fields in the z direction can thus be determined by considering the $\mathrm{k_z}$ vector in the metal and dielectric.

$$\mathrm{k_{z_d}} = \frac{\omega}{c}\sqrt{\frac{-\varepsilon_d^2}{\varepsilon_m + \varepsilon_d}} \tag{63a}$$

$$\mathrm{k_{z_m}} = \frac{\omega}{c}\sqrt{\frac{-\varepsilon_m^2}{\varepsilon_m + \varepsilon_d}} \tag{63b}$$

The field decay length, $\mathrm{L_z}$ can thus be determined by $1/\mathrm{k_z}$. While bulk plasmons, lying to the left of the light line can be excited from air, SPPs require prism coupling to match the momentum of light to the mode. Prism coupling allows access to greater angles of incidence, θ and hence higher values of k_x, this is typically achieved using the Kretschmann excitation geometry.

2.4 Epsilon – Near – Zero (ENZ) Modes

Epsilon – Near – Zero (ENZ) modes are plasmon modes that result from materials having a near-zero dielectric permittivity. In this thesis, two of these modes will studied, The radiative ENZ mode, more commonly known as the "Ferrell – Berreman" mode and the non-radiative ENZ mode, simply referred to as the "ENZ mode". These modes are labelled on the dispersion plots in Figure 2.4. As shown, the Ferrell – Berreman mode is a radiative bulk plasmon mode, which is a quantised oscillation of the charge density over the bulk of the film, transverse to the surface.

The ENZ mode is a dispersionless, long – range, surface plasmon polariton mode as shown, however the existence of this mode is highly dependent on the skin depth, δ_s of the material. The skin depth is the distance at which the magnitude of an incident electric field drops to a value of $1/e$ of the incident field, where e is Euler's mathematical constant.

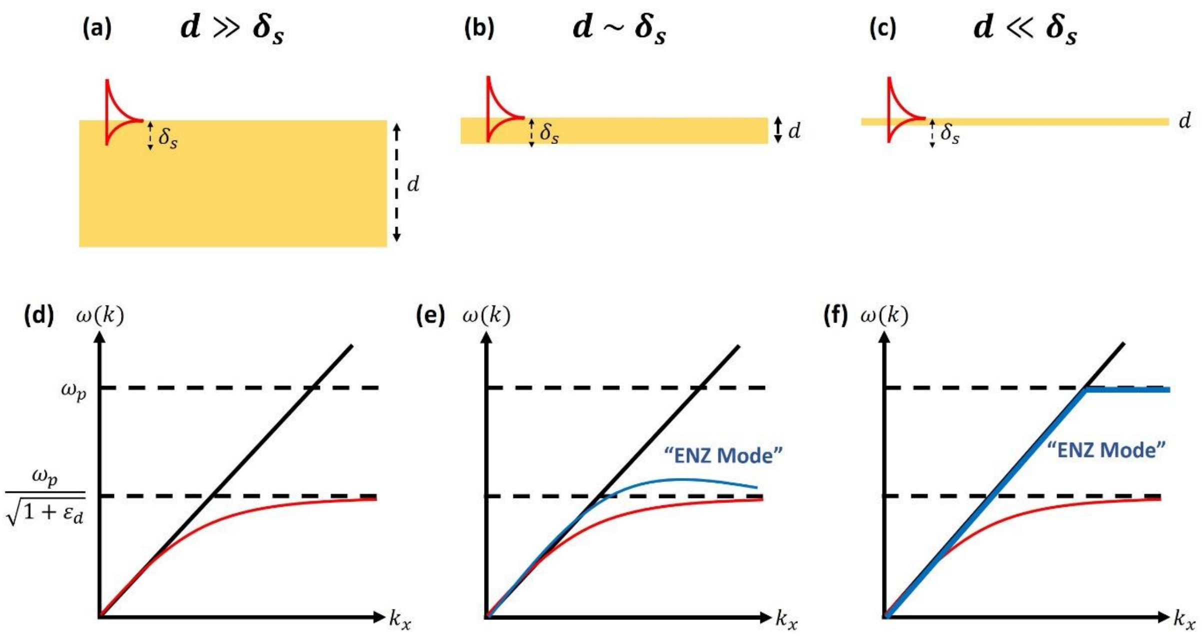

Figure 2.5 (a – b) Schematic diagram of the thickness of a material relative to its skin depth, and (d – f) the corresponding surface plasmon modes than can be excited in such a film.

Figure 2.5 (a – c) presents schematic diagrams of a metal films compared to their skin depths and (d – f) shows the surface plasmon modes that can be excited in such films. Three cases are shown; where the thickness is much larger than the skin depth ($d \gg \delta_s$), where the two thicknesses are comparable ($d \sim \delta_S$), and where the thickness is much smaller than the skin depth ($d \ll \delta_S$). As shown, when the thickness is much larger than the skin depth, only a bound, short-range, surface plasmon mode can be excited. However, when the thickness is comparable to the skin depth, a quasi-bound, long-range, surface plasmon can now be excited. This is the ENZ mode. In materials where the thickness is much smaller than the skin depth, the ENZ mode follows the light line and plateaus at the plasma frequency, ω_p resulting in a dispersionless surface plasmon mode. These modes will be discussed in further detail in Chapter 4.

2.5 The Fresnel Equations for Reflectivity and Transmission

In Section 2.2 we arrived at an expression for the dielectric permittivity of a metal / conductive oxide in Equation 20. This the permittivity can be related to the refractive index of the medium by the expression

$$n = \sqrt{\varepsilon_r \mu_r} \tag{64}$$

where μ_r is the relative magnetic permeability. The purpose of using this model was to simulate the reflection and transmission from thin films via the Transfer Matrix Method which will be discussed in Chapter 4. The basis of this method is solving the Fresnel equations for thin films. The Fresnel equations are a set of equations that relate the amplitudes, phases, and polarisations of transmitted and reflected waves at the boundary between two materials of different refractive indices. We consider a plane wave propagating towards the boundary between two materials of refractive indices n_1 and n_2 as depicted in Figure 2.6.

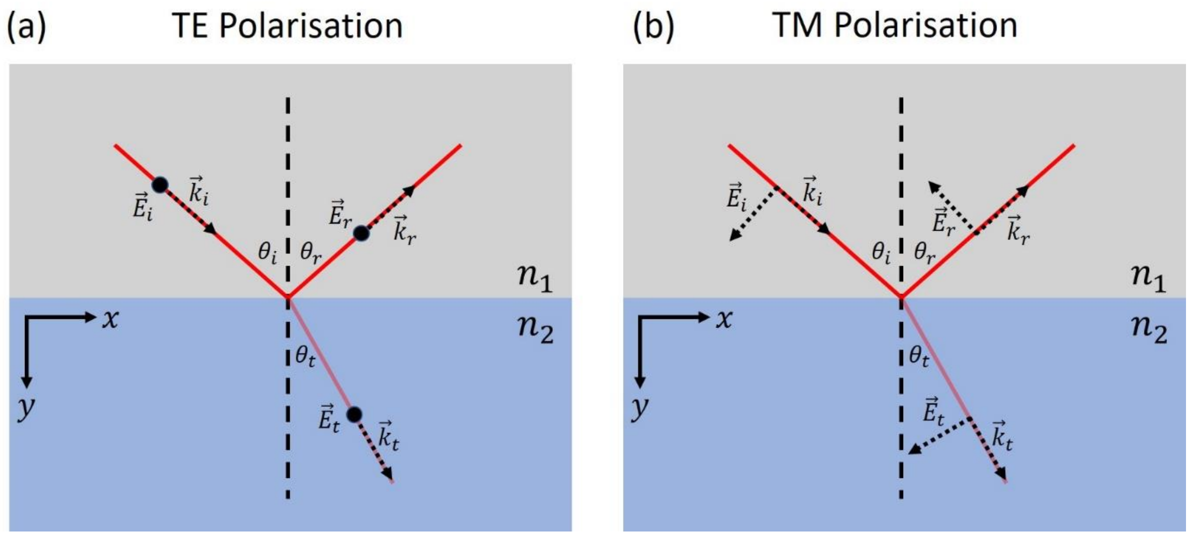

Figure 2.6 Schematic of light incident on the boundary between two media of refractive indices n_1 and n_2 with electric field orientations for (a) TE and (b) TM polarisation.

The incident wavevector, $\vec{k}_i$ is oriented an angle θ_i from the surface normal of the boundary. The incident and transmitted angles can thus be related using Snell's Law

$$n_1 \sin\theta_i = n_2 \sin\theta_t \tag{65}$$

where θ_t is the angle of transmission with respect to the surface normal. As all the films considered in this research are non-magnetic, we can assume that the magnetic permeability is unity for all media. We can also split the incident field into two components, one component with the electric field transverse to the surface, TE (s-polarisation) and one component parallel to the surface, TM (p-polarisation). The Fresnel equations are thus derived by considering the continuity condition of the tangential component of electric field, $\vec{E}$ at the boundary. We can thus relate the amplitudes of the incident, E_i, reflected, E_r, and transmitted, E_t as

$$E_i \cos\theta_i + E_r \cos\theta_r = E_t \cos\theta_t \tag{66}$$

and for the magnetic field for which all components are colinear

$$H_i - H_r = H_t. \tag{67}$$

The magnetic field can be related to the electric field as

$$\vec{H} = \sqrt{\frac{\varepsilon_r}{\mu_r}}\vec{E}$$

which for μ_r = 1 becomes

$$\vec{H} = \sqrt{\varepsilon_r}\vec{E} = n\vec{E}. \tag{68}$$

Equation 67 then becomes

$$n_1(E_i - E_r) = n_2 E_t \tag{69}$$

and by defining the reflection and transmission coefficients as $r = {}^{E_r}/_{E_i}$ and $t = {}^{E_t}/_{E_i}$ respectively, we can combine these with Equation 66 to obtain these components in terms of the refractive indices and incident angles, i.e.

$$r_{TM} = \frac{(n_1 \cos\theta_t - n_2 \cos\theta_i\,)}{(n_1 \cos\theta_i + n_2 \cos\theta_t\,)} \tag{70a}$$

$$r_{TE} = \frac{(n_1 \cos\theta_i - n_2 \cos\theta_t\,)}{(n_1 \cos\theta_i + n_2 \cos\theta_t\,)} \tag{70b}$$

$$t_{TM} = \frac{2n_1 \cos\theta_i}{(n_1 \cos\theta_t + n_2 \cos\theta_i\,)} \tag{70c}$$

$$t_{TE} = \frac{2n_1 \cos\theta_i}{(n_1 \cos\theta_i + n_2 \cos\theta_t\,)} \tag{70d}$$

where the TE and TM subscripts denote the corresponding polarisations. To calculate the absolute reflectivity and transmission, we use

$$R = |r|^2 \tag{71a}$$

$$T = \frac{n_2 \cos\theta_t}{n_1 \cos\theta_i}|t|^2. \tag{71b}$$

The absorption in a thin film can also be calculated from these parameters for either polarisation by using the rather simple expression

$$A = 1 - T - R \tag{72}$$

where A is the absorption.

2.5.1 The Brewster Angle

There exists a particular case when $\theta_i + \theta_t = 90°$ where all incident light polarised parallel to the plane of incidence is transmitted, and thus all reflected light is of TE polarisation, and TM polarisation is zero. To demonstrate this, the TE and TM reflectivity is plotted as a function of angle from Equations (71a) and (71b) for light incident on Si (n_{Si} = 1.54) from air (n_{air} = 1.00). As shown in Figure 2.7, the reflectivity for TM polarisation reaches a minimum of zero at 55.6° incidence, corresponding to the Brewster angle.

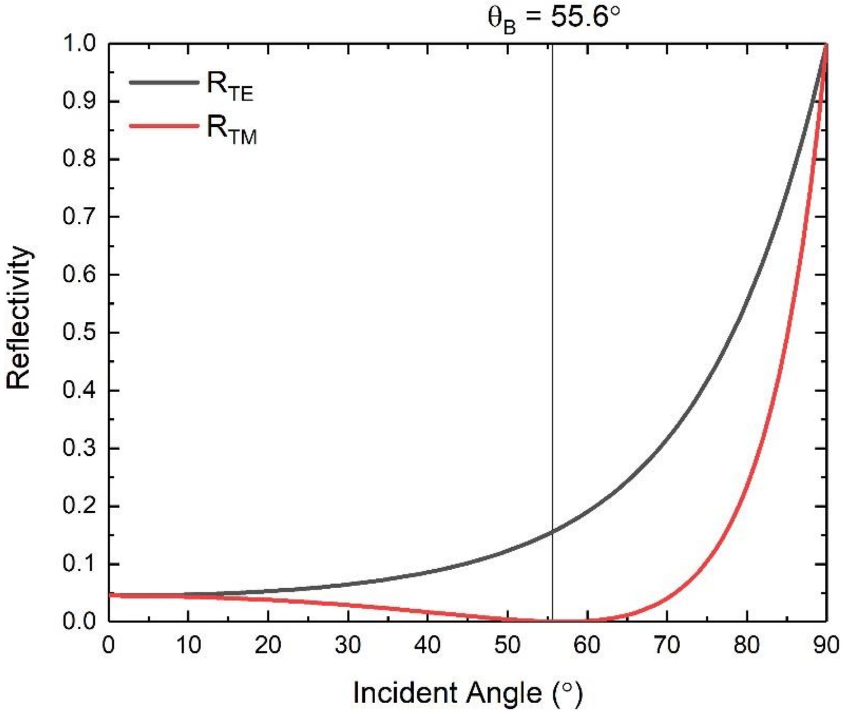

Figure 2.7 Calculation for TE (black) and TM (red) polarised reflectivity of light incident from air on Si as a function of angle. The reflectivity at θ_B = 55.6° reaches zero, corresponding to the Brewster angle for Si.

This phenomenon will used in Figure 4.3 of Chapter 4 as a calibration of the lowest measurable reflectivity signal that can be measured by the custom-built angle-resolved reflectivity system used for experimental measurements. The specifications and layout of this system will also be discussed in Chapter 4.

2.6 Conclusion

In this chapter we discussed plasma oscillations in the free-electron gas and plasmons. Derivations were carried for the dispersion relations of both bulk plasmons and surface plasmon polaritons. Furthermore, the Drude free-electron model for metals was discussed and how it can be used to devise a robust and surprisingly accurate expression for the dielectric permittivity of a metal and other materials with free-electrons. Finally, we briefly discussed the Fresnel equations for measuring the reflectivity and transmission from thin films in terms of the optical constants and the angles of incidence and transmission. The theory presented in this chapter forms the basis for the physics discussed in later chapters. The Drude model discussed in this chapter will be used to model the permittivity as a function of frequency for ITO, and the plasmon dispersions discussed will be applied to plasmon modes excited in thin-film ITO. Furthermore, the Fresnel equations outlined here will be solved by means of the Transfer Matrix Method for multilayer thin films.

References

[1] C. Kittel, P. McEuen, and P. McEuen, "*Introduction to Solid State Physics,*" vol. 8. Wiley New York, 1996.

[2] Y. Baer, P. F. Heden, J. Hedman, M. Klasson, C. Nordling, and K. Siegbahn, “Band structure of transition metals studied by ESCA,” *Phys. Scr.*, vol. 1, no. 1, p. 55, 1970.

[3] N. W. Ashcroft and N. D. Mermin, "*Solid State Physics*." Cengage Learning, 2011.

[4] M. Fox, *"Optical Properties of Solids",* American Journal of Physics 70, 1269, 2002.

[5] R. A. Ferrell, “Predicted radiation of plasma oscillations in metal films,” *Phys. Rev.*, vol. 111, no. 5, p. 1214, 1958.

[6] H. R. Philipp and H. Ehrenreich, “Optical properties of semiconductors,” *Phys. Rev.*, vol. 129, no. 4, p. 1550, 1963.

[7] D. C. Paine, B. Yaglioglu, and J. Berry, “Characterization of TCO materials,” in *Handbook of Transparent Conductors*, Springer, 2011, pp. 111–148.

[8] S. Zeng, D. Baillargeat, H.-P. Ho, and K.-T. Yong, “Nanomaterials enhanced surface plasmon resonance for biological and chemical sensing applications,” *Chem. Soc. Rev.*, vol. 43, no. 10, pp. 3426–3452, 2014.

[9] H. M. Hiep *et al.*, “A localized surface plasmon resonance based immunosensor for the detection of casein in milk,” *Sci. Technol. Adv. Mater.*, vol. 8, no. 4, pp. 331–338, 2007.

[10] A. M. Livani and H. Kaatuzian, “Design and simulation of an electrically pumped Schottky-junction-based plasmonic amplifier,” *Appl. Opt.*, vol. 54, no. 9, pp. 2164–2173, 2015.

[11] K. Lewotsky, “The promise of plasmonics,” *SPIE Prof.*, 2007.

[12] Y. Kim, S. Kim, H. Jung, E. Lee, and J. W. Hahn, “Plasmonic nano lithography with a high scan speed contact probe,” *Opt. Express*, vol. 17, no. 22, pp. 19476–19485, 2009.

[13] T. Huang and X.-H. N. Xu, “Synthesis and characterization of tunable rainbow colored colloidal silver nanoparticles using single-nanoparticle plasmonic microscopy and spectroscopy,” *J. Mater. Chem.*, vol. 20, no. 44, pp. 9867–9876, 2010.

[14] K. M. Wilson and L. Bradley, *“Dynamic structural colour in thin film stacks and patterned nanoparticle arrays,”* PhD Thesis, Trinity College Dublin, 2018.

[15] B. H. Chung, Y. T. Lim, J. K. Kim, J. Y. Jeong, and T. H. Ha, “Cosmetic pigment composition containing gold or silver nano-particles.” Patent No. EP1909745A1, Korea Research Institute of Bioscience and Biotechnology KRIB, 2009.

[16] S. Chapman, T. G. Cowling, and D. Burnett, *"The mathematical theory of non-uniform gases: an account of the kinetic theory of viscosity, thermal conduction and diffusion in gases,"* Cambridge University Press, 1990.

[17] J. O. Hirschfelder, C. F. Curtiss, R. B. Bird, and M. G. Mayer, "*Molecular Theory of Gases and Liquids,*" vol. 165. Wiley New York, 1964.

[18] R. L. Liboff, *"Kinetic Theory: Classical, Quantum, and Relativistic Descriptions,"* Springer Science & Business Media, 2003.

[19] D. J. Griffiths, "*Introduction to Electrodynamics*," Prentice Hall, New Jersey, 1962.

[20] H. D. Young, R. A. Freedman, T. R. Sandin, and A. L. Ford, "*University Physics*," vol. 9. Addison-Wesley Reading, MA, 1996.

[21] M. W. C. Dharma-Wardana, “Static and dynamic conductivity of warm dense matter within a density-functional approach: Application to aluminum and gold,” *Phys. Rev. E,* vol. 73, no. 3, p. 36401, 2006.

[22] V. M. Adamyan, A. A. Mihajlov, N. M. Sakan, V. A. Srećković, and I. M. Tkachenko, “The dynamic conductivity of strongly non-ideal plasmas: is the Drude model valid?,” *J. Phys. A Math. Theor.*, vol. 42, no. 21, p. 214005, 2009.

[23] A. V Pronin, A. Pimenov, A. Loidl, and S. I. Krasnosvobodtsev, “Optical Conductivity and Penetration Depth in MgB_2,” *Phys. Rev. Lett.*, vol. 87, no. 9, p. 97003, Aug. 2001.

[24] J. F. Cochran and C. A. Shiffman, “Magnetic-Field Dependence of the Rf Skin Depth of Gallium,” *Phys. Rev.*, vol. 140, no. 5A, pp. A1678–A1688, Nov. 1965.

[25] J. M. G. Barthel and R. Buchner, “High frequency permittivity and its use in the investigation of solution properties,” *Pure Appl. Chem.*, vol. 63, no. 10, pp. 1473–1482, 1991.

[26] J. Yoon, M. Zhou, M. A. Badsha, T. Y. Kim, Y. C. Jun, and C. K. Hwangbo, “Broadband Epsilon-Near-Zero Perfect Absorption in the Near-Infrared,” *Sci. Rep.*, vol. 5, p. 12788, 2015.

[27] M. Fox, *"Optical Properties of Solids"*, American Journal of Physics 70, 1269, 2002.

[28] S. A. Maier, "*Plasmonics: Fundamentals and Applications*," Springer Science & Business Media, 2007.

[29] S. Zouhdi, A. Sihvola, and A. P. Vinogradov, "*Metamaterials and Plasmonics: Fundamentals, Modelling, Applications*," Springer Science & Business Media, 2008.

Chapter 3: Optical Properties and Characterisation of Indium Tin Oxide

3.1 Introduction

Indium tin oxide (ITO) is a ternary compound consisting of indium (In), tin (Sn) and oxygen (O) in varying proportions. It is a material that has garnered much attention and has readily worked its way into our daily lives due to its unique and tuneable electrical [1], optical [2], and thermal properties [3]. Depending on the oxygen content, it can be considered a ceramic or an alloy [4]. Typically, ITO is sold commercially as an oxygen saturated material. Its attraction to the industrial and research worlds is due to a combination of two properties that together make the material rather special: it is highly transparent at visible wavelengths with transmission values of 90 – 95% [5]. and exhibits a high conductivity [6][7][8], allowing it to be used in the production of transparent electronics. It also exhibits exceptional thermal stability with a very high melting point of between 1530 – 1930˚C [9]. ITO is classified as a transparent conductive oxide (TCO), however specifically, it is a degenerately doped semiconductor (Sn doped In_2O_3) with a large concentration of dopant Sn and a large direct bandgap of in the range 3.5 – 4.3 eV [10]. Typically, ITO is sold commercially as a 10:90 wt.% proportion of SnO_2 and In_2O_3 however other stoichiometries can be purchased or deposited. While the electrical conductivity and the visible range transparency make this such an attractive material, there is a trade-off in both of these parameters; as thickness and conductivity of an ITO film increase, the transparency decreases [5]. Careful control of the deposition conditions, particularly the temperature and oxygen content of the atmosphere are required [11][12][13]. The usual methods of deposition are radio-frequency (RF) [14][15][16] and direct current (DC) [17][18][19] magnetron sputtering, however other physical vapour deposition (PVD) techniques are also possible. ITO is predominantly used as an optoelectronic material with applications ranging from capacitive touchscreens for smart phones [20], smart windows [21], infrared anti-reflective coatings [22] to electromagnetic interference shielding [23]. ITO is even used on aeroplane windows [24] as a means of defrosting the windows via resistive heating when applying a current through the ITO film.

In this chapter, the basic optical and electrical properties of ITO will be discussed, particularly the application of the Drude model to commercial ITO films. The ITO examined in this chapter was purchased from Sigma-Aldrich as thin-films deposited on a glass substrate. The films had quoted sheet resistances of 8 – 12 Ω sq^{-1}, 30 – 60 Ω sq^{-1}, and 70 – 100 Ω sq^{-1}. This chapter will focus on the properties of ITO using these commercial samples as a basis and will include optical characterisations that will be used in further chapters.

3.2 Transmission Spectra of ITO Thin Films

The transmission (T), reflection (R), and absorption (A) data of our commercial ITO samples are presented in Figure 3.1. These measurements, taken using a Perkin-Elmer Lambda 1050 UV-Vis-NIR spectrophotometer at normal incidence, show a transmission of > 85% at visible wavelengths for all samples as would be expected of ITO. While all samples also exhibit a gradual decrease in transmission at longer wavelengths, the thicker, 8 – 12 Ω sq^{-1} sample exhibits significantly larger decrease in the region above 1000 nm. This decrease in transmission can be attributed to the significant difference in thickness of this samples (127 nm) for the 30 – 60 Ω sq^{-1} and 70 – 1000 Ω sq^{-1} samples (17 nm and 11 nm respectively) as well as the oxygen content. The thicknesses of these films was determined using spectroscopic ellipsometry as outlined in Section 3.4. This aligns well with what is expected of ITO. At longer wavelengths in the NIR range the film becomes more metallic behaving and highly reflective. The 8 – 12 Ω sq^{-1} ITO sample visually showed a slight yellow coloration and this corresponds to a decrease in transmission (and hence an increase in reflection) shown about 550 nm. In Figure 3.1(c) the absorption, calculated by taking $A = 1 - T - R$, of the ITO films is shown to be relatively low, particularly for the thicker 8 – 12 Ω sq^{-1} film. While the absorption is relatively low at normal incidence, it is important to note that ITO can also exhibit very high absorption features at oblique angles in the NIR as a result of a near-zero permittivity. The reflectivity as a function of wavelength and incident angle will be discussed in Chapter 4.

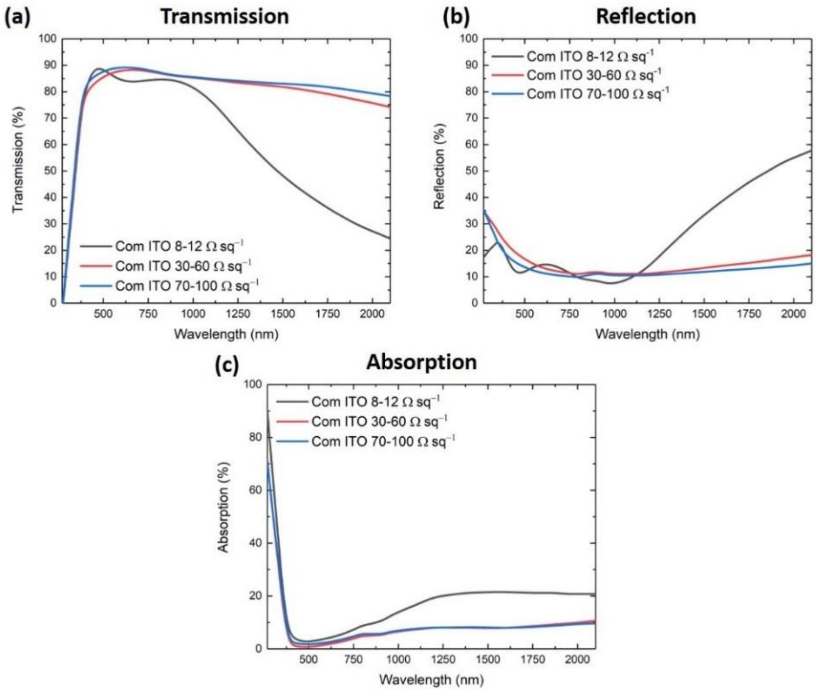

Figure 3.1 (a) Transmission, (b) reflection, and (c) absorption of thin-film commercial ITO samples at normal incidence.

3.3 Bandgap of ITO

As previously mentioned, ITO is a highly degenerately doped semiconductor with a large bandgap between 3.5 – 4.3 eV. The bandgap of ITO and many other materials can be determined from absorption data by representing the data on a Tauc plot. A Tauc plot, first devised by Jan Tauc [25] is plot of the parameter $(\alpha h\nu)^r$against the energy, $h\nu$, where α is the absorption coefficient, h is Planck's constant, ν is the frequency, and the exponent r describes the type of transition. The value of r used in these plots is indicative of different types of transitions from the valence to the conduction band. The significance of r and the corresponding types of transitions is outlined in Table 3.1.

r	Transition Type
$1/2$	Direct Allowed
$3/2$	Direct Forbidden
2	Indirect Allowed
3	Indirect Forbidden

Table 3.1 Significance of the values of the exponent, r to the transitions they describe.

Figure 3.2 shows Tauc plots for the three Sigma-Aldrich commercial samples. These plots were produced from the absorption data for the ITO films presented in Figure 3.1(c). Since ITO is a direct bandgap semiconductor, a value of $r = 1/2$, corresponding to direct allowed transitions, was used. The linear regions shown in plots the in Figure 3.2 were fitted and extrapolated to the abscissa. The energy value on the abscissa with which the extrapolated linear trend intersects gives the bandgap of the material being examined. All plots in Figure 3.2 give a bandgap value of around $E_g = 4.04$ eV. This is within the range of values expected of ITO. All trendlines fit the measured data with coefficients of determination, $R^2 > 0.97$ for all samples.

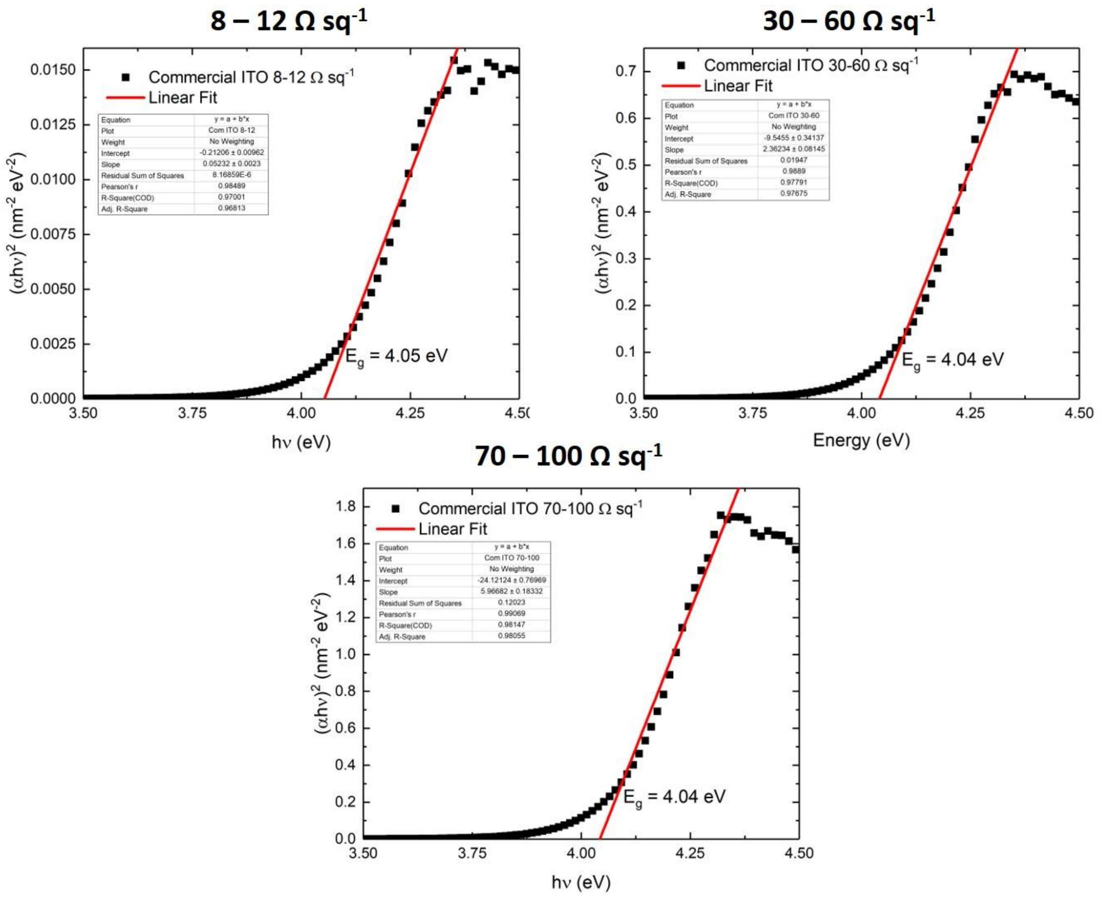

Equation	y = a + b*x
Plot	Com ITO 8-12
Weight	No Weighting
Intercept	-0.21206 ± 0.00962
Slope	0.05232 ± 0.0023
Residual Sum of Squares	8.16859E-6
Pearson's r	0.98489
R-Square(COD)	0.97001
Adj. R-Square	0.96813

Equation	y = a + b*x
Plot	Com ITO 30-60
Weight	No Weighting
Intercept	-9.5455 ± 0.34137
Slope	2.36234 ± 0.08145
Residual Sum of Squares	0.01947
Pearson's r	0.9889
R-Square(COD)	0.97791
Adj. R-Square	0.97675

Equation	y = a + b*x
Plot	Com ITO 70-100
Weight	No Weighting
Intercept	-24.12124 ± 0.76969
Slope	5.96682 ± 0.18332
Residual Sum of Squares	0.12023
Pearson's r	0.99069
R-Square(COD)	0.98147
Adj. R-Square	0.98055

Figure 3.2 Tauc Plots for absorption data obtained thin-film commercial ITO samples (a) 8 – 12 Ω sq^{-1}, (b) 30 – 60 Ω sq^{-1}, and 70 – 100 Ω sq^{-1}. All samples exhibit a bandgap of around 4.04 eV.

3.4 Spectroscopic Ellipsometry of ITO

Spectroscopic ellipsometry measurements in the 500 nm – 1650 nm spectral range were performed using a J. A. Woollam Co. HS-190 ellipsometer at discrete incident angles of 65˚, 70˚, 75˚, and 80˚. For each sample measured, the optical properties of the films were fitted to experimental data measured between 65° and 80° with a 5° step, while the optical constants of the substrate were considered known. Here, the unscreened plasma frequency is given by ω_p, while f_j, γ_j, and $E_{0_j} = \hbar\omega_{0_j}$ define the Lorentz oscillator term according to strength, damping factor, and energy respectively.

$$\varepsilon(\omega) + i\varepsilon(\omega) = \varepsilon_\infty - \frac{\omega_p^2}{\omega^2 - i\gamma_D\omega} + \sum_{j=1}^{m} \frac{f_j\omega_p^2}{\omega_{0_j}^2 - \omega^2 - i\gamma_j\omega} \tag{1}$$

Surface roughness was accounted for in each of the samples through the Bruggeman effective-medium approximation, as described by Aspnes et al. [26]. The complex permittivity was thus determined from this data using the relations

$$\varepsilon_r = n^2 - \kappa^2 \tag{2a}$$

$$\varepsilon_i = 2n\kappa \tag{2b}$$

where ε_r and ε_i are the real and imaginary components of the complex permittivity respectively. Of particular interest in this thesis is the region about 1200 nm where $n = \kappa$ and $\varepsilon_r = 0$. This is the epsilon-near-zero region which while be discussed in Chapter 4.

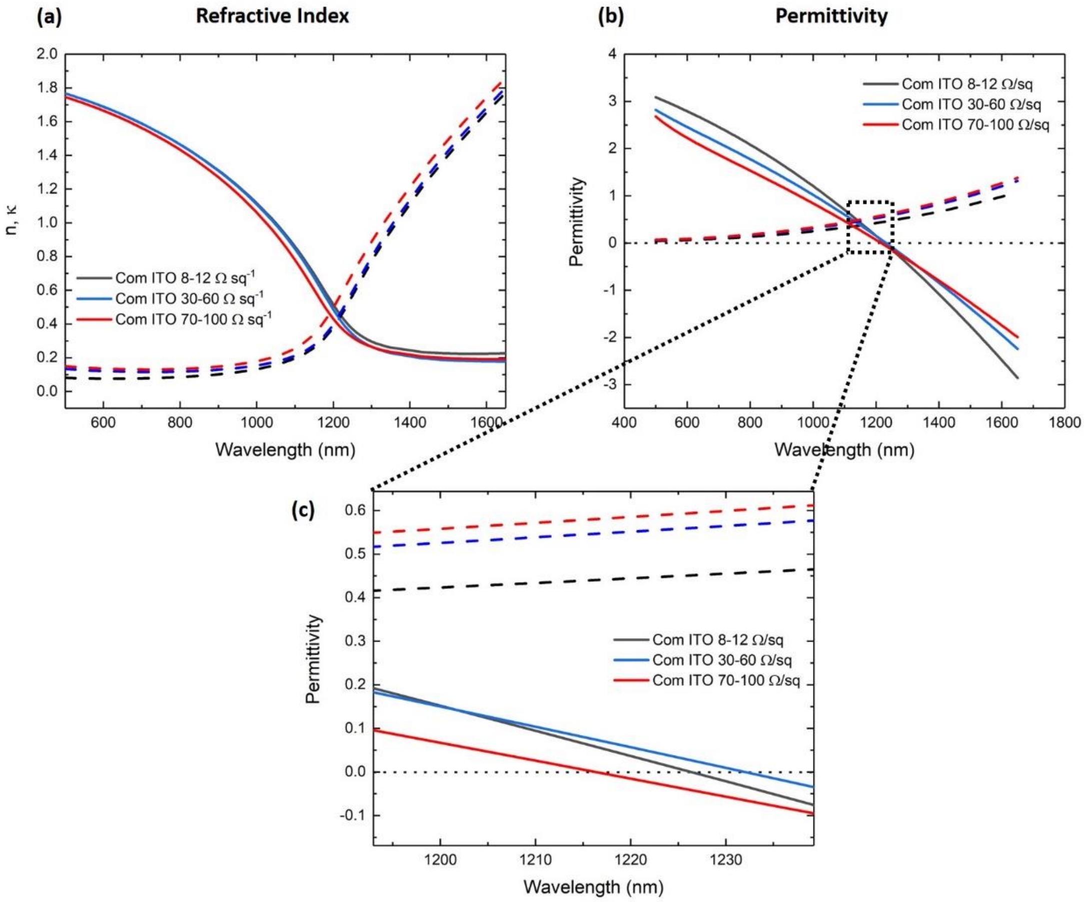

Figure 3.3 Real (solid lines) and imaginary (dashed lines) components of the complex refractive index of commercially purchased thin film samples of ITO on Glass and (b) the corresponding real and imaginary components of the dielectric permittivity. As shown in (c) the real component of the permittivity reaches zero (black dashed line) about 1225 nm.

The ITO films were reported by the manufacturer as having nominal thicknesses of 140 nm, 45 nm, and 20 nm for the 8 – 12 Ω sq^{-1}, 30 – 60 Ω sq^{-1}, and 70 – 100 Ω sq^{-1} samples respectively. However, to determine the precise thickness of each ITO film, further visible range ellipsometry was carried out on one sample from each range using an ITO library file in the CompleteEASE software. Four measurements were carried out on each sample at different incident angles. The true respective film thicknesses were thus determined to be 127 nm, 17 nm, and 11 nm with an error margin of ± 10 nm for each sample. Table 3.2 presents this data as well as the ENZ wavelength, λ_{ENZ} calculated from Equation 22 of Chapter 2, and the real and imaginary values of the permittivity of the films at λ_{ENZ}. As shown, λ_{ENZ} varies by 16 nm between the thinnest and thickest samples and $Im(\varepsilon)$ varies by a value of 0.12, suggesting lower absorption in the thinner samples, as expected and consistent with Figure 3.1(c).

Sample	**Thickness (nm)**	**λ_{ENZ} (nm)**	**$Re(\varepsilon)$ at λ_{ENZ}**	**$Im(\varepsilon)$ at λ_{ENZ}**
8 – 12 Ω sq^{-1}	127 ± 10	1216	0	0.58
30 – 60 Ω sq^{-1}	17 ± 10	1226	0	0.56
70 – 100 Ω sq^{-1}	11 ± 10	1232	0	0.46

Table 3.2 Measured sheet resistances, thicknesses, ENZ wavelength, and the real and corresponding components of the dielectric permittivity at that wavelength for the commercial samples of ITO purchased from Sigma Aldrich.

ITO can readily be modelled using the rather simple Drude free-electron model [27][28][29], and hence the data in Figure 3.3(b) was fitted to a Drude model and is presented in Figure 3.4. The following section will outline the basis of the Drude model and a derivation of the relations that will be readily used throughout this thesis to model the electrical and optical properties of ITO.

3.5 Drude Model Fits for ITO Thin Films

The real and imaginary components of the complex permittivity from Figure 3.3(b) were simultaneously fitted to the real and imaginary components of the Drude model dielectric dispersion expression in Equation 20 of Chapter 2. The results of those of fits are presented in Figure 3.4 and the fitted parameters are presented in Table 3.3. As shown in Figure 3.4 and as would be expected from ITO, the experimental ellipsometry data fit a Drude model exceptionally well with a correlation coefficient of > 0.98 for all samples. Some minor variation in the plasma frequency, ω_p is noted between samples as well as a significant variation in the high-frequency permittivity limit and the damping parameter, γ which suggests significantly more scattering in the thinner ITO films. The standard errors on all fitted parameters in Table 3.3 were less than 0.02.

Sample	**ε_∞**	**ω_p (rad fs^{-1})**	**γ (rad fs^{-1})**
8 – 12 Ω sq^{-1}	3.65960	2.95757	0.189305
30 – 60 Ω sq^{-1}	3.15153	2.74525	0.278178
70 – 100 Ω sq^{-1}	2.82058	2.63297	0.325611

Table 3.3 Fitted parameters of the Drude model for commercial ITO films.

Extracting these fitted parameters from Table 3.3 was essential as these values were required to properly model the behaviour of our ITO films in our various simulations and numerical calculations throughout this thesis. The transfer-matrix method, complex eigenfrequency analysis, and COMSOL finite element method (FEM) simulations discussed in Chapter 4 and Chapter 6 all required these parameters as input.

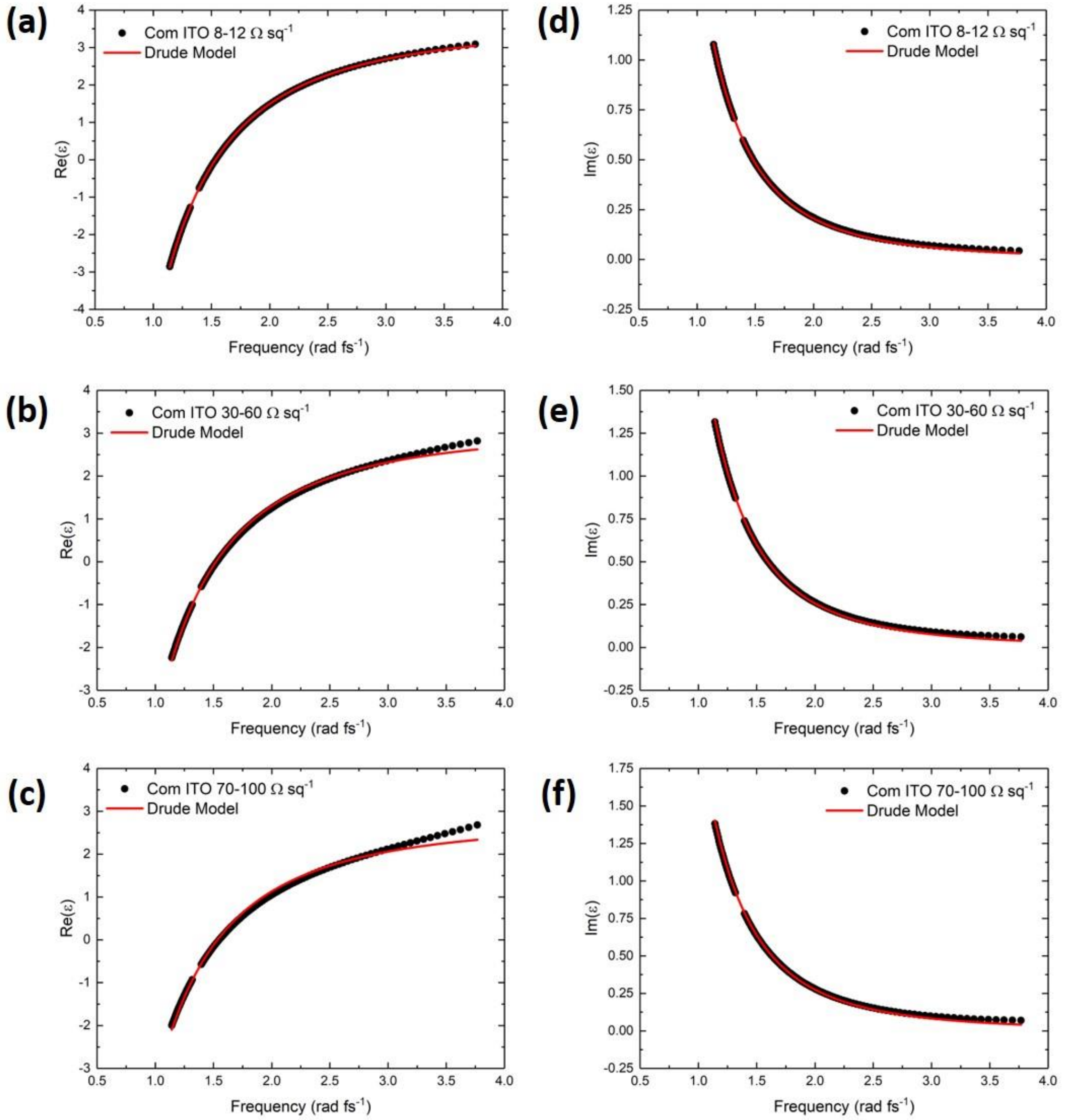

Figure 3.4 Drude models fits for the ellipsometry data carried out on the commercial samples of ITO thin films. (a – c) show the fits of the real component of the permittivity for the 8 – 12 Ω sq^{-1}, 30 – 60 Ω sq^{-1}, and the 70 – 100 Ω sq^{-1} samples and (d – f) show the fits for the corresponding imaginary components.

3.6 Resistivity, Conductivity, and Carrier Concentration of ITO

As previously mentioned, the conductivity of ITO is one of the properties that make it such an attractive material in both industry and research. The samples thus far have been referred to by the range of sheet resistances specified by the manufacturer. The ranges given for these films are quite broad, particularly for the thinner 30 – 60 Ω sq^{-1}and 70 – 100 Ω sq^{-1} samples. The reason for this is that sheet resistance, measured in ohms per square (Ω sq^{-1}) varies significantly with film thickness. The sheet resistance is defined more precisely as the bulk resistivity, ρ (in Ω·cm) divided by the film thickness, t (in cm) [43], i.e.

$$R_s = \frac{\rho}{t} \tag{3}$$

The sheet resistances and hence conductivities of the ITO films were determined precisely using a four-point probe system.

3.6.1 Four-Point Probe Technique

The four-point probe technique to measure the resistivity of a bulk or thin film material consists of four colinear metallic pins contacting the surface of the material to be measured. Figure 3.5 presents a schematic of the setup used.

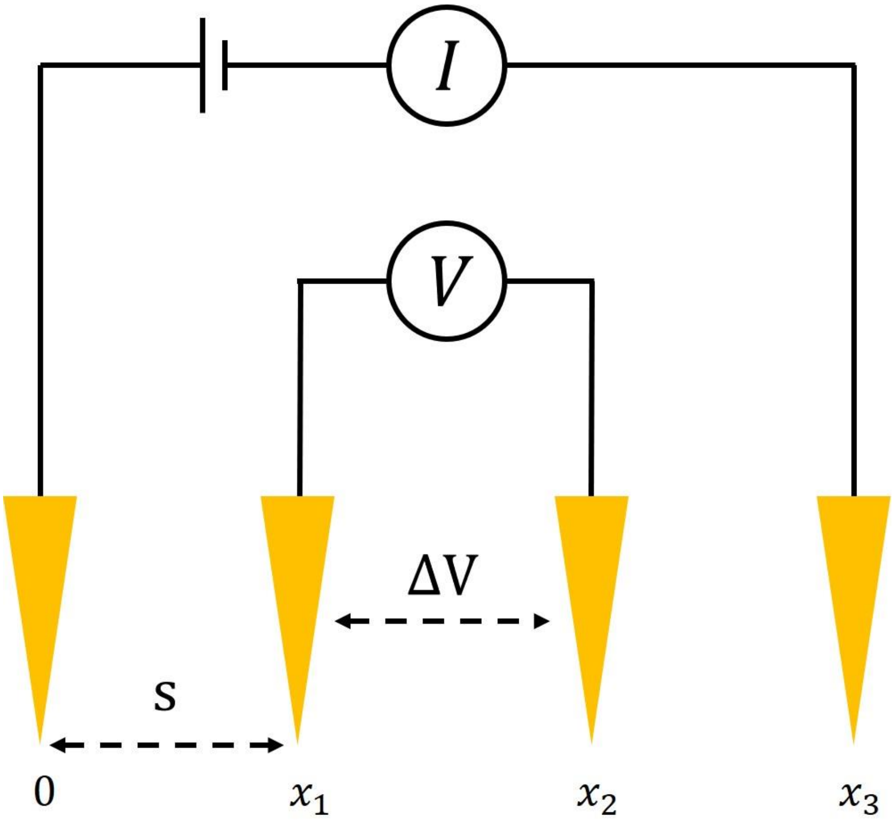

Figure 3.5 Schematic of the operation of a four-point probe system.

A high impedance current source supplies current through the two outer probes and a voltmeter then measured the voltage drop, ΔV across the inner two probes to measure the resistivity. This technique can be used to measure the bulk resistivity of a material or the resistivity of a thin film, however the calculation required is different for both cases.

Bulk Samples:

To measure the resistivity of a bulk material we assume that the tips of the metallic pins are infinitesimally small, and that the sample is semi-infinite in thickness, i.e. $t \gg s$ where t is the sample thickness. In this case, we consider the protrusion of the current into the sample from the outer probes as being spherical. Therefore, we can describe the resistance differential, ΔR as

$$\Delta R = \rho\left(\frac{dx}{A}\right) \tag{4}$$

where A is the surface area of the sample. Integrating this expression between the inner probes gives an expression for the resistance.

$$R = \int_{x_1}^{x_2} \rho\frac{dx}{2\pi x^2} = \frac{\rho}{2\pi}\left(-\frac{1}{x}\right)\Bigg|_{x_1}^{x_2} = \frac{\rho}{2\pi}\left(-\frac{1}{(x_2 - x_1)}\right) = \frac{\rho}{4\pi s} \tag{5}$$

Due to the superposition of current at the outer two tips, the resistance is also given by

$$R = \frac{V}{2I} \tag{6}$$

which can be equated to Equation 5 and rearranged to determine an expression for the bulk resistivity

$$\rho = 2\pi s\left(\frac{V}{I}\right) \tag{7}$$

and from Equation 3, an expression for the sheet resistance can be obtained.

$$R_s = \frac{2\pi s}{t}\left(\frac{V}{I}\right) \tag{8}$$

Thin Film Resistivity:

For the case of a thin film where $t \ll s$, we consider the protrusion of the current from the two outer probes to form current rings in the sample rather than spheres. Thus, we consider once again the integral from Equation 5, but with an area, $A = 2\pi xt$.

$$R = \int_{x_1}^{x_2} \rho\frac{dx}{2\pi xt} = \int_{s}^{2s} \frac{\rho}{2\pi t}\frac{dx}{x} = \frac{\rho}{2\pi t}\ln x|_{s}^{2s} = \frac{\rho}{2\pi t}\ln 2 \tag{9}$$

Again, we have $R = \frac{V}{2I}$ at the outer probes and hence the resistivity is given by

$$\rho = \frac{\pi t}{\ln 2}\left(\frac{V}{I}\right) \tag{10}$$

Which can again be related to Equation 3.

$$R_s = \frac{\pi}{\ln 2}\left(\frac{V}{I}\right) \tag{11}$$

This technique was applied using a custom-built four-point probe system with copper pins with a 1 mm spacing. The measured sheet resistances, and subsequent calculated parameters are presented in Table 3.4. Three measurements of sheet resistance were taken for one sample of each thickness.

Sample	***t*** **(nm)**	**R_s (Ω sq^{-1})**	**ρ (Ω·cm) [×10^{-4}]**	**σ (S cm^{-1})**
8 – 12 Ω sq^{-1}	127 ± 10	12 ± 0.33	1.52 ± 0.13	6478.94 ± 554.12
30 – 60 Ω sq^{-1}	17 ± 10	42 ± 0.33	0.71 ± 0.41	14005.60 ± 8087.74
70 – 100 Ω sq^{-1}	11 ± 10	108 ± 0.33	1.19 ± 1.08	8403.36 ± 7626.59

Table 3.4 Thickness, sheet resistance, bulk resistivity, and bulk conductivity of ITO thin films.

The electron mobility, μ_e and carrier concentration, N in the ITO was estimated using the expressions [42] [44]

$$\mu_e = \frac{e}{m_e^* \gamma} \tag{12}$$

$$N = \frac{\omega_p^2 m_e^* \varepsilon_0}{e^2} \tag{13}$$

where e is the charge of an electron, m_e^* is the effective mass of an electron in ITO, and γ and ω_p are the scattering rate and plasma frequency obtained by fitting the ellipsometry data to a Drude model. The effective mass of the electron was estimated as $m_e^* = 0.35m_0$, where m_0 is the rest mass of an electron. This value of m_e^* was chosen based on the published work of Lin *et al.* [45] who studied the electrical properties of ITO films having very similar resistivity values as the ITO films in this research. The electron mobilities and electron concentrations are presented in Table 3.5.

Sample	**μ_e (cm^2 V^{-1} s^{-1})**	**N (cm^{-3})[×10^{20}]**
8 – 12 Ω sq^{-1}	26.54 ± 0.05	9.62021 ± 0.00682
30 – 60 Ω sq^{-1}	18.06 ± 0.12	8.28854 ± 0.03159
70 – 100 Ω sq^{-1}	15.43 ± 0.16	7.62441 ± 0.05614

Table 3.5 Electron mobility and electron concentration in ITO thin films.

The calculated carrier concentration is consistent with the work of Lin *et al.* who obtained a value of about 1×10^{21} cm^{-3}. The values of N decrease with decreasing thickness as would be expected as the films thickness limits the amount of charge carriers the ITO film can physically contain.

3.7 Conclusion

ITO is a material that exhibits incredibly unique and useful properties for both industry and research. It is an incredibly versatile material with a high optical transparency at visible wavelengths and a rather high electrical conductivity. The combination of these two properties make it an ideal material for use in transparent electronics. While ITO is a rather easy material to produce using PVD methods, making ITO with specific combinations of electrical and optical properties is a rather difficult task. As discussed in this chapter, the oxygen content, crystallinity, thickness, and deposition/annealing temperature are all factors that have to be considered for the fabrication of ITO for specific purposes. In this Chapter, the basic electric and optical characterisation of our commercial ITO films has been presented. We use these samples as reference for high-quality research/industry-grade ITO, however in Chapter 5, further research will be presented on locally fabricated ITO, specifically for use as an ENZ material. The results of those fabrications will be compared to the commercial ITO samples discussed in this chapter.

References

[1] W. J. Y. Duan *et al.*, “Highly efficient gate-tunable photocurrent generation in vertical heterostructures of layered materials,” *Nat. Nanotechnol.*, vol. 8, pp. 952–958, 2013.

[2] J. Park, J. H. Kang, X. G. Liu, and M. L. Brongersma, “Electrically Tunable Epsilon-Near-Zero (ENZ) Metafilm Absorbers,” *Sci. Rep.*, vol. 5, 2015.

[3] T. P. Nguyen, P. Le Rendu, N. N. Dinh, M. Fourmigué, and C. Mézière, “Thermal and chemical treatment of ITO substrates for improvement of OLED performance,” *Synth. Met.*, vol. 138, no. 1, pp. 229–232, 2003.

[4] C. May and J. Strümpfel, “ITO coating by reactive magnetron sputtering–comparison of properties from DC and MF processing,” *Thin Solid Films*, vol. 351, no. 1, pp. 48–52, 1999.

[5] P. Kuang *et al.*, “A New Architecture for Transparent Electrodes: Relieving the Trade-Off Between Electrical Conductivity and Optical Transmittance,” *Adv. Mater.*, vol. 23, no. 21, pp. 2469–2473, Jun. 2011.

[6] T. Minami, H. Sonohara, T. Kakumu, and S. Takata, “Physics of very thin ITO conducting films with high transparency prepared by DC magnetron sputtering,” *Thin Solid Films*, vol. 270, no. 1, pp. 37–42, 1995.

[7] H.-S. Roh, S.-H. Cho, and W.-J. Lee, “Study on the durability against heat in ITO/Ag-alloy/ITO transparent conductive multilayer system,” *Phys. Status Solidi*, vol. 207, no. 7, pp. 1558–1562, Jul. 2010.

[8] M. Bender, W. Seelig, C. Daube, H. Frankenberger, B. Ocker, and J. Stollenwerk, “Dependence of film composition and thicknesses on optical and electrical properties of ITO–metal–ITO multilayers,” *Thin Solid Films*, vol. 326, no. 1, pp. 67–71, 1998.

[9] G. Legeay, “Couches minces amorphes d'ITO : caractérisation, structure, évolution et fonctionnalisation sous rayonnements UV," PhD Thesis, European University of Brittany, 2011

[10] Y. Wang, A. Capretti, and L. Dal Negro, “Wide tuning of the optical and structural properties of alternative plasmonic materials,” *Opt. Mater. Express*, vol. 5, no. 11, pp. 2415–2430, 2015.

[11] C. Guillén and J. Herrero, “Influence of oxygen in the deposition and annealing atmosphere on the characteristics of ITO thin films prepared by sputtering at room temperature,” *Vacuum*, vol. 80, no. 6, pp. 615–620, 2006.

[12] C. Guillén and J. Herrero, “Comparison study of ITO thin films deposited by sputtering at room temperature onto polymer and glass substrates,” *Thin Solid Films*, vol. 480–481,

pp. 129–132, 2005.

[13] H.-N. Cui, V. Teixeira, L.-J. Meng, R. Martins, and E. Fortunato, “Influence of oxygen/argon pressure ratio on the morphology, optical and electrical properties of ITO thin films deposited at room temperature,” *Vacuum*, vol. 82, no. 12, pp. 1507–1511, 2008.

[14] Y. Hu, X. Diao, C. Wang, W. Hao, and T. Wang, “Effects of heat treatment on properties of ITO films prepared by rf magnetron sputtering,” *Vacuum*, vol. 75, no. 2, pp. 183–188, 2004.

[15] E. Terzini, P. Thilakan, and C. Minarini, “Properties of ITO thin films deposited by RF magnetron sputtering at elevated substrate temperature,” *Mater. Sci. Eng. B*, vol. 77, no. 1, pp. 110–114, 2000.

[16] T. C. Gorjanc, D. Leong, C. Py, and D. Roth, “Room temperature deposition of ITO using R.F. magnetron sputtering,” *Thin Solid Films*, vol. 413, no. 1, pp. 181–185, 2002.

[17] F. Kurdesau, G. Khripunov, A. F. da Cunha, M. Kaelin, and A. N. Tiwari, “Comparative study of ITO layers deposited by DC and RF magnetron sputtering at room temperature,” *J. Non. Cryst. Solids*, vol. 352, no. 9, pp. 1466–1470, 2006.

[18] Y. Shigesato and D. C. Paine, “A microstructural study of low resistivity tin-doped indium oxide prepared by d.c. magnetron sputtering,” *Thin Solid Films*, vol. 238, no. 1, pp. 44–50, 1994.

[19] H. P. Löbl, M. Huppertz, and D. Mergel, “ITO films for antireflective and antistatic tube coatings prepared by d.c. magnetron sputtering,” *Surf. Coatings Technol.*, vol. 82, no. 1, pp. 90–98, 1996.

[20] S. Ko *et al.*, “Low noise capacitive sensor for multi-touch mobile handset’s applications,” in *2010 IEEE Asian Solid-State Circuits Conference*, 2010, pp. 1–4.

[21] C. G. Granqvist, “Electrochromism and smart window design,” *Solid State Ionics*, vol. 53–56, pp. 479–489, 1992.

[22] W.-F. Wu and B.-S. Chiou, “Mechanical and optical properties of ITO films with anti-reflective and anti-wear coatings,” *Appl. Surf. Sci.*, vol. 115, no. 1, pp. 96–102, 1997.

[23] J. H. Lee, J. W. Jang, S. H. Sohn, S. G. Lee, and M. S. Park, “Electromagnetic Interference (EMI) Shielding Efficiency (SE) Characteristics of the ITO/Ag Multilayer Structure,” *Mol. Cryst. Liq. Cryst.*, vol. 470, no. 1, pp. 107–120, Aug. 2007.

[24] P. Boire, R. Fix, and J.-C. Giron, “*Glazing with optical and/or energetic properties capable of being electrically controlled*,” Patent No. US7074486B2, Saint-Gobain Glass France SAS, 2004.

[25] J. Tauc, “Optical properties and electronic structure of amorphous Ge and Si,” *Mater. Res. Bull.*, vol. 3, no. 1, pp. 37–46, 1968.

[26] D. E. Aspnes, “Optical properties of thin films,” *Thin Solid Films*, vol. 89, no. 3, pp. 249–262, 1982.

[27] S. H. Brewer and S. Franzen, “Indium tin oxide plasma frequency dependence on sheet resistance and surface adlayers determined by reflectance FTIR spectroscopy,” *J. Phys.*

Chem. B, vol. 106, no. 50, pp. 12986–12992, 2002.

[28] K. F. Shi and Z. L. Lu, “Field-effect optical modulation based on epsilon-near-zero conductive oxide,” *Opt. Commun.*, vol. 370, pp. 22–28, 2016.

[29] M. Bender, W. Seelig, C. Daube, H. Frankenberger, B. Ocker, and J. Stollenwerk, “Dependence of oxygen flow on optical and electrical properties of DC-magnetron sputtered ITO films,” *Thin Solid Films*, vol. 326, no. 1, pp. 72–77, 1998.

[30] S. Chapman, T. G. Cowling, and D. Burnett, "*The mathematical theory of non-uniform gases: an account of the kinetic theory of viscosity, thermal conduction and diffusion in gases*," Cambridge University Press, 1990.

[31] J. O. Hirschfelder, C. F. Curtiss, R. B. Bird, and M. G. Mayer, *Molecular theory of gases and liquids*, vol. 165. Wiley New York, 1964.

[32] R. L. Liboff, "*Kinetic Theory: Classical, Quantum, and Relativistic Descriptions*," Springer Science & Business Media, 2003.

[33] N. W. Ashcroft and N. D. Mermin, "*Solid State Physics*," Cengage Learning, 2011.

[34] D. J. Griffiths, "*Introduction to electrodynamics*," Prentice Hall, New Jersey, 1962.

[35] H. D. Young, R. A. Freedman, T. R. Sandin, and A. L. Ford, "*University Physics*," vol. 9. Addison-Wesley Reading, MA, 1996.

[36] M. Fox, “*Optical Properties of Solids*,” American Journal of Physics 70, 1269, 2002.

[37] M. W. C. Dharma-Wardana, “Static and dynamic conductivity of warm dense matter within a density-functional approach: Application to aluminum and gold,” *Phys. Rev. E*, vol. 73, no. 3, p. 36401, 2006.

[38] V. M. Adamyan, A. A. Mihajlov, N. M. Sakan, V. A. Srećković, and I. M. Tkachenko, “The dynamic conductivity of strongly non-ideal plasmas: is the Drude model valid?,” *J. Phys. A Math. Theor.*, vol. 42, no. 21, p. 214005, 2009.

[39] A. V Pronin, A. Pimenov, A. Loidl, and S. I. Krasnosvobodtsev, “Optical Conductivity and Penetration Depth in MgB_2,” *Phys. Rev. Lett.*, vol. 87, no. 9, p. 97003, Aug. 2001.

[40] J. F. Cochran and C. A. Shiffman, “Magnetic-Field Dependence of the RF Skin Depth of Gallium,” *Phys. Rev.*, vol. 140, no. 5A, pp. A1678–A1688, Nov. 1965.

[41] J. M. G. Barthel and R. Buchner, “High frequency permittivity and its use in the investigation of solution properties,” *Pure Appl. Chem.*, vol. 63, no. 10, pp. 1473–1482, 1991.

[42] J. Yoon, M. Zhou, M. A. Badsha, T. Y. Kim, Y. C. Jun, and C. K. Hwangbo, “Broadband Epsilon-Near-Zero Perfect Absorption in the Near-Infrared,” *Sci. Rep.*, vol. 5, p. 12788, 2015.

[43] P. Van Zant and P. Chapman, "*Microchip Fabrication: A Practical Guide to Semiconductor Processing*," vol. 5. McGraw-Hill, New York, 2000.

[44] P. Y. Yu and M. Cardona, "*Fundamentals of Semiconductors: Physics and Materials Properties*," Springer, 2010.

[45] J. J. Lin and Z. Q. Li, “Electronic conduction properties of indium tin oxide: Single-particle and many-body transport,” *J. Phys. Condens. Matter*, vol. 26, no. 34, pp. 1–39, 2014.

[46] A. Facchetti and T. J. Marks, "*Transparent Electronics: From Synthesis to Applications,*" Wiley, 2010.

[47] C. Guillén and J. Herrero, “Influence of oxygen in the deposition and annealing atmosphere on the characteristics of ITO thin films prepared by sputtering at room temperature,” *Vacuum*, vol. 80, no. 6, pp. 615–620, 2006.

[48] S. R. S. Kumar and S. Kasiviswanathan, “Role of oxygen vacancies in the high-temperature thermopower of indium oxide and indium tin oxide films,” *Semicond. Sci. Technol.*, vol. 24, no. 2, p. 25028, 2009.

[49] D.-K. Hwang, M. Misra, Y.-E. Lee, S.-D. Baek, J.-M. Myoung, and T. Il Lee, “The role of Ar plasma treatment in generating oxygen vacancies in indium tin oxide thin films prepared by the sol-gel process,” *Appl. Surf. Sci.*, vol. 405, pp. 344–349, 2017.

Chapter 4: Epsilon-Near-Zero Induced Near-Perfect Absorption in Thin-Film ITO – Pt Structures

4.1 Introduction

The interaction of light with matter and its propagation within a given medium is governed mostly by two complex parameters, ε, the dielectric permittivity, and μ, the magnetic permeability of the material. These two parameters are in essence a measure of how an electric and magnetic field, respectively, interact with a given material. Figure 4.1 shows a representative graph of the real components of the permittivity and permeability of both natural and artificially realised materials.

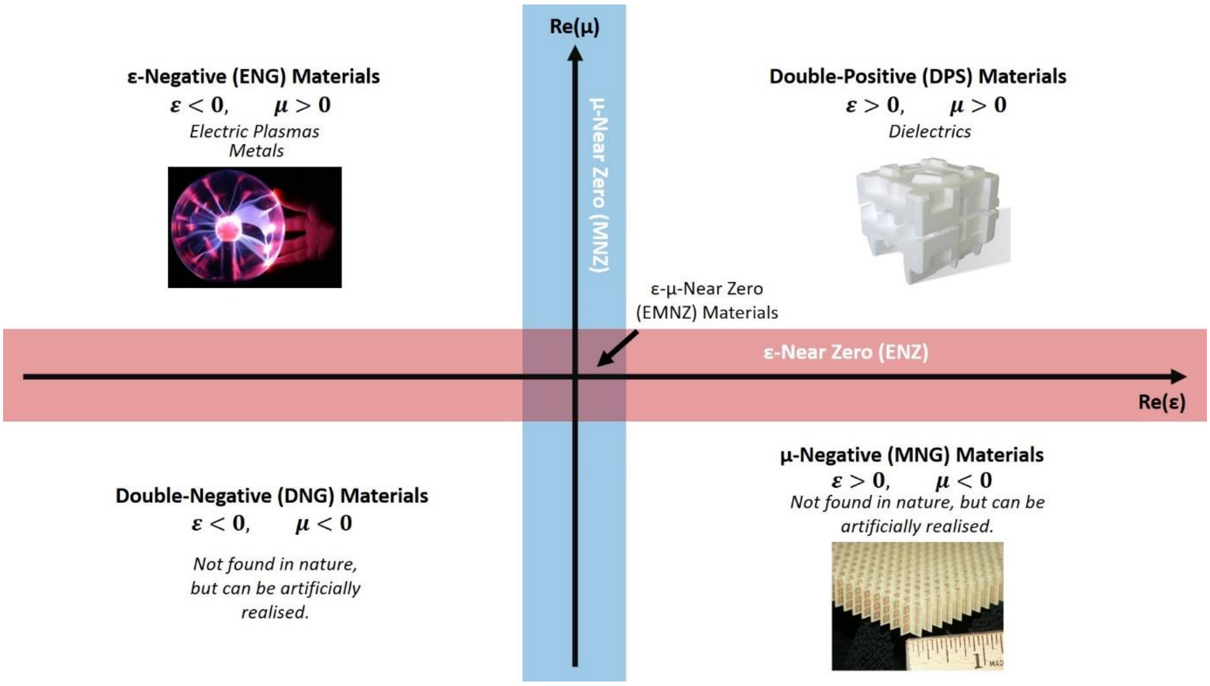

Figure 4.1 Map of the real values permittivity and permeability and how they relate to both natural and artificially realised materials.

The ability to control or tune these two parameters is the key to controlling the wave dynamics of an electromagnetic wave within a given medium. For most dielectric materials $\varepsilon_r > 0$ and for metals/plasmas $\varepsilon_r < 0$ [1]. For practically all naturally occurring materials, $\mu_r > 0$ and for nonmagnetic materials $\mu_r \approx 1$ at optical frequencies [2]. However, recent advances in materials fabrication that give a high degree of control over film dimensions, especially thickness, has facilitated the design and fabrication of novel materials that break the boundaries of the naturally occurring. Metamaterials with indices approaching zero have been experimentally realised in the microwave [3][4][5][6], near-infrared [7][8][9][10], and visible regimes [11][12][13][14]. These near-zero index materials have three categories, ε-near-zero (ENZ) which have near-zero dielectric permittivity, μ-near-zero (MNZ), with near-zero magnetic permeability, and ε-μ-near-zero (EMNZ) with both parameters simultaneously near-zero. The category examined in this chapter is the ENZ materials. Structures with near-zero permittivity display a whole host of novel and unusual properties such as near-zero refractive index [15][16][17], a decoupling of electricity and magnetism [18], significantly enlarged wavelength [15][19][20][21], decoupling of spatial and temporal field variations [18], infinite phase velocity [22][23][24], and slow light effects [25][26][27]. The refractive index of a medium is given by

$$n = \sqrt{\varepsilon_r \mu_r} \tag{1}$$

However, n, ε_r, and μ_r are all complex parameters and thus equation 1 can be written as

$$\tilde{n} = n + i\kappa = \sqrt{(\varepsilon_r' + i\varepsilon_r'')(\mu_r' + i\mu_r'')} \tag{2}$$

where $\tilde{n}$ now denotes the complex refractive index, n is the real component, and κ is the imaginary component which is also called the extinction coefficient. The single and double dashes after the ε and μ parameters represent the real and imaginary components respectively. For a non-magnetic ENZ material, $\varepsilon_r' = 0$, $\mu_r' + i\mu_r'' = 1 + 0i$, and a non-zero ε_r'', the refractive index of the material can become negative, and if both complex ε_r and μ_r are simultaneously near-zero, the refractive index can be zero itself [15]. Furthermore, given that the wavenumber is $k = \frac{2\pi}{\lambda}$ and the refractive can also be described as

$$n = \frac{k\omega}{c} = 0 \tag{3}$$

it follows that λ approached infinity and thus ENZ materials exhibit a significant enlargement of the wavelength of electromagnetic waves. This enlargement can be viewed as a spatially static electric field through the medium and can be used to enhance the emission from fluorescent emitters [28] and to give Purcell factor enhancements and Dicke superradiance effects [29]. It can then be shown that for a material with $\varepsilon_r = 0$ that the phase velocity,

$$v_p = \frac{c}{\sqrt{\varepsilon_r \mu_r}} \to \infty \tag{4}$$

where c is the speed of light in vacuum [30]. Although the phase velocity can be considered to be infinite in a zero permittivity material and the phase of the wave as being instantaneously transmitted, the electromagnetic waves in the material are still subject to causality as the group velocity and the speed of propagation of energy through the material remain below c due to the time taken to build up a solution in the medium in the steady-state regime [31], thus it is more accurate to consider this phenomenon of infinite phase velocity as the transmission of a steady-state wave through the material with zero phase delay or advance [22]. In this case, the wave effectively "tunnels" through the ENZ medium, which Engheta et al. have called "supercoupling" [24]. The decoupling of electricity and magnetism in zero index materials can be demonstrated by considering the source-free Maxwell curl equations and the effects of setting ε or µ to zero. In particular

$$\nabla \times \vec{H} = i\omega\varepsilon_r\varepsilon_0\vec{E} \tag{5a}$$

$$\nabla \times \vec{E} = i\omega\mu_r\mu_0\vec{H} \tag{5b}$$

where $\vec{H}$ and $\vec{E}$ are the magnetic and electric fields respectively. Equations 5a and 5b thus become zero valued. In this case the curls of the electric and magnetic fields lose their co-dependence and become effectively decoupled. Similarly, the temporal and spatial field become effectively separated as frequency and wavelength also lose their co-dependent. The confinement of light within these materials is also possible [32] and can be demonstrated by considering the electric and magnetic flux densities in ENZ and MNZ media and the effects of zero permittivity and permeability.

$$\vec{D} = \varepsilon_r\varepsilon_0\vec{E} \tag{6a}$$

$$\vec{B} = \mu_r\mu_0\vec{H} \tag{6b}$$

These vanish in ENZ and MNZ media as a result of the zero permeability and permittivity. As a result, strong discontinuities at the boundaries of the medium of the $\vec{E}$ and $\vec{H}$ fields are induced due to the required continuity of the displacement field, $\vec{D}$ and the magnetic $\vec{B}$ field at these boundaries [33][34]. If one considers an ENZ medium with an air exclusion within, then it follows from above that the displacement current,

$$\overrightarrow{J_D} = -i\omega\vec{D} \tag{7}$$

would be non-zero inside the exclusion, and zero everywhere else in the ENZ medium. The light in the material is essentially confined or "trapped" within the ENZ structure. Amazingly, this confinement is independent of the geometry of the ENZ medium and has been suggested as an ideal candidate for the design of geometry-invariant cavities [35]. There are many materials that exhibit ENZ behaviour over different frequency ranges. Several materials exhibit zero permittivity at their plasma frequencies, including silicon carbide [36], potassium and transparent conducting oxides (TCOs)[37] such as aluminium doped zinc oxide (AZO) [38][39] and indium tin oxide (ITO) [40][41][42], which is the ENZ material utilised in this research. The optical properties of ITO and the physics of its ENZ behaviour are discussed in this chapter. Of particular interest in ITO is its ability to exhibit a bulk plasmon mode known as the Ferrell-Berreman mode [43][44][45], and another bound mode known as the ENZ mode [46].

4.2 Plasma Frequency and Epsilon-Near-Zero Wavelength of ITO

As discussed in Chapter 3, ITO is a transparent conducting oxide with an ENZ wavelength about 1200 nm. The Drude model discussed in Chapter 2 can be used to model the optical and electrical properties of ITO and an expression for the plasma wavelength of ITO was derived as

$$\lambda_p = 2\pi c\left(\frac{Ne^2}{m\varepsilon_0}\right)^{-\frac{1}{2}} \tag{8}$$

where N is charge carrier concentration, m is the electron mass, e is the charge of an electron, and ε_0 is the permittivity of free space. The ENZ frequency is related to the plasma wavelength as

$$\lambda_{ENZ} = 2\pi c\left(\frac{4\pi^2c^2}{\lambda_p^2\varepsilon_\infty} - \gamma^2\right)^{-1} \tag{9}$$

where ε_∞ is the high-frequency permittivity and γ is the scattering rate. These two expressions are used readily to describe the ENZ behaviour of ITO.

4.3 The Ferrell-Berreman Mode and ENZ Mode

The Ferrell-Berreman mode and the non-radiative ENZ mode are quantised oscillations of the charge density of a metal or polar dielectric thin film. The Ferrell – Berreman mode specifically is a radiative bulk plasmon polariton, lying to the left of the light line, and the non-radiative ENZ mode is a long-range surface plasmon polariton lying to the right of the light line. The foundation for these modes was set in 1958 by Richard A. Ferrell [44] wherein the excitation of plasma oscillations in metal thin films were experimentally confirmed by studying the energy loss of electrons passing though metallic thin films. Ferrell discovered that the energy lost by electrons passing through these films lost specific values of energy equal to multiples of Planck’s constant times the characteristic frequency of the free-electron gas. Two types of plasma oscillations, transverse optic (TO), and longitudinal optic (LO) oscillations were described. Due to the longitudinal nature of plasmons in an infinite electron gas, i.e. the electrons move in the direction of the plasmon momentum, these oscillations cannot be excited by TM waves because they are transverse, and hence these modes do not radiative. However, due the confinement of charge in thin films, some uncertainty is contributed to the momentum and hence a degree of transversality is awarded to the plasmon allowing it to both radiate and couple to TM waves. It follows that for a bulk electron gas in the absence of external sources, the displacement field

$$\vec{D} = \varepsilon_r\varepsilon_0\vec{E} = 0.$$

However, due to the continuity condition of the displacement field at the boundary of the electron gas, and to maintain a non-zero $\vec{E}$-Field, the relative permittivity, ε of the gas must be zero at the frequency of excitations. Further contributions to this field were made by D. W. Berreman in 1963 [45], who studied both LO and TO oscillations and their resulting absorption as a consequence of the ENZ effect. Berreman studied long-wavelength TO frequency modes, characterised by an angular frequency, ω_{TO}, and long-wavelength LO modes with a characteristic frequency, ω_{LO} which has now become to be known as the Berreman mode or Ferrell – Berreman mode. This mode is connected to the TO mode via the Lyddane – Sachs – Teller [47][48] relationship

$$\omega_{LO} = \omega_{TO}\left(\frac{\varepsilon_s}{\varepsilon_\infty}\right)^{\frac{1}{2}} \tag{10}$$

where ε_s and ε_∞ are the low and high frequency limits of the permittivity. Since only plasma oscillations transverse to the surface of the film can radiative, TO modes do not radiative and cannot be excited from air as they lie to the right of the light line. The LO / FB mode, however, lies to the left of the light line, is radiative, and can be excited by TM waves. When infrared light with an $\vec{E}$-field component normal to the surface is incident on the film large-amplitude oscillations normal to the surface are set up. This is a direct consequence of a small value of ε_r due to the continuity condition of the $\vec{D}$-field at the surface boundary. At this boundary, polarised oscillations normal to the surface generate a surface polarization that is equal in magnitude and opposite in direction such that the value of $|\varepsilon_r|$ is minimized. In fact, both TO and LO mode oscillations can be attributed to high and low values of $|\varepsilon_r|$ respectively. Oscillations of this nature have been shown both theoretically and experimentally to exhibit reflectance and transmittance maxima / minima at their mode frequencies.

$$T_{TE} = 1 - \frac{\delta\varepsilon''}{\cos\theta} \tag{11a}$$

$$T_{TM} = 1 - \delta(\varepsilon''\cos\theta + \left(\frac{\varepsilon''}{\varepsilon'^2 + \varepsilon''^2}\right)\frac{\sin^2\theta}{\cos\theta} \tag{11b}$$

Equations 11a and 11b give expressions for the transmission of TE and TM waves, where δ is the thickness of the film in vacuum wavelengths and θ is the angle of incidence relative to the surface normal. Both T_{TE} and T_{TM} have minima at ω_{TO}, however only T_{TM} has a minimum when both ε' and ε'', the real and imaginary components respectively, are small. Similarly, the reflectance at ω_{TO} is a maximum, and a minimum at ω_{LO}, thus we expect significant absorption from TO plasmon modes due to the coinciding minima of the reflectance and transmittance at this frequency. Since practically no $\vec{E}$-field can exist parallel to a conductive metal, transverse modes are not excited and only absorption from LO modes in possible, meaning that such TO modes can be excited by TM light at oblique incidence. In this scenario, the reflectance of TE polarised light becomes unity, and the reflectance of TM light is given by equation 12b.

$$R_{TE} = 1 \tag{12a}$$

$$R_{TM} = 1 - 4\delta\left(\frac{\varepsilon''}{\varepsilon'^2 + \varepsilon''^2}\right)\frac{\sin^2\theta}{\cos\theta} \tag{12b}$$

However, these expressions are highly dependent on $|\varepsilon_m| \gg |\varepsilon|$ being true. For quite some time it was believed that such oscillations could only be excited in metallic films. However, with the discovery of materials such as ITO, a transparent conducting oxide whose optical properties are describable by the Drude free-electron model, extensive research has been carried out on the ENZ behaviour of such materials and its applications [42][49][42]. Near-perfect absorption (NPA) as a result of exciting the Ferrell – Berreman (also known as the “radiative ENZ mode”) and the non-radiative ENZ mode has been experimentally observed by Campione et al. (2016) in ITO thin films without a metal backing [46][50]. The dispersion of both modes was theoretically calculated using complex eigenfrequency analysis and matched exceptionally well with experiment. Particularly, Campione noted that the frequency at which NPA occurs is close to, but not at the ENZ frequency, ω_{ENZ} and attributed this NPA to a significantly enhanced electric field confined within the ITO layer. However, the range of angles available to study the non-radiative ENZ mode were limited to just a few discrete angles above the critical angle. Further work by Luk et al. and Campione examined NPA in films of ITO of thicknesses 24 nm, 53 nm, 88 nm, and 137 nm on an Ag substrate [50]. In this study, we extend the work of Campione and Luk by studying NPA in both the Ferrell-Berreman and non-radiative ENZ modes over a significantly broader angular range. Furthermore, we add to this work by studying this NPA and the mode dispersion in ITO films backed by a Pt layer of varying thicknesses, as well as theoretically studying the effects of depositing ITO on other metals. Furthermore, we study the confinement of the electric field in the ITO layer with and without the presence of a metal backing using COMSOL finite element method simulations.

The Ferrell-Berreman mode and non-radiative ENZ modes were also studied in other ENZ materials, such as in silver/silica multi-layered structure studied by Newman et al. [43], and near-perfect absorption in films of Ge on Ag studied by Park et al who achieved an absorption of up to 80% [51]. Perfect absorption has also been predicted via numerical simulation in graphene layers separated by a PMMA polymer spacer on an ENZ substrate [52]. ENZ metamaterials have also been demonstrated to exhibit non-linear effects such as second-harmonic generation [53] and enhanced non-linear refractive index. [54]

Significant research has been carried out on the perfect absorption achievable via the ENZ effect, both with and without the presence of a metallic backing, however, to date the most successful studies have been limited in the capabilities of their measurements, having the ability to measure only at discrete angles. In this study, we further the work on NPA in ITO films. We study the excitation of these modes over a significantly broader angular range, and particularly of the Ferrell – Berreman mode, excited from air, and the enhancement of the absorption provided by the application of metal backing. We also experimentally demonstrate NPA by exciting the non-radiative ENZ mode in the Kretschmann geometry. To date, the excitation of these modes in ITO boosted with a metallic backing has been limited to Ag and Au. We contribute to this research field by examining the effects of varying the thickness of the metallic backing, as well as a simulation study of the effects of using different metals.

4.4 Broad-spectrum Angle Resolved Reflectivity, Transmission, and Absorption

Angle resolved reflectivity, transmission, and absorption measurements were carried out on all ITO films. The apparatus used to make these measurements was a custom-built setup consisting of a Thorlabs halogen lamp light source polarised to TM polarisation and weakly focused onto a sample mounted on an inner rotating stage using a convex lens of focal length, f = 100 mm (TE polarisation was also possible by adjusting the orientation of the optic axis of the polariser). The receiving end of an Ocean Optics optical fibre with numerical aperture, NA = 0.22 was mounted on an outer rotating stage which revolved at twice the rate of the inner stage to detect the light reflected from the sample's surface. The fibre was connected to an Ocean Optics NIRQuest spectrometer operating in the wavelength range 1000 – 2000 nm. As the light source had both visible and NIR output, it was possible to take visible range (300 – 900 nm) measurements by swapping out the spectrometer for an Ocean Optics USB4000 spectrometer. The motion of the inner and outer stages was controlled using a code written in LabView and allowed a measurable angular range of 10 – 85˚ with 0.5˚ increments. In order to take transmission measurements, the settings of the code were changed to allow only motion of the inner stage, thus detecting the light transmitted through the sample as it rotated. The light detected by the spectrometer was monitored using Spectra Suite software and a matrix of reflectivity/transmission values for each wavelength and angle were taken and plotted in Origin. Absorption could then be determined using the expression

$$A = 1 - T - R$$

where T is the transmission and R is the reflectivity.

Coupling into higher momenta modes was possible by placing a BK7 glass prism (n = 1.51) onto the surface of the sample by means of index matching fluid. The resulting data allowed for the generation of a contour plot of the reflectivity, transmission, and absorption as a function of both angle and wavelength. Figure 4.2 shows a diagram of the described setup.

As a test of the sensitivity and lowest possible reflectivity that the system can measure a measurement was taken on a pure silica sample and the value of reflectivity measured at the Brewster angle of the SiO_2 sample was taken as the lower limit of detectability. Figure 4.3(a) presents the broad-spectrum angle-resolved reflectivity surface map of an samples of SiO_2 with TM polarisation and (b) presents the TE and TM reflectivities as a function of angle at 633 nm incidence. Figure 4.3(b) follows the expected trend for the reflectivity of SiO_2, with a gradual increase in reflectivity with higher angles for TE light, and a gradual decrease to a minimum value at an angle of 55° followed by a large increase at higher angles. For SiO_2, the Brewster angle, θ_B at 633 nm incidence is 55.537° [55][56] in excellent agreement with the experimental data. This graph also agrees very well with the calculation carried out in Figure 2.6 of Chapter 2. In theory, the reflectivity measured at this angle is zero, thus the value of reflectivity measured at this angle was taken as the minimum measurable value of the spectrometer. The reflectivity measured at this angle was $R(\theta_B)$ = 0.192%.

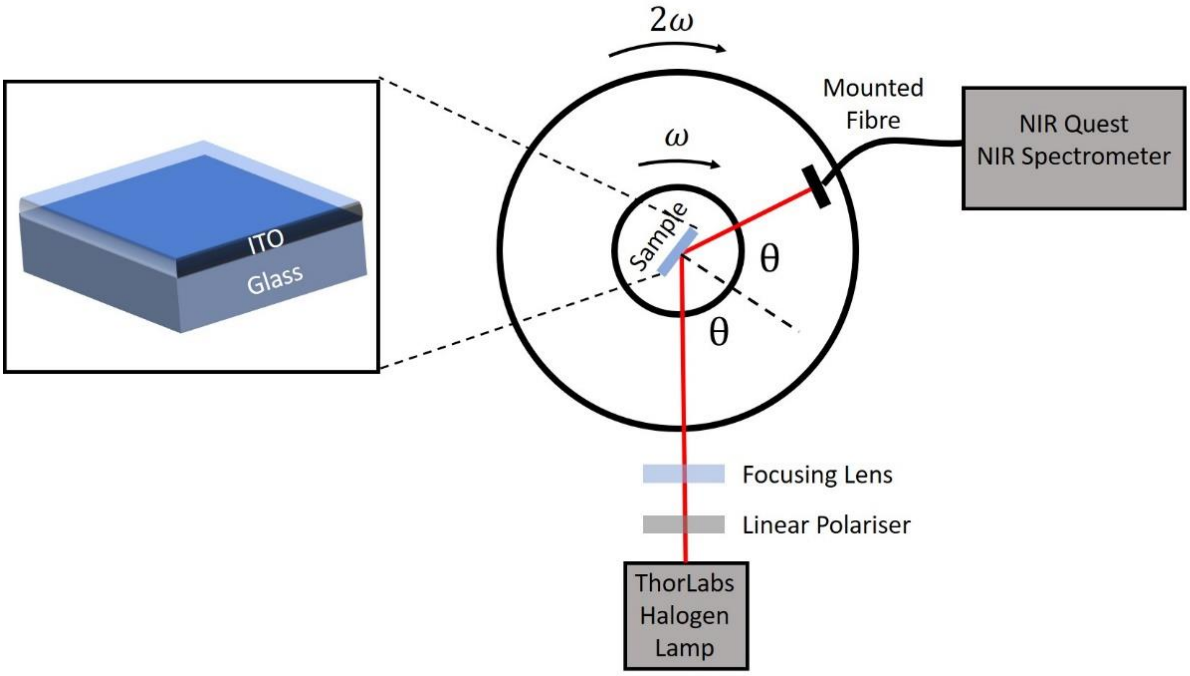

Figure 4.2 Schematic of the angular resolved system for measuring broad spectrum reflectivity, transmission and absorption of thin film samples.

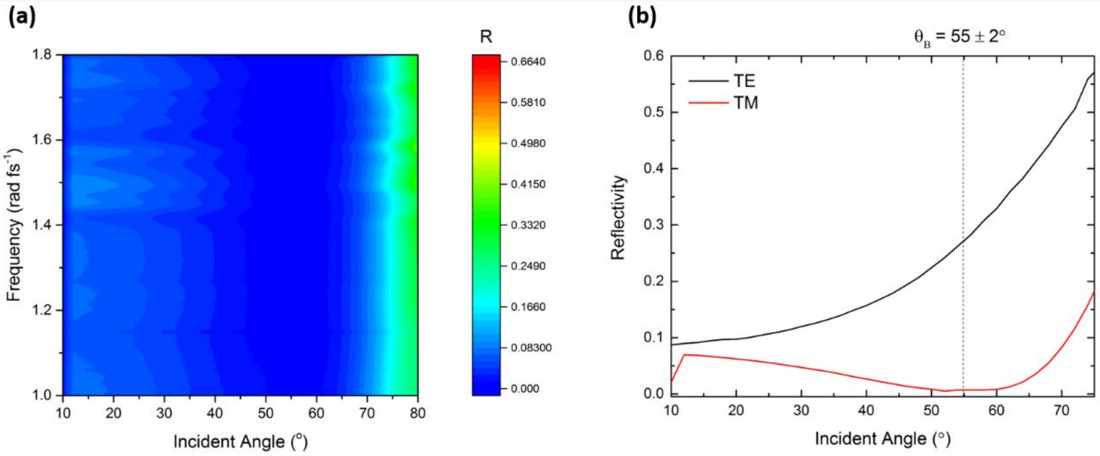

Figure 4.3 (a) Broad-spectrum angle resolved TM polarised reflectivity measurement of bare SiO_2 and (b) TE and TM reflectivity as a function of angle at 633 nm. The Brewster angle located at 55˚ shows a reflectivity of 0.0192% which is taken as the lowest possible value measurable by the system.

4.5 Transfer Matrix Method

In this work we have a series of samples composed of different layers and we need to examine how light propagates through the layers of each structure. We do this by utilizing the Transfer Matrix Method (TMM) which is used to examine the reflected (E^+) and transmitted (E^-) components of the incident TE and TM polarised electric field at the boundaries of a layer *i* and *i+1* for a film of thickness *d*. The propagation of the electric field through successive layers can be described using a 2×2 transfer matrix, $A_{i,i+1}$, which is composed of the Fresnel reflection and transmission coefficients.

$$\begin{pmatrix} E_i^+ e^{ik_{z_i} d_i} \\ E_i^- e^{-ik_{z_i} d_i} \end{pmatrix} = \begin{pmatrix} 1/t_{i,i+1} & r_{i,i+1}/t_{i,i+1} \\ r_{i,i+1}/t_{i,i+1} & 1/t_{i,i+1} \end{pmatrix} \begin{pmatrix} E_{i+1}^+ e^{ik_{z_{i+1}} d_{i+1}} \\ E_{i+1}^- e^{-ik_{z_{i+1}} d_{i+1}} \end{pmatrix} \tag{13}$$

Here k_{z_i} is the wavevector normal to the incident plane of the layer and is given by

$$k_{z_i} = \sqrt{\frac{\varepsilon_i \omega^2}{c^2} - k_0^2 \varepsilon_i \sin^2 \theta_i} \tag{14}$$

where k_0 is the wavevector incident from free space. The transfer matrix of the overall structure of *N* layers can then be obtained by taking the product of the successive transfer matrices for each layer, i.e.

$$M = \prod_i^N A_{i,i+1} \tag{15}$$

From this, the reflection and transmission coefficients for composite structures can be obtained from the expressions

$$t = 2ik_i e^{-ik_i d}\left[\frac{1}{-M_{2,1} + k_i k_N M_{1,2} + i\left(k_N M_{1,1} + k_N M_{2,2}\right)}\right] \tag{16a}$$

$$r = \left[\frac{M_{2,1} + k_i k_N M_{1,2} + i\left(k_i M_{2,2} - k_N M_{1,1}\right)}{-M_{2,1} + k_i k_N M_{1,2} + i\left(k_i M_{2,2} + k_N M_{1,1}\right)}\right] \tag{16b}$$

where the subscripts represent the elements of the 4 × 4 transfer matrix for the entire composite structure. The transmission, T and reflection, R can thus be found to be

$$T = \frac{k_{i+1}}{k_i} t\bar{t} \tag{17a}$$

$$R = r\bar{r} \tag{17b}$$

where the overbar notation represents the complex conjugate of the coefficients.

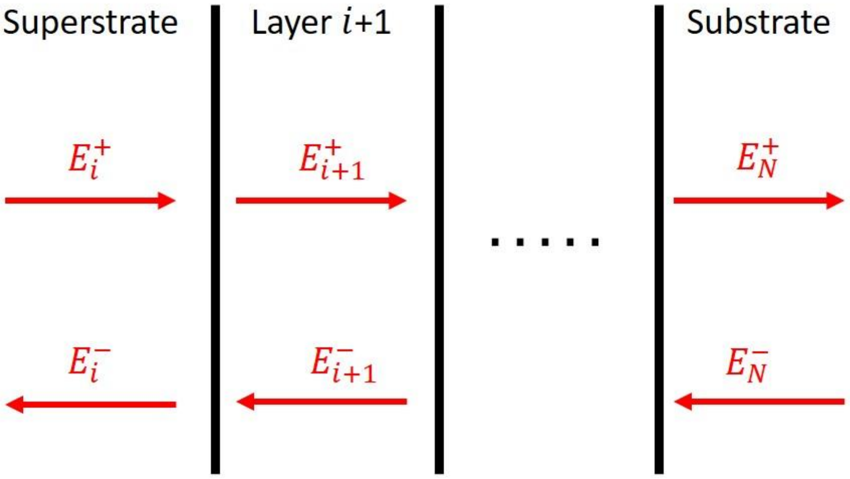

Figure 4.4 Representative diagram showing the reflected and transmitted electric fields.

A TMM code was written in Wolfram Mathematica which takes the real and imaginary components of the refractive index of the materials being examined as input. The thickness of each layer, wavelength range and angular range are specified in the code. A Drude free electron model was used to model the optical properties of ITO as discussed in Chapter 2.

4.6 Complex Eigenfrequency – Real Wavevector Root Solving Method

The complex eigenfrequency – real wavevector root solving method for determining the mode dispersion of multilayer structure works by utilising the afore mentioned T-Matrix method and using a root solving method to find solutions to the equation

$$\sin^{-1}\left(\frac{c\beta}{\omega}\right) = 0$$

where β is real wavevector and ω is the complex frequency. The result is a range of values of ω as a function of β for which the above equation hold true, corresponding to the dispersion of plasmon mode. The particular advantage to considering the frequency as a complex value is that a real mode is a standing wave that assumed there is no net flux of energy in the system, whereas by treating the frequency as a complex value we can obtain information about the transfer of energy from one part of the system to another. The resulting simulated mode-dispersion curve is derived by taking the complex frequency within the transfer matrix analysis and assuming the plasmon decays away as one moves away from the stack in the super and substrate.

4.7 Ferrell-Berreman Mode Excitation in Thin-Film ITO

As mentioned previously, the Ferrell-Berreman, also known as the radiative ENZ mode [12] is a radiative bulk plasmon mode lying to the left of the light line and thus it can be excited from air. Angle-resolved reflectivity, transmission, and absorption measurements were carried out on the commercial ITO samples by exciting them from air. Figure 4.5(a) and (b) shows a comparison of the broadspectrum angle resolved reflectivity measurements of the commercial ITO samples compared to those calculated using the transfer matrix method. The superstrate was air ($n_a = 1.00$) and the subrstrate was glass ($n_g = 1.51$). There is significant agreement between experiment and simulation, both show the expected region of extremely low reflectivity below $\lambda_{ENZ} \approx 1225$ nm. From the experimental data, there are reflectivity minima of 6.8% at 49˚, 1.9% at 56˚, and 0.9% at 56˚ for the commercial samples 8 – 12 Ω sq^{-1}, 30 – 60 Ω sq^{-1}, and 70 – 100 Ω sq^{-1} respectively, which were discussed in Chapter 3. The film thicknesses used in the simulations for these films were 127 nm, 17 nm, and 11 nm respectively. These regions of ultra-low reflectivity correspond to the excitation of the Ferrell-Berreman mode. At around 70˚ incidence for samples 30 – 60 Ω sq^{-1} and 70 – 100 Ω sq^{-1} there is prominent high reflectivity feature which for thin films of ITO occurs within a few nanometres of λ_{ENZ}.

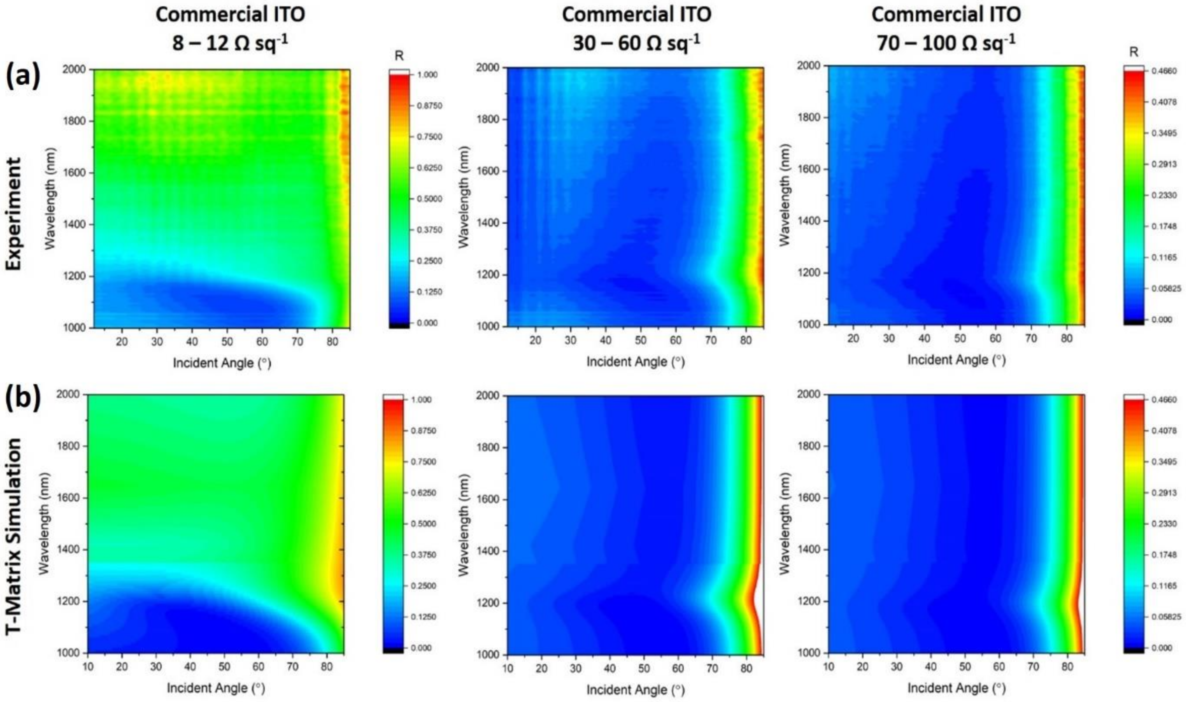

Figure 4.5 Experimental data for the angle-resolved reflectivity of ITO films purchased from Sigma Aldrich. The films are quoted in terms of their sheet resistance range, 8 – 12, 30 – 60, and 70 – 100 Ω sq^{-1} with thicknesses 127 nm, 17 nm, and 11 nm respectively. (b) The corresponding T-matrix simulations. The glass substrate refractive index was taken to be n = 1.51 and the thicknesses of the ITO films were taken to be 127 nm, 17 nm, and 11 nm respectively for each film.

Figure 4.6 shows the data from Figure 4.5 presented on a log scale to highlight the low-reflectivity region. Figure 4.6(c) shows a comparison of experiment and simulation for the reflectivity as a function of wavelength for the ITO films at 49˚, 56˚, and 56˚ for samples 8 – 12 Ω sq^{-1}, 30 – 60 Ω sq^{-1}, and 70 – 100 Ω sq^{-1} respectively. These values of the incident angle were chosen as they contained the points of lowest reflectivity. A high degree of agreement can be observed between simulation and experiment for the reflectivity.

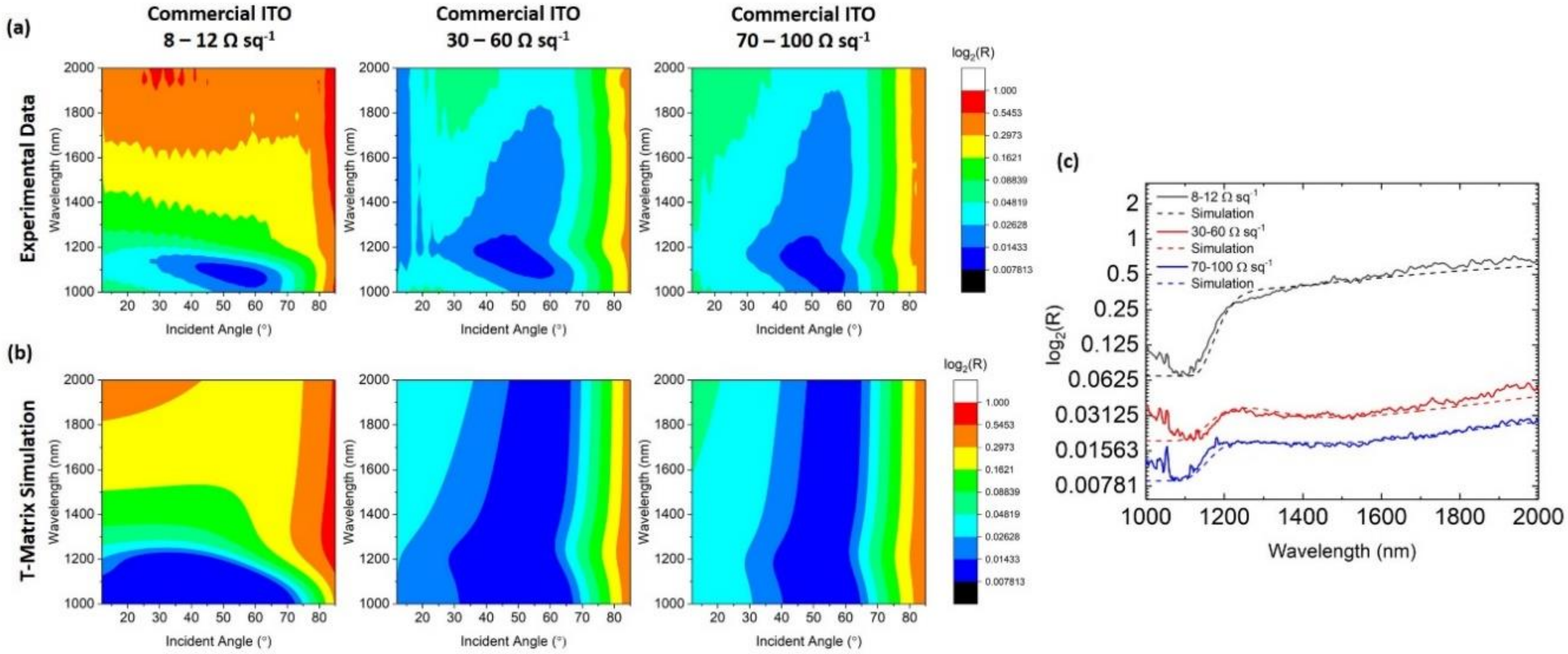

Figure 4.6 A comparison of the experimentally measured (a) angle dependent reflectivity with simulations (b) carried out via the transfer matrix method and (c) the reflectivity profile as a function of wavelength on a log scale for ITO films at the incident angle exhibiting the lowest reflectivity for each film(49˚, 56˚, and 56˚ respectively). The solid lines show the experimentally measured values and the dashed lines represent the corresponding simulated value. The glass substrate refractive index was taken to be $n_g = 1.51$ and the thicknesses of the ITO films were taken to be 127 nm, 17 nm, and 11 nm respectively for each film.

This agreement between experiment and simulation in Figure 4.5 and Figure 4.6 demonstrates the ability to model ITO and its ENZ behaviour using the relatively simple Drude model coupled with the T-matrix method. In both experiment and simulation, a region of increased reflectivity about 1200 nm and at higher angles appear consistently about λ_{ENZ}. Figure 4.7 shows T-matrix simulations of 50 nm of ITO on soda lime glass with a constant loss of $\gamma = 0.1$ rad fs^{-1} and plasma frequencies in the range ω_p = 2.00 – 3.00 rad fs^{-1}. The aforementioned ITO feature at larger angles progressively blueshifts with increasing ω_p. The spectral position of this feature appears at λ_{ENZ} for each simulation and thus this method can be used to estimate λ_{ENZ} to within a few nanometres. This is demonstrated in Figure 4.7(c) which shows the reflectivity profiles as a function of wavelength at 65° incidence for each simulation. The solid lines show the calculated position of λ_{ENZ}. The ITO feature blueshifts and decreases in reflected intensity with increasing ω_p but always remains a few nanometres below λ_{ENZ} . The dashed lines show the actual λ_{ENZ} calculated using Equation 9. As shown, the calculated λ_{ENZ} lines appear consistently a few nanometres above the peak of this feature. This demonstrates that the ENZ wavelength of ITO thin films can be reasonably estimated using this simple and relatively quick angle-resolved technique.

As well as providing a reasonable estimate of λ_{ENZ} the angle-resolved technique is also capable of making a qualitative analysis of the loss in ITO. Figure 4.7(b) shows a set of T-matrix simulations of a 50 nm film of ITO on soda lime glass. In these simulations the plasma frequency was kept at a constant value of ω_p = 3.00 rad fs^{-1} and the loss was varied between γ = 0.1 – 0.3 rad fs^{-1}. These values for the loss were chosen as they are close to the range of γ parameters experimentally measured for the commercial samples using NIR ellipsometry.

As shown the ITO feature appears consistently about 1200 nm, coinciding with λ_{ENZ}. However, it can also be seen in both Figure 4.7(b) and (d) that the broadness of the feature increases with increasing scattering rate. Thus, depending on the broadness/sharpness of the profile, it's possible to make a qualitative estimate the loss of the ITO film. It is also important to note that an increase in loss also causes a small redshift in the ITO feature consistent with Equation 9. However, as the shift with increasing γ is small compared to the shift caused by ω_{p} it is still possible to estimate λ_{ENZ} to a reasonable degree, but the higher the loss in the ITO films, the less accurate the estimate. Transmission measurements for the Commercial ITO films were also carried and the absorption was calculated by using $\mathrm{A} = 1 - \mathrm{T} - \mathrm{R}$. The transmission measurements are presented in Figure 4.8(a). There is significant transmission through the ITO as one would expect from a transparent material, and indeed for the thinner samples of ITO, samples 30 – 60 Ω sq^{-1} and 70 – 100 Ω sq^{-1}, the transmission is significantly larger in line with what would be expected from the Beer-Lambert Law. However, at higher incident angles around λ_{ENZ} we see a suddenly drop in transmission. This coincides with an increase in absorption as presented in the same regions as shown in (b). Here we see a lobe of absorption extending across the angular range from 30˚ – 80˚ incidence. This region of absorption in the ITO films is attributed to the excitation of the Ferrell-Berreman mode. At longer wavelength, about 1800 nm, and across the entire angular range, there are periodic dips in the measured intensity. These are artefacts of the experimental setup and are caused by a minor delay in the motors which cause the reflected image to move slightly off the collecting fibre. From this data it appears that there is a thickness dependence on the relative absorption by the excitation of this mode. In Figure 4.9 the absorption profile for the ITO samples at 62˚ (8 – 12 Ω sq^{-1}), 76˚(30 – 60 Ω sq^{-1}), and 82˚ (70 – 100 Ω sq^{-1}) are plotted and their respective absorption maxima take values of 52.6%, 40.8%, and 38.9%. While the commercial samples vary minutely in terms of their Drude parameters, the most notable difference between the samples are their thickness. The 8 – 12 Ω sq^{-1} sample exhibits the largest absorption due to its greater thickness.

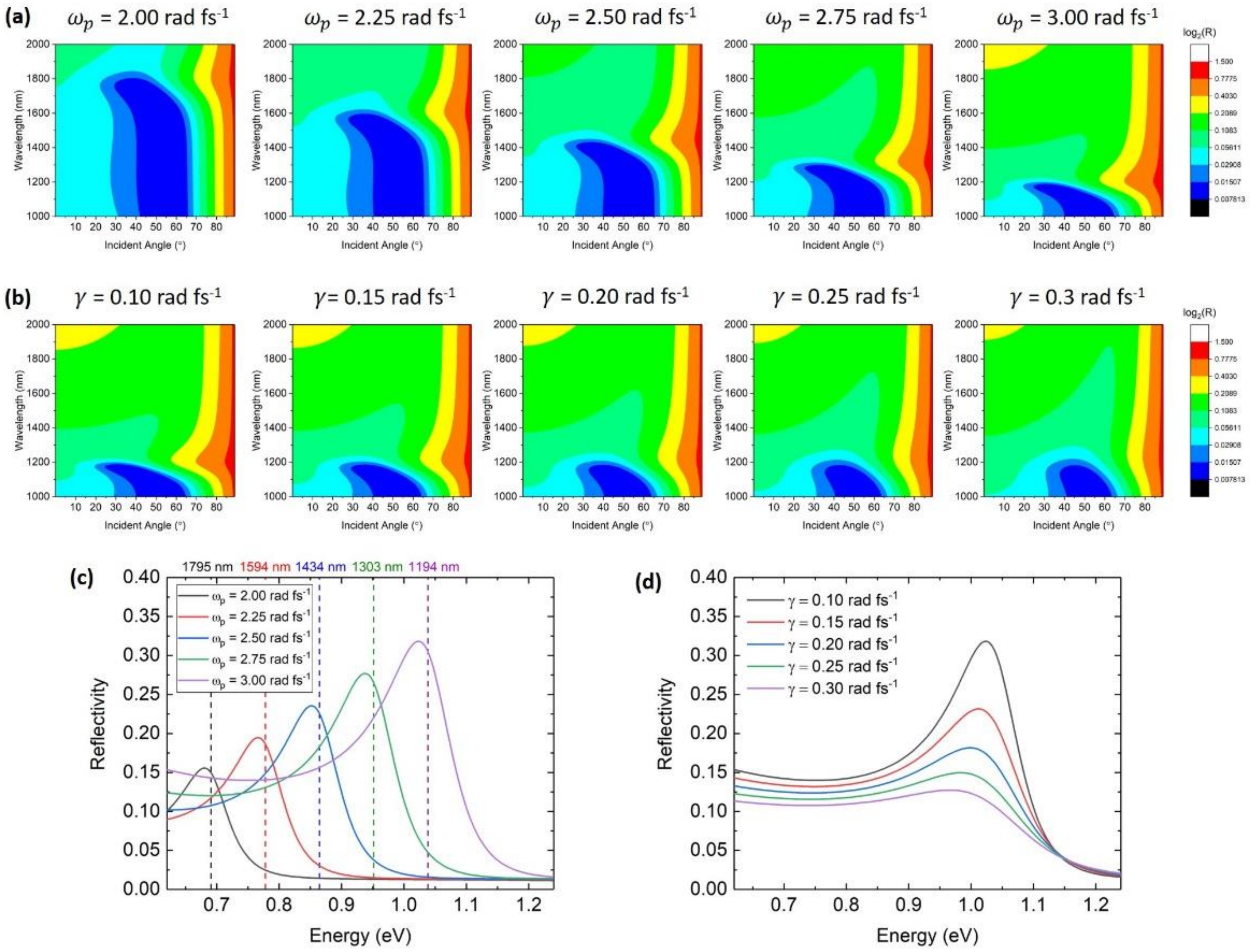

Figure 4.7 T-matrix simulations for a 50 nm film of ITO on soda lime glass with (a) a constant γ = 0.1 and ω_p = 2.00 - 3.00 rad fs^{-1} and (b) a constant ω_p = 3.00 rad fs^{-1} with a range of loss values, γ = 0.1 – 0.3 rad fs^{-1}. (c) Reflectivity profile of the ITO feature as a function of energy at 65˚ for the data in (a) and (d) the reflectivity profile at 65˚ as a function of energy for the data in (b).

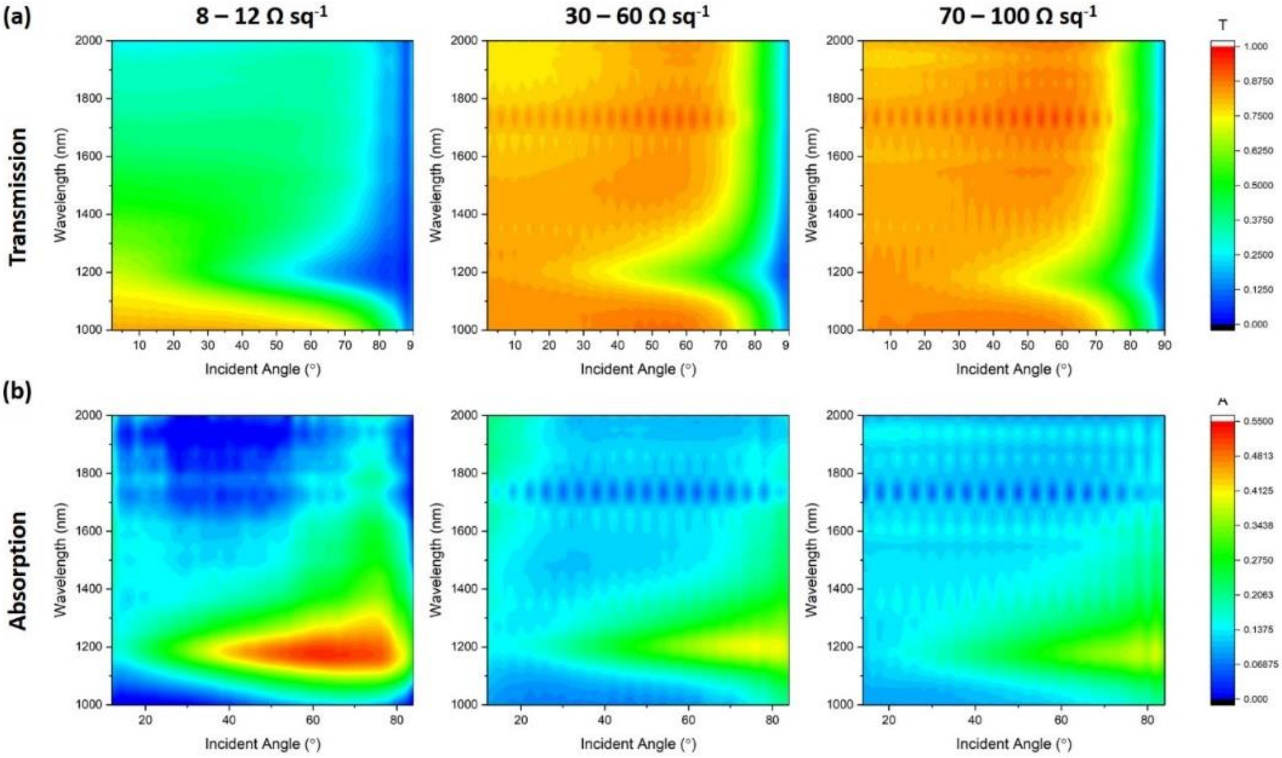

Figure 4.8 Broadspectrum angle resolved transmission (a) and absorption (b) measurements for commercial ITO thin films, 8 – 12 Ω sq^{-1}, 30 – 60 Ω sq^{-1}, and 70 – 100 Ω sq^{-1}.

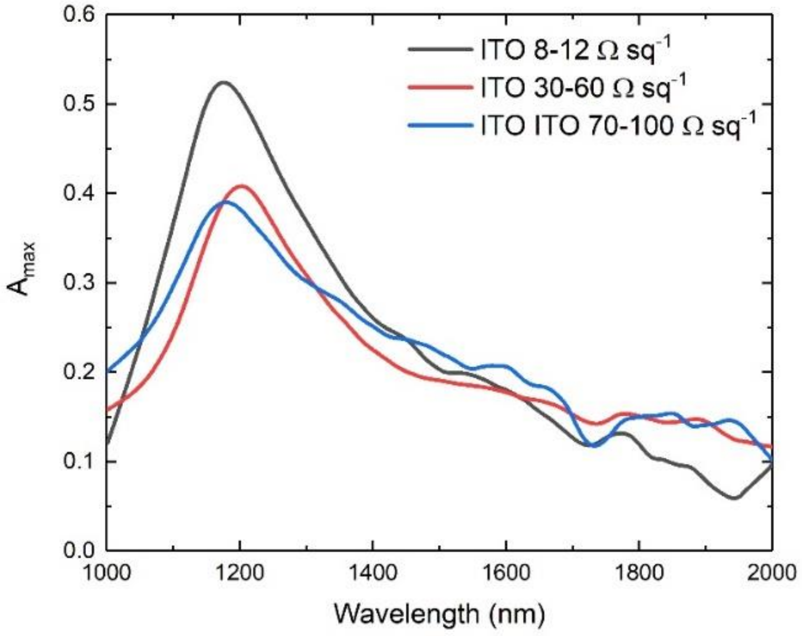

Figure 4.9 Absorption profile for commercial ITO samples at angle of maximum absorption for each. The maximum absorption 52.6% at 62˚, 40.8% at 76 ˚, and 38.9% at 82 ˚ for samples 8 – 12 Ω sq^{-1}, 30 – 60 Ω sq^{-1}, and 70 – 100 Ω sq^{-1} respectively.

Real wavevector – complex eigenfrequency simulations were carried out using the root solving method discussed in Section 4.6. The resulting data was converted to wavelength – incident angle plots and superimposed on the angle-resolved absorption data presented in Figure 4.10. In these calculations the superstrate was specified as glass ($n_g = 1.51$), the ITO was modelled using the Drude parameters fitted from the ellipsometry data in Chapter 3, and the superstrate was air ($n_a = 1.00$). The thicknesses of the ITO films were specified as 127 nm (a), 17 nm (b), and 11 nm (c). The solid lines tracing the absorption features in (a – c) are the Ferrell-Berreman mode dispersions for the three commercial ITO samples. The dashed lines represent the light line. Figure 4.10(d) replots these mode dispersions in the typical frequency – wavevector representation. As shown, all three modes lie to the left of the light line and match perfectly with the experimentally measured high absorption features. However, the downward curve of the dispersion lines about the light line (dashed green line) for the 30 – 60 Ω sq^{-1} and 70 – 100 Ω sq^{-1} films are non-physical and hence these films were not chosen for further study. The kink in the dispersion curve for the 8 – 12 Ω sq^{-1} film is a result of a discontinuity about that region in the refractive index data for this film. This provides clear confirmation that the absorption about 1200 nm in all samples is the excitation of the Ferrell-Berreman mode. Particularly, the mode dispersion of the 8 – 12 Ω sq^{-1} film approaches the light line with increasing wavevector, agreeing well with what would be expected of a bulk. A minor discontinuity is noted in the calculated mode dispersion of this sample about 0.005 nm^{-1}, however it is suspected that this is a minor artefact of the code.

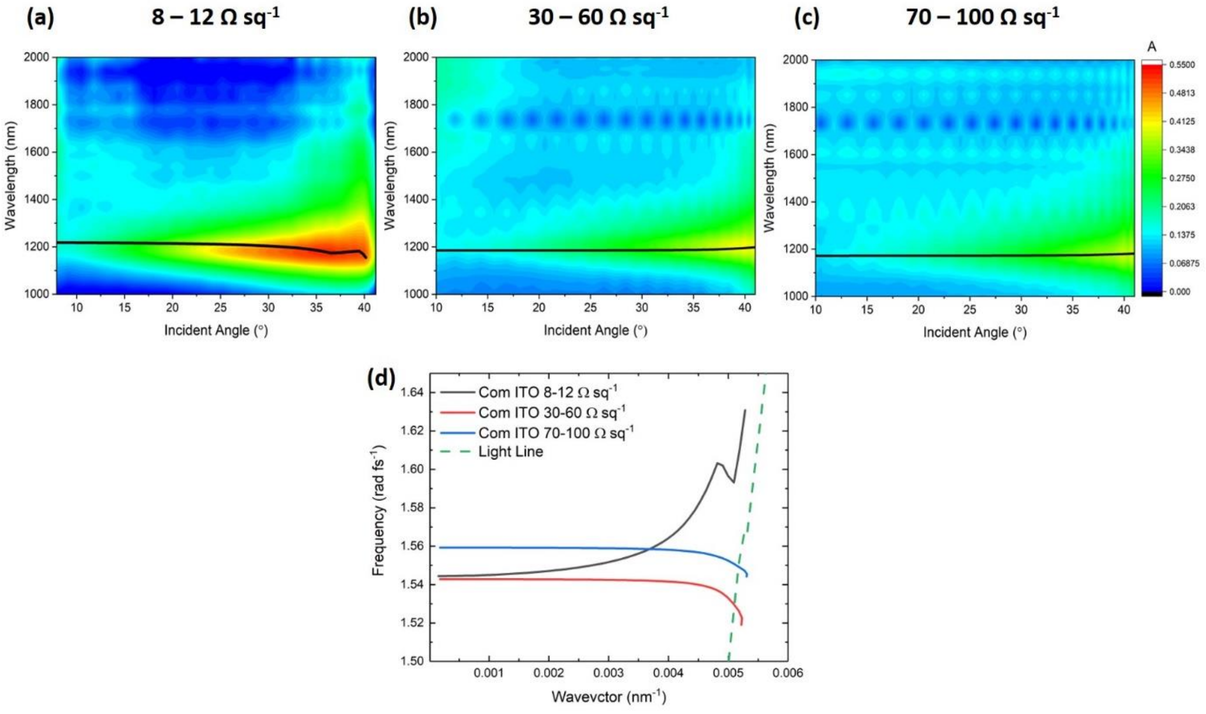

Figure 4.10 Angle resolved absorption measurements for commercial ITO films (a) 8 – 12 Ω sq^{-1}, (b) 30 – 60 Ω sq^{-1}, and 70 – 100 Ω sq^{-1}with the simulated Ferrell-Berreman mode dispersion overlaid. The mode dispersions are replotted in the standard frequency – wavevector representation in (d).

4.8 Enhancement of Ferrell-Berreman Mode Absorption in Thin-Film ITO with a 10 nm Pt Backing

While all commercial samples exhibited a λ_{ENZ} about 1200 nm as shown in Figure 4.9 and high transmittance in the visible range as shown in Figure 3.1(a) of Chapter 3, the 8 – 12 Ω sq^{-1} ITO film exhibited the lowest scattering rate, γ when fitted to a Drude model. As a result, this sample was chosen for further study. For quite some time there has been debate as to whether Ferrell-Berreman modes can be excited in dielectric films without the presence of a metallic backing. Several publications have since demonstrated the excitation of this mode in ITO [43][57][58]. Furthermore, as mentioned in Section 4.3, the presence of a metal backing can cause significant enhancement of the Ferrell-Berreman mode absorption. Here, we theoretically and experimentally measure the differences in Ferrell – Berreman mode excitation with and without the addition of a metal backing. 10 nm of Pt metal were deposited on the ITO-containing side of this sample using argon ion sputtering as discussed in Section 5.3.1 of Chapter 5. Reflection, transmission, and hence absorption measurements were carried out as before, exciting the sample from the glass side. Figure 4.11 shows a comparison of the experimentally determined angle-resolved absorption for the ITO film with and without the addition of this 10 nm Pt backing. The refractive index data for ITO was determined using a Drude model with the aforementioned parameters for the 8 – 12 Ω sq^{-1} film fitted from near-infrared spectroscopic ellipsometry. The refractive index data for Pt was taken from the published work of Werner *et al.* [59]. The superstrate was again take to be glass ($n_g = 1.51$) and the substrate was air ($n_a = 1.00$). As shown, both the experiment and simulation reveal a region of increased absorption about λ_{ENZ} which extends across the 15° – 40° angular range. The incident angles quoted here are the angles made inside the superstrate to the surface normal of the ITO, hence why the angular range only extends to 43° as the incident angle in the glass, θ_{i_g} relative to the incident angle for the air – glass interface is given by $\theta_{i_g} = \sin^{-1}\left(\frac{1}{1.51}\sin\theta_{i_a}\right)$, where 1.51 is the real component of the refractive index of the glass substrate. The spectral and angular position of this absorption feature is indicative of the excitation of a bulk plasmon mode attributed to the near-zero permittivity of ITO in this spectral region. The addition of 10 nm of Pt shows a significant enhancement of the absorption in the ITO across the entirety of the mode. The dashed lines shown are the light lines in glass. Figure 4.11(e) shows a profile of this mode taken at the angle of highest mode absorption (39° incidence) for the ITO with (black) and without (red) the addition of Pt. The solid lines represent experimental data and the dashed lines represent the corresponding T-matrix simulation. Both experiment and simulation clearly show a significant enhancement of the absorption with the addition of Pt.

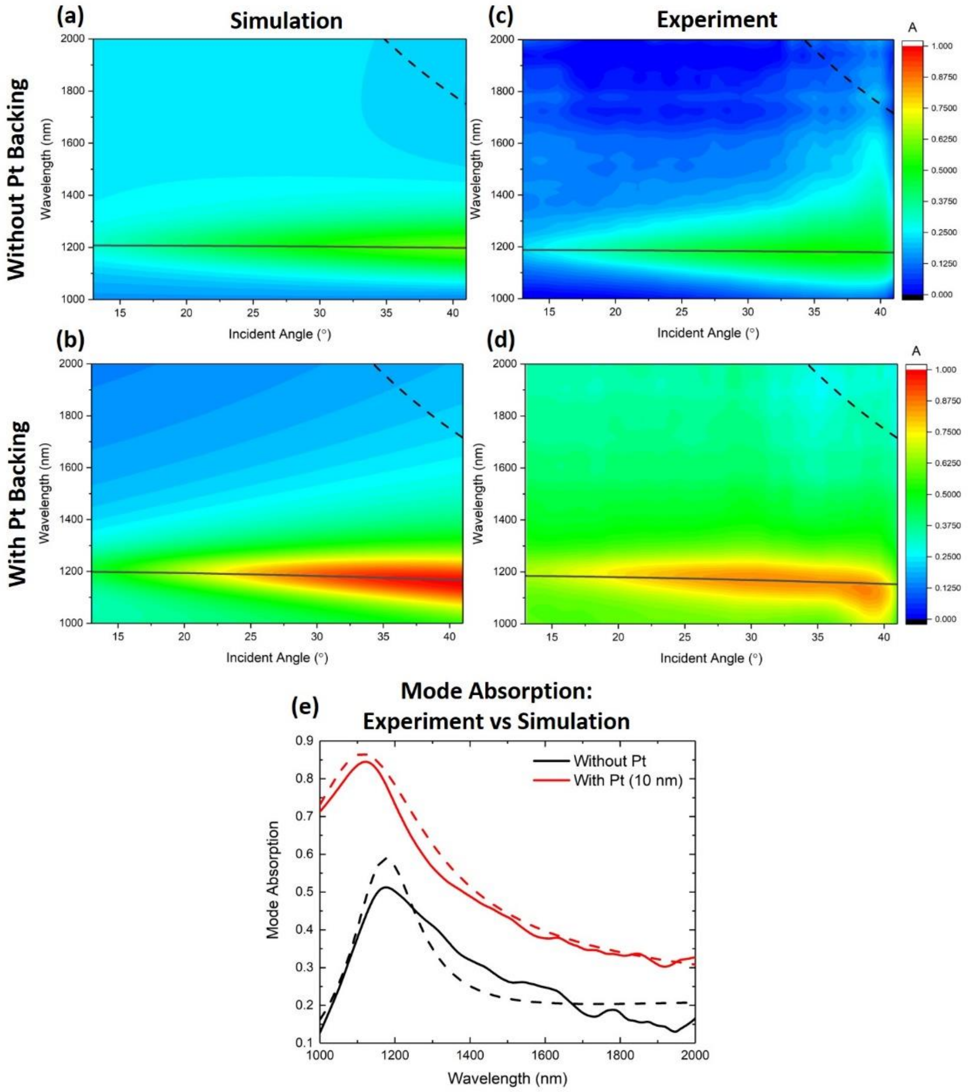

Figure 4.11 An angle-resolved absorption comparison of simulation (a and b) and experiment (c and d) for the 127 nm commercial 8 – 12 Ω sq^{-1} ITO film with and without the addition of 10 nm of Pt metal deposited on the ITO side and excited in the near-infrared from the glass side and (e) a comparison of the mode absorption profile at 39˚ incidence in glass for simulation and experiment with and without the addition of the Pt metal. The solid lines extending across the angular range of the mode absorption is the mode dispersion calculated using a complex eigenfrequency root-finding method. The dashed lines shown are the light lines in glass.

The maximum absorption for the mode about 1170 nm is 52.5% for ITO without the Pt and this reaches a value of 85.6% with the addition of Pt. It is also to be noted that the addition of just 10 nm of Pt appears to cause significant blue-shifting of the NPA region from 1174 nm to around 1125 nm. The origin of this blueshift is uncertain, however it may be due to a relative change to lower values in the proximal refractive index at the boundary between the ITO and Pt layers as a result of the surface roughness of both the ITO and Pt films at their interface. The relative intensities of experimental data are less than those of the simulation and the spectral broadness of the absorption is significantly larger for the experimental data, however this is most likely due to the surface roughness and defects in the samples that the parameters of the T-matrix simulation do not account for. The solid black lines tracing the absorption mode along the angular range is the mode dispersion for each sample calculated from the complex eigenfrequency analysis previously described. In Figure 4.11, the dashed black lines in each plot is the light line in the ITO film. The positioning and extent of the mode dispersion agree exceptionally well with experiment. A significant confinement is expected in the ITO film leading to this Ferrell – Berreman mode absorption and hence finite element method (FEM) simulations were carried out in COMSOL to determine the electric field strength in the ITO layer.

4.9 Electric Field Confinement of the Ferrell-Berreman Mode

The near-perfect absorption (NPA) wavelength for the ITO with and without Pt was determined from both T-matrix simulation, simulations in COMSOL, and experimental data to be around 1175 nm for ITO alone and 1125 nm with the addition of Pt. Note that the region of near-perfect absorption (NPA) is found at shorter wavelengths to λ_{ENZ}. This is consistent with previous literature that shows that the NPA wavelength occurs below λ_{ENZ} but is a result of the near-zero permittivity of the ITO layer. [50] COMSOL FEM simulations were carried out for the time averaged propagation of the electric field in the multilayer structures with and without the Pt layer. COMSOL Multiphysics is Finite Element Method (FEM) software that carries out numerical simulations on user-defined geometric structures. As shown in Figure 4.12, glass (n = 1.51) was chosen as the superstrate, the thickness of the ITO was set to 127 nm, and the simulation was carried out for 10 nm of Pt below the ITO layer and above air. The index data for Pt was again taken from the published work of Werner *et al.* [59], and the index data for ITO was assigned using the Drude model and the fitted parameters of the experimental data obtained via NIR ellipsometry. The simulations carried out were two-dimensional, 1000 nm in width and between 1127 nm – 1137 nm in height. The tessellation selected for the mesh was "Automatic" with a minimum element size of 0.0227 nm and a maximum element size of 1.5 nm. The total number of degrees of freedom solved for were 566,666. To test for convergence the absorption was calculated for a known sample of thin-film gold and the mesh size adjusted until the calculated values agreed with experimental values and previous T-Matrix simulations of the same film. Figure 4.12(a) shows the ratio of the electric field modulus (given by $\sqrt{\left|\vec{E}_x\right|^2 + \left|\vec{E}_y\right|^2}$) to the magnitude of the incident electric field, $\left|\vec{E}_0\right|$ for ITO alone with a noticeable enhancement of about 1.5 times the incident magnitude of the electric field in the ITO layer. While (a) shows the enhancement of the modulus of the field, in reality the enhancement is occurring only in the vertical (y-component) of the field and not the horizontal (x-component) which is consistent with what is excepted of the Ferrell – Berreman plasmon mode. As shown, there is no enhancement of the field in the ITO layer in (b), however the y-component in (c) shows an enhancement of the field of $2.5\left|\vec{E}_0\right|$. The data shows that the confinement of the electric field in the ITO layer as a result of the near-zero permittivity and the continuity condition of the normal component of the electric field at the boundaries results in enhanced absorption in the NPA region. Figure 4.12 (d) and (f) show further confinement of the electric field in the ITO layer with the addition of Pt. (f) demonstrates an enhancement of the y-component of the field of $3.14|\vec{E}_0|$. Comparing (c) and (f), it’s clear that the presence of the 10 nm Pt layer causes a greater enhancement of the field in the ITO layer. As well as the enhancement of the electric field strength in the ITO film, there is a minor decrease in the electric field strength in the air superstrate with the application of the 10 nm Pt layer. This is due to the added reflectivity provided by the Pt layer which suppresses the transmission into the air substrate. Comparative FEM simulations of the ITO and ITO – Pt films away from the ENZ spectral region at 1800 nm are presented in Figure 4.13. This wavelength was chosen for comparison as no resonant behaviour was observed at this value. As shown, no substantial confinement of the electric field is noted in the ITO layer in any of the plots (a – f) as would be expected in the off-resonance spectral region. There is a decrease in the transmission into the air substrate as a result of the Pt layer.

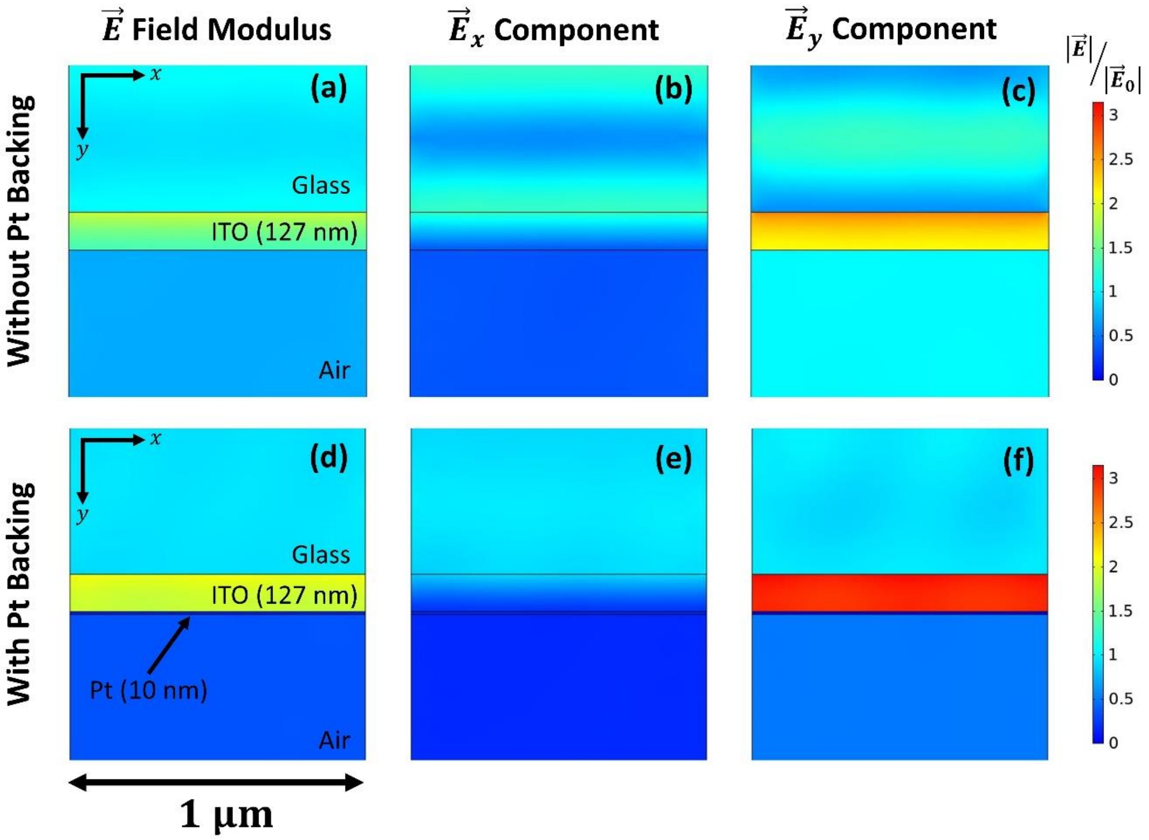

Figure 4.12 COMSOL simulations of ITO for the electric field enhancement without (a – c) and with (d – f) a 10 nm Pt backing at the NPA wavelength of 1125 nm (for ITO alone) and 1175 nm (For ITO with Pt) and 39˚ incidence. (a – c) show the electric field modulus, the x-component and y-component of the electric field, respectively. (d – f) shows the same data for ITO with 10 nm Pt. An enhancement of the electric field of about 1.5 times the incidence field strength is observed in the ITO layer which is enhanced further to two times the incident value via the application of the Pt backing.

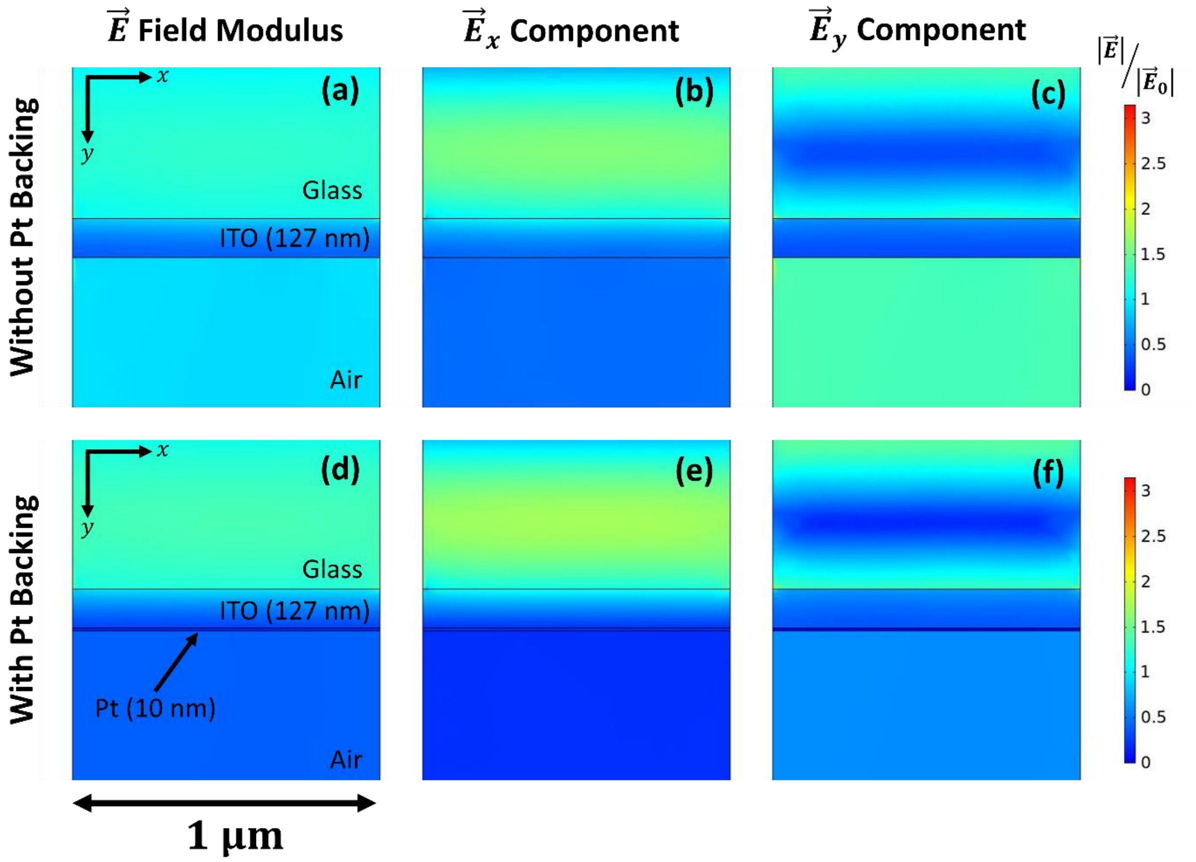

Figure 4.13 COMSOL simulations of the electric field enhancement in ITO without (a – c) and with (d – f) a 10 nm Pt backing away from the ENZ region at 1800 nm and 39° incidence. (a – c) show the enhancement of the electric field modulus, the x-component and y-component of the electric field, respectively. (d – f) shows the same data for ITO with 10 nm Pt. The application of the Pt layer in this off-resonance region appears to cause little to no change in the field within the ITO layer.

4.10 Thickness Dependence on Metal Backing for Enhanced Ferrell-Berreman Mode Absorption

In order to understand the thickness dependence of the metal backing and to optimise the absorption from the Ferrell-Berreman mode, several thickness of Pt in the range 2 – 25 nm were deposited on the ITO-containing side of several identical 8 – 12 Ω sq^{-1} commercial samples of thicknesses around 127 nm. The reflection, transmission, and hence absorption for these samples were also measured. Figure 4.14(a – f) presents the broadspectrum angle resolved absorption data for the 127 nm ITO films with a metallic Pt backing of thicknesses 2 nm – 15 nm excited from the glass side of the samples. In all samples, a distinctive high reflectivity feature is again noted across the measured angular range. The solid black lines tracing these absorption features are the mode dispersions theoretically calculated using the real wavevector – complex eigenfrequency analysis described previously. The calculated mode dispersions agree extremely well with the position of the absorption features. The dashed line is again the light line and each mode frequency can be seen to slowly increase towards the light line, consistent with what is expected of a radiative bulk plasmon mode. This confirms that the measured absorption feature is the

Ferrell – Berreman mode of ITO. Comparisons between experimentally measured absorption and the absorption measured by T-matrix simulations for each sample are presented in Figure 4.14. The absorption profiles were all compared at an incident angle of 39˚, corresponding the region of maximum absorption in both experiment and simulation. As shown, for each sample the addition of a few nanometres of Pt causes increased absorption above 80% compared to just 52.5% for ITO alone. There is very close agreement between simulation and experiment, however it is important to note that due to the fact that the addition of sputtered material adds further scattering to the multi-layered structure in the form of defects and surface roughness, particularly for smaller values of thickness. To account for this, the scattering rate, γ was increased to a value of 0.40 rad fs^{-1} for all samples, and the value of the plasma frequency, ω_p was adjusted slightly for each sample. The values of ω_p used for each thickness of Pt is presented in Table 4.1.

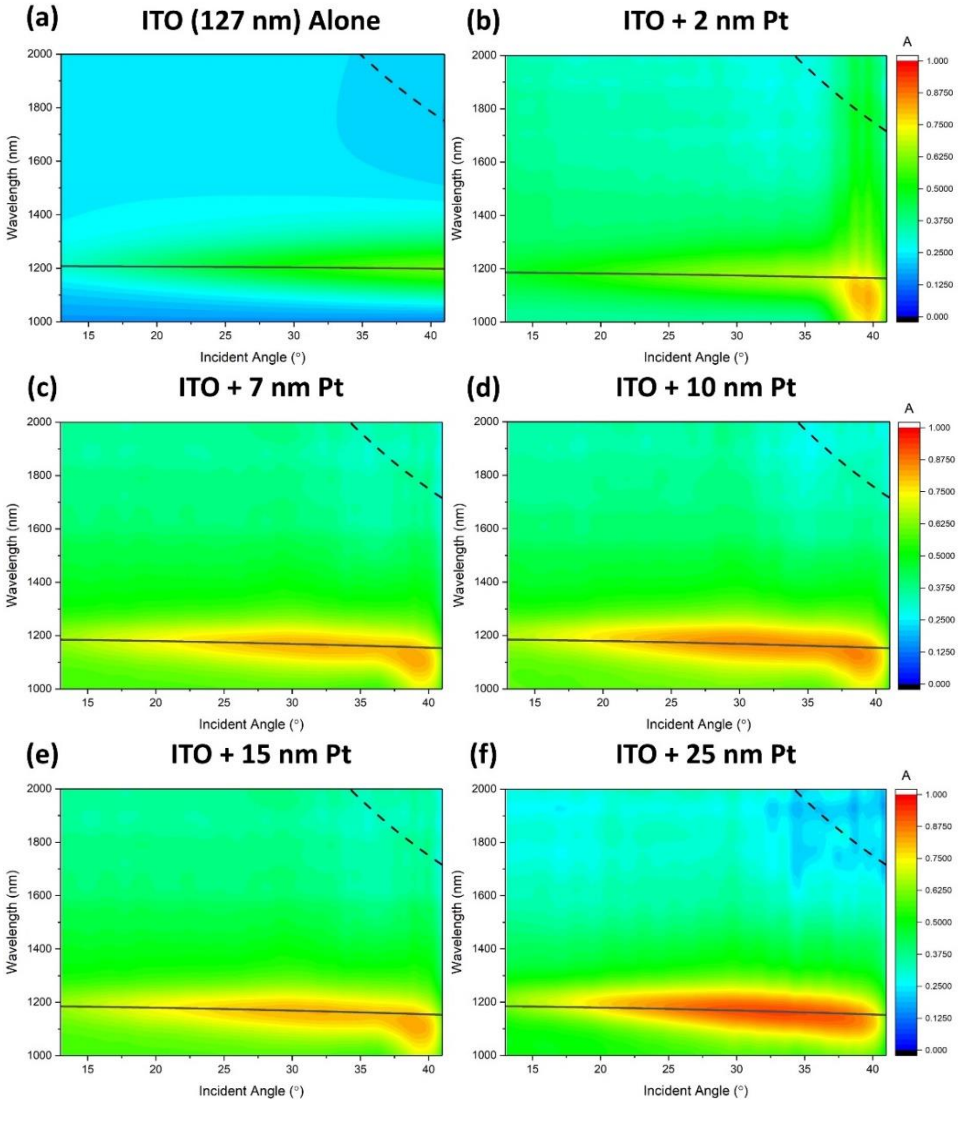

Figure 4.14 Broadspectrum angle resolved absorption profiles measured for 127 nm of ITO (a) with Pt metal backings of (b) 2 nm, (c) 7 nm, (d) 10 nm, (e) 15 nm, and (f) 25 nm. The black solid lines tracing the high absorption features are the theoretically calculated mode dispersion for the samples and the black dashed lines represent the light line.

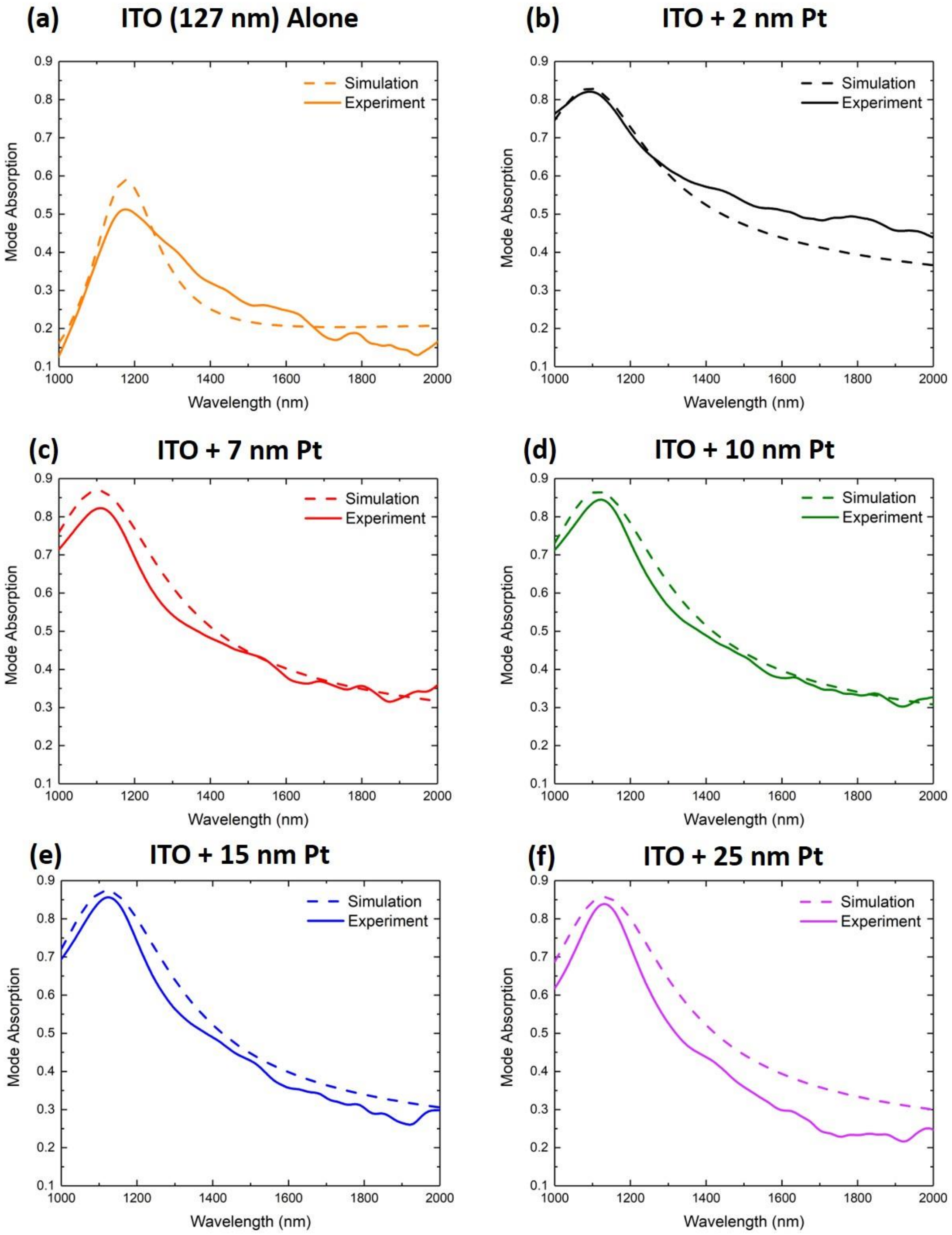

Figure 4.15 Mode absorption profile at 39˚ for 127 nm films of ITO with the addition of 2 – 25 nm (a – f) of Pt metal on the ITO-containing side of the samples.

Pt Thickness (nm)	ε_∞	ω_p (rad fs^{-1})
2	3.6959	3.20
7	3.6959	3.13
10	3.6959	3.10
15	3.6959	3.08
25	3.6959	3.06

Table 4.1 Drude parameters values used in the simulation of the Pt backed ITO samples of thicknesses 2 – 25 nm on 127 nm of ITO.

Figure 4.16 presents the Ferrell – Berreman mode dispersions from Figure 4.16 in the typical frequency – wavevector representation. These were calculated using the complex frequency – real wavevector root finding method discussed in Section 4.6. All samples exhibit the characteristic dispersion of bulk plasmon polariton, with the mode frequency increasing towards the light line (dashed line) as the wavevector increases. There is a very clear effect on the mode dispersion with the application of Pt; the mode frequency increases significantly relative the mode frequency in the ITO film with the application of just 2 nm of Pt. Thicker Pt further increases the mode frequency about the light line, however no further increase is noted above 10 nm and all samples appear to cluster about the same value. The rather striking change in the mode dispersion of the ITO with the application of just 2 nm of Pt is consistent with the blueshift in the mode absorption observable in Figure 4.21(a).

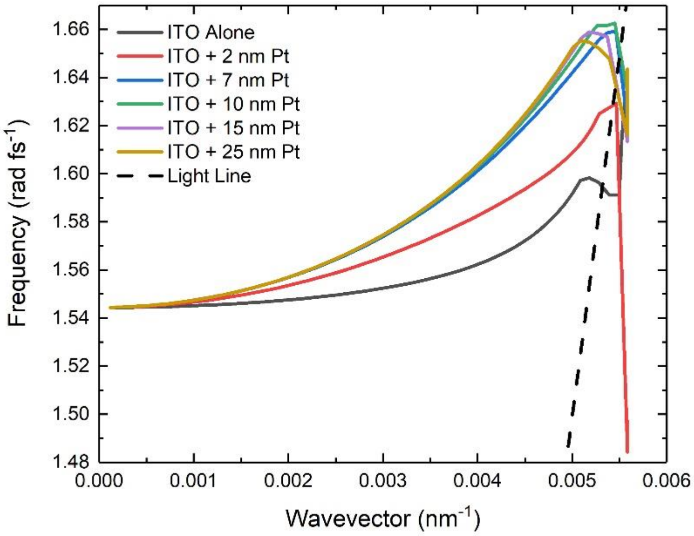

Figure 4.16 Ferrell-Berreman mode dispersion for a 127 nm ITO thin film with 2 nm – 25 nm of Pt deposited on the ITO-containing side and excited from the planar glass interface.

4.11 Transmission and Absorption in the Ferrell-Berreman Mode Spectral Region

To better understand the optical behaviour in our ITO – Pt films, the transmission and reflectivity data used to calculate the absorption in Figure 4.14 were extracted at 39° and plotted as a function of Pt thickness in Figure 4.17. The addition of a highly reflective material such as Pt of course decreases the transmission through the structure, but significant transmission still occurs for thicknesses of Pt below the skin depth. The skin depth of Pt at 1125 nm was determined to be 9.05 nm using an interpolation of the complex refractive index data published by Werner et al. 2009 [59] and Equation 18 [60]

$$\delta_s = \sqrt{\frac{2\rho}{\omega\mu}}\sqrt{\sqrt{1+(\rho\omega\varepsilon)^2}+\rho\omega\varepsilon} \tag{18}$$

where ω is the angular frequency of incident light, ρ is the resistivity of Pt taken to be 1.06×10^{-7} Ω m, $\mu = \mu_r\mu_0$ is the permeability. For non-magnetic platinum, μ_r is taken to be unity. As shown in Figure 4.17(a) the transmission through the multilayer structure decreases exponentially with the thickness of the Pt backing, consistent with the Beer-Lambert law. As the transmission is suppressed there is an increase in absorption about the NPA and ENZ regions. The respective exponential and linear trends in Figure 4.17(a) and (b) confirm that the thicker the layer of Pt metal the more suppressed the transmission. By plotting the natural logarithm of the transmission against thickness we can achieve an effective extinction coefficient for the multilayer stack by taking the slope of the fitted trend line. The magnitude of the slope for the experimental data is larger than that of the simulated data which suggests that the transmission through the ITO – Pt samples is falls off more slowly than simulated structures, however this is to be expected as the samples likely exhibit surface roughness and other scattering-causing defects. Figure 4.17(c) shows that the reflection at 1125 nm is also suppressed with increasing Pt thickness and (d) shows a coinciding increase in absorption. The absorption as a function of Pt thickness appears to follow an asymptotic trend with the turning point appearing to coincide with the skin depth of Pt at about 9 nm. The asymptotic nature of the curve suggests that increasing thicknesses of Pt enhances the absorption up to a maximum value, thus we can conclude that a Pt thickness of no more than 15 – 25 nm is necessary to achieve extremely high values of absorption. Again, due to imperfections in the samples that the simulations cannot account for, the experimentally measured reflection through the structure is higher than simulated values and the absorption is lower. The agreement in the trends, however, clearly demonstrates that the application of a metallic backing can induce significant enhancement of the absorption of the Ferrell – Berreman mode of ITO. It was deduced from COMSOL FEM simulations of the structures that the suppressed transmission and reflection and hence enhanced absorption was a result of a significant impedance mismatch at the boundary of the ITO – Pt interface which causes further reflection back into the ITO layer wherein the reflected light at the NPA wavelength undergoes further absorption by exciting the Ferrell-Berreman mode.

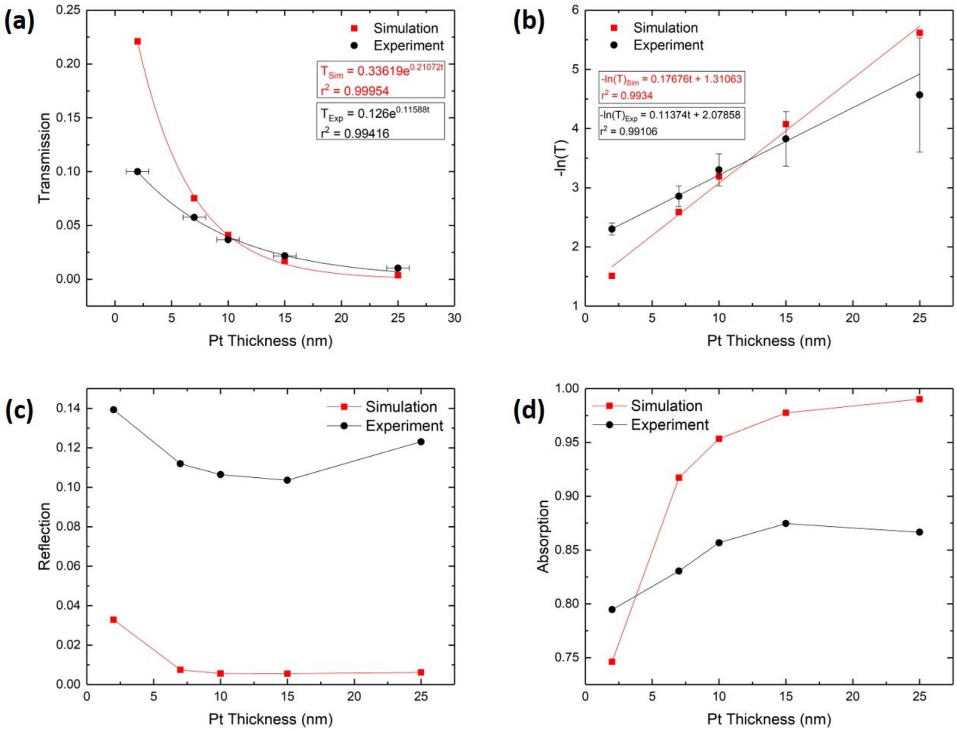

Figure 4.17 A comparison of simulation (red) and experiment (black) for (a) the linear transmission and (b) the natural logarithm of transmission through the ITO – Pt multilayer structure as a function of Pt thickness at 1125 nm and 39˚ incidence. The slope of the linear fit in (b) gives the penetration depth of the Pt layer. The experimental and simulated data for reflection (c) and absorption (d) show a minor suppression of reflection and an increase in absorption with increasing Pt thickness.

4.12 Non-Radiative ENZ Mode Excitation in ITO Thin Films

While it has been demonstrated theoretically and experimentally that ITO exhibits a highly absorptive bulk plasmon polariton, another higher momentum plasmon mode can also be excited in ITO thin films; a long-range surface plasmon polariton known as the "non-radiative ENZ mode", or simple the "ENZ mode". To excite this higher momentum mode, the ITO samples had to be excited using the Kretschmann geometry. A BK7 glass coupling prism was used with index matching fluid ($n = 1.48$). Angle-resolved absorption measurements were carried out using this configuration and are presented in Figure 4.18. The use of the coupling prism not only allowed higher momentum and greater coupling efficiency into the ENZ mode, but also allowed a greater measurable angular range of 29˚ – 70˚ incidence. The critical angle for the glass superstrate was 43˚ and hence both the Ferrell-Berreman mode, below this angle, and the ENZ mode, above this angle were measurable. The ENZ mode is clearly visible in the ITO film in Figure 4.18(a), and the ITO films with Pt backings of thicknesses 7 nm – 25 nm in Figure 4.18(c – f). The ITO film with 2 nm of Pt, however, doesn't appear to show excitation of the ENZ mode, but rather another unidentified high absorption feature in the spectral range 1600 nm – 2000 nm. The data clearly shows a significant enhancement of the absorption with the presence of the Pt backing. Similar enhancement of absorption in observed for the Ferrell-Berreman mode below the critical angle also.

Figure 4.19 presents plots of the ENZ mode absorption as a function of wavelength at an incident angle of 47˚ compared to the same data calculated from the T-matrix method. Experiment and simulation agree quite well and are consistent with previous findings. The application of a Pt backing greatly increases the absorption of the ENZ mode across all samples. The initial application of 2 nm of Pt appears to cause a blueshift of about 90 nm compared to the ITO film alone. The ITO film alone exhibits an ENZ mode absorption of 71.5%, which for all samples except the ITO film with 2 nm of Pt (b) is pushed to values > 90%. There is also some minor spectral shifting of the mode for each thickness which could be a result of different surface roughness for each sample or some minor experimental error in index matching the prism and the ITO film. In both experiment and simulation, the Ferrell-Berreman mode below the critical angle, and the non-radiative ENZ mode above the critical angle are clearly visible about the ENZ region of 1200 nm. The absorption region attributed to the ENZ mode occurs at shorter wavelengths as the incident angle increases and a clear blueshift in the ENZ mode absorption is noted with the application of the Pt backing layer. The ENZ mode NPA peak for each sample appears in the 900 nm – 1000 nm range. The experimentally measured absorption in each sample is somewhat larger than the simulated value, however only by about 5%. This is likely due to use of the index matching fluid which was placed between the coupling prism and the glass side of the sample and exhibits some absorption in the near infrared. In particular, a consistent peak at 1400 nm is noted across the entire sample set which corresponds perfectly to a peak in the absorption spectrum of the fluid. The fluid also absorbs quite strongly about 1800 nm – 2000 nm which could explain why the absorption at longer wavelengths is greater than suggested by the T-matrix simulations across all samples. This may also explain the anomalous absorption feature in the ITO sample with 2 nm Pt shown in Figure 4.18(b) and Figure 4.19(b).

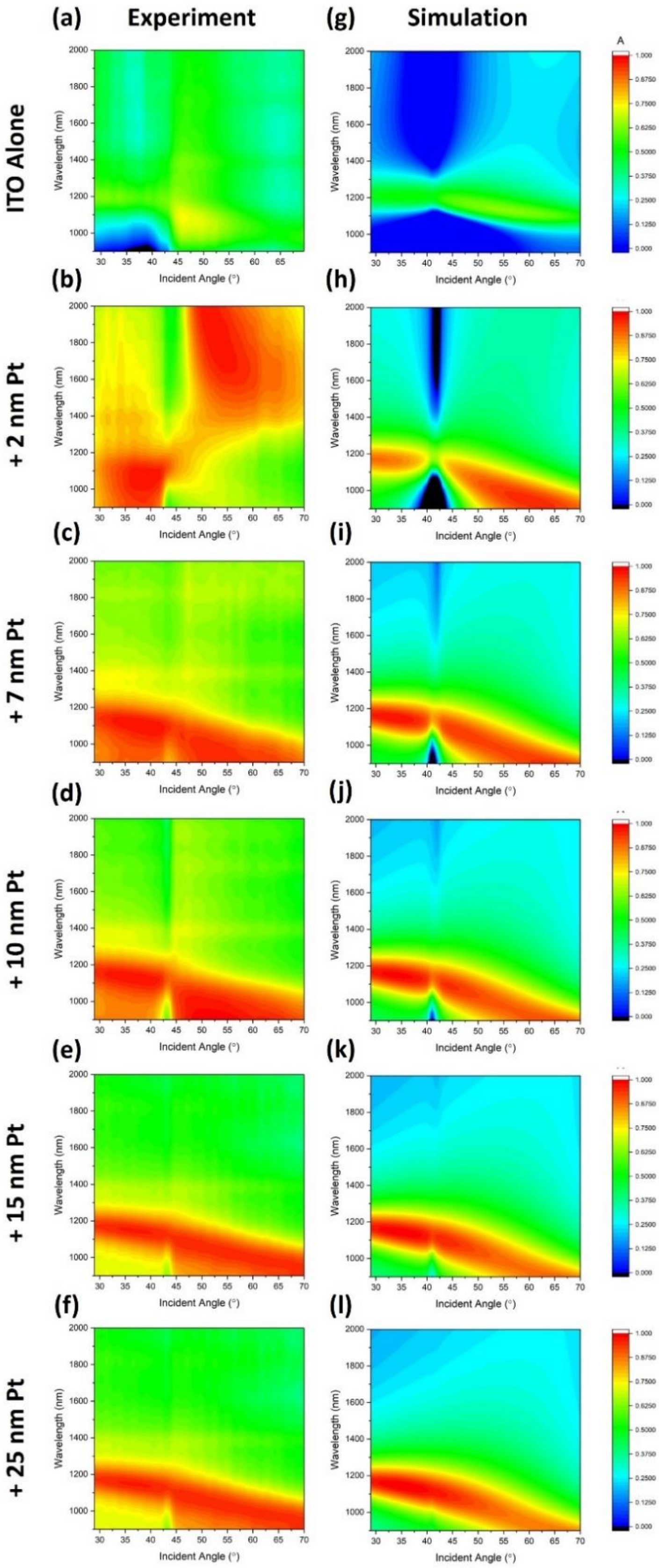

Figure 4.18 Angle resolved absorption measurement using the Kretschmann geometry of a 127 nm ITO film (a) and identical ITO films with the addition of (b) 2 nm, (c) 7 nm, (d) 10 nm, (e) 15 nm, and (f) 25 nm of Pt metal deposited on the ITO containing side. (g – l) presents the corresponding T-matrix simulations.

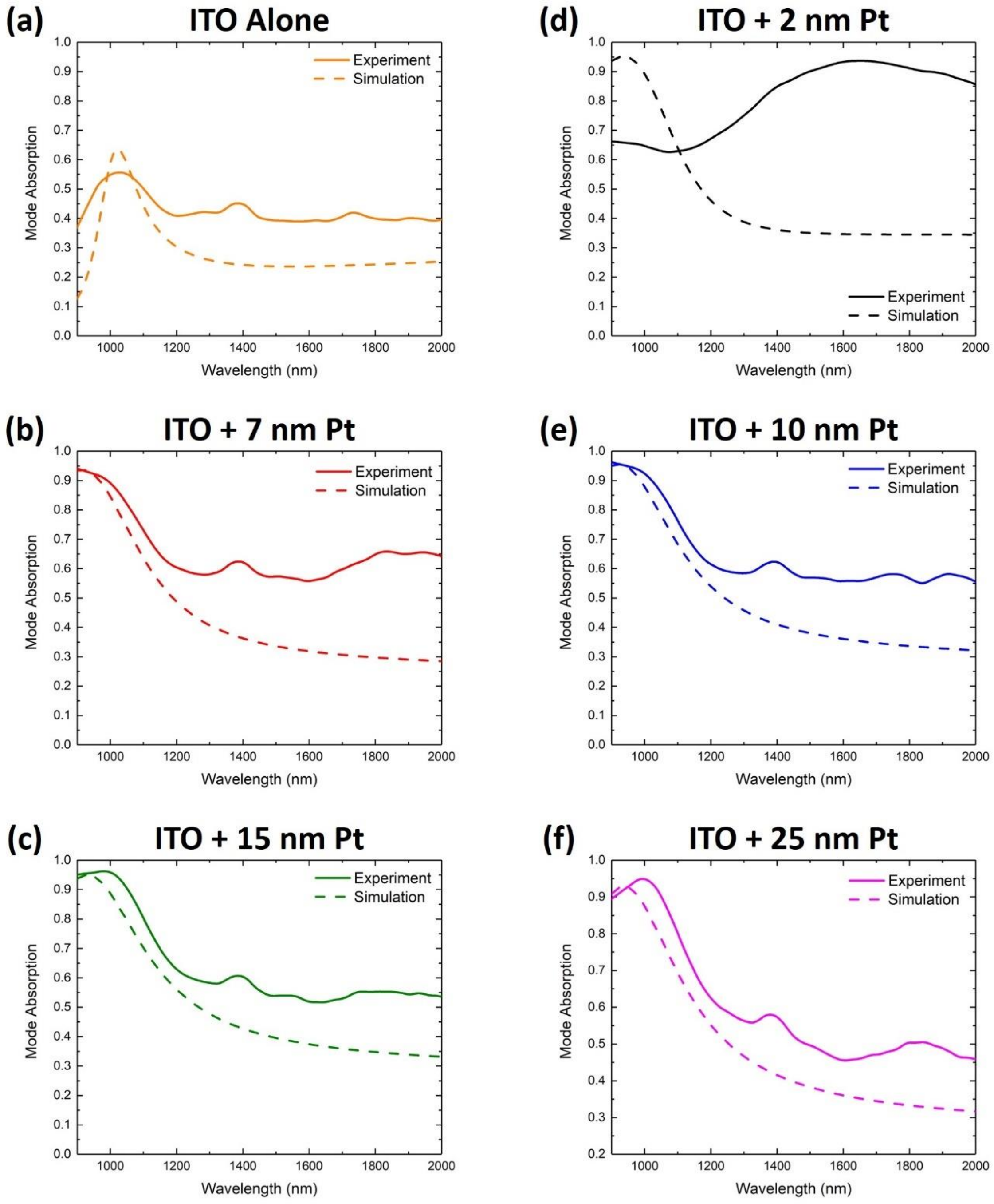

Figure 4.19 A comparison of experiment (solid lines) and simulation (dashed lines) for the ENZ mode absorption as a function of wavelength and at 47˚ incidence for a 127 nm ITO film (a) and identical ITO films with (b) 2 nm, (c) 7 nm, (d) 10 nm, (e) 15, and (f) 25 nm of Pt as a backing. These measurements were carried out using the Kretschmann geometry with a BK7 coupling prism.

4.13 Ferrell-Berreman Mode Excitation using the Kretschmann Geometry

While the ENZ mode is most apparent when exciting in the Kretschmann geometry, a significant portion of the Ferrell-Berreman mode is also measurable below the critical in the 29˚ – 43˚ incidence angular range. The ITO film alone achieves a Ferrell-Berreman mode absorption of

81.8%, significantly higher than the single-pass absorption in Figure 4.15(a) which is a result of using the Kretschmann geometry.

Figure 4.21 presents the Ferrell – Berreman (a) and ENZ (b) mode absorptions together for comparison as a function of wavelength and at incident angles of 39˚ and 47˚ respectively for the various thicknesses of Pt. In Figure 4.21, the application of just 2 nm of Pt causes a significant blueshift of about 90 nm and a substantial enhancement of the absorption to > 95%. This enhanced absorption persists for thicker films of Pt, however the NPA peak appears to slowly redshift back towards the initial NPA peak of ITO alone, but with much higher values. This blueshifting and subsequent redshifting behaviour with increased thickness could be a result of the surface roughness and quality of the Pt film's surface. Previous work by Berreman [45] predicted that roughness in ENZ thin-film samples would cause spectral shifting of the mode. As the Ar-ion sputtering technique used to deposit these Pt films has a tendency to produce rough films, it would suggest that the 2 nm deposition is not a continuous film and hence has the lowest quality and largest surface roughness. As the Pt films become thicker, the effective contribution of the surface roughness to the overall quality of the film becomes less, and hence the mode redshifts back towards the wavelength for an ITO film alone. Figure 4.20 presents the NPA wavelength shift, $\Delta\lambda_{NPA}$ as a function of the Pt film thickness. This spectral shift in the mode absorption was calculated using

$$\Delta\lambda_{NPA} = \lambda_{ITO+Pt} - \lambda_{ITO} \tag{19}$$

where λ_{ITO+Pt} is the NPA wavelength for each of the ITO – Pt structures, and λ_{ITO} is the NPA wavelength for ITO alone. The graph shows that the spectral shift in the wavelength of NPA follows a trend of exponential decay with increasing Pt thickness.

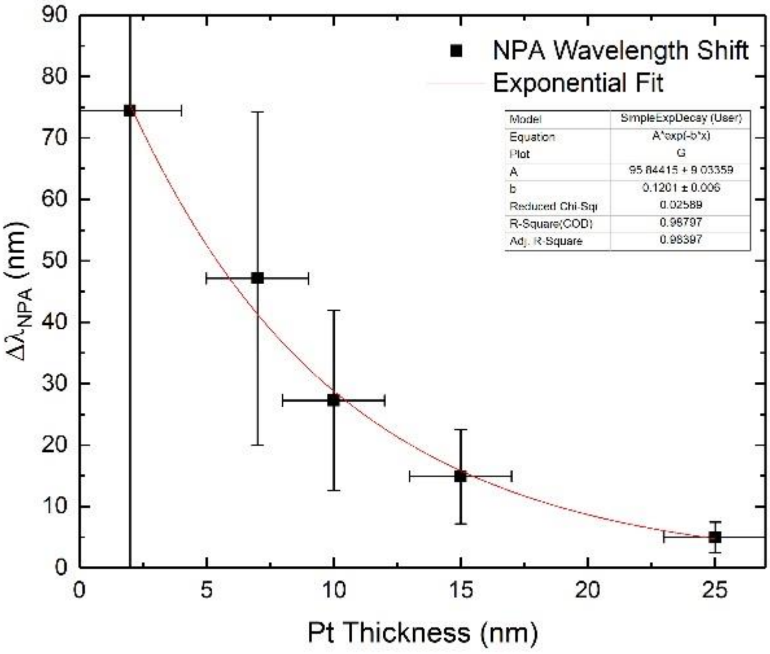

Figure 4.20 The shift in the NPA wavelength for ITO films with a Pt backing as a function of the Pt layer thickness.

While the mode absorption shifts by a maximum value of about 75 nm, the results from Figure 4.20 allows us the ability to tune the spectral position of the absorption by selecting the appropriate thickness of Pt. However, it is important to note that these results may only apply to the deposition technique and equipment used in this work. Whether identical or similar results would occur with other deposition techniques and deposition tools remains, as of yet, unknown, however this may be an avenue to pursue in further research.

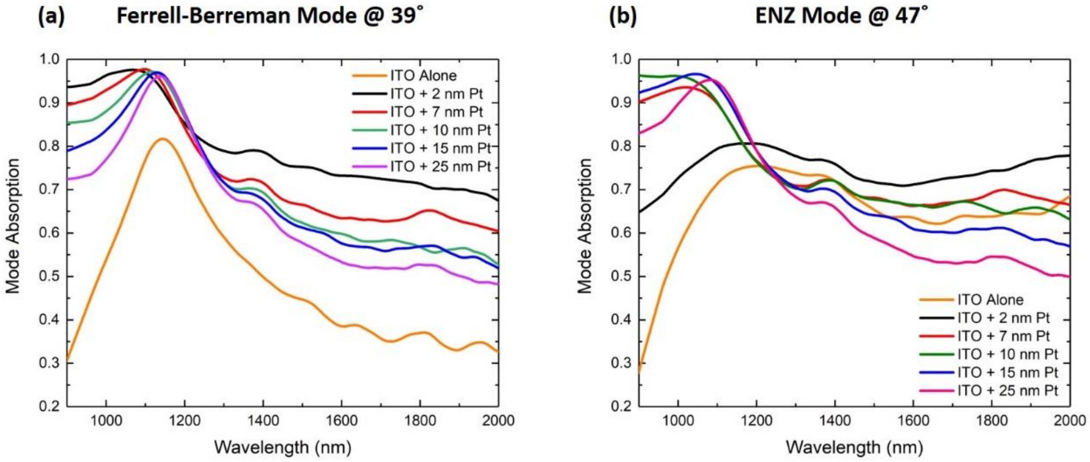

Figure 4.21 (a) Ferrell-Berreman mode absorption for ITO films with various thicknesses of Pt as a backing and (c) the non-radiative ENZ mode absorption of the same samples.

An interesting trend notable in Figure 4.21(a) and (b) is the decrease in absorption with a thicker Pt backing layer. This is most noticeable when examining an off-resonance region, such as 1800 nm. Figure 4.22 presents a comparison of simulation and experiment for the absorption in the off-resonance 1800 nm region of the ITO – Pt films as a function of Pt thickness at 47° incidence. Both experiment and simulation show the same decreasing trend in absorption with increasing Pt thickness, however the experimental absorption is significantly higher than simulation which is likely due to the high absorption of the index matching fluid at this wavelength. While at first appearance it may seem counter-intuitive for a thinner sample to exhibit higher absorption, it was posited that this greater absorption for thinner samples is a result of the excitation of an insulator – metal – insulator (IMI) mode. Because the thickness of the Pt is so small, and for some of the samples, smaller than the skin depth, incident light excites an SPP at the boundaries of the ITO – Pt interface and the Pt – Air interface. If the Pt layer is sufficiently thin, these two modes on either interface can be simultaneously excited and coupled. Thus, the thinner the Pt layer, the greater the absorption as the light can penetrate down to the Pt – Air interface to excite this SPP mode.

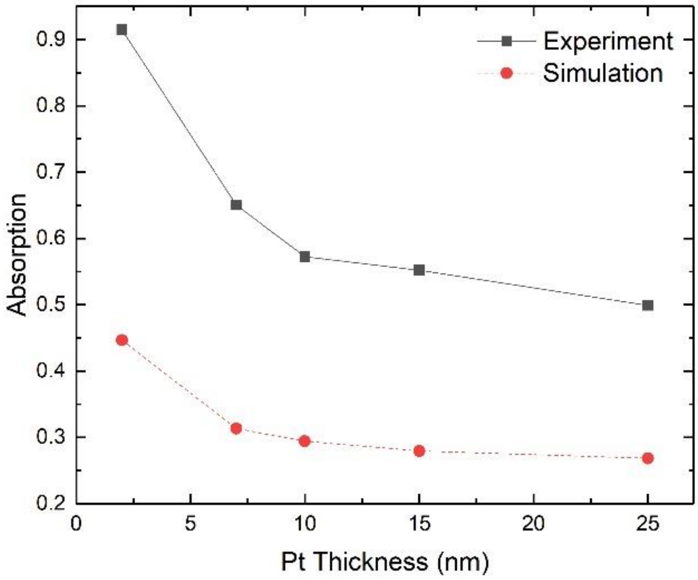

Figure 4.22 Experiment (black) and simulation (red) for the absorption as a function of thickness in the ITO – Pt films at 1800 nm. Both experiment and simulation follow the same trend, however the experimental absorption is significantly higher than simulated values.

To achieve such high values of absorption via the addition < 25 nm of Pt is a significantly important result as previous work has shown that the maximum achievable absorption of light by a free-standing thin film is 50% [61]. By combining such films with ITO we can achieve much higher absorptions in the ITO layer as a result of adding the metal.

4.14 Impedance Mismatching as a Route to Enhanced Ferrell-Berreman and ENZ Mode Absorption

The absorption enhancement of the Ferrell-Berreman mode observed with the addition of a Pt backing is a result of reflection from the Pt surface back into the ITO layer wherein it undergoes further absorption by exciting the mode again. This reflectivity back into the ITO layer is a result of a large mismatch between the impedances of the ITO and Pt layers. Figure 4.23(a) and (b) present the relative complex impedances of the ITO and Pt layers respectively. The complex wave impedance, Z is given by the following expression

$$Z = \sqrt{\frac{i\omega\mu_0\mu_r}{\sigma + i\omega\varepsilon_0\varepsilon_r}} \tag{20}$$

where ω is the incident frequency, σ is the electrical conductivity, μ_0 and μ_r are the magnetic permeability of free space and the relative permeability respectively, and ε_0 and ε_r are the respective permittivity of free space and relative permittivity. Here, we plot the real and imaginary components of the relative impedance, ${}^{Z}/_{Z_0}$ where $Z_0 = \frac{1}{\varepsilon_0 c} \approx 120\pi\,\Omega$. The impedance of a material is a phase vector quantity or “phasor” represented by a complex number. While the imaginary part carries some useful information regarding the phase, it is the real component we are most concerned with for calculating the reflectivity from the ITO – Pt and ITO – Air interfaces of our samples. Figure 4.23 (a) and (b) show the real (solid lines) and imaginary (dashed lines) components of this complex impedance of the 127 nm 8 – 12 Ω sq^{-1} ITO film and Pt. As shown, there is a large mismatch between the impedances of the two materials and hence both data sets had to be plotted on separate graphs for visibility. This suggests that at an interface between the two materials, a large reflectivity is expected. A reflection coefficient between two interfaces, 1 and 2 can be determined from the impedances of these layers using the following expression

$$\Gamma_{12} = \left|\frac{Z_1 - Z_2}{Z_1 + Z_2}\right| \tag{21}$$

where Γ_{12} denotes the reflection coefficient of an EM wave propagating in medium 1 and incident on the boundary of medium 2. The reflectivity can thus be determined by taking the square of Γ_{12}. Equation 21 was used to calculate the reflectivity at the boundaries of the ITO – Pt interface, and the ITO – Air interface. Figure 4.23 presents these calculations as a function of wavelength. As shown, the reflectivity expected for light at and below 1250 nm propagating from the ITO layer to the air substrate is close to zero at the NPA wavelength of ITO alone (1175 nm), whereas the reflectivity of an EM wave at the NPA wavelength for the ITO – Pt interface (1125 nm) is greater than 90%. Thus, we would expect a high transmission of light travelling from the ITO layer into the air superstrate and a high reflection for light travelling from the ITO layer into the

Pt layer of the other samples. This confirms that the increase in absorption as a result of a Pt backing is due to reflection of the remaining light at the NPA wavelength that is not absorbed after its first pass through the ITO being reflected back into the ITO layer and exciting the Ferrell-Berreman mode once more and thus being further absorbed. Figure 4.23(d) and (e) present a representative diagram of the interfaces examined in this calculation. While a large proportion of the absorption can be attributed to the high reflectivity as a result of the impedance mismatch between the ITO and Pt layers, there is also evidence to suggest the excitation of an IMI mode in the ITO – Pt structures also occurs for sufficiently thin layers of Pt.

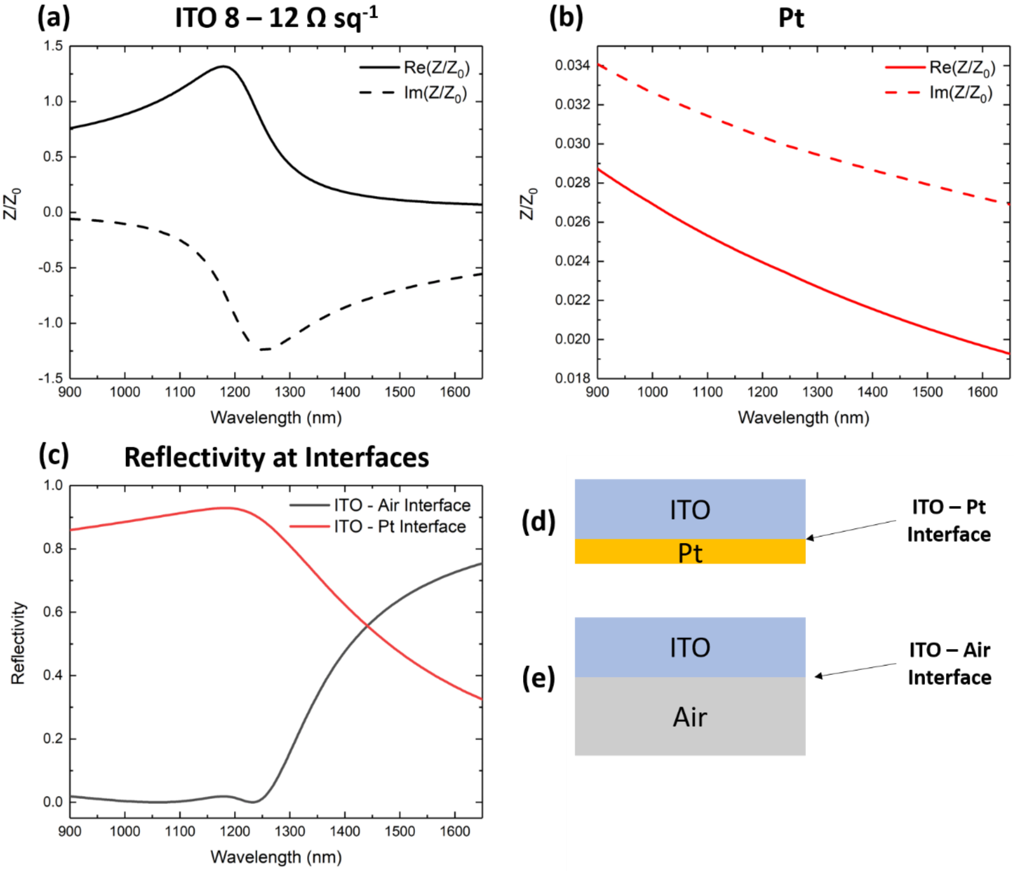

Figure 4.23 The real (solid lines) and imaginary (dashed lines) components of the complex impedance of (a) the 127 nm 8 – 12 Ω sq^{-1} and (b) the Pt layer. (c) presents the calculated reflectivity at these interfaces and (d) and (e) present a schematic representation of the ITO – Pt and ITO – Air interfaces considered in this calculation.

4.15 Conclusions

In this chapter we presented experimental observation of the excitation of both the Ferrell-Berreman, a bulk plasmon polariton, and the non-radiative ENZ mode, a long-range surface plasmon polariton mode in commercial thin-film ITO samples. We map these modes more precisely and over a larger angular and spectral range that precious work carried on these mode and ITO. Along with our mapping of the absorption we also calculate the mode dispersion of the

Ferrell-Berreman mode with and without the presence of a Pt backing. The Ferrell-Berreman mode achieved a single-pass absorption of 52.5% in the ITO film alone which was pushed to a value of 85.6% via the application of a 10 nm Pt backing. The ENZ mode in an ITO film alone achieved a maximum absorption of 71.5% and with the application of the Pt backing of just 10 nm this absorption was increased to over 90%. This work provides the first demonstration that such high values of ENZ absorption can be achieved from much thinner metal backings than previously considered. Furthermore, we provide the first study of the dependence of this absorption as a function of the metal backing thickness. The enhancement of these plasmon mode absorptions was demonstrated theoretically and experimentally to be assisted by the application of Pt to the ITO-containing side of the commercial ITO films and it was shown using FEM simulations that the absorption is a result of a rather substantial electric field confinement in the ITO layer, and reflection back into this layer of light at the NPA wavelength incident on the Pt layer. Furthermore, a comparison of these mode absorptions for various thicknesses of Pt were carried out. It was shown that the transmission through the structures followed an exponential trend with increased Pt thickness consistent with the Beer-Lambert law. It was also demonstrated the absorption follows an asymptotically increasing trend with increasing Pt thickness. Spectral shifting of the NPA Ferrell-Berreman mode absorption excited in the Kretschmann geometry was also observed and that the wavelength of NPA could be tuned within a 75 nm window by selecting an appropriate Pt thickness. Finally, it was also noted that in the off-resonant lower wavelengths, particularly 1800 nm, that the absorption in the ITO – Pt structures was greater for thinner samples of Pt. This counterintuitive result was posited to be the excitation of an IMI mode which will be discussed in further detail in Chapter 6.

References

[1] W. Cai and V. Shalaev, "*Optical Metamaterials: Fundamentals and Applications*," Springer New York, 2009.

[2] F. Abbasi and N. Engheta, “Roles of epsilon-near-zero (ENZ) and mu-near-zero (MNZ) materials in optical metatronic circuit networks,” *Opt. Express*, vol. 22, no. 21, p. 25109, 2014.

[3] R. Liu *et al.*, “Experimental Demonstration of Electromagnetic Tunneling Through an Epsilon-Near-Zero Metamaterial at Microwave Frequencies,” *Phys. Rev. Lett.*, vol. 100, no. 2, p. 23903, 2008.

[4] S. Zhong and S. He, “Ultrathin and lightweight microwave absorbers made of mu-near-zero metamaterials,” *Sci. Rep.*, vol. 3, p. 2083, 2013.

[5] Y. Wang, Y. Qin, Z. Sun, and P. Xu, “Magnetically controlled zero-index metamaterials based on ferrite at microwave frequencies,” *J. Phys. D. Appl. Phys.*, vol. 49, no. 40, p. 405106, 2016.

[6] S. Hrabar, I. Krois, and A. Kiricenko, “Towards active dispersionless ENZ metamaterial for cloaking applications,” *Metamaterials*, vol. 4, no. 2, pp. 89–97, 2010.

[7] J. Yoon, M. Zhou, M. A. Badsha, T. Y. Kim, Y. C. Jun, and C. K. Hwangbo,

“Broadband Epsilon-Near-Zero Perfect Absorption in the Near-Infrared,” *Sci. Rep.*, vol. 5, p. 12788, 2015.

[8] S. Campione, J. R. Wendt, G. A. Keeler, and T. S. Luk, “Near-Infrared Strong Coupling between Metamaterials and Epsilon-near-Zero Modes in Degenerately Doped Semiconductor Nanolayers,” *ACS Photonics*, vol. 3, no. 2, 2016.

[9] T. Y. Kim, M. A. Badsha, J. Yoon, S. Y. Lee, Y. C. Jun, and C. K. Hwangbo, “General Strategy for Broadband Coherent Perfect Absorption and Multi-wavelength All-optical Switching Based on Epsilon-Near-Zero Multilayer Films,” *Sci. Rep.*, vol. 6, 2016.

[10] C. H. T. E. Llis *et al.*, “Role of epsilon-near-zero substrates in the optical response of plasmonic antennas,” *Optica*, vol. 3, no. 3, 2016.

[11] E. J. R. Vesseur, T. Coenen, H. Caglayan, N. Engheta, and A. Polman, “Experimental verification of n=0 structures for visible light,” *Phys. Rev. Lett.*, vol. 110, no. 1, p. 013902, Jan. 2013.

[12] J. Gao, L. Sun, H. Deng, C. J. Mathai, S. Gangopadhyay, and X. Yang, “Experimental realization of epsilon-near-zero metamaterial slabs with metal-dielectric multilayers,” *Appl. Phys. Lett.*, vol. 103, no. 5, 2013.

[13] R. Maas, J. Parsons, N. Engheta, and A. Polman, “Experimental realization of an epsilon-near-zero metamaterial at visible wavelengths,” *Nat Phot.*, vol. 7, no. 11, pp. 907–912, 2013.

[14] C. Rizza, A. Di Falco, and A. Ciattoni, “Gain assisted nanocomposite multilayers with near zero permittivity modulus at visible frequencies,” *Appl. Phys. Lett.*, vol. 99, no. 22, p. 221107, Nov. 2011.

[15] Y. Li *et al.*, “On-chip zero-index metamaterials,” *Nat Phot.*, vol. 9, no. 11, pp. 738–742, 2015.

[16] X. Huang, Y. Lai, Z. H. Hang, H. Zheng, and C. T. Chan, “Dirac cones induced by accidental degeneracy in photonic crystals and zero-refractive-index materials,” *Nat. Mater.*, vol. 10, no. 8, p. 582, 2011.

[17] I. Liberal and N. Engheta, “Near-zero refractive index photonics,” *Nat. Photonics*, vol. 11, no. 3, pp. 149–158, 2017.

[18] I. Liberal and N. Engheta, “Zero-Index Platforms: Where Light Defies Geometry,” vol. 2016. OSA, Optics & Photonics News, 2017.

[19] W. Cai, “Metal-coated waveguide stretches wavelengths to infinity,” *Physics (College. Park. Md).*, vol. 6, p. 1, 2013.

[20] V. Pacheco-Peña, V. Torres, M. Beruete, M. Navarro-Cía, and N. Engheta, “ε-near-zero (ENZ) graded index quasi-optical devices: steering and splitting millimeter waves,” *J. Opt.*, vol. 16, no. 9, p. 094009, 2014.

[21] A. J. Labelle *et al.*, “Broadband epsilon-near-zero reflectors enhance the quantum efficiency of thin solar cells at visible and infrared wavelengths,” *ACS Appl. Mater. Interfaces*, vol. 9, no. 6, pp. 5556–5565, 2017.

[22] A. Alù and N. Engheta, “Dielectric sensing in $ϵ$-near-zero narrow waveguide channels,” *Phys. Rev. B*, vol. 78, no. 4, p. 45102, 2008.

[23] H. Lobato-Morales, D. V. B. Murthy, A. Corona-Chavez, J. L. Olvera-Cervantes, J. Martinez-Brito, and L. G. Guerrero-Ojeda, “Permittivity Measurements at Microwave Frequencies Using Epsilon-Near-Zero (ENZ) Tunnel Structure,” *IEEE Trans. Microw. Theory Tech.*, vol. 59, no. 7, pp. 1863–1868, 2011.

[24] B. Edwards, A. Alù, M. E. Young, M. Silveirinha, and N. Engheta, “Experimental Verification of Epsilon-Near-Zero Metamaterial Coupling and Energy Squeezing Using a Microwave Waveguide,” *Phys. Rev. Lett.*, vol. 100, no. 3, p. 33903, 2008.

[25] F. Bello, A. F. Page, A. Pusch, J. M. Hamm, J. F. Donegan, and O. Hess, “Combining ε-Near-Zero Behavior and Stopped Light Energy Bands for Ultra-Low Reflection and Reduced Dispersion of Slow Light,” *Sci. Rep.*, vol. 7, no. 1, p. 8702, 2017.

[26] A. Ciattoni, A. Marini, C. Rizza, M. Scalora, and F. Biancalana, “Polariton excitation in epsilon-near-zero slabs: Transient trapping of slow light,” *Phys. Rev. A - At. Mol. Opt. Phys.*, vol. 87, no. 5, pp. 1–9, 2013.

[27] A. Marini and F. J. G. De Abajo, “Self-organization of frozen light in near-zero-index media with cubic nonlinearity,” *Sci. Rep.*, vol. 6, p. 20088, 2016.

[28] C. Argyropoulos, P.-Y. Chen, G. D’Aguanno, N. Engheta, and A. Alù, “Boosting optical nonlinearities in ε-near-zero plasmonic channels,” *Phys. Rev. B*, vol. 85, no. 4, p. 45129, 2012.

[29] R. Fleury and A. Alù, “Enhanced superradiance in epsilon-near-zero plasmonic channels,” *Phys. Rev. B*, vol. 87, no. 20, p. 201101, 2013.

[30] R. W. Ziolkowski, “Propagation in and scattering from a matched metamaterial having a zero index of refraction,” *Phys. Rev. E*, vol. 70, no. 4, p. 46608, 2004.

[31] I. I. Smolyaninov, “Modeling of causality with metamaterials,” *J. Opt.*, vol. 15, no. 2, p. 25101, 2013.

[32] M. G. Silveirinha, “Trapping light in open plasmonic nanostructures,” *Phys. Rev. A*, vol. 89, no. 2, p. 23813, 2014.

[33] A. Alù and N. Engheta, “All optical metamaterial circuit board at the nanoscale,” *Phys. Rev. Lett.*, vol. 103, no. 14, p. 143902, 2009.

[34] D. de Ceglia, M. A. Vincenti, S. Campione, F. Capolino, and M. Scalora, “Nonlocal effects on second harmonic generation in low-damping epsilon-near-zero slabs,” in *Nonlinear Optics*, 2013, pp. NTu2A-4.

[35] I. Liberal, A. M. Mahmoud, and N. Engheta, “Geometry-invariant resonant cavities,” *Nat Commun*, vol. 7, 2016.

[36] W. G. Spitzer, K. D.A., and D. J. Walsh, "*Infrared Properties of Hexagonal Silicon Carbide*," vol. 113. 1959.

[37] J. Kim *et al.*, “Transparent conducting oxides as plasmonic component in near infrared (Presentation Recording),” in *Proc.SPIE*, 2015, vol. 9544.

[38] N. Kinsey, C. DeVault, J. Kim, M. Ferrera, V. M. Shalaev, and A. Boltasseva, “Epsilon-near-zero Al-doped ZnO for ultrafast switching at telecom wavelengths,” *Optica*, 2015.

[39] Z. Lu, W. Zhao, and K. Shi, “Ultracompact electroabsorption modulators based on tunable epsilon-near-zero-slot waveguides,” *IEEE Photonics J.*, vol. 4, no. 3, pp. 735–740, 2012.

[40] Y. Wang, A. Capretti, and L. Dal Negro, “Wide tuning of the optical and structural properties of alternative plasmonic materials,” *Opt. Mater. Express*, vol. 5, no. 11, pp. 2415–2430, 2015.

[41] A. P. Vasudev, J.-H. Kang, J. Park, X. Liu, and M. L. Brongersma, “Electro-optical modulation of a silicon waveguide with an ‘epsilon-near-zero’ material,” *Opt Express*, vol. 21, no. 22, pp. 26387–26397, 2013.

[42] U. Koch, C. Hoessbacher, J. Niegemann, C. Hafner, and J. Leuthold, “Digital Plasmonic Absorption Modulator Exploiting Epsilon-Near-Zero in Transparent Conducting Oxides,” *IEEE Photonics J.*, vol. 8, no. 1, 2016.

[43] W. D. Newman, C. L. Cortes, J. Atkinson, S. Pramanik, R. G. DeCorby, and Z. Jacob, “Ferrell–Berreman Modes in Plasmonic Epsilon-near-Zero Media,” *ACS Photonics*, vol. 2, no. 1, pp. 2–7, 2015.

[44] R. A. Ferrell, “Predicted Radiation of Plasma Oscillations,” *Phys. Rev.*, vol. 111, no. 1956, p. 1214, 1958.

[45] D. W. Berreman, “Infrared Absorption at Longitudinal Optic Fretluency in Cubic Crystal Films,” *Phys. Rev. A Mater.*, vol. 130, no. 6, 1963.

[46] S. Campione, I. Kim, D. De Ceglia, G. A. Keeler, and T. S. Luk, “Experimental verification of epsilon-near-zero plasmon polariton modes in degenerately doped semiconductor nanolayers,” *Opt. Express*, vol. 24, no. 16, pp. 18782–18789, 2016.

[47] R. H. Lyddane, R. G. Sachs, and E. Teller, “On the Polar Vibrations of Alkali Halides,” *Phys. Rev.*, vol. 59, no. 8, pp. 673–676, Apr. 1941.

[48] N. W. Ashcroft and N. D. Mermin, "*Solid State Physics*," Cengage Learning, 2011.

[49] K. F. Shi and Z. L. Lu, “Field-effect optical modulation based on epsilon-near-zero conductive oxide,” *Opt. Commun.*, vol. 370, pp. 22–28, 2016.

[50] T. S. Luk *et al.*, “Directional perfect absorption using deep subwavelength low-permittivity films,” *Phys. Rev. B - Condens. Matter Mater. Phys.*, vol. 90, no. 8, pp. 1–10, 2014.

[51] J. Park, J. H. Kang, X. G. Liu, and M. L. Brongersma, “Electrically Tunable Epsilon-Near-Zero (ENZ) Metafilm Absorbers,” *Sci. Rep.*, vol. 5, 2015.

[52] M. Lobet, B. Majerus, L. Henrard, and P. Lambin, “Perfect electromagnetic absorption using graphene and epsilon-near-zero metamaterials,” *Phys. Rev. B*, vol. 93, no. 23, p. 235424, 2016.

[53] A. Capretti, Y. Wang, N. Engheta, and L. Dal Negro, “Comparative Study of Second-Harmonic Generation from Epsilon-Near-Zero Indium Tin Oxide and Titanium Nitride Nanolayers Excited in the Near-Infrared Spectral Range,” *ACS Photonics*, vol. 2, no. 11, pp. 1584–1591, 2015.

[54] L. Caspani *et al.*, “Enhanced Nonlinear Refractive Index in E -Near-Zero Materials,” *Phys. Rev. Lett.*, vol. 116, no. 23, 2016.

[55] I. H. Malitson, “Interspecimen Comparison of the Refractive Index of Fused Silica*,†,” *J. Opt. Soc. Am.*, vol. 55, no. 10, pp. 1205–1209, 1965.

[56] C. Z. Tan, “Determination of refractive index of silica glass for infrared wavelengths by IR spectroscopy,” *J. Non. Cryst. Solids*, vol. 223, no. 1, pp. 158–163, 1998.

[57] V. Caligiuri, M. Palei, G. Biffi, S. Artyukhin, and R. Krahne, “A Semi-Classical View on Epsilon-Near-Zero Resonant Tunneling Modes in Metal/Insulator/Metal Nanocavities,” *Nano Lett.*, p. acs.nanolett.9b00564, 2019.

[58] T. S. Luk *et al.*, “Enhanced third harmonic generation from the epsilon-near-zero modes of ultrathin films,” *Appl. Phys. Lett.*, vol. 106, no. 15, 2015.

[59] W. S. M. Werner, K. Glantschnig, and C. Ambrosch-Draxl, “Optical constants and inelastic electron-scattering data for 17 elemental metals,” *J. Phys. Chem. Ref. Data*, vol. 38, no. 4, pp. 1013–1092, 2009.

[60] E. C. Jordan, "*Electromagnetic waves and radiating systems*," Prentice-Hall, 1950.

[61] C. Hilsum, “Infrared Absorption of Thin Metal Films,” *J. Opt. Soc. Am.*, vol. 44, no. 3, pp. 188–191, 1954.

Chapter 5: Fabrication of Thin-Film Indium Tin Oxide for ENZ Applications

5.1 Introduction

In Chapter 4 we demonstrated the excitation of the Ferrell – Berreman and non-radiative ENZ modes in commercial films of ITO and demonstrated near-perfect absorption via the application of a metallic backing. However, in order to use ITO in novel and unique ENZ structures we must be able to tune the thickness of ITO layers with great precision. This in itself is not a difficult task as modern deposition techniques such as Ar^+ ion sputtering [1], atomic layer deposition (ALD) [2] and DC [3][4][5] and RF magnetron sputtering [6][7][8] allow very precise control of film thicknesses, however the true challenge lies in producing ITO of a given thickness while maintaining ENZ behaviour in the narrow 1200 – 1400 nm NIR range. The majority of work to date on the fabrication of ITO is for use in transparent electronic devices [9][10][11] and solar cells [12][13][14]. In this chapter, we will focus on the production of ITO for use an ENZ material and the achievement of perfect absorption in the NIR range. While various techniques and techniques exist for the production of ITO, the properties of this material are highly sensitive to the specific condition under which it is fabricated which can vary from apparatus to apparatus, and thus it is important to devise and test one's own recipe. The goal of the work in this chapter was to devise a recipe for the production of high-quality ITO using the tools and techniques available to us. However, in order to understand how to achieve an ENZ wavelength in the specified range, it is first necessary to understand how charge carriers are generated in ITO films and the effects of various deposition and annealing variables on this carrier generation.

5.2 Charge Carrier Generation in ITO

In particular, the effects of several variables such as temperature, oxygen content, and deposition technique and how they affect the carrier concentration will be discussed. The ENZ wavelength, λ_{ENZ} of ITO is highly dependent on the value of the plasma frequency, ω_p which is itself highly dependent on the carrier concentration, N and thus generation of sufficient carriers is essential to produce ITO with ENZ behaviour [15][16]. To achieve this, we must first examine how charge carriers are generated in ITO. There are two main ways to generate charge carriers in ITO; the activation of Sn^{4+} ions on In^{3+} sites and the generation of oxygen vacancies [17][18]. When ITO is deposited, it often deposits in the form of an amorphous composite of In_3O_2 and SnO_2[19][20]. To free up electrons for conduction, a post-deposition annealing process (or an in-situ annealing process) is required to induce the afore mentioned ion activation. The difference of -1 in the valency of Sn^{4+} and In^{3+} contributes one electron per substitution for conduction. Very high temperatures of greater than 425˚C are needed to take ITO from an amorphous to polycrystalline state as shown in Figure 5.1.

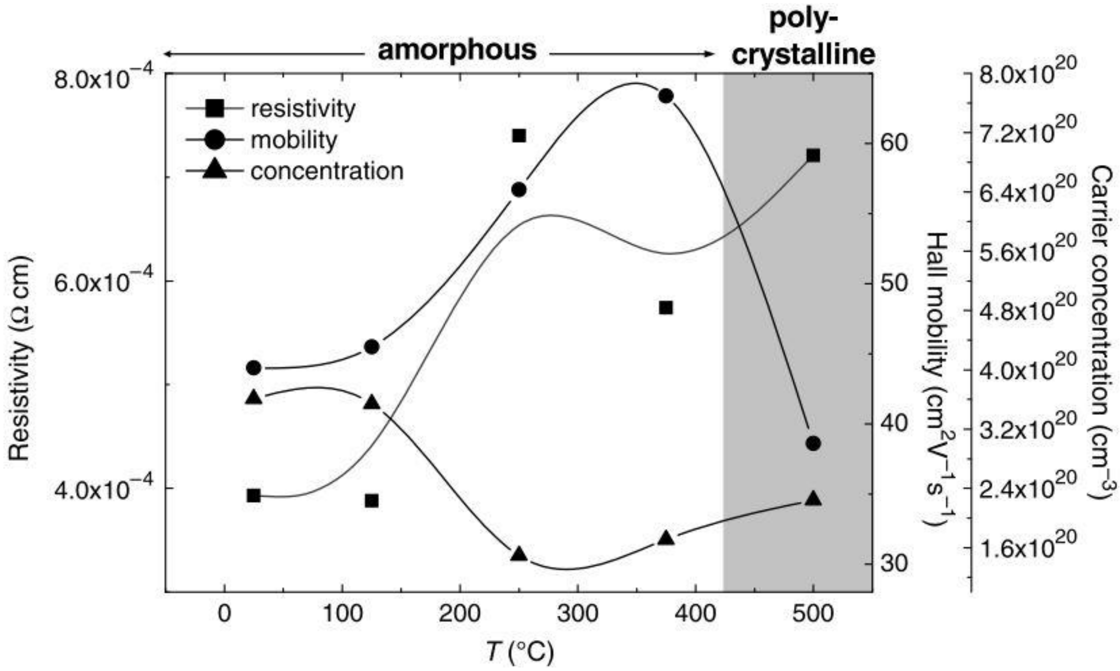

Figure 5.1 Resistivity, carrier mobility, and carrier concentration of ITO thin films as a function of annealing temperature. The data indicates a temperature of >425˚C is needed to produce polycrystalline ITO [17].

A more efficient method of producing charge carriers is to induce oxygen vacancies in the ITO, which can be achieved by annealing in vacuum which causes outward diffusion of oxygen [21][22]. As the valency of oxygen is 2, each O-vacancy contributes two electrons for conduction. However, ion activation and generation of O-vacancies alone are not sufficient to produce high quality ITO as the crystallinity of the ITO is also a factor. Thus, a fine balance between both methods of charge carrier generation are necessary to achieve ITO of commercial quality. Particularly, the oxygen content of the deposition / annealing atmosphere is significantly important [23]. ITO that is deficient in oxygen tends to behave somewhat like a metal, and ITO that is over-saturated with oxygen tends to behave as more of an oxide [17]. A fine balance is needed in the oxygen content as demonstrated in Figure 5.2 which presents the “oxygen – resistivity well” for ITO. The O_2 flow rate is presented on the x-axis and the bulk resistivity on the y-axis. This graph shows that too little oxygen and too much oxygen result in an increase in resistivity (and hence a decrease in conductivity). As shown, O_2 flow rates at the bottom of the well of between 2 – 7 sccm are ideal for conducive ITO films.

A simplified 2D atomic representation showing the structure of ITO and the two methods of charge carrier generation is presented in Figure 5.3.

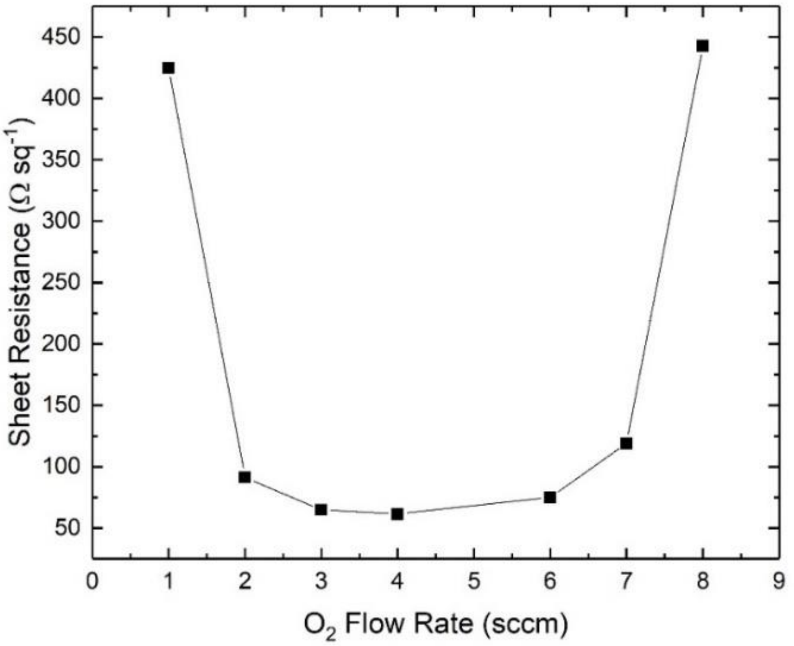

Figure 5.2 Sheet resistance for ITO thin films as function of the O_2 flow rate in the annealing atmosphere. This graph was plotted from data published by the Society of Vacuum Coaters 2009 [17].

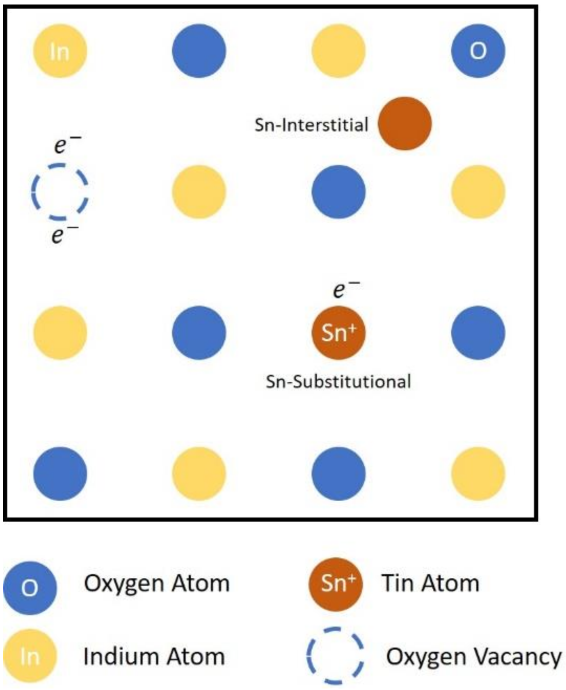

Figure 5.3 Simplified atomic model of ITO demonstrating the origin of charge carrier generation in the material.

The oxygen content of ITO also plays a rather significant role in the optical transmission of the films. ITO films with a large oxygen content display higher optical transmission at NIR wavelengths. Figure 5.4 presents the transmission spectra of indium zinc oxide (IZO), which is another TCO with almost identical properties to ITO. The data shows that as the oxygen content increases, so does the optical transmission in the NIR range. For ITO with a lower oxygen content, we see that the transmission gradually decreases at longer wavelengths. This particular "without oxygen" plot appears quite similar to the transmission of the 127 nm 8 – 12 Ω sq^{-1} commercial ITO film mentioned in precious chapters.

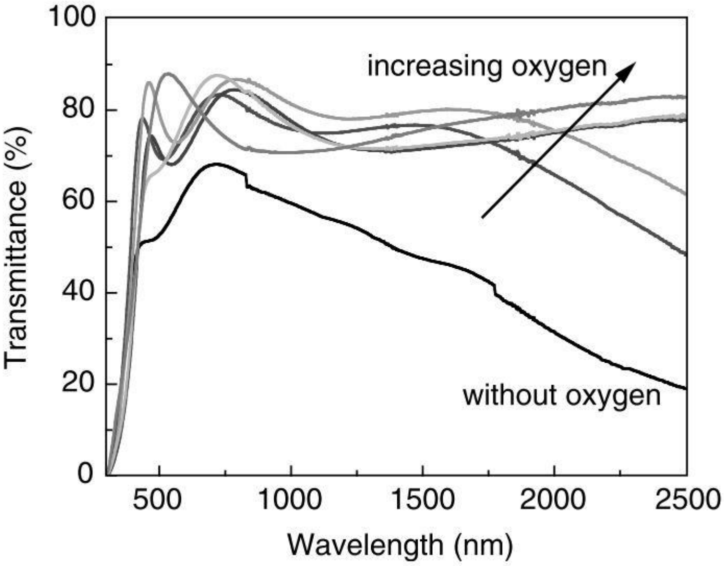

Figure 5.4 Optical transmission for indium zinc oxide (IZO) films as a function of wavelength and oxygen content. Increased oxygen content corresponds to a higher optical transmission in the NIR regime. This graph was taken from Transparent Electronics by Facchetti and Marks [17].

5.3 ITO Thin Film Deposition Techniques

ITO is a rather versatile material which can be deposited using various techniques such as RF magnetron sputtering. DC magnetron sputtering [24][3], argon ion sputtering [1], pulsed laser deposition [25][26], atomic layer deposition [27][28][29], and even chemical vapour deposition [30][31]. In this chapter, we focus on two techniques which were locally available: argon ion sputtering and RF magnetron sputtering.

5.3.1 Argon Ion Sputtering

Argon ion sputtering is a physical vapour deposition (PVD) technique for producing thin films of material [32]. As demonstrated in Figure 5.5, the technique involves ejecting material from a target via argon ion bombardment of a target material and the adhesion of the ejected material onto a substrate. The argon ion sputtering carried out in this research was performed using a Gatan Model 682 Precision Etching and Coating System (PECS) tool. The tool operates under a vacuum of 4 – 5 Torr, a beam energy of around 5 keV, and a beam current of 150 µA with argon gas flow into the chamber. The deposition rate and thickness were monitored using a quartz crystal monitor (QCM). This technique was used to produced Batch 1 and Batch 2 of the ITO samples as well as the platinum samples used in this research.

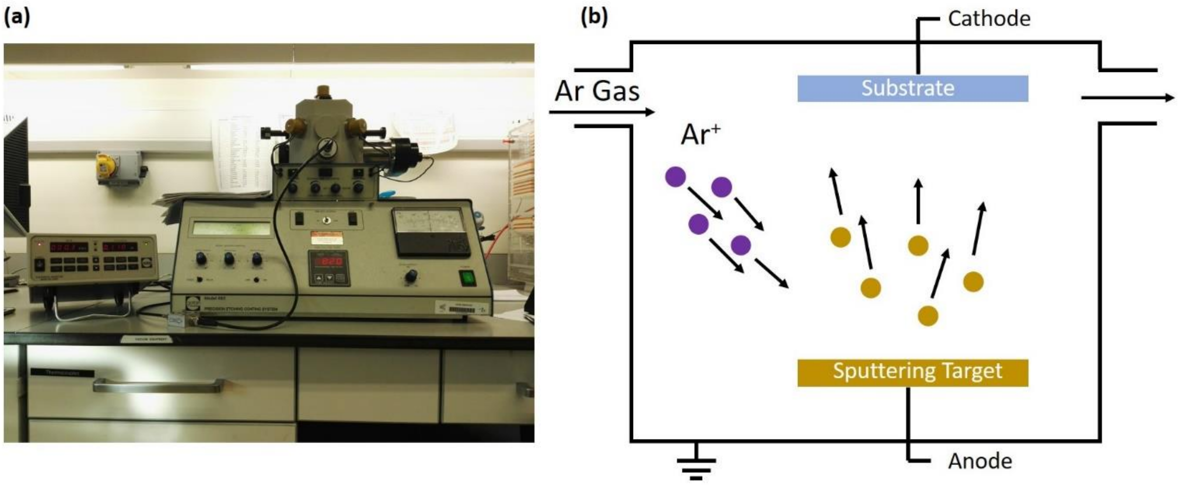

Figure 5.5 (a) A Gatan PECS system and (b) a schematic showing the technique of argon ion sputtering. Argon ions bombard a target material in vacuum ejecting material from target which adheres to a substrate. An anode is placed below the target and a cathode above the substrate to aid adhesion of the ejected material onto the substrate by applying a voltage across the target and substrate.

5.3.2 Radio Frequency Magnetron Sputtering

Radio Frequency (RF) Magnetron Sputtering is a physical vapour deposition technique for depositing thin films [33]. It works by running current through an inert gas, usually argon, under high vacuum to ionise the Ar gas forming a plasma of Ar^+ and electrons. These energetic Ar^+ ions then bombard the target ejecting ions of the target material which are attracted to the substrate cathode and thus adhering to the substrate. Magnets are placed under the target anode to trap electrons so as not to bombard the substrate and to thus allow faster deposition rates. Typically, the temperature of the substrate stage can be varied to allow for heated depositions and the stage can rotate to produce a more even deposition. RF and DC magnetron sputtering typically can be performed in the same apparatus by changing the power supply. In DC magnetron sputtering, cessation of the sputtering process can occur as a result of arcing due to charge build-up on non-conductive dielectric targets. RF Magnetron Sputtering remedies this issue by alternating the electrical potential of current across the target anode at radio frequencies (13.56 MHz), effectively “cleaning” the target material of charge. RF Magnetron Sputtering also has other advantages over DC as RF plasmas tend to diffuse throughout the chamber rather than concentrate around the anode. RF can also sustain plasmas at much lower vacuum pressures (1 – 15 mTorr) which results in fewer ionised gas collisions and hence a more efficient deposition.

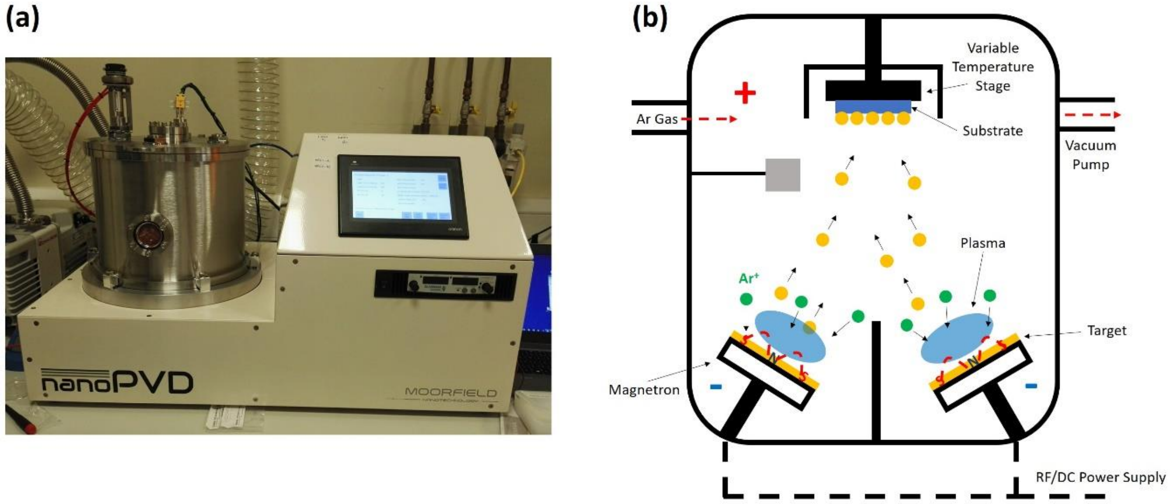

Figure 5.6 (a) A Moorfield NanoPVD DC/RF Magnetron Sputtering system and (b) a schematic diagram of the process of DC/RF Magnetron Sputtering.

This technique was used to deposit ITO on quartz substrates in collaboration with Nokia Bell Labs. The deposition was carried out at a vacuum pressure of 2.25 mTorr, an RF power of 10 mW, a deposition temperature of 300˚C, and an Ar gas flow rate of 5 sccm. Unfortunately, at the time of deposition, the quartz crystal monitor was not operational, and thus the thickness could not be selected. The deposition was instead carried out for 30 mins and the thickness was determined post-deposition by spectroscopic ellipsometry to be 130 nm.

5.4 Depositing ITO for ENZ Applications

In this section we'll discuss the effects of various deposition and annealing conditions that were examined in an ultimately successful effort at achieving locally deposited ITO with an ENZ wavelength in the 1200 nm – 1400 nm range. The goal of this was to devise a recipe for producing ITO thin films for future work on ITO ENZ structures.

5.4.1 Depositing ITO using Argon Ion Sputtering

An initial attempt at producing thin film ITO was carried out using argon ion sputtering described in Section 5.3.1. A 10 nm film was deposited on a quartz substrate. The deposition was carried out under vacuum and at room temperature without any in-situ annealing or post-annealing of the film. Angle-resolved reflectivity measurements were carried out on the 10 nm ITO film and unsurprisingly, no evidence of reduced reflection attributed to ENZ behaviour was observed. The angle-resolved surface map of the reflectivity is presented in Figure 5.7. As shown, the reflectivity across the entirety of the NIR range is rather low but no region of ultra-low reflectivity indicative of ENZ behaviour is noted. The reason for the absence of ENZ behaviour is most likely due to the formation of an amorphous film of SnO_2 and In_2O_3 complexes. Without an annealing step to activate 4-valent Sn ions on 3-valent In sites, no electrons are given up for conduction, and thus the film behaves more like a non-conductive oxide.

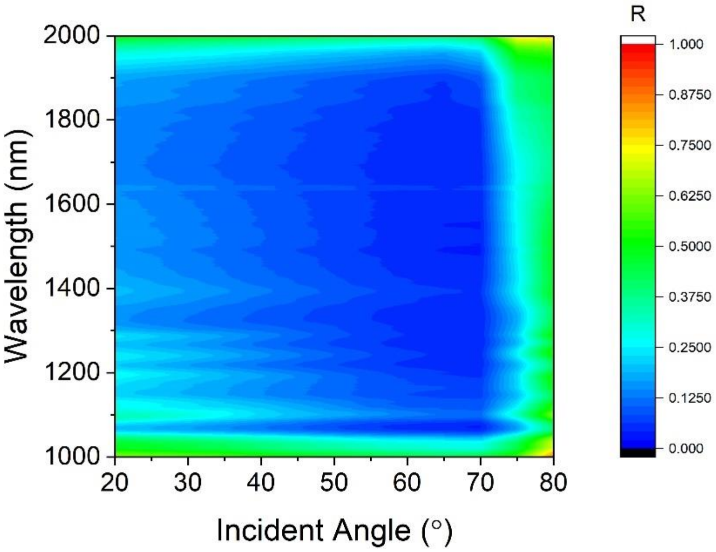

Figure 5.7 Angle-resolved reflectivity of a 10 nm ITO film on quartz. The film was deposited using Ar^+ ion sputtering under vacuum and at room temperature.

5.4.1.1 Vacuum Annealing of Ar^+ Ion Sputtered ITO Thin Film

Following on from the results of Figure 5.7, a further set of samples of thicknesses 20 nm, 50 nm, 70 nm, 100 nm, and 150 nm were deposited on quartz. However, on this occasion the films were subjected to annealing at 300˚C in vacuum for one hour. The system used for annealing was the four-point probe system described in Chapter 3 with a heating plate, bell-jar and vacuum pump attached to the system. The benefit of using this system was that the sheet resistance, R_s could be monitored throughout the annealing process. The utility of measuring the sheet resistance is that it can be indirectly used an estimate of the ENZ frequency without the need to directly measure it. This is based on an approximate expression devised by Brewer and Franzen who studied the dependence of sheet resistance on the plasma frequency of ITO thin films. Their approximate expression is given by [34]

$$\nu_p = \sqrt{\frac{1}{R_s t \varepsilon_0 \tau}} \tag{1}$$

where ν_p is the plasma frequency in wavenumbers (cm^{-1}), t is the thickness (in cm), $\tau = \frac{1}{\gamma}$ is the electron scattering time, and ε_0 is the permittivity of free space. Converting this to angular frequency (in rad s^{-1}), i.e. $\omega_p = 2\pi\nu_p$ and using the expression for the ENZ wavelength [35] derived in Equation 22 of Chapter 2, i.e.

$$\omega_{ENZ} = \frac{2\pi c}{\lambda_{ENZ}} = \sqrt{\frac{\omega_p^2}{\varepsilon_\infty} - \gamma^2} \tag{2}$$

where ω_p is the angular plasma frequency, ε_∞ is the high-frequency permittivity, and γ is the scattering rate, the ENZ wavelength, λ_{ENZ} can thus be related to the sheet resistance by

$$\lambda_{ENZ} = 2\pi c \left(\frac{4\pi^2 \gamma}{R_s t \varepsilon_0 \varepsilon_\infty} - \gamma^2 \right)^{-\frac{1}{2}} \tag{3}$$

where ε_∞ is the high-frequency permittivity. We can see from Equation 3 that the lower the sheet resistance, the shorter the ENZ wavelength, thus the goal of the annealing process is to decrease R_s to as low values as possible. The ability to measure R_s during the annealing process is a great advantage, however, the system also had some trade-offs, the temperature of 300˚C was chosen as it was the maximum achievable temperature of the system, there was no control over the vacuum pressure, nor could the deposition be carried out in the presence of oxygen.

Figure 5.8 presents a comparison of experimental (a – e) and T-matrix simulations (f – j) for the broad-spectrum angle-resolved reflectivity of these ITO films. While all experimental samples show regions of very low reflectivity, none of these regions exhibit ENZ behaviour. Particularly the data in Figure 5.8(a) which shows very low reflectivity about 1100 nm may appear similar to the low-reflectivity measured in the commercial samples in Chapter 4, however in reality this region is simply a result of thin-film interference as a result of depositing the ITO on an SiO_2 (300 nm) – Si substrate. This conclusion becomes clearer when examining the experimental data on a logarithmic scale to highlight any discrete regions of ultra-low reflectivity. These logarithmic plots are presented in Figure 5.9.

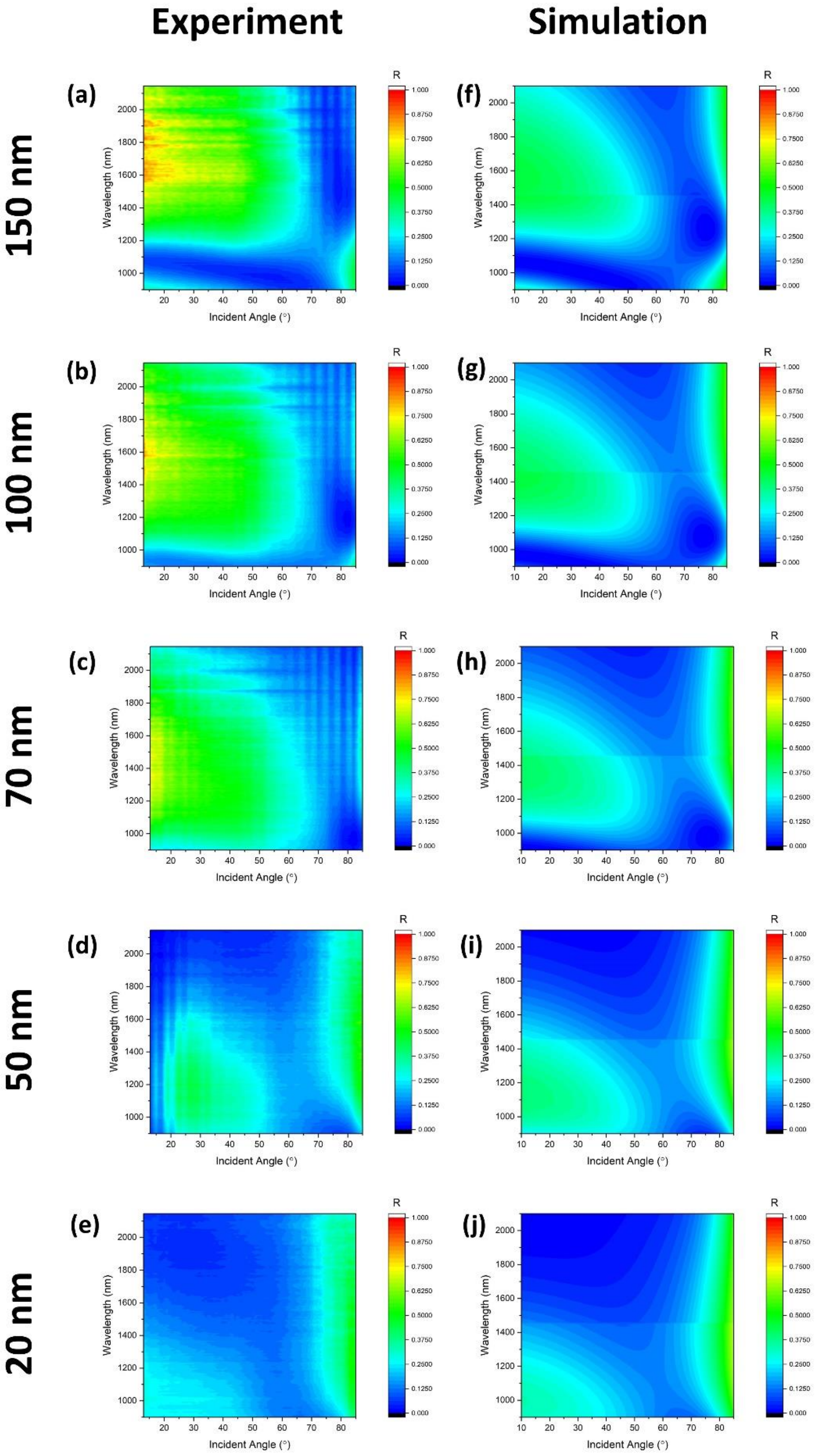

Figure 5.8 Experimental (a – e) and simulated data (f – j) of the angle-resolve reflectivity of ITO thin films on an SiO$_2$ (300 nm) – Si substrate deposited using Ar$^+$ ion sputtering and annealed in vacuum at 300˚C for one hour.

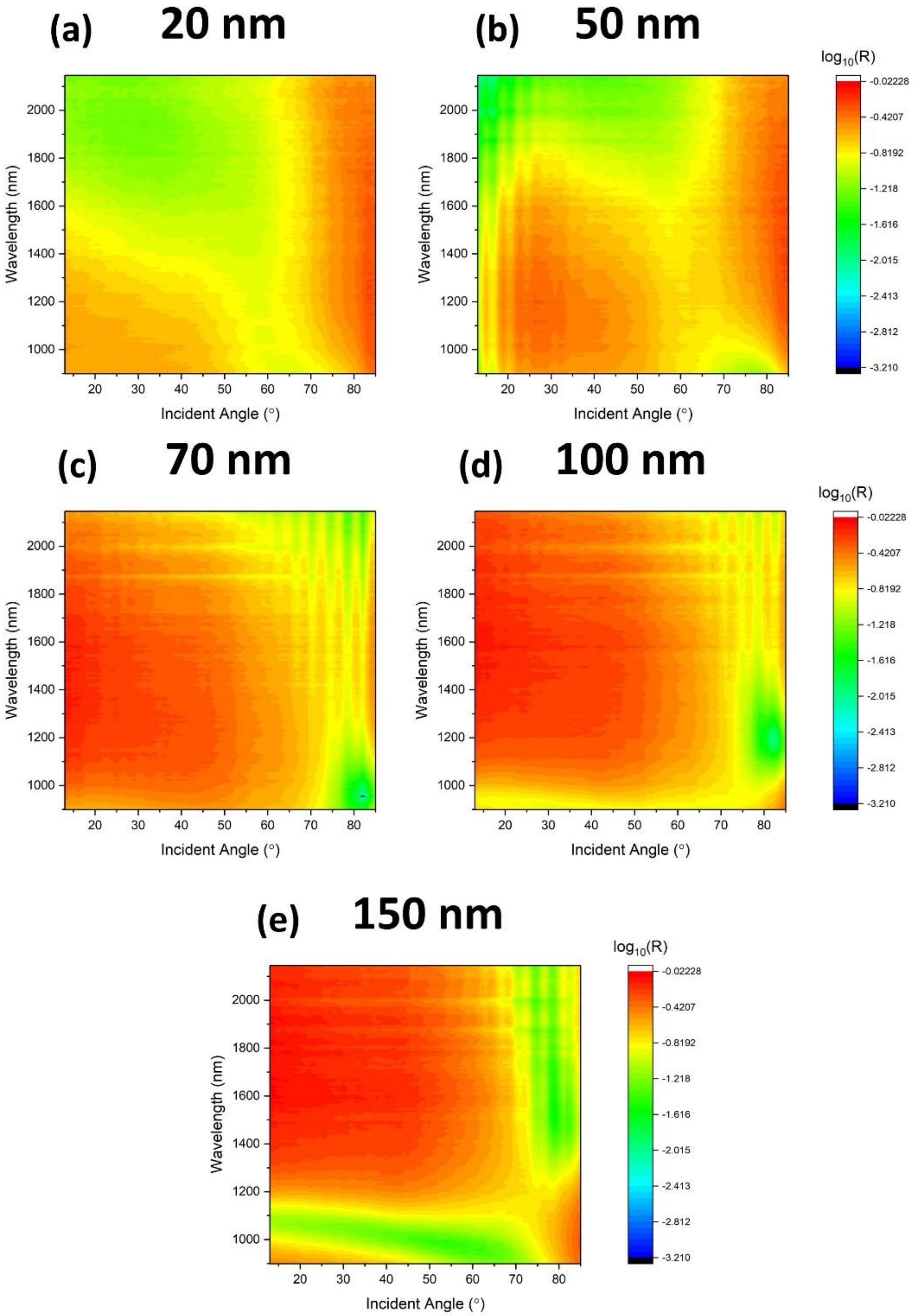

Figure 5.9 Logarithmic plot of the angle-resolved reflectivity of ITO films deposited on an SiO_2 (300 nm) – Si substrate using Ar^+ ion sputtering and treated to one hour of annealing in vacuum at 300˚C. The log plots reveal no distinct regions of ultra-low reflectivity.

The log plots reveal no regions of distinct ultra-low reflectivity suggesting that no ENZ is present in the films in the measurable range. This is further supported by the results of the T-matrix simulations in Figure 5.8(f – j) which agree very well with experimental data. The agreement between simulation and experiment was achieved by setting the plasma frequency, ω_p in the Drude Model of the T-matrix simulations to zero, setting the scattering rate to a value of $\gamma = 0.1$, and maintaining the high-frequency permittivity at $\varepsilon_\infty = 3.68$. The fact that simulation and experiment agree in the absence of a plasma frequency suggests that, despite the annealing process, the films behave just as an oxide with no plasma oscillations in the measurable range.

However, while no ENZ behaviour was observed from these films, the annealing process was successful in significantly decreasing the sheet resistance, and hence increasing the conductivity of the films. The sheet resistance for each film before the annealing process were measuring using the four-point probe system described in Chapter 3 and the results are presented in Table 5.1. One sample of each thickness was measured and the quoted sheet resistance values are an average of three measurements carried out on each sample.

ITO Film Thickness (nm)	Sheet Resistance (kΩ sq^{-1})
150 ± 10	3.52 ± 0.01
100 ± 10	8.57 ± 0.01
70 ± 10	12.75 ± 0.01
50 ± 10	287.85 ± 0.01
20 ± 10	982.33 ± 0.01

Table 5.1 Sheet resistance for ITO films of thicknesses 20 nm – 150 nm deposited using Ar$^+$ ion sputtering. The measured values are for the films before annealing.

Plots of the sheet resistance as a function of annealing time are presented in Figure 5.10. The first 3 – 5 minutes of each annealing process shows large fluctuations as there is a delay between the hot plate reaching the quoted temperature and the films reaching that temperature. However, the rest of the data shows a significant decrease in the sheet resistance compared to the data in Table 5.1. The sheet resistance values are taken from the order of kΩ sq^{-1} to hundreds of Ω sq^{-1}. The 150 nm ITO film in Figure 5.10(e) exhibits the lowest post annealing sheet resistance at around 15.5 Ω sq^{-1}. The 100 nm film, however, appears to exhibit an increase in the sheet resistance.

While the annealing temperature of 300°C is not high enough to cause sufficient ion activation, the process of annealing in vacuum leads to outward diffusion of oxygen [36][37], creating oxygen vacancies that lead to a significant increase in the film conductivity, and hence a decrease in the sheet resistance. The increase in conductivity from the annealing process and the absence of ENZ behaviour in the ITO films shows clearly that annealing in vacuum alone is not enough to produce the desired ENZ behaviour.

In comparison with the data from the literature in Figure 5.2, the sheet resistances of the annealed films are of the same order of magnitude as films produce in the absence of oxygen. In order to achieve a lower sheet resistance, it appears that oxygen in the annealing environment is essential. Figure 5.1, also from the literature, suggests that the 300˚C at which the films were annealed is too low and a temperature of at least 400˚C is required to take the films from an amorphous state to a polycrystalline one. The combination of these conditions should allow sufficient ion activation in the ITO and ensure that too much oxygen isn't removed from the films during the annealing process, leading to a highly conductive crystalline film.

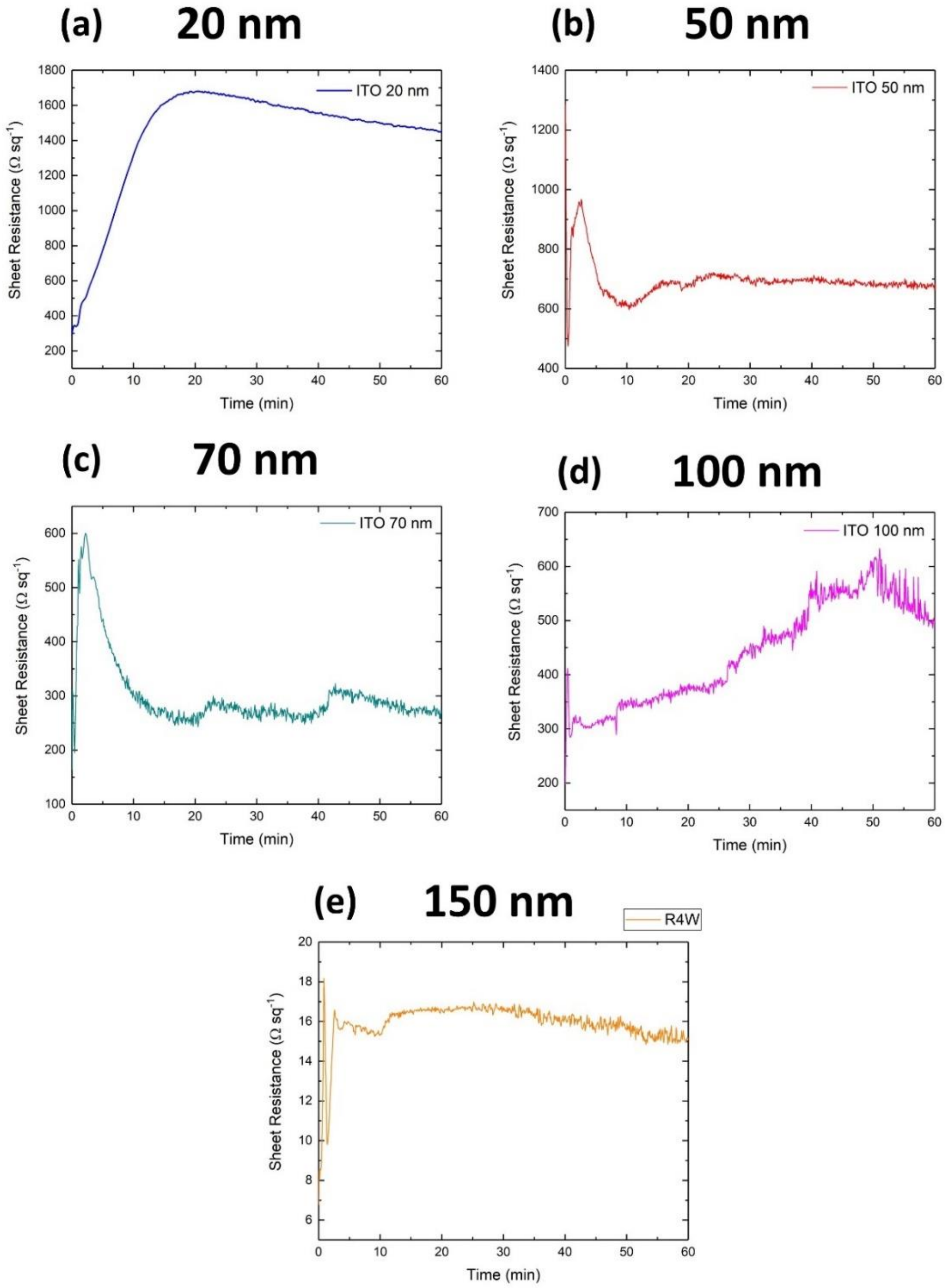

Figure 5.10 Sheet resistance of ITO films as a function of time during the 300˚C annealing process in vacuum.

5.4.1.2 High Temperature Annealing in Vacuum

To achieve a lower sheet resistance and ENZ behaviour, the ITO films from Section 5.4.1.1 were reannealed in a vacuum tube furnace at 500˚C for one hour with an O_2 flow rate of 4 sccm. The value of 500˚C was chosen as it was sufficiently above the temperature required for polycrystallinity suggested in Figure 5.1 to ensure that all samples were above the necessary temperature in case there was a temperature variation in the tube furnace away from the centre. Angle-resolved reflectivity measurements were again carried out and are presented in Figure 5.11. In all deposited films, the reflectivity is very low, however there exists a region of ultra-low reflectivity about 1600 nm – 1800 nm and 15˚ incidence which becomes much more apparent when plotted on a logarithmic scale in Figure 5.12.

The transfer matrix simulations presented in Figure 5.11(f – j) were carried out by selecting the Drude parameters by trial-and-error and comparing to the experimental until a sufficient match to the experimental data was obtained. A value of ε_∞ = 3.6 was chosen for the high frequency permittivity, a value of ω_p = 2.10 rad fs^{-1} was chosen for the plasma frequency, and a scattering rate of γ = 0.1 rad fs^{-1} was chosen. Clear agreement between experiment and simulation was thus achieved. These Drude parameters correspond to an ENZ wavelength of λ_{ENZ} = 1709 nm, which is beyond the desired range for the ENZ behaviour in the ITO films as typically the imaginary component of the complex refractive index increases rapidly at wavelengths longer than λ_{ENZ}.

The ITO annealed using these conditions also exhibited rather low sheet resistances in line with the thinner commercial samples discussed in Chapter 4 with thicker films exhibiting values as low as 50 Ω sq^{-1}. Figure 5.13 presents this data along with a comparison of the previous annealing process discussed in Section 5.4.1.1. The graph presents the sheet resistances for ITO films annealed at 300˚C in absence of oxygen for the SiO_2 (300 nm) on a Si substrate as well as an additional deposition which was carried out on quartz, but also yielded no ENZ behaviour. As shown, both sets of films annealed at 300˚C achieve the same values, suggesting that the choice of substrate has little effect on the conductivity of the films. However, we see that the annealing process at 500˚C in the presence of oxygen yields higher sheet resistances for thinner samples, but the lowest sheet resistance for thicker films, particularly the 70 nm film.

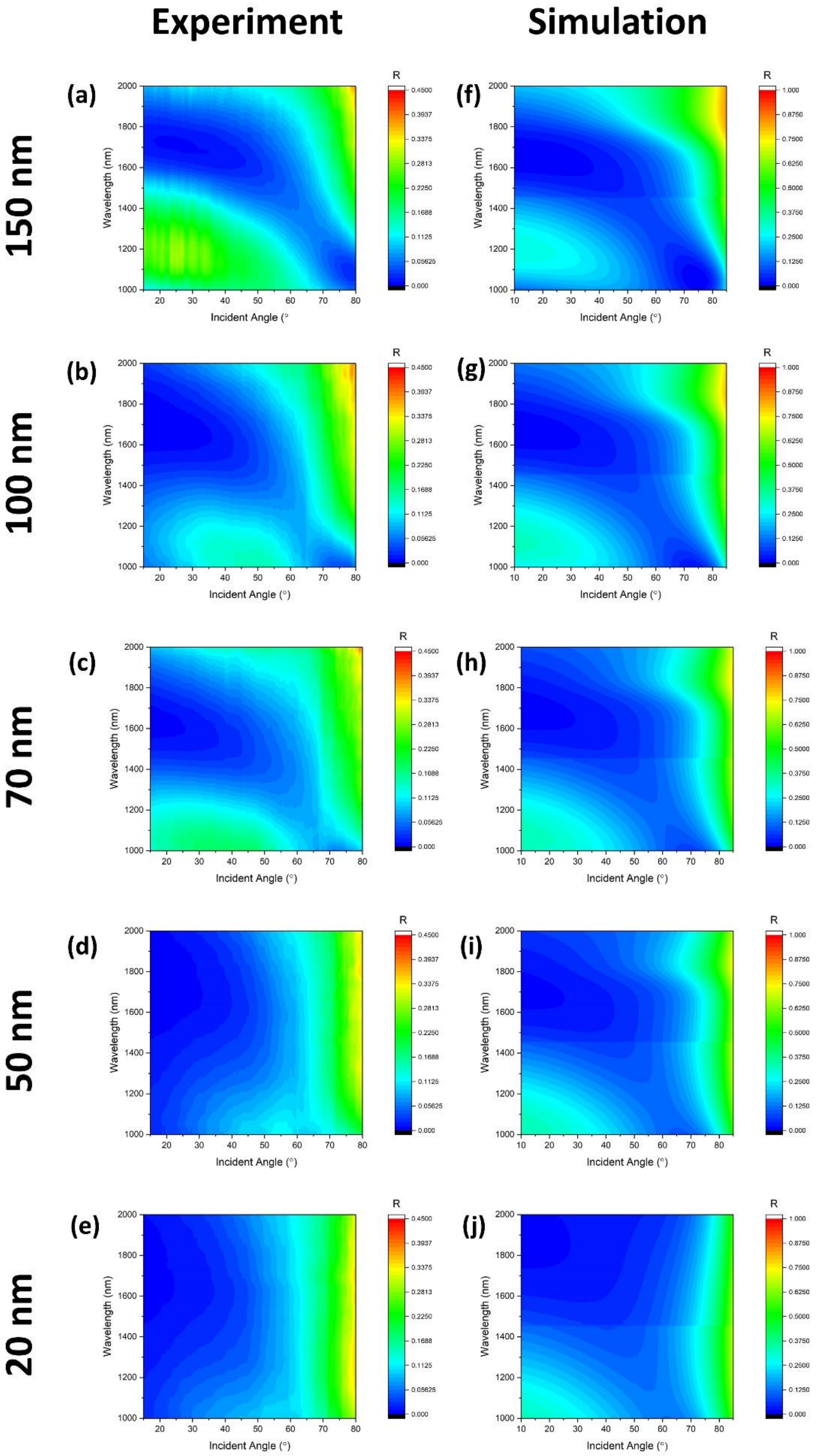

Figure 5.11 Experimental (a – e) and T-matrix (f – j) data for the angle-resolved reflectivity of the Ar^+ ion sputtered ITO films on an SiO_2 (300 nm) – Si substrate annealed at 500˚C for one hour with 4 sccm of O_2 gas flow.

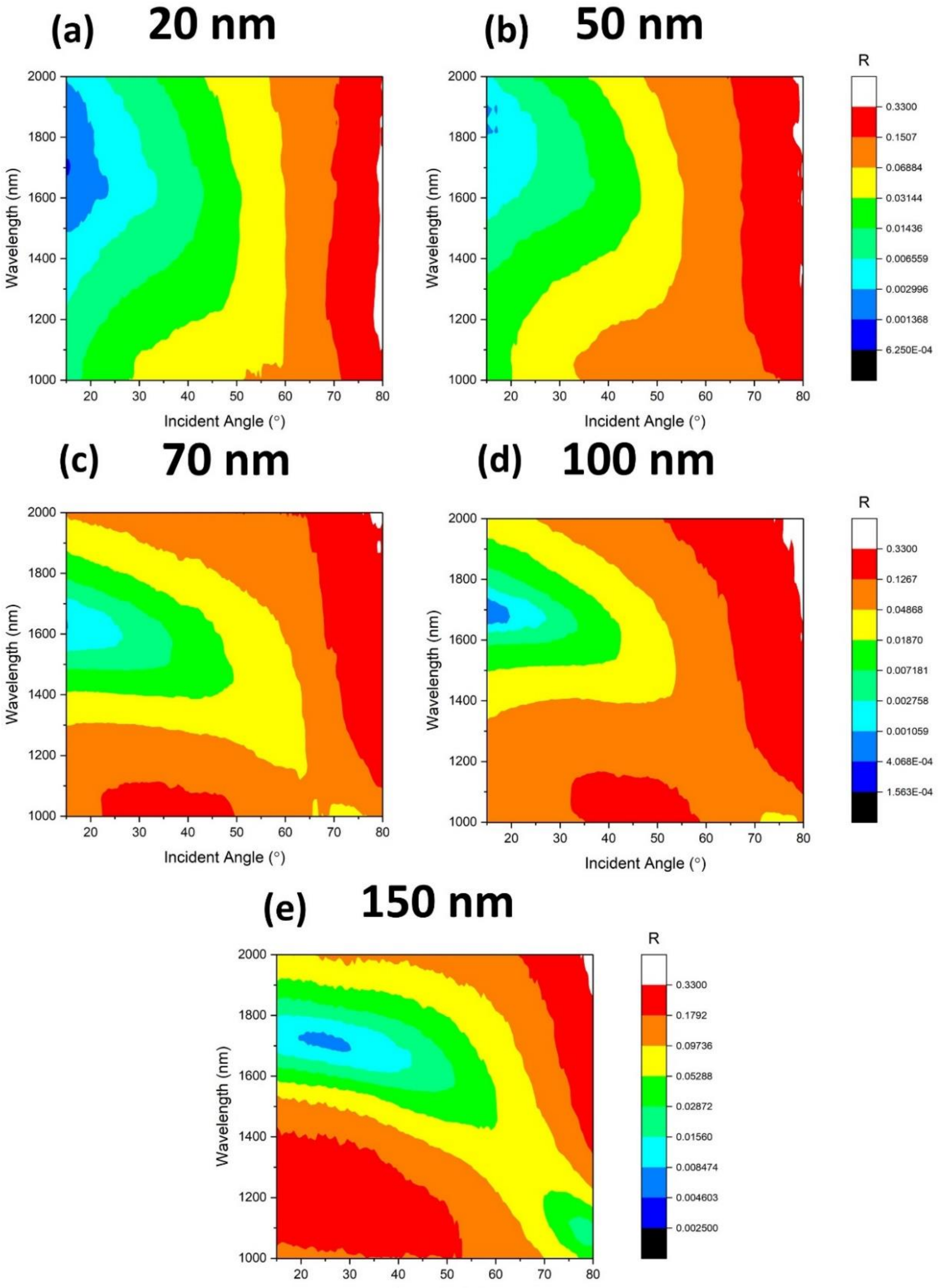

Figure 5.12 Logarithmic plot of the angle-resolved reflectivity of ITO films deposited on an SiO_2 (300 nm) – Si substrate using Ar^+ ion sputtering and treated to one hour of annealing in vacuum at 500˚C with an O_2 flow rate of 4 sccm. All films exhibit an ultra-low reflectivity about 1600 nm – 1800 nm and 15˚ incidence which is attributed to the excitation of the Ferrell-Berreman mode.

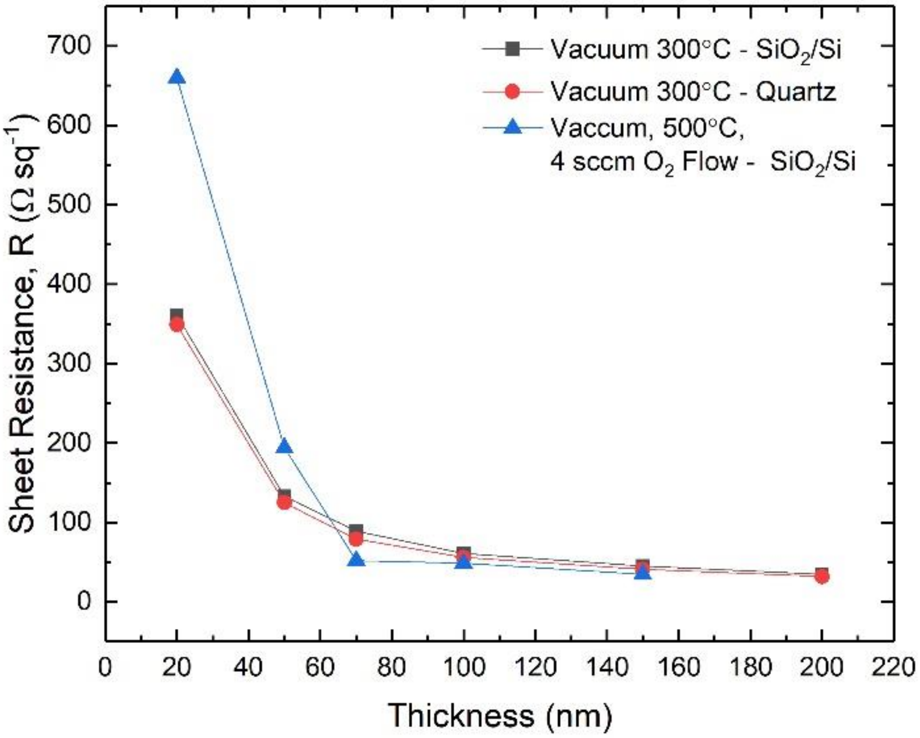

Figure 5.13 Comparison of the sheet resistance as a function of ITO film thickness for various annealing conditions.

The combination of data from Figure 5.11, Figure 5.12, and Figure 5.13 suggests that we were successful in our attempt to achieve ENZ behaviour in locally deposited ITO films, however the ENZ wavelength of the films is at far longer wavelengths than the 1200 nm – 1400 nm that is typical of commercial ITO.

5.4.1.3 Broadspectrum Spectroscopic Ellipsometry of Locally Deposited ITO Films

To confirm the presence of the an ENZ wavelength about 1600 nm – 1800 nm, broadspectrum spectroscopic ellipsometry measurements were carried out on the ITO films which were annealed at 500˚C in the presence of oxygen. A further 200 nm film was also deposited and annealed and subjected to ellipsometry. The ellipsometry measurements were carried out as previously described in Chapter 4. The resulting complex refractive indices and complex permittivities are presented in Figure 5.14. The real and imaginary components of the complex refractive index are presented in Figure 5.14(a) and (b), respectively, and the real and imaginary components of the complex permittivity are presented in Figure 5.14(c) and (d), respectively. Focusing on the real component of the permittivity, the 150 nm and 200 nm show a clear ENZ wavelength about 1600 nm, while the other films have ENZ wavelengths at outside of the measurable range. This confirms the existence of ENZ behaviour in the thicker ITO films, however the imaginary component of the refractive index increases with ITO film thickness suggesting there is significant absorption in the films. To confirm this, normal incidence transmission measurements were carried out on the ITO films using a Perkin-Elmer Lambda 1050 UV – Visible – NIR spectrophotometer. The resulting transmission data is presented in Figure 5.15.

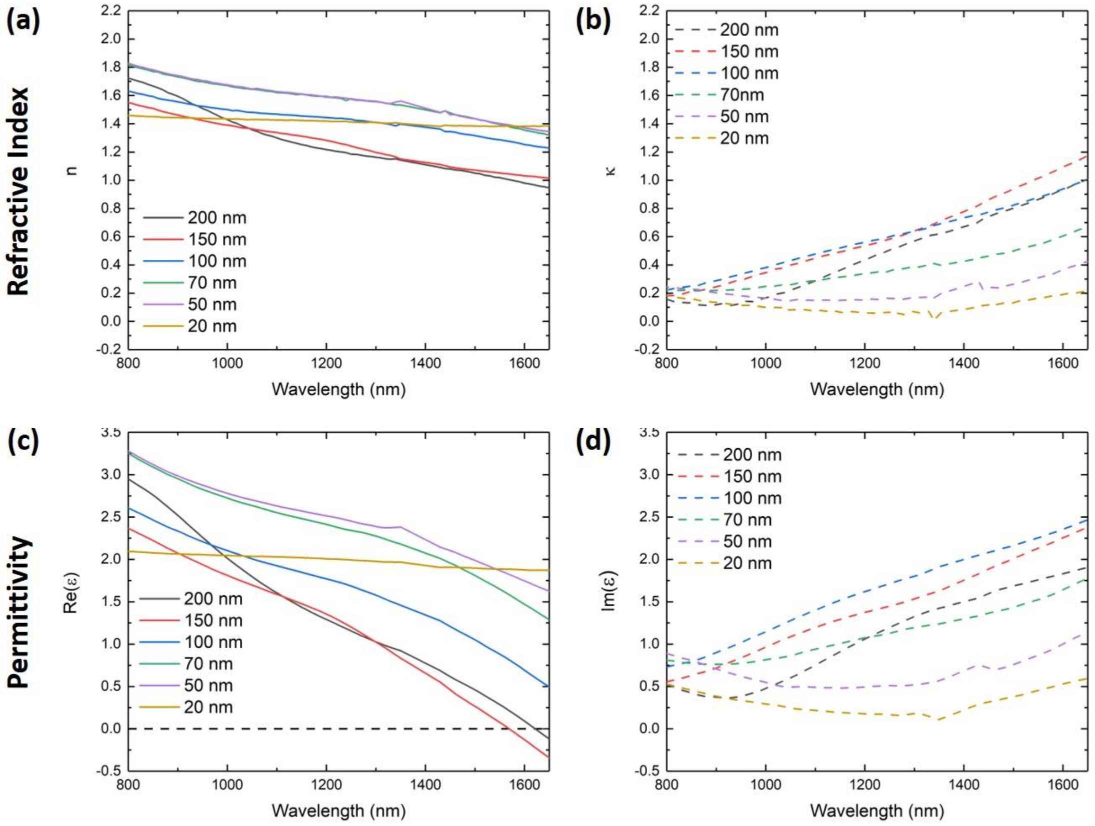

Figure 5.14 Real and imaginary components of the complex refractive index of argon ion sputtered ITO films of varying thicknesses and (b) the corresponding real and imaginary components of the dielectric permittivity.

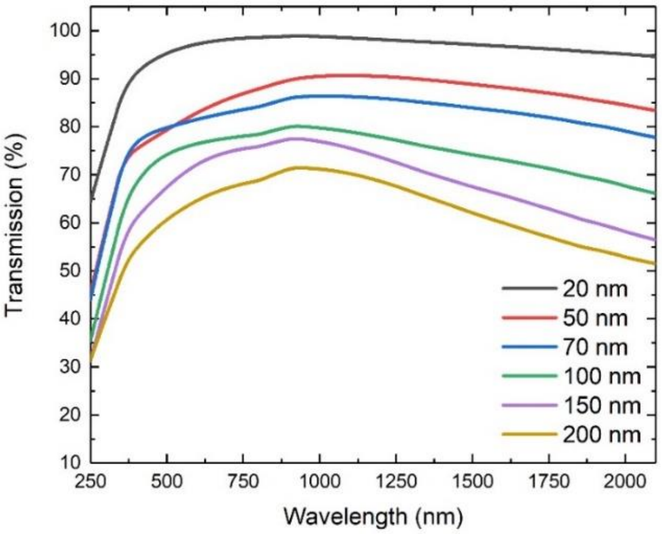

Figure 5.15 Normal incidence transmission of ITO films annealed at 500˚C for one hour in the presence of 4 sccm O_2 gas flow.

A clear thickness dependence of the transmission is present in Figure 5.15. While such a thickness would commonly be expected in accordance with the Beer-Lambert law [38], typically high-quality ITO of any thickness exhibits a visible transmission of > 90% [4]. Comparing Figure 5.15 to Figure 5.4, the low values of transmission in the near-infrared may be indicative that the ITO films are still deficient in oxygen, which led us to suspect that the quality, transmission, and ENZ wavelength of the ITO films may be limited by the sputtering technique used and thus alternative sputtering techniques should be considered.

5.4.1.4 Applying the Drude Model to Locally Deposited ITO Films

As with the commercial samples in Chapter 4, the locally deposited ITO films exhibiting ENZ behaviour were fitted to a Drude model to extract the plasma frequency, scattering rate, and high-frequency permittivity. The fits shown in Figure 5.16. The thicker 100 nm, 150 nm, and 200 nm films fit a Drude model quite well with correlation coefficients of > 0.9, however the fits for the thinner 20 nm, 50 nm, and 70 nm samples are quite poor, particularly for the imaginary components of the permittivity which diverge greatly from the Drude model. The extracted Drude parameters are presented in Table 5.2.

The fact that the fit to the Drude model becomes worse as the films gets thinner may be a result of the effective contribution of surface roughness to the overall film quality. While Ar^+ ion sputtering is a useful technique, it tends to produce quite rough films. For a thinner sample, the surface roughness will have a greater relative contribution to the overall quality of the film than for a thicker sample. This further suggests that the quality of these films and their optical properties are limited by the sputtering technique.

ITO Thickness (nm)	ω_p (rad fs^{-1})	γ (rad fs^{-1})	ε_∞	R^2 Coefficient
200 ± 10	2.58 ± 0.01	0.63 ± 0.01	3.77 ± 0.03	0.97182
150 ± 10	2.70 ± 0.01	0.81 ± 0.01	3.58 ± 0.04	0.96239
100 ± 10	2.72 ± 0.01	1.16 ± 0.03	3.61 ± 0.04	0.91403
70 ± 10	2.40 ± 0.04	0.91 ± 0.05	4.18 ± 0.07	0.84306
50 ± 10	2.11 ± 0.05	0.55 ± 0.05	4.26 ± 0.09	0.83504
20 ± 10	95.05 ± 1.6×10^6	5440.02 ± 1.9×10^6	1.26 ± 103.93	-1.50607

Table 5.2 Fitted Drude parameters for ITO films of thicknesses 20 nm – 200 nm annealed at 500˚C for one hour and with 4 sccm of O_2 gas flow.

An attempt was made to determine λ_{ENZ} for these films using these Drude parameters in Table 5.2 and the sheet resistance values from Table 5.1, however upon substituting these values into Equation 3 the equation did not converge to a real value of λ_{ENZ}. The reason for this is that Equation 3 is an approximate expression that only works when applied to conductive ITO. The sheet resistance values, which were in the order of kΩs, are far too high. To demonstrate this, we consider the limit of λ_{ENZ} as R_s.

$$\lim_{R_s\to\infty}\lambda_{ENZ} = \lim_{R_s\to\infty}\left(2\pi c\left[\frac{4\pi^2\gamma}{R_s t\varepsilon_0\varepsilon_\infty}-\gamma^2\right]^{-\frac{1}{2}}\right) = 0 + i2\pi c\gamma$$

As shown, as R_s approaches infinity, the value of λ_{ENZ} approaches a purely imaginary value dependent on γ which provides no physical insight into the properties of the ITO films. When applied to the deposited films, the very large sheet resistances resulted in an imaginary value of λ_{ENZ}. Thus, we can conclude that while this expression is a useful approximation when working with high quality conductive ITO, it only works for reasonably low values of the sheet resistance.

All films, except the 20 nm appear to fit the Drude model somewhat, however the 100 nm – 200 nm films fit the trend with reasonably large correlation coefficients and reasonable values of ω_p, γ, and ε_∞. As the films become thinner, the quality of the fit and the correlation coefficient becomes less. The 20 nm sample however appears to not fit the trend at all with a negative R^2 value and as a result the standard error on each measurement was larger than the parameter value.

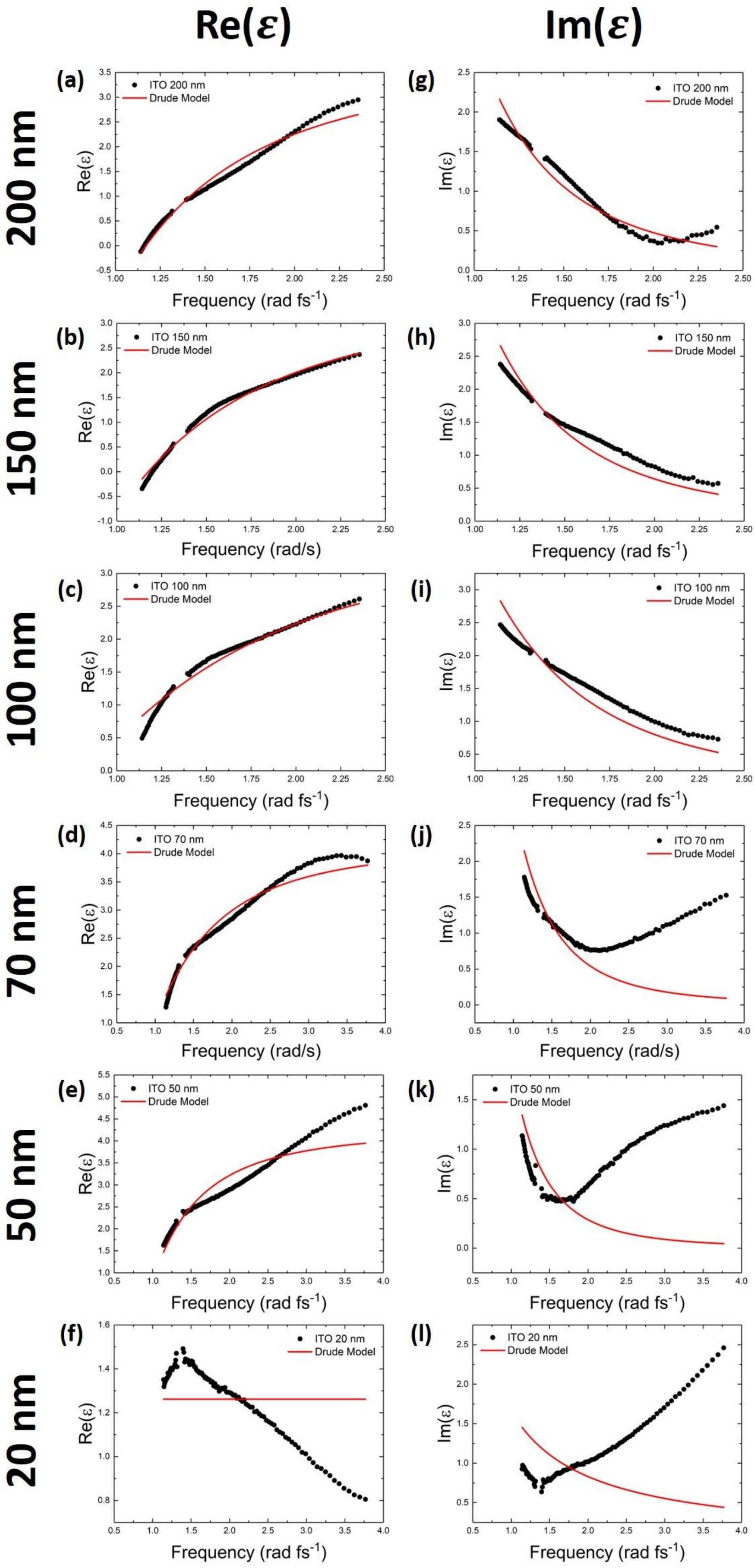

Figure 5.16 Drude models fits for the ellipsometry data carried out on the argon ion sputtered samples of ITO thin films. (a – f) show the fits of the real component of the permittivity and (g – l) show the fits for the imaginary components.

5.4.2 Depositing ITO using RF Magnetron Sputtering

A further set of ITO thin films were deposited on quartz using the technique of RF magnetron sputtering as described in Section 5.3.2 in collaboration with Ryan Enright and Kenny Wu of Nokia Bell Labs. These films were deposited in vacuum under a pressure of 2.37 mTorr and at a deposition temperature of 200˚C. Unfortunately, no quartz crystal monitor was present in the system at the time of measurement, and thus a deposition time of 30 minutes was chosen to ensure the films remained sufficiently thin. Five films were produced, labelled N1 – N5. These films were then subjected to one hour of annealing in a vacuum tube furnace under a pressure of 3.00 mTorr and at an annealing temperature of 500˚C. 4 sccm of O_2 gas flow was pumped into the tube furnace throughout the annealing process.

5.4.3 Linear Transmission through RF Magnetron Sputtering ITO Thin Films

Linear transmission measurements at normal incidence were carried out the RF magnetron sputtered ITO films and the resulting data is presented in Figure 5.17. As shown, all samples exhibit a very large transmission in the visible range of > 95%. This is significantly larger than the values achieved by the commercial ITO films. While there is some variation in transmission cross the samples, this is likely a result of slight variations in thickness as a result of their relative positions during the deposition.

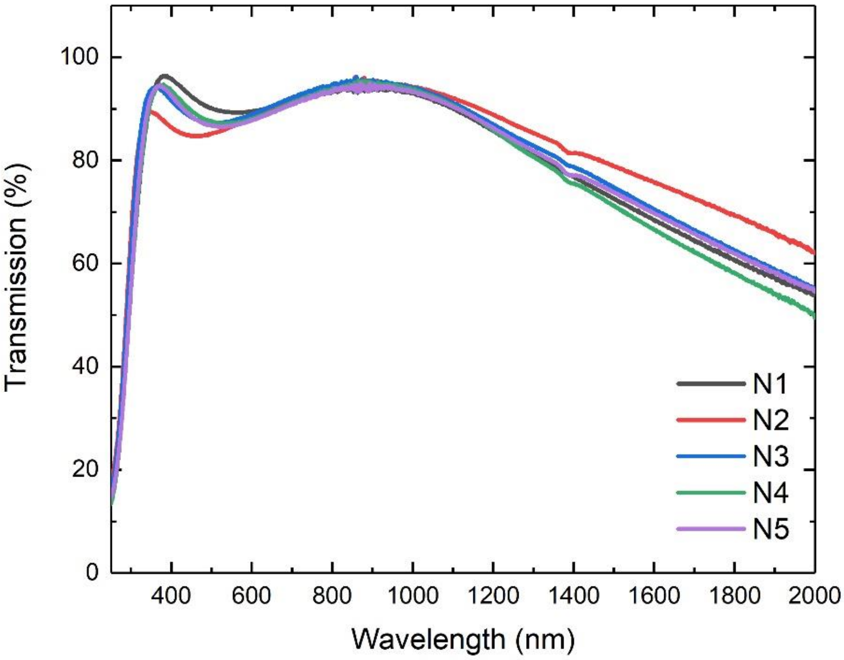

Figure 5.17 Linear transmission of RF magnetron sputtered ITO thin films. The films were heated during deposition at 200˚C and then treated to one hour of annealing at 500˚C, a vacuum pressure of 3.00 mTorr, and 4 sccm of O_2 gas flow.

Of particular note is the decrease in the transmission to about 60% at longer wavelengths (1700 nm – 2000 nm), which is very similar to the transmission of the 127 nm 8 – 12 Ω sq^{-1} commercial ITO film in this range. This suggests that the film contains sufficient oxygen vacancies, and thus must be quite conductive.

5.4.4 Spectroscopic Ellipsometry of RF Magnetron Sputtered ITO Thin Films

As the thickness of the RF magnetron sputtered ITO film could not be controlled upon deposition, spectroscopic ellipsometry measurements in the visible range were carried out on the ITO films to determine the thickness and the optical constants of the films. The resulting data is presented in Figure 5.18.

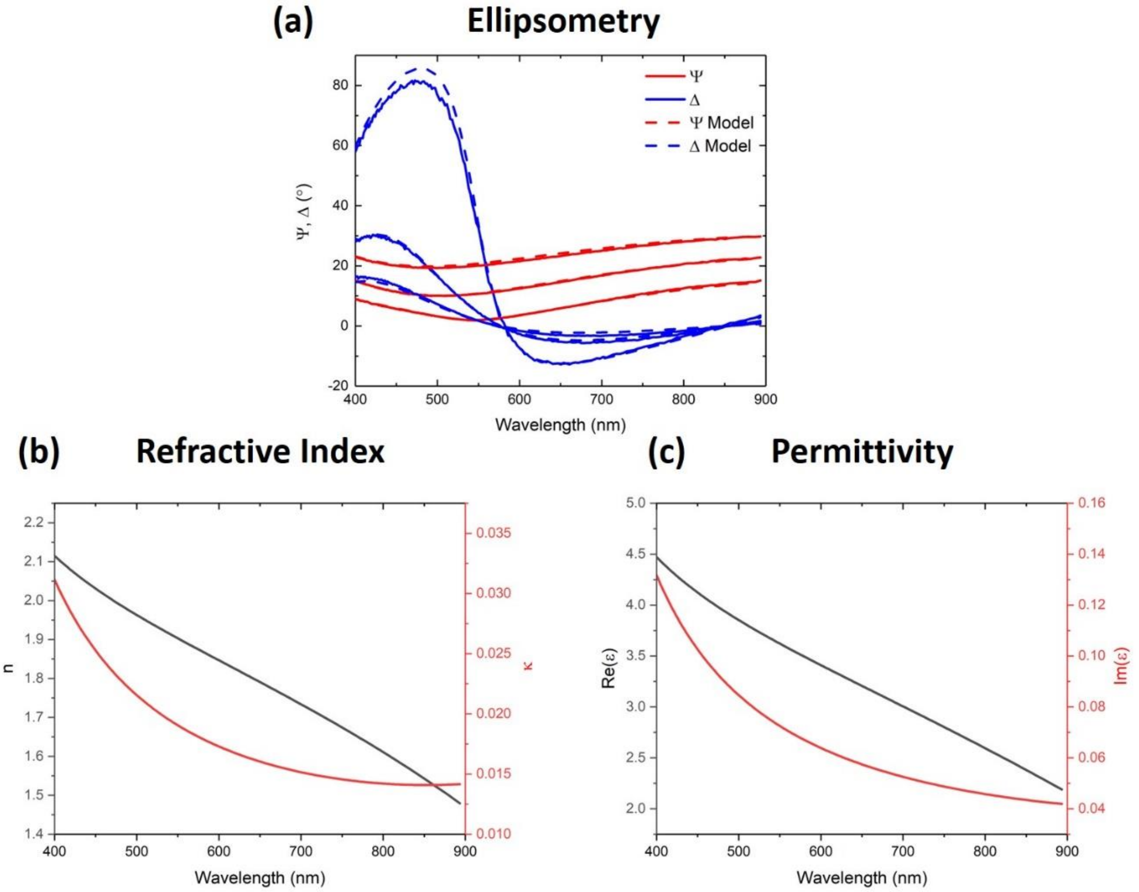

Figure 5.18 (a) A comparison of the experimentally measured Ψ and Δ values (solid lines) and the Drude model fits (dashed lines) used in the CompleteEASE software, (b) the real and imaginary components of the complex refractive index, and (c) the real and imaginary components of the complex permittivity. From the fits in (a) the film was determined to be approximately 130 nm in thickness.

Figure 5.18 (a) shows the experimentally measure Ψ and Δ values (solid lines) compared to the Drude Model (dashed lines) used in the CompleteEASE software for incident angle of 65°, 70°, and 75° for one of the ITO films. As shown, there is excellent agreement between the measured values and the model. The thickness was thus determined to be around 130 nm for each film. Figure 5.18(b) and (c) present the real (black) and imaginary (red) components of the complex refractive index and the complex permittivity respectively. The optical constants of the ITO films are consistent with what is expected of ITO, with both the real and imaginary components decreasing at longer wavelengths in the visible range. Of particularly benefit is the relatively low values of the imaginary components which suggests the RF magnetron sputtered ITO films exhibit low loss, which is consistent with the very high values of transmission in Figure 5.17. Having thus determined the average thickness of the films, it was possible to determine the electrical properties of the ITO films.

5.4.5 Bandgap, Conductivity and Electrical Properties of RF Magnetron Sputtered ITO Thin Films

Figure 5.19 presents Tauc plots for the RF magnetron sputtered ITO thin films which were calculated from absorbance data taken using a Lambda 1050 UV-Visible-NIR spectrophotometer. As with the commercial samples in Chapter 4 the plots present the parameter $(\alpha h\nu)^2$ against the energy $h\nu$ in eV [39]. Here, α is the absorption coefficient determined by taking the ratio of the absorbance values to the film thickness of 130 nm, h is Planck's constant, and ν is the frequency in Hz. The exponent of 2 on the y-axis corresponds to direct allowed transitions. By fitting the linear region of the data and extending the trendline to the abscissa a value for the bandgap was determined. All films exhibit a bandgap in the range 4.20 eV – 4.26 eV, in the expected range for ITO [40]. The optical bandgap values obtained from this analysis provides further suggestion that RF magnetron sputtering produces ITO of far higher quality that Ar^+ ion sputtering. Using the four-point probe technique previously discussed, the sheet resistances before and after the annealing process of these films were measured. The sheet resistance data before and after the annealing process is presented in Figure 5.20. As shown, after the deposition and before the annealing process, the sheet resistances of the films are of the order of several hundred Ω sq^{-1} with significantly large variation across all films. After the annealing process, the sheet resistance drops to values ≤ 60 Ω sq^{-1} with the lowest sheet resistance measuring 31 Ω sq^{-1}. This suggests that the annealing process caused sufficient ion activation and generation of oxygen vacancies to contribute to the conductivity of the film. The sheet resistance, bulk resistivity, and bulk conductivity are presented for the annealed films in Table 5.3. The presented sheet resistance values are an average of three measurements taken on each sample.

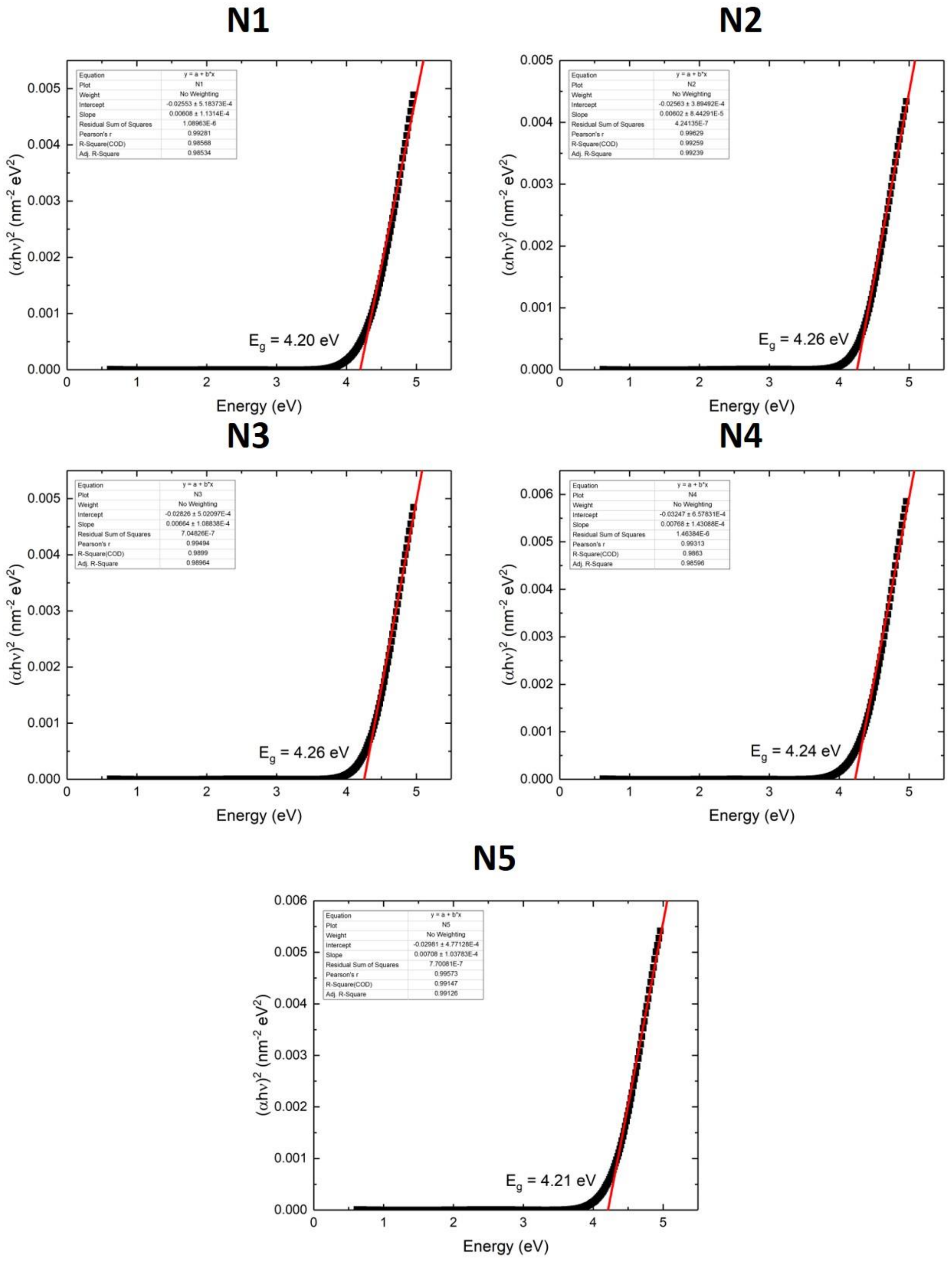

Figure 5.19 Tauc plots for ITO samples N1 – N5 produced by RF Magnetron sputtering at a deposition temperature of 200˚C and then treated to one hour of annealing at 500˚C under vacuum with an O_2 flow rate of 4 sccm.

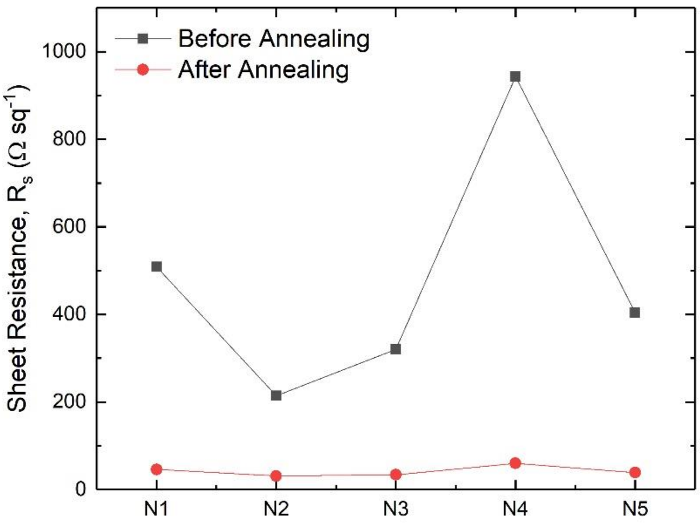

Figure 5.20 Comparison of the sheet resistance of RF magnetron sputtered ITO films before and after annealing for one hour at 500˚C with 4 sccm of O_2 gas flow.

Sample	R_S (Ω sq^{-1})	ρ (Ω·cm)[×10^{-4}]	σ (S cm^{-1})
N1	46 ± 0.33	5.98 ± 0.46	1672.24 ± 129.19
N2	31 ± 0.33	4.03 ± 0.31	2481.39 ± 192.70
N3	34 ± 0.33	4.42 ± 0.34	2262.44 ± 175.41
N4	60 ± 0.33	7.80 ± 0.60	1282.05 ± 98.87
N5	39 ± 0.33	5.07 ± 0.39	1972.39 ± 152.63

Table 5.3 Sheet resistance, bulk resistivity, and bulk conductivity of RF magnetron sputtered ITO thin films deposited at 200˚C and then annealed for one hour at 500˚C under vacuum with 4 sccm of O_2 gas flow.

5.4.6 Ferrell-Berreman Mode Excitation in RF Magnetron Sputtered ITO Thin Films

All characterisation of the RF magnetron sputtered ITO thin films thus far exhibited significantly high quality electrical and optical properties in line with the commercial samples discussed in Chapter 4. To determine whether the films exhibited an ENZ wavelength in the 1200 nm – 1400 nm range , angle-resolved absorption measurements were carried out on one of the films to excite the Ferrell – Berreman mode. 10 nm of Pt were also deposited on the ITO containing side of this films and angle-resolved absorption measurements were carried out on this ITO – Pt combination exciting from the quartz side. The measurements were carried out between 1000 nm and 2000 nm with 5 nm wavelength increments and across the 13˚ – 41˚ angular range with 1˚ increments. Figure 5.21 presents a comparison of simulation and experiment for the angle-resolved absorption of this film with and without the presence of a 10 nm Pt backing. Figure 5.21(b) and (d) present the experimentally measured absorption which clearly shows the presence of a high-absorption feature about 1300 nm which is significantly enhanced by the application of 10 nm of Pt. The

ITO alone exhibits a peak absorption of 47.6% at 1333 nm, and with the application of 10 nm Pt, exhibits a peak absorption of 90.1% at 1243 nm. As before, the presence of the Pt backing causes a very large enhancement of the absorption and a blueshift of 90 nm of the peak absorption.

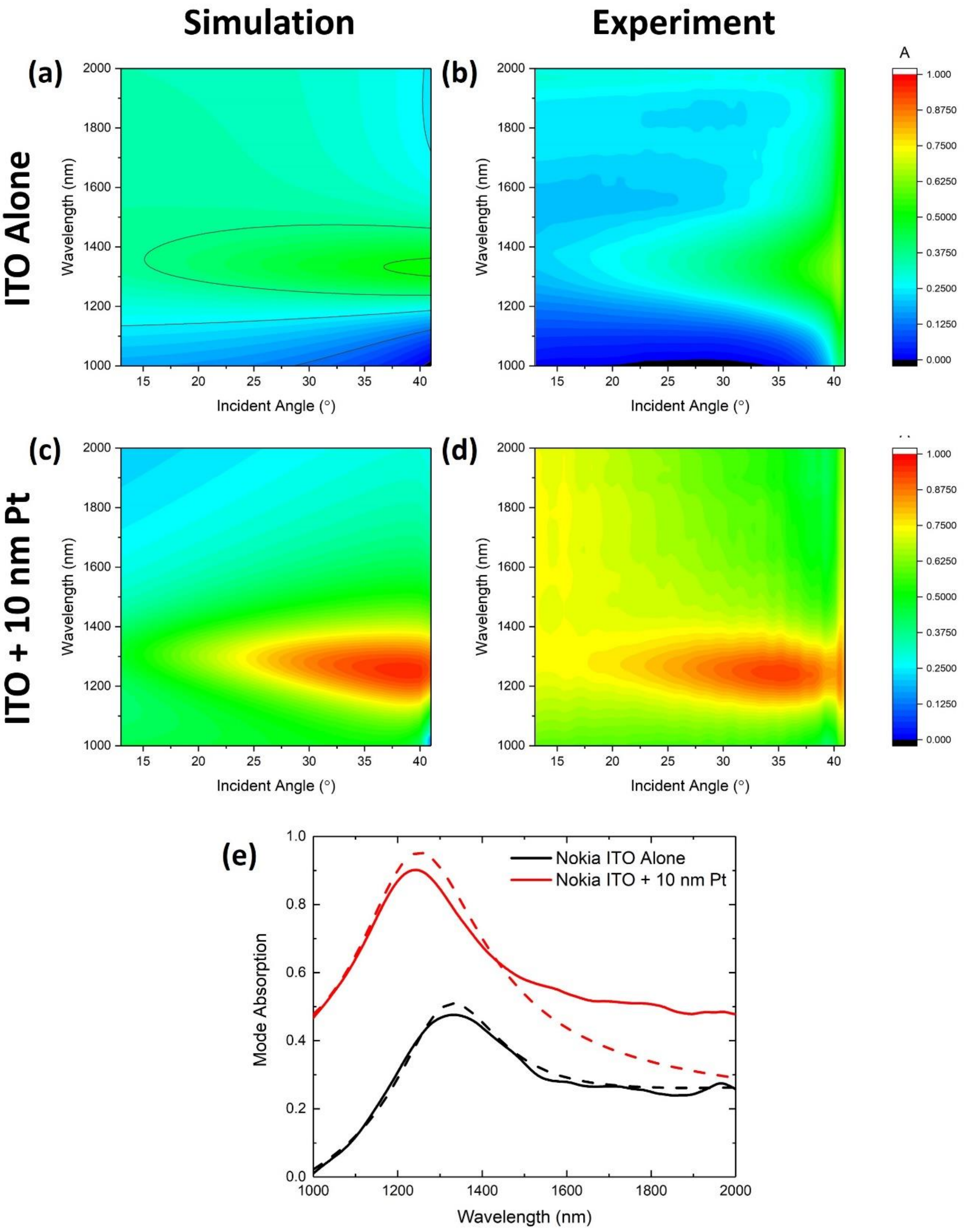

Figure 5.21 A comparison of simulation and experiment for a 130 nm RF magnetron sputtered and annealed ITO thin film without (a – b) and with (c – d) a 10 nm Pt backing, and (e) a comparison of simulation (dashed lines) and experiment (solid lines) for the Ferrell-Berreman mode absorption of the ITO film.

This becomes more apparent in Figure 5.21(e) which presents the Ferrell – Berreman mode absorption at 39° incidence as a function of wavelength.

At the time of fabrication of these films, NIR range spectroscopic ellipsometry was not available, and thus the Drude parameters used in the simulations in Figure 5.21(a) and (c) had to be selected by trial-and-error comparison to the experimental data. From the permittivity data presented in Figure 5.18(c), a value of $\varepsilon_\infty = 4.5$ was chosen for the high-frequency permittivity as the real component of the permittivity reached this value about 400 nm. A value of γ = 0.25 was chosen for the scattering rate to match the broadness of the mode absorption, and a value of ω_p = 3.00 was chosen for the plasma frequency. These parameters correspond to an ENZ wavelength of λ_{ENZ} = 1355 nm. The resulting simulations match very well with experimental data. The contour lines in Figure 5.21(a) are shown to increase visibility of the mode. In Figure 5.21(e) the dashed lines represent the simulated data and match exceptionally well with the experimental data, showing conclusively that ITO films produced by RF magnetron sputtering do indeed exhibit ENZ behaviour in the 1200 nm – 1400 nm range and near-perfect absorption via the application of a Pt backing. This result opens up an exciting host of future opportunities for manipulating this near-perfect absorption.

5.5 Conclusion

In this chapter we discussed the necessary parameters for consideration when fabricating high-quality ITO such as deposition atmosphere, annealing temperature, annealing atmosphere, oxygen content, and how they affect the conductivity and transparency of ITO thin films. We discovered than a fine balance between all these parameters is needed to produce ITO of industrial and research quality. However, little previous work had been carried out on producing ITO specifically for its ENZ applications in the near-infrared, particularly the 1200 nm – 1400 nm range. In this chapter, we carried out a novel study of the necessary conditions for producing high-quality ITO with ENZ behaviour in the aforementioned spectral region. Several attempts were made at producing ITO with ENZ behaviour in this range: Ar^+ ion sputtering and RF magnetron sputtering. Several attempts were made in particular at varying the annealing conditions of Ar^+ ion sputtered ITO such as oxygen content and annealing temperature. ENZ behaviour was successfully achieved about 1700 nm using this deposition technique by annealing at 500°C in low pressure vacuum for one hour with 4 sccm of O_2 gas flow. However, the ENZ behaviour of the ITO films produced using this combination of techniques was further in the near-infrared than desired, and the films exhibiting poor transparency for thicker films. Using RF magnetron sputtering instead yielded far more promising results. A recipe for producing ITO locally was devised which consisted of a 200°C deposition temperature in an argon environment and then post deposition annealing in a vacuum tube furnace for one hour at 500°C with an O_2

flow rate of 4 sccm. The resulting films not only exhibited relatively high conductivity for ITO, but also high transparency in the visible, a band gap of about 4.20 eV and an ENZ wavelength of about 1335 nm. The Ferrell – Berreman mode was also successfully excited in thin films correspond to a peak absorption of 47.6% at 1333 nm for the ITO film alone, and an enhanced peak absorption of 90.1% at 1243 nm when 10 nm of Pt was deposited on the ITO containing side of the sample.

This ability to locally fabricate ITO thin films with an ENZ wavelength in the 1200 nm – 1400 nm opens up a whole host of exciting possibilities for future work on this near-perfect absorption and ENZ behaviour. Future multilayer structured of various thicknesses of ITO and various geometries can now be considered.

References

[1] D. Kim, Y. Han, J.-S. Cho, and S.-K. Koh, “Low temperature deposition of ITO thin films by ion beam sputtering,” *Thin Solid Films*, vol. 377, pp. 81–86, 2000.

[2] S.-H. K. Park, J.-I. Lee, C.-S. Hwang, and H. Y. Chu, “Characteristics of organic light emitting diodes with Al-doped ZnO anode deposited by atomic layer deposition,” *Jpn. J. Appl. Phys.*, vol. 44, no. 1L, p. L242, 2005.

[3] T. Minami, H. Sonohara, T. Kakumu, and S. Takata, “Physics of very thin ITO conducting films with high transparency prepared by DC magnetron sputtering,” *Thin Solid Films*, vol. 270, no. 1, pp. 37–42, 1995.

[4] M. Bender, W. Seelig, C. Daube, H. Frankenberger, B. Ocker, and J. Stollenwerk, “Dependence of film composition and thicknesses on optical and electrical properties of ITO–metal–ITO multilayers,” *Thin Solid Films*, vol. 326, no. 1, pp. 67–71, 1998.

[5] M. Bender, W. Seelig, C. Daube, H. Frankenberger, B. Ocker, and J. Stollenwerk, “Dependence of oxygen flow on optical and electrical properties of DC-magnetron sputtered ITO films,” *Thin Solid Films*, vol. 326, no. 1, pp. 72–77, 1998.

[6] F. Kurdesau, G. Khripunov, A. F. da Cunha, M. Kaelin, and A. N. Tiwari, “Comparative study of ITO layers deposited by DC and RF magnetron sputtering at room temperature,” *J. Non. Cryst. Solids*, vol. 352, no. 9, pp. 1466–1470, 2006.

[7] W.-F. Wu and B.-S. Chiou, “Mechanical and optical properties of ITO films with anti-reflective and anti-wear coatings,” *Appl. Surf. Sci.*, vol. 115, no. 1, pp. 96–102, 1997.

[8] Y. Hu, X. Diao, C. Wang, W. Hao, and T. Wang, “Effects of heat treatment on properties of ITO films prepared by rf magnetron sputtering,” *Vacuum*, vol. 75, no. 2, pp. 183–188, 2004.

[9] D. A. Alsaid, E. Rebrosova, M. Joyce, M. Rebros, M. Atashbar, and B. Bazuin, “Gravure printing of ITO transparent electrodes for applications in flexible electronics,” *J. Disp. Technol.*, vol. 8, no. 7, pp. 391–396, 2012.

[10] G. A. Salvatore *et al.*, “Wafer-scale design of lightweight and transparent electronics that wraps around hairs,” *Nat. Commun.*, vol. 5, p. 2982, 2014.

[11] H.-D. Kim, H.-M. An, Y. Seo, and T. G. Kim, “Transparent resistive switching memory using ITO/AlN/ITO capacitors,” *IEEE Electron Device Lett.*, vol. 32, no. 8, pp. 1125–1127, 2011.

[12] Z. Tan *et al.*, “High-Performance Inverted Polymer Solar Cells with Solution-Processed Titanium Chelate as Electron-Collecting Layer on ITO Electrode,” *Adv. Mater.*, vol. 24, no. 11, pp. 1476–1481, 2012.

[13] O. Lupan *et al.*, “Well-aligned arrays of vertically oriented ZnO nanowires electrodeposited on ITO-coated glass and their integration in dye sensitized solar cells,” *J. Photochem. Photobiol. A Chem.*, vol. 211, no. 1, pp. 65–73, 2010.

[14] T. Kawashima, T. Ezure, K. Okada, H. Matsui, K. Goto, and N. Tanabe, “FTO/ITO double-layered transparent conductive oxide for dye-sensitized solar cells,” *J. Photochem. Photobiol. A Chem.*, vol. 164, no. 1–3, pp. 199–202, 2004.

[15] J. Yoon, T. Y. Kim, W. Kim, Y. C. Jun, and C. K. Hwangbo, “Tunable Epsilon-Near-Zero ITO Thin Films and Broadband Perfect Absorption in the Near-Infrared,” in *Optical Interference Coatings 2016*, 2016, p. MD.7.

[16] J. Yoon, M. Zhou, M. A. Badsha, T. Y. Kim, Y. C. Jun, and C. K. Hwangbo, “Broadband Epsilon-Near-Zero Perfect Absorption in the Near-Infrared,” *Sci. Rep.*, vol. 5, p. 12788, 2015.

[17] A. Facchetti and T. J. Marks, "*Transparent Electronics: From Synthesis to Applications*," Wiley, 2010.

[18] C. Guillén and J. Herrero, “Influence of oxygen in the deposition and annealing atmosphere on the characteristics of ITO thin films prepared by sputtering at room temperature,” *Vacuum*, vol. 80, no. 6, pp. 615–620, 2006.

[19] V. Teixeira, H. N. Cui, L. J. Meng, E. Fortunato, and R. Martins, “Amorphous ITO thin films prepared by DC sputtering for electrochromic applications,” *Thin Solid Films*, vol. 420, pp. 70–75, 2002.

[20] P. K. Song, H. Akao, M. Kamei, Y. Shigesato, and I. Yasui, “Preparation and crystallization of tin-doped and undoped amorphous indium oxide films deposited by sputtering,” *Jpn. J. Appl. Phys.*, vol. 38, no. 9R, p. 5224, 1999.

[21] S. R. S. Kumar and S. Kasiviswanathan, “Role of oxygen vacancies in the high-temperature thermopower of indium oxide and indium tin oxide films,” *Semicond. Sci. Technol.*, vol. 24, no. 2, p. 25028, 2009.

[22] D.-K. Hwang, M. Misra, Y.-E. Lee, S.-D. Baek, J.-M. Myoung, and T. Il Lee, “The role of Ar plasma treatment in generating oxygen vacancies in indium tin oxide thin films prepared by the sol-gel process,” *Appl. Surf. Sci.*, vol. 405, pp. 344–349, 2017.

[23] C. Guillén and J. Herrero, “Influence of oxygen in the deposition and annealing atmosphere on the characteristics of ITO thin films prepared by sputtering at room temperature,” *Vacuum*, vol. 80, no. 6, pp. 615–620, 2006.

[24] C. May and J. Strümpfel, “ITO coating by reactive magnetron sputtering–comparison of properties from DC and MF processing,” *Thin Solid Films*, vol. 351, no. 1, pp. 48–52, 1999.

[25] F. Hanus, A. Jadin, and L. D. Laude, “Pulsed laser deposition of high quality ITO thin films,” *Appl. Surf. Sci.*, vol. 96–98, pp. 807–810, 1996.

[26] E. Holmelund *et al.*, “Deposition and characterization of ITO films produced by laser ablation at 355 nm,” *Appl. Phys. a-Materials Sci. Process.*, vol. 74, no. 2, pp. 147–152, 2002.

[27] Y. Zhou, H. Cheun, W. J. Potscavage Jr, C. Fuentes-Hernandez, S.-J. Kim, and B. Kippelen, “Inverted organic solar cells with ITO electrodes modified with an ultrathin

Al_2O_3 buffer layer deposited by atomic layer deposition," *J. Mater. Chem.*, vol. 20, no. 29, pp. 6189–6194, 2010.

[28] R. Matero, A. Rahtu, M. Ritala, M. Leskelä, and T. Sajavaara, "Effect of water dose on the atomic layer deposition rate of oxide thin films," *Thin Solid Films*, vol. 368, no. 1, pp. 1–7, 2000.

[29] J. W. Elam, D. A. Baker, A. B. F. Martinson, M. J. Pellin, and J. T. Hupp, "Atomic layer deposition of indium tin oxide thin films using nonhalogenated precursors," *J. Phys. Chem. C*, vol. 112, no. 6, pp. 1938–1945, 2008.

[30] J. M. Gaskell and D. W. Sheel, "Deposition of indium tin oxide by atmospheric pressure chemical vapour deposition," *Thin Solid Films*, vol. 520, no. 12, pp. 4110–4113, 2012.

[31] K. Maki, N. Komiya, and A. Suzuki, "Fabrication of thin films of ITO by aerosol CVD," *Thin Solid Films*, vol. 445, no. 2, pp. 224–228, 2003.

[32] M. P. Seah and T. S. Nunney, "Sputtering yields of compounds using argon ions," *J. Phys. D. Appl. Phys.*, vol. 43, no. 25, p. 253001, 2010.

[33] H. Adachi, T. Hata, and K. Wasa, "5 - Basic Process of Sputtering Deposition," K. Wasa, I. Kanno, and H. B. T.-H. of S. T. (Second E. Kotera, Eds. Oxford: William Andrew Publishing, 2012, pp. 295–359.

[34] S. H. Brewer and S. Franzen, "Indium tin oxide plasma frequency dependence on sheet resistance and surface adlayers determined by reflectance FTIR spectroscopy," *J. Phys. Chem. B*, vol. 106, no. 50, pp. 12986–12992, 2002.

[35] S. Vassant, J.-P. Hugonin, F. Marquier, and J.-J. Greffet, "Berreman mode and epsilon near zero mode," *Opt. Express*, vol. 20, no. 21, p. 23971, 2012.

[36] L. Bárdoš and M. Libra, "Effect of the oxygen absorption on properties of ITO layers," *Vacuum*, vol. 39, no. 1, pp. 33–36, 1989.

[37] M. Higuchi, S. Uekusa, R. Nakano, and K. Yokogawa, "Postdeposition annealing influence on sputtered indium tin oxide film characteristics," *Jpn. J. Appl. Phys.*, vol. 33, no. 1R, p. 302, 1994.

[38] D. F. Swinehart, "The Beer-Lambert Law," *J. Chem. Educ.*, vol. 39, no. 7, p. 333, 1962.

[39] J. Tauc, "Optical properties and electronic structure of amorphous Ge and Si," *Mater. Res. Bull.*, vol. 3, no. 1, pp. 37–46, 1968.

[40] E. Terzini, P. Thilakan, and C. Minarini, "Properties of ITO thin films deposited by RF magnetron sputtering at elevated substrate temperature," *Mater. Sci. Eng. B*, vol. 77, no. 1, pp. 110–114, 2000.

Chapter 6: Optimising Ferrell – Berreman and ENZ Mode Absorption in ITO – Metal Multilayers: Choice of Metal Backing and Thickness Dependence

6.1 Introduction

In Chapter 4 we demonstrated the excitation of the Ferrell – Berreman mode in ITO and demonstrated near-perfect absorption by depositing a 10 nm Pt backing on the ITO film, and in Chapter 5 we again demonstrated the achievement of near-perfect absorption by applying a 10 nm Pt backing on locally fabricated ITO. In both these cases, significant enhancements of the Ferrell – Berreman mode were obtained, and enhancement of the ENZ mode absorption was observed in commercial ITO films. However, the metal used as the backing in all cases was platinum as a result of its particularly large κ value, however near-perfect absorption is also achievable using a whole host of other common metals. Previous work on near-perfect absorption (NPA) in ITO has been carried out for ITO alone, or with an Au or Ag metal backing layer [1][2][3][4][5][6]. However, little research into the thickness or the metal layer or the type of metal used has been carried out. This chapter will focus on the role of the metal backing as well as modelling of the Ferrell – Berreman mode absorption and NPA when utilising different metals in the ITO – Metal structure and using different thicknesses of these metal.

6.2 Complex Refractive Index of Common Metals

While work on the coupling of ENZ materials has previously been published by Luk et al. [3] the work carried out was for ITO on an Ag metal backing of 100 nm thickness and no other metals were considered. Theoretical work has also been published by Krayer et al. [6] expanding on the analysis of perfect absorption by coupling with various metals, but in this case the simulated ENZ material was assumed to be a perfect ENZ material across a broad range of wavelengths. In this chapter, we expand further on the work of Luk and Krayer by considering the effects of coupling various different and commonly used metals to the backing of our ITO films. Furthermore, we not only consider the effects of various metals in a realistic ENZ material, but also the effect of the metal backing thickness. As already mentioned, the near-perfect absorption achieved by Luk et al. was achieved by coupling ITO with a 100 nm Ag backing, however we have demonstrated in previous chapters that a thickness of just 10 nm is sufficient to achieve near perfect absorption. Thus, in this chapter we also consider the effect of the metal backing thickness. By utilising ITO, we demonstrate this effect in a real ENZ material with scattering included. The metals considered and simulated in this work were Cr [7], Ni [7], Pd [8], Sn [9], Ag [10], Au [11], Cu [10], In [12], Bi [8], and Al [10]. Figure 6.1(a – e) and Figure 6.2 (a – e) present the real and imaginary components of the complex refractive index and (f – j) in both figures present the real and imaginary components of the complex permittivity for each metal. These optical constants were obtained from the literature and the corresponding publications from which they were obtained are cited. As shown, in the case of all metals except Cr, there is a very large κ-value and a small n-value which corresponds to a relatively small imaginary component of the permittivity and a large negatively valued real component of the permittivity. However, in the case of Cr, the real and imaginary components of the complex refractive index are roughly equal in the ENZ region of ITO and diverge at larger wavelengths. The real and imaginary components of the complex refractive index and the complex permittivity of each metal at an incident wavelength of 1125 nm, corresponding to the Ferrell – Berreman mode absorption in ITO is presented in Figure 6.3 as in order of increasing κ-value. Again, as shown, there is a significant difference between the real and imaginary components of both the refractive index and permittivity for all metals, except Cr which overlap at 1125 nm. This data was utilised in all subsequent simulations considered in this work.

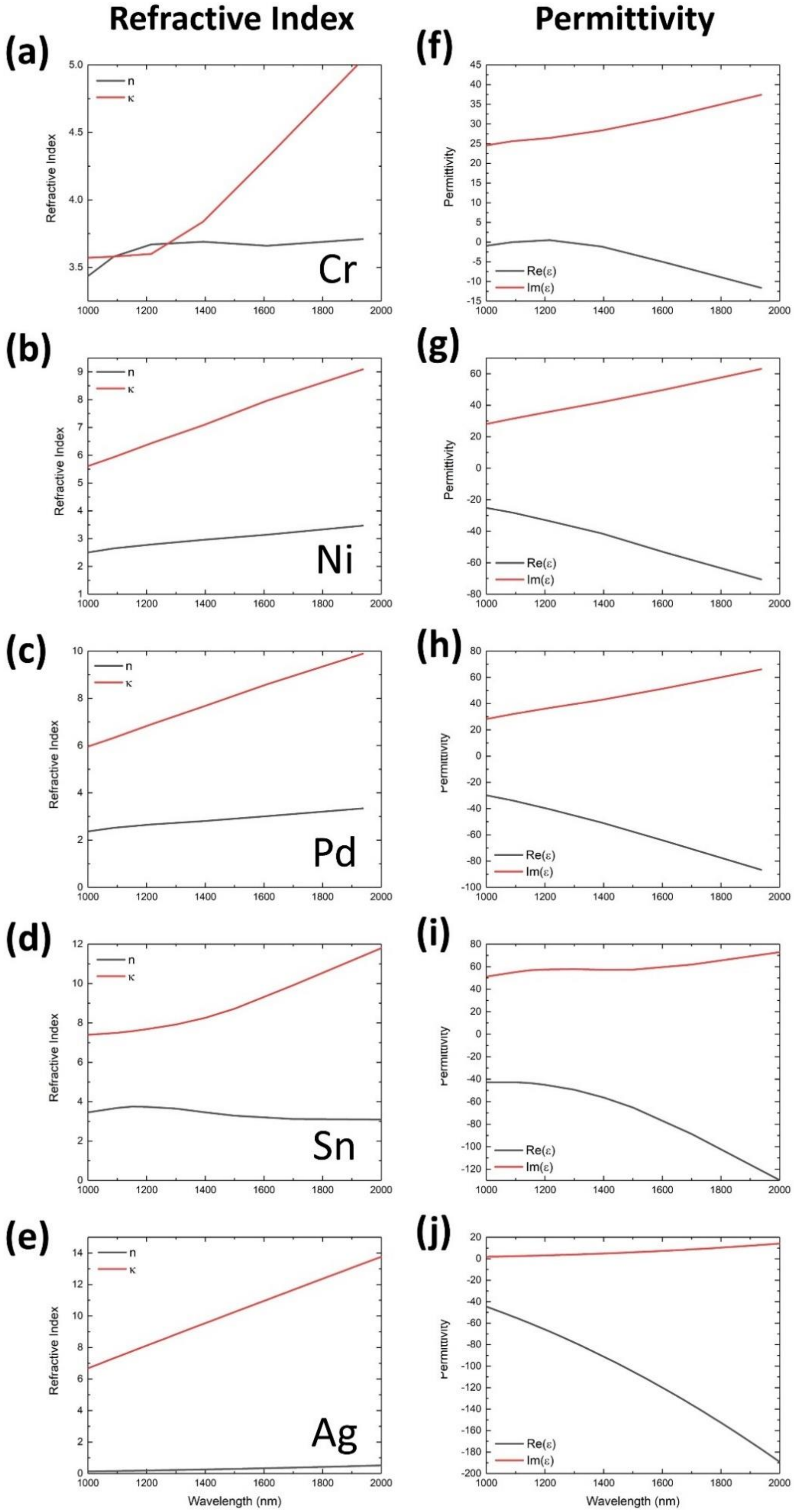

Figure 6.1 Real (black) and imaginary (red) components of (a – e) the complex refractive index and (f – j) the complex permittivity of Cr, Ni, Pd, Sn, and Ag.

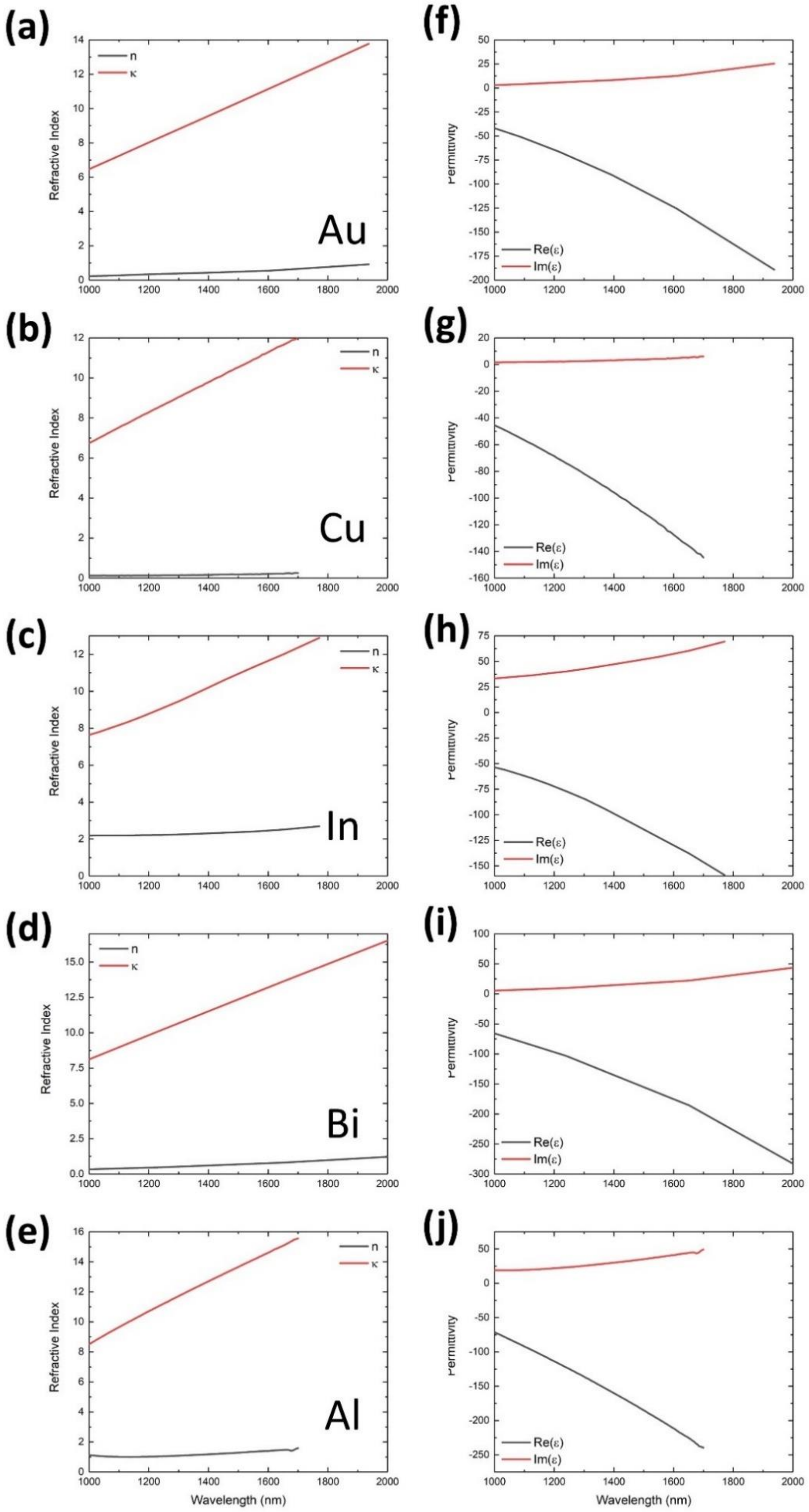

Figure 6.2 Real (black) and imaginary (red) components of (a – e) the complex refractive index and (f – j) the complex permittivity of Au, Cu, In, Bi, and Al.

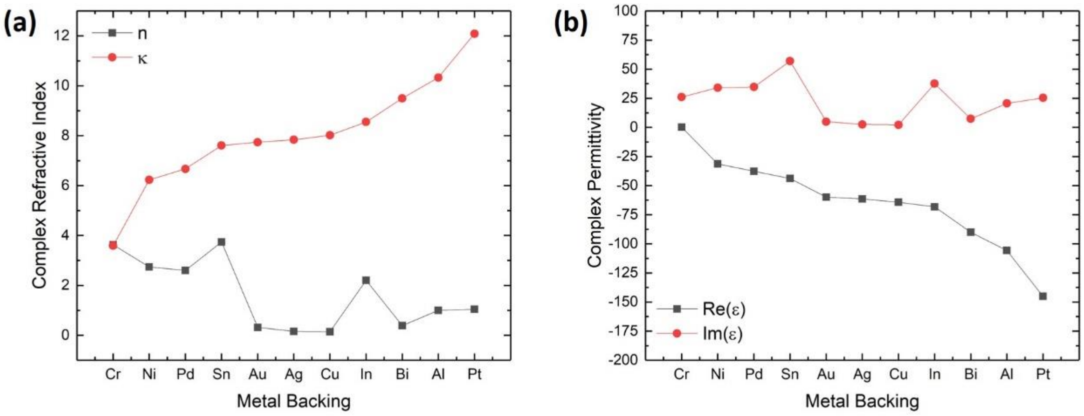

Figure 6.3 Complex refractive index (a) and complex permittivity (b) of various metals at a wavelength of 1125 nm.

6.3 Dependence of Metal Backing on Ferrell – Berreman and ENZ Mode Absorption in ITO – Metal films.

To theoretically determine the effects of changing the previously used Pt backing for other common metals, transfer-matrix simulations were carried out for a 127 nm ITO film with a 10 nm layer of the common metals Cr, Ni, Pd, Sn, Ag, Au, Cu, In, Bi, and Al. The ITO film in all simulations was maintained constant in both thickness and the Drude parameters, which were taken from experimental data obtained by NIR spectroscopic ellipsometry and are presented in Table 3.3 of Chapter 3 The optical constants of the various metals were obtained from literature and are cited above in Section 6.1. The simulations were carried for a glass superstrate (n = 1.51), a 127 nm ITO film, a 10 nm metal backing, and an air substrate (n = 1.00) as shown in Figure 6.4. the simulations were separated into the two angular ranges, 13˚ – 41˚ for the Ferrell – Berreman mode and 41˚ – 90˚ for the non-radiative ENZ mode above the critical angle.

T-Matrix simulations of the metal-backing-enhanced Ferrell-Berreman mode absorption are presented in Figure 6.5 and Figure 6.6. The data is separated into two figures to aid visibility. Figure 6.5(a – e) and Figure 6.6(a – e) present the simulated broadspectrum angle-resolved absorption and the black line tracing the high absorption feature is the calculated mode dispersion for each ITO – Metal combination. The mode dispersions were calculated using the previously described real – wavevector complex eigenfrequency root solving method in Mathematica and are in reasonable agreement with previous calculations on ITO by Campione et al. [13] The mode dispersions follow the absorption features perfectly for all simulations except Cr. Several attempts were made at calculating the mode dispersion of an ITO – Cr structure, however the code did not converge at a particular solution, and as a result, the mode dispersion could not be calculated and is not included in Figure 6.55(a). Figure 6.5(f – j) and Figure 6.6(f – j) present the Ferrell – Berreman mode absorption at the angle of maximum absorption, 39˚ incidence. This data is reprinted together for comparison in Figure 6.7(a) and the peak mode absorption for each metal is presented in Figure 6.7(b). As shown, the greatest absorption of 98% is achieved with a 10 nm Pt layer and the lowest absorption of 79% is obtained with a 10 nm Cr backing. However, all other metals except Cr produce an absorption of > 92%. This clearly demonstrates that that Ferrell – Berreman mode absorption can be significantly enhanced from a value of about 60% for ITO alone (as demonstrated in Chapter 4) to values greater than 92% by the application of just 10 nm of almost any common metal.

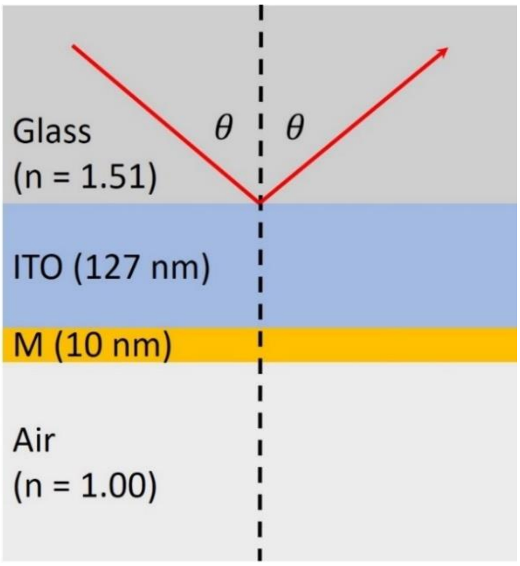

Figure 6.4 2D Schematic showing the ITO – Metal (M) multilayer structure simulated in this chapter. The superstrate is glass (n = 1.51) and the substrate is air (n = 1.00). The optical parameters of the ITO layer are simulated using the Drude model with previously determined Drude parameters and the optical constants of the metals are taken from the literature.

To determine why certain metals, achieve greater absorption than others, the complex refractive index data and the complex permittivity data were again considered for each of these metals. Comparing the refractive index and permittivity data previously discussed in Figure 6.1 and Figure 6.2, a clear trend in visible across all metals in both the refractive index and permittivity data. All metals appear to exhibit a large imaginary (κ) value and a rather small real (n) value which progressively diverge at larger wavelengths. Particularly, the difference between the real and imaginary components of for each metal appears to be quite large across all metals except for Cr. Cr has a small κ-value about the ENZ region of the ITO films (≈ 1200 nm) and is the only metal which has a real component larger than its κ-value in this region. Cr also has two points of overlap in its n and κ values which correspond to two points in the permittivity where $Re(\varepsilon)$ = 0, making Cr another ENZ material. However, the imaginary component of the permittivity is quite high (about 25) at these points and previous reports in the literature of fitting Cr to a Drude Lorentz model has shown that that the scattering rate is very high at γ = 2.58 rad fs^{-1} [14], which suggests that while Cr could be considered an ENZ material, it's not an ideal candidate for examining ENZ behaviour. Furthermore, the resulting difference between the real and imaginary components is rather small and this may be the reason for the relatively poor performance of Cr compared to the other metals considered. As the real component of the dielectric permittivity can be related to the real and imaginary components of the complex refractive index by

$$\mathrm{Re}(\varepsilon) = \mathrm{n}^2 - \kappa^2 \tag{1}$$

where n is the real component of the refractive index, we can see that a large difference in the n- and κ-values results in a large value of $\mathrm{Re}(\varepsilon)$. Thus, we suggest that in order to achieve near-perfect absorption or even perfect absorption, a lossy metal is the ideal candidate, and particularly a metal with a low n-value and a very large κ-value. This requirement for a metal with a large difference between its real and imaginary components of the refractive index was previously discussed by Krayer et al. [6], however they assumed an ENZ material with homogenous ENZ behaviour, i.e. with $\mathrm{Re}(\varepsilon) = 0$ across all frequencies. Here we demonstrate this for a real ENZ material with scattering included.

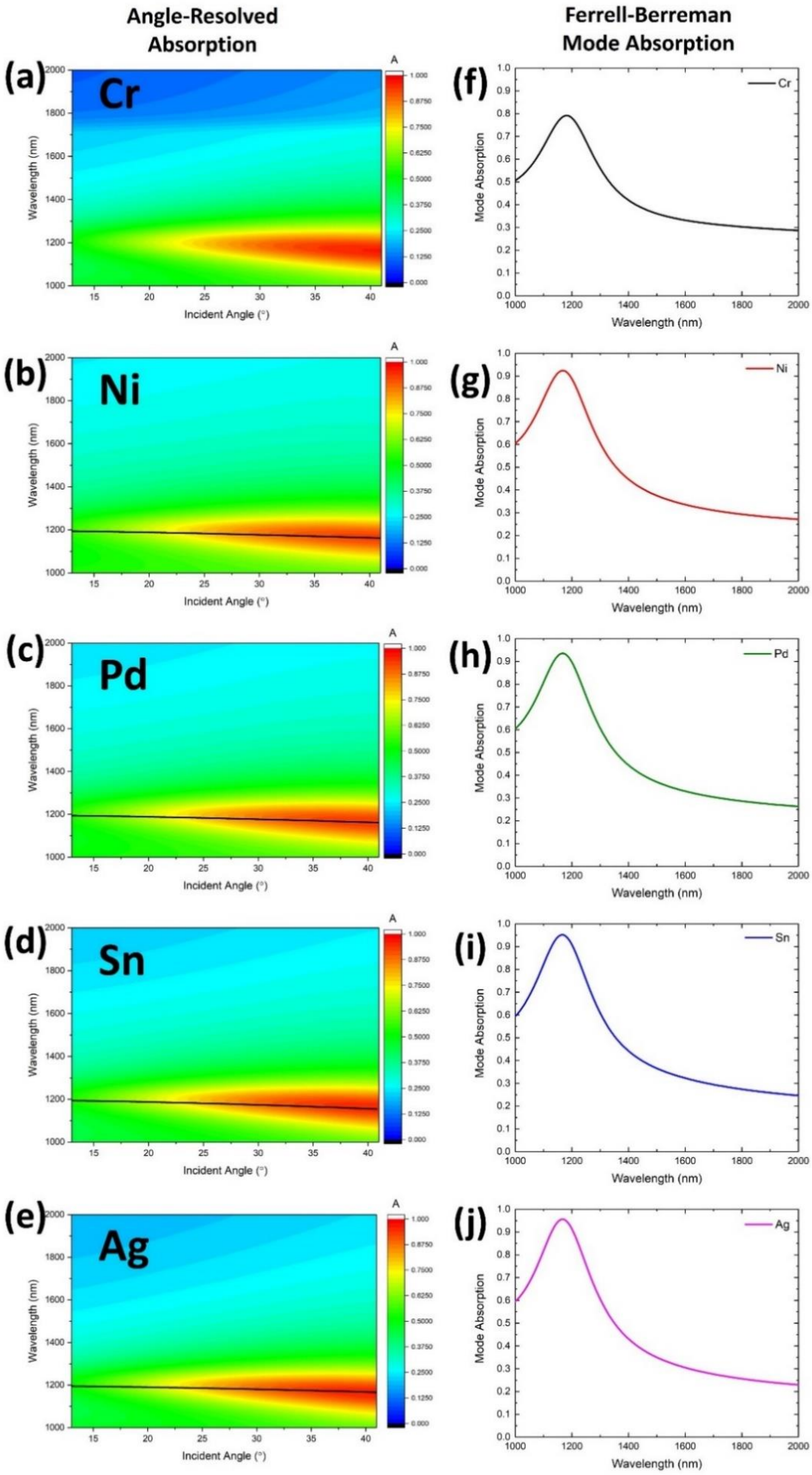

Figure 6.5 Broadspectrum angle-resolved absorption (a – e) and Ferrell-Berreman mode absorption at 39˚ incidence as a function of angle for a structure composed of ITO (127 nm) on a metal backing of Cr, Ni, Pd, Sn, and Ag.

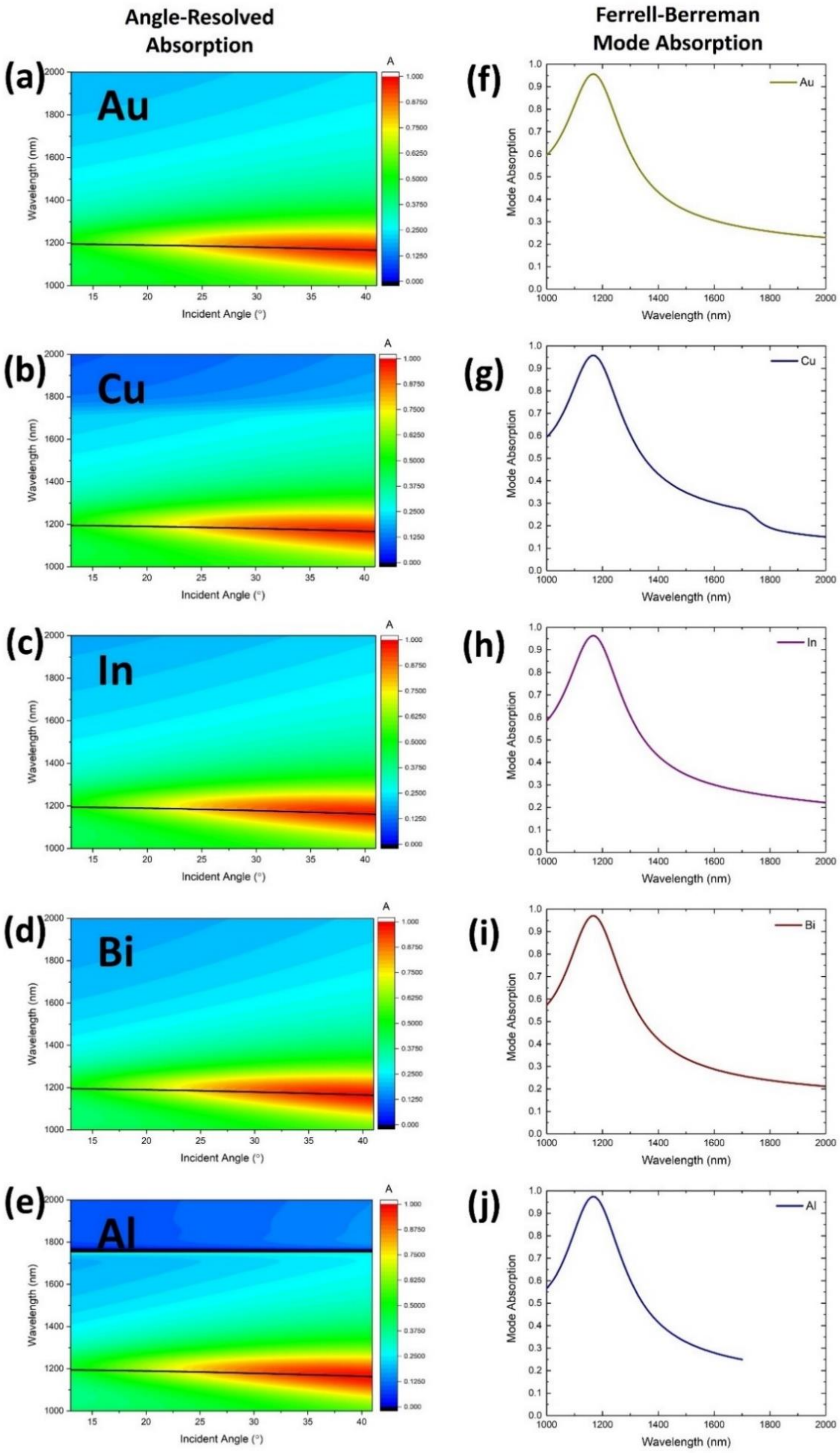

Figure 6.6 Broadspectrum angle-resolved absorption (a – e) and Ferrell-Berreman mode absorption at 39˚ incidence as a function of angle for a structure composed of ITO (127 nm) on a metal backing of Au, Cu, In, Bi, and Al.

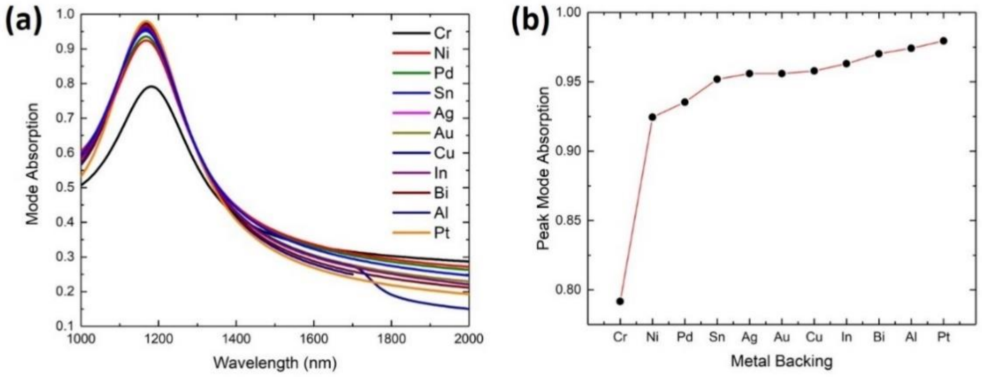

Figure 6.7 (a) Ferrell – Berreman mode absorption as a function of wavelength for a 127 nm ITO film with a 10 nm metal backing of various metals and (b) the peak mode absorption for each metal.

6.3.1 Ferrell – Berreman Mode Dispersion in ITO – Metal Film Structures

As mentioned above, the Ferrell – Berreman mode dispersions for each sample were calculated using a real wavevector – complex eigenfrequency root solving method. These mode dispersions are replotted in Figure 6.8(a) in the typical frequency versus wavevector representation showing the characteristic behaviour of a bulk plasmon, i.e. the frequency of the mode curving upwards towards the light line (black dashed line) [15][16][17]. All variations of the ITO – Metal structure show this same behaviour, and at $\mathrm{k} = 0$ all ITO – Metal structures converge at the same value of around 1.545 rad fs^{-1} which is the ENZ frequency of the ITO film, however as the value of the wavevector increases the mode frequencies begin to diverge from each other. A commonly expected phenomenon in ENZ materials and particularly in exciting the Ferrell – Berreman mode is a significant reduction in the group velocity, $\mathrm{v_g}$ [18][19] of light and a significant increase in the phase velocity, $\mathrm{v_p}$ [20][21][22]. Using the definition of the group and phase velocities [23][24], i.e.

$$\mathrm{v_g} = \frac{\partial \omega}{\partial \mathrm{k}} \tag{2a}$$

$$\mathrm{v_p} = \frac{\omega}{\mathrm{k}} \tag{2b}$$

it was possible to calculate both by taking the first derivative of the frequency with respect to the wavevector to obtain the group velocity, and by taking the ratio of the frequency to the wavevector to obtain the phase velocity. These are plotted in Figure 6.8(b) and (c) respectively as the relative group and phase velocities, i.e. divided by the vacuum speed of light, c. As expected, the group velocity in the structure is reduced to values between 0.005c and 0.12c. However, the group velocity appears to have some dependence on the choice of metal backing which may be a result of exciting surface plasmon polaritons with different dispersions for each metal. Interestingly, the phase velocity for all structures appears the same regardless of the metal backing used and as expected is superluminal ranging from c to 50c. Both these phenomena are expected from ENZ materials and provides further confirmation that the excitation of this mode in ITO is a result of its ENZ behaviour [25][26][27][28].

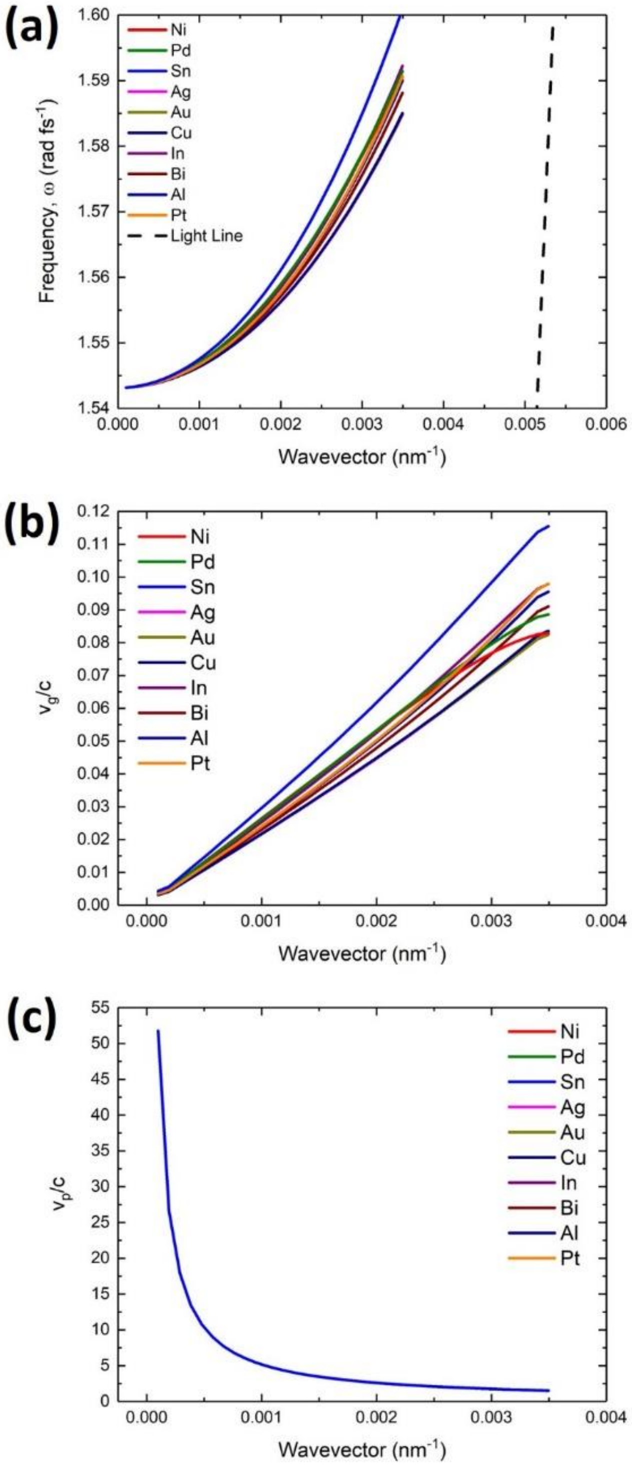

Figure 6.8 (a) Ferrell-Berreman mode dispersion for a 127 nm ITO film with various metals backings calculated from real-wavevector complex eigenfrequency analysis and the subsequently calculated relative (b) group velocity, ${}^{v_g}/_{c}$ and (c) phase velocity ${}^{v_p}/_{c}$.

To determine whether the κ-value or the real component of the permittivity were the deciding factor in the absorption enhancement, the κ-value and the real component of the dielectric permittivity were plotted on two-scale plots in Figure 6.9(a) and (b) respectively, alongside the peak mode absorption for each metal. A clear correlation between the κ-value and the peak mode absorption is apparent. As the κ-value increases, so too does the peak mode absorption, almost identically. An inverse correlation is noted between the real component of the permittivity and the peak mode absorption. As shown, the lower the value of $Re(\varepsilon)$, the higher the peak mode absorption. This suggests that both these parameters are indeed the deciding factors to deciding which metal is best for achieving the highest absorption possible form the ITO – Metal structures. This also confirms previous suggestions to why the performance of Cr is so much poorer than the other metals. From Figure 6.9(a), we see that Cr has the lowest κ-value and that the small difference between the n- and κ-values that leads to a positive and very small real component of the permittivity.

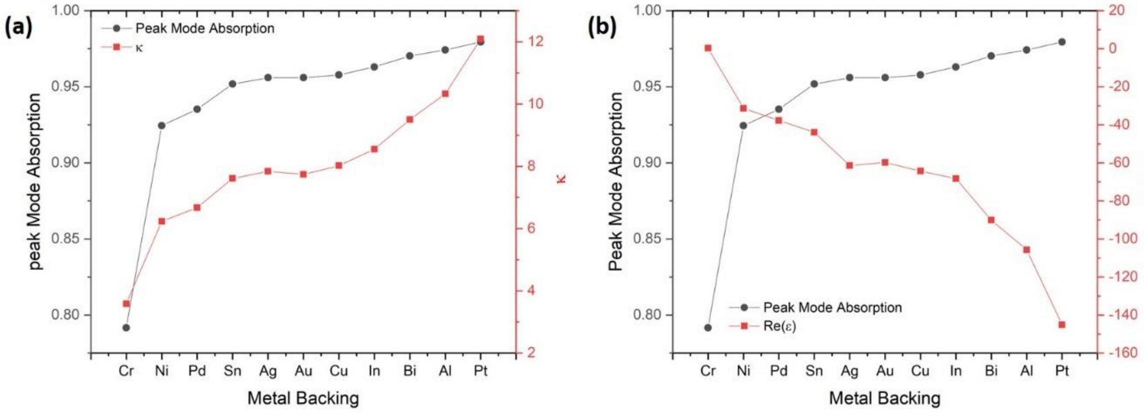

Figure 6.9 (a) Peak Ferrell – Berreman mode absorption (black) compared to the imaginary component of the complex refractive index (red) at 1125 nm for various metals and (b) compared to the real component of the dielectric permittivity at 1125 nm.

Furthermore, we can conclude that exceptional performance of Pt in achieving significant enhancement of the Ferrell – Berreman mode absorption is a result of it being a very high κ-value metal with a significantly large difference between its real and imaginary components of the refractive which leads to the largest value of $\mathrm{Re}(\varepsilon)$. To further demonstrate this, the peak mode absorption was plotted as a function of the κ-value and is presented in Figure 6.10. There is a clear, almost asymptotic, trend in the peak mode absorption with increasing κ. While any metal backing is sufficient to achieve extremely high absorption, this plot demonstrates that the correct choice of a high-loss metal as the backing can greatly assist the achievement of near-perfect absorption.

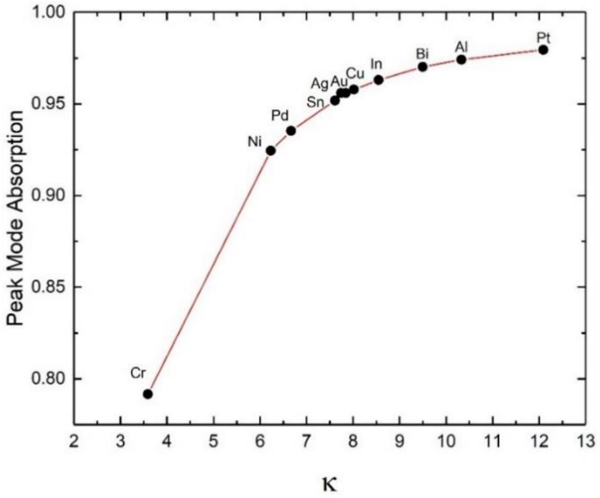

Figure 6.10 Peak Ferrell – Berreman mode absorption as a function of the imaginary component of the complex refractive index for various metals.

6.3.2 Thickness Dependence of Metal Backing on Ferrell – Berreman Mode Absorption

As well as studying the effects of using different metal backings on the Ferrell – Berreman mode absorption, we also examined the thickness dependence of the metal backings. Previous data in Chapter 4 for ITO with a Pt backing showed that the absorption increased with increasing Pt thickness. To gain further insight into this effect, COMSOL FEM simulations were carried out on the structure represented in Figure 6.4. The simulations were carried at the NPA wavelength of 1125 nm and an incident angle of 39°. A parametric sweep was carried out varying the thickness of the metal backing layer between 1 nm – 130 nm in increment of 1 nm. The resulting calculated absorption, transmission, and reflectivity were plotted as a function of the metal backing thickness for various metals and this data is presented in Figure 6.11. A clear asymptotic dependence on the thickness is noted, with all ITO – Metal structures experiencing a large increase in absorption via the application of just a few nanometres of metal, however the absorption reached a maximum value and plateaus at thicknesses below 30 nm for most metals, except Cr. Furthermore, each metal reaches its plateau at a different value of the metal backing thickness. Pt reaches its plateau about 20 nm, while Cr reaches its absorption plateau about 60 nm. The order in which each metal reaches its plateau appears to correspond very well with the imaginary component of the refractive index, κ from Figure 6.10 with the metals having a higher κ-value reaching their plateaus at much thinner thicknesses. A similar trend is noted in the transmission data in Figure 6.11(b), with the lowest loss metals such as Cr exhibited the greatest transmission, and the highest κ-valued metals such as Pt exhibiting the lowest. However, the transmission data for all metals follows an exponential decay with increasing thickness as would be expected. The reflectivity data in Figure 6.11(c) is low for all metals which shows that the Ferrell – Berreman mode absorbs almost all of the light in such thin layers. The intuitive expectation when adding a metal to any structure would be an increase in reflectivity, however in this case, by placing the metal on the back of an ENZ material, the metallic layer works to enhance the absorption while increasing reflectivity in the off-resonant regions, but maintaining near-zero reflectivity in the Ferrell – Berreman and ENZ regions, and in the case of the ENZ mode, the reflectivity is actually suppressed with the 10 nm backing. This is demonstrated in Figure 6.12. While the values of the reflectivity are very low, an interesting feature is also noted in the data. For each metal, at very small thicknesses there is a minimum in the reflectivity which varies in position for each metal.

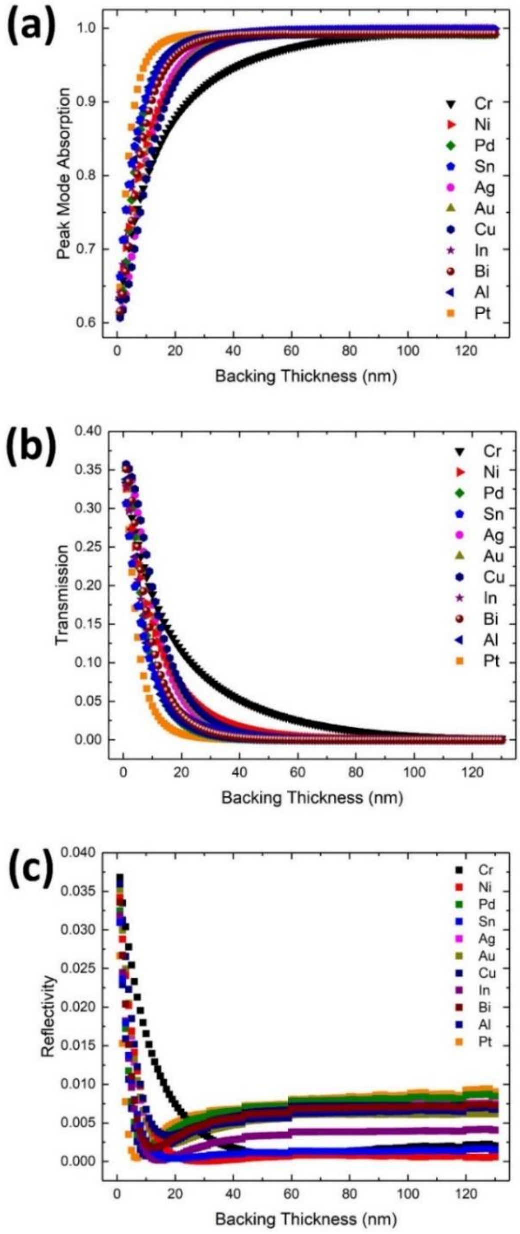

Figure 6.11 COMSOL FEM simulations of (a) absorption, (b) transmission, and (c) reflectivity from a structure composed of a 127 nm ITO film with a metal backing of various thicknesses and materials at the NPA wavelength of 1125 nm and 39˚ incidence.

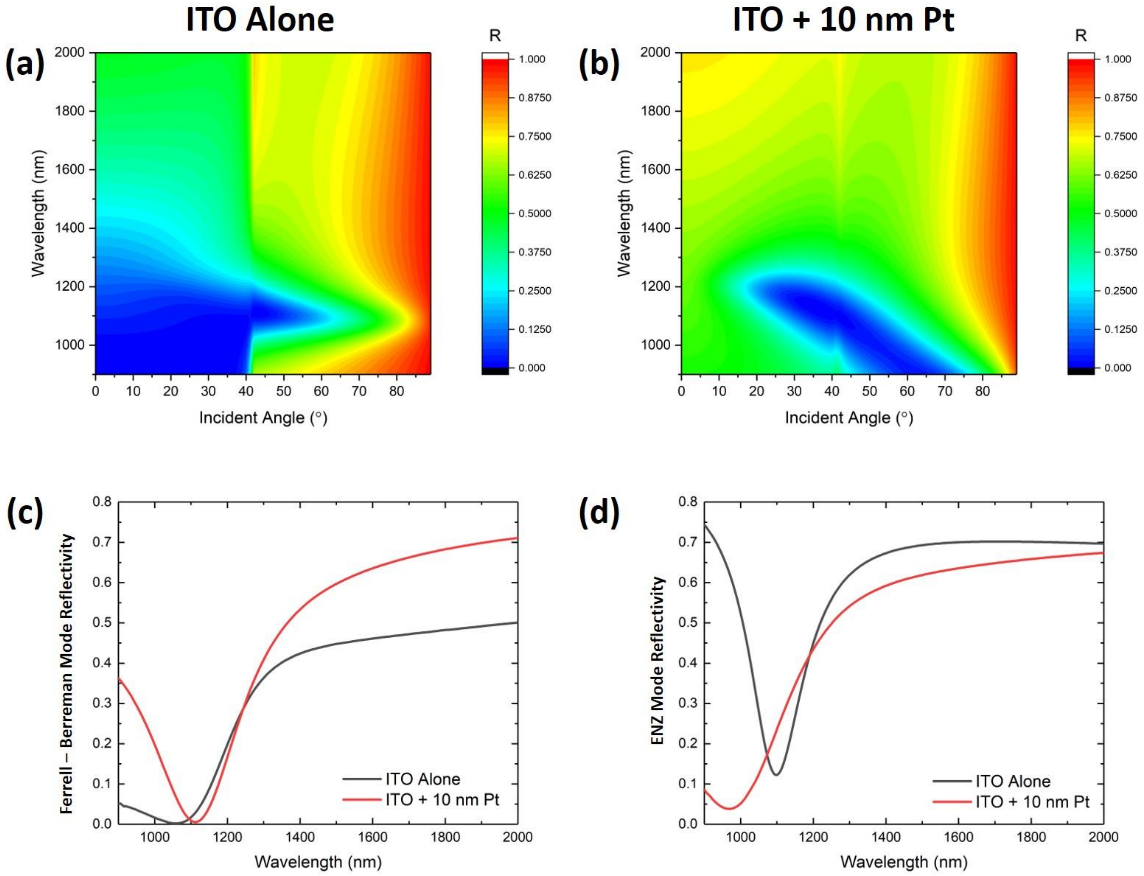

Figure 6.12 T-Matrix simulated broadspectrum angle-resolved reflectivity data for a 127 nm ITO film without (a) and with (b) a 10 nm metal backing. The reflectivity of the Ferrell – Berreman mode and ENZ modes with (red) and without (black) are presented in (b) and (c) respectively taken at incident angles of 39˚ and 55˚.

Figure 6.12 presents T-Matrix simulations of the angle resolved reflectivity of a 127 nm ITO film with (b) and without (a) a 10 nm Pt backing, and the resulting Ferrell – Berreman mode (c) and ENZ mode (d) reflectivities taken at 39˚ and 55˚ incidence respectfully. In Figure 6.12(c) we see that the there is little to no change in the magnitude of the reflectivity with the addition of the 10 nm Pt layer, however there is a red-shifting of the reflectivity minimum. The interesting feature to note is that in all spectral regions outside of the Ferrell – Berreman region, the presence of the 10 nm layer causes an increase in reflection, except in the Ferrell – Berreman mode region itself, where it remains unchanged. Another interesting effect is noted in Figure 6.12(d) which shows the ENZ reflectivity. The presence of the metal backing this time causes a blue-shift in the reflectivity minimum to shorter wavelengths as well as a reduction in the reflectivity in the ENZ mode region. Since the ENZ mode also lies to beyond the critical angle for glass, the ENZ mode transmission is zero, this this zero-transmission coupled with suppressed reflection by the 10 nm backing leads to a huge increase in absorption as previously demonstrated both experimentally and by simulation. Similar results can also be observed in the other metals.

As well as having different value of the refractive index, each metal also has a different skin depth. The skin depth is defined as the distance from the surface of a conductor at which the AC current density drops to a value of $1/_{e}$ of the current density at the surface. It can also be thought of as the distance at which the electric field interacts most with the charge carriers in the material. Another relevant parameter for each metal is the wave impedance. Typically, metals have a very low wave impedance in the near-infrared and it's the substantial mismatch between the ITO and metal layers that cause significant reflection back into the ITO layer in which it undergoes further absorption. The wave impedance, Z and skin depths, δ_s can be calculated using the following expressions [29]

$$Z = \sqrt{\frac{i\omega\mu}{\sigma + i\omega\varepsilon}} \tag{3}$$

$$\delta_s = \sqrt{\frac{2}{\sigma\omega\mu}} \sqrt{\sqrt{1 + \left(\frac{\omega\varepsilon}{\sigma}\right)^2} + \frac{\omega\varepsilon}{\sigma}} \tag{4}$$

where ω is the incident frequency of light, μ is the magnetic permeability, ε is the dielectric permittivity of the metal, and σ is its electrical conductivity. A code was written in Matlab to calculate the skin depth and the relative wave impedance of light at 1125 nm in each metal. Figure 6.13(a) and (b) present the real and imaginary components of the relative wave impedance, $Z/_{Z_0}$ where $Z_0 \approx 120\pi\ \Omega$ is the impedance of free space. As shown, all metals exhibit a very low value of both real and imaginary components of the impedance, across all wavelengths in the near-infrared. Figure 6.13(c) presents the reflectivity as a function of wavelength calculated using the wave impedance obtained from Equation 3 for ITO and the metals. The reflectivity in terms of the impedance was calculated for an ITO – Air interface and the ITO – Metal interfaces using the expression [3]

$$R = \left|\frac{Z_m - Z_{ITO}}{Z_m + Z_{ITO}}\right|^2 \tag{5}$$

where Z_m and Z_{ITO} are the wave impedance of the metal and ITO respectively. As shown, very high reflectivity is expected at the ITO – Metal interface from all metals leading to significant absorption from excitation of the Ferrell-Berreman mode. Figure 6.13(d) presents the skin depth calculated using Equation 5. The lowest skin depth of about 4 nm is achieved by Ag and the largest of about 18 nm is achieved by Bi. Pt, the best performer for achieving enhanced absorption has a skin depth of around 9 nm. While the skin depth itself appears to have little effect on the perfect absorption in the films, it does explain the exponential trend in the transmission through the structures as a function of thickness. When light is incident on metal layer at oblique incidence, light can still be transmitted through the layer if the thickness of the metallic layer is below the skin depth. Even in the case where the angle is above the critical value, light can still be transmitted by the process of frustrated total internal reflection (FTIR).

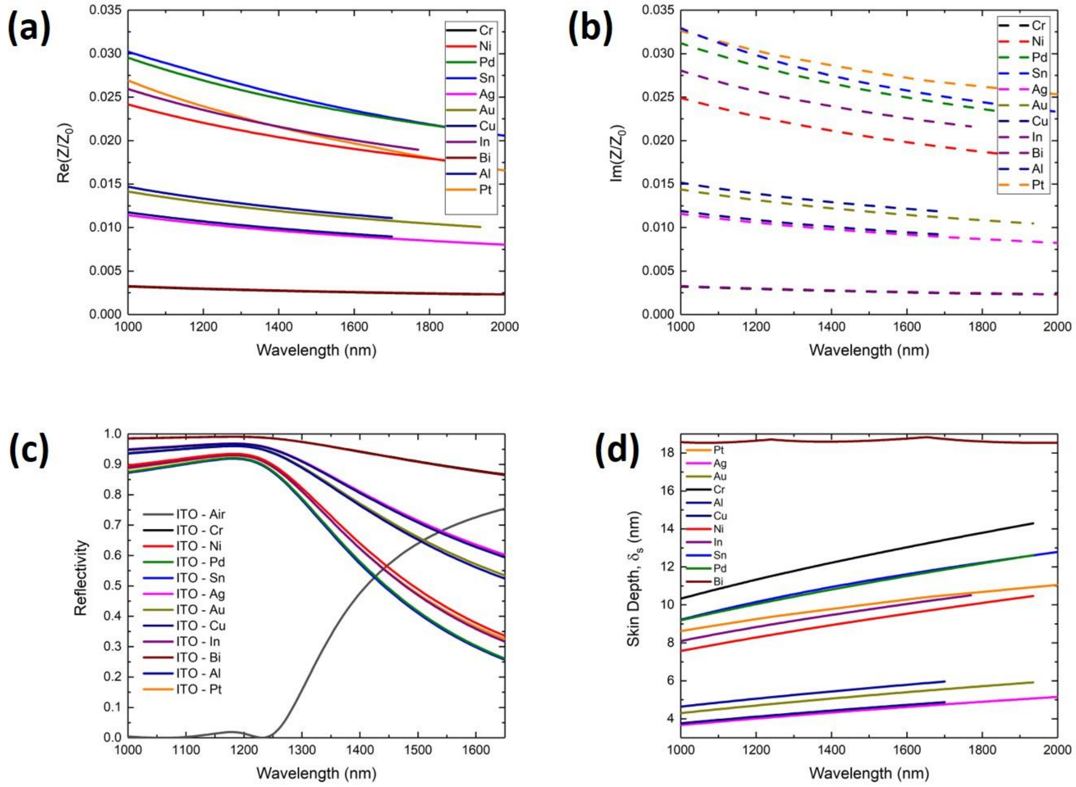

Figure 6.13 Real (a) and imaginary (b) components of the relative wave impedance $\left(Z/_{Z_0}\right)$ where Z_0 is the wave impedance of free space as is approximately $Z_0 \approx 120\pi\ \Omega$. (c) The normal incidence reflectivity at the interface between ITO and various metals and (d) the skin depths of these metals as a function of wavelength.

6.3.3 Dependence of Metal Backing on non-radiative ENZ Mode Absorption in ITO – Metal films.

Further T-Matrix simulations were carried out in the 41˚ – 90˚ range of incident angles to simulate the ENZ mode in the ITO – Metal multilayer films. Figure 6.14(a – e) presents the simulated broadspectrum angle-resolved absorption data for a 127 nm ITO film with a 10 nm layer of Cr, Ni, Pd, Sn, and Ag. Figure 6.15(a – e) presents the same data for an Au, Cu, In, Si, and Al backing. It was noted during preliminary simulation across the 100 nm – 2000 nm range that the non-radiative ENZ mode for the ITO films with a metal backing appeared to extend further into the visible, whereas in the case of an ITO film alone, the absorption feature remained confined to the ENZ spectral region about 1200 nm, thus these simulations were carried out over the 500 nm – 2000 nm spectral range. Figure 6.14(f – j) and Figure 6.15(f – j) present the corresponding ENZ mode absorption at 65˚ incidence. Again, in all samples, a very clear high absorption feature is clearly visible starting at 1200 nm at 41˚ and then moving towards shorter wavelengths as the incident angle increases. As show, the ENZ mode absorption gradually extends to shorter wavelengths with increased incident angle. For this reason, the non-radiative ENZ mode absorption as a function of wavelength was taken at 65˚ to show the near-perfect absorption further into the visible range. Figure 6.16 presents these EMZ mode absorption profiles at 65˚ in a single plot for comparison. All metals exhibit a theoretical absorption value of greater than 95% for all metals except Pt which has an absorption just above 90%.

In Figure 6.14(a), Figure 6.15(e) there is a discontinuity in the simulation at 1700 nm. This is a result of the simulation switching to an extrapolation as the refractive index data for both Cr and Al only extended as far as 1700 nm. This results in a small discontinuity across the entire angular range at this wavelength.

The non-radiative ENZ mode absorption was also taken at 55˚ across the 900 nm – 2000 nm range as these were the spectral and angular ranges compared in experiment in Chapter 4. This data is presented in Figure 6.17(a). In Chapter 4, the excitation of the non-radiative ENZ mode in a 127 nm ITO film alone achieved a peak absorption of 71.5%, but as can be seen here, a thin film of only 10 nm of any metal except Cr is sufficient to enhance ENZ mode absorption to values greater than 90%. Although the ITO – Cr structure exhibits the lowest absorption due its low κ-value and the relatively small difference between the real and imaginary components of its refractive index, the absorption achieved with this metal is still significantly enhanced to a peak value just below 85%. All other metals achieve an absorption $\gtrapprox$ 90% as shown in the peak mode absorption at 55˚ incidence. The absorption achieved by exciting the non-radiative ENZ mode is in general greater than the absorption achieved by exciting the Ferrell – Berreman. The reason for this is that the ENZ mode lies beyond the critical angle and to the right of the light line and beyond the critical angle only total internal reflection can occur, thus transmission is suppressed and is zero regardless of the metal used. This very low transmission is due to the greater absorption in the ITO – Metal films.

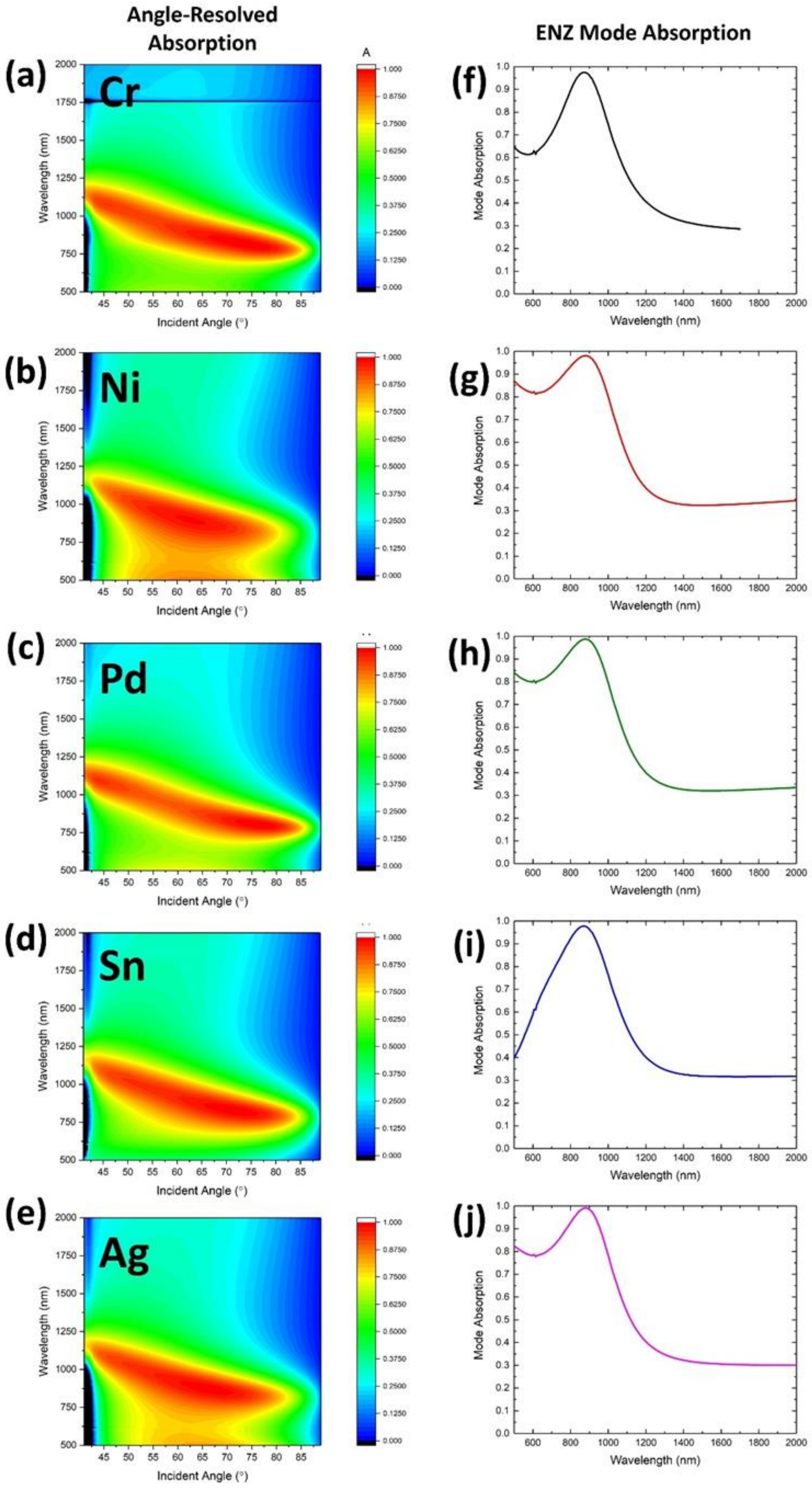

Figure 6.14 Broadspectrum angle-resolved absorption (a – e) and non-radiative ENZ mode absorption at 55˚ incidence as a function of angle for a structure composed of ITO (127 nm) on a metal backing of Cr, Ni, Pd, Sn, and Ag.

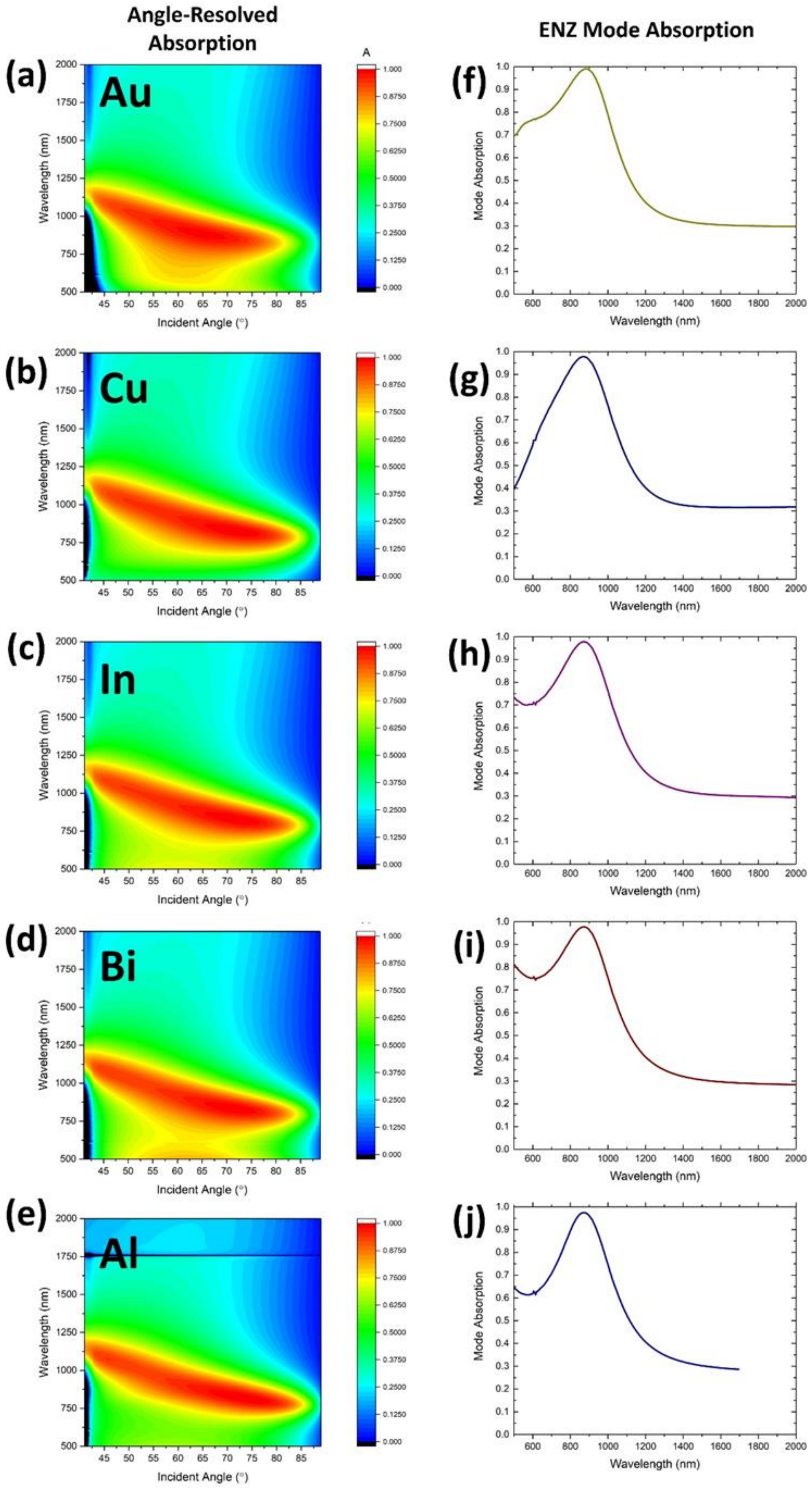

Figure 6.15 Broadspectrum angle-resolved absorption (a – e) non-radiative ENZ mode absorption at 55˚ incidence as a function of angle for a structure composed of ITO (127 nm) on a metal backing of Au, Cu, In, Bi, and Al.

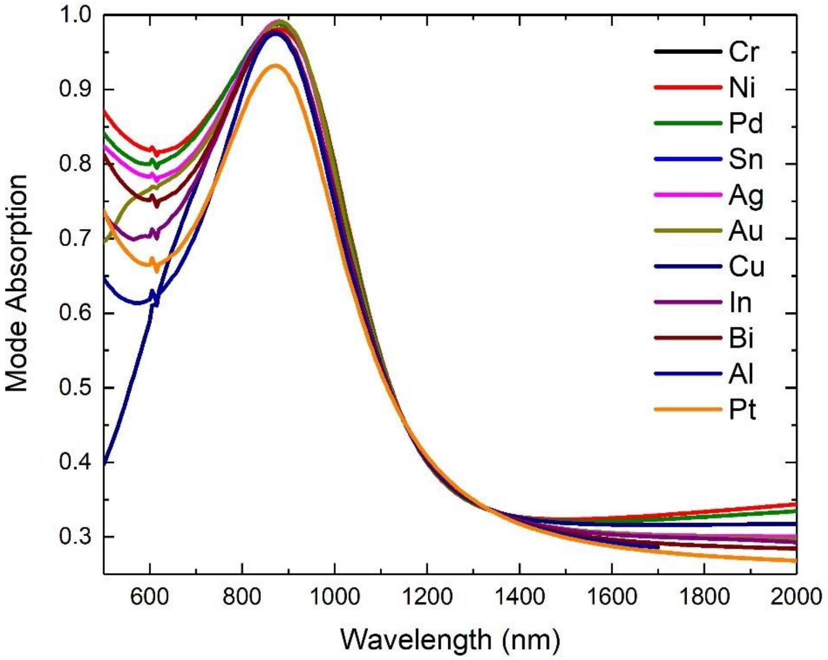

Figure 6.16 Simulated non-radiative ENZ mode absorption from a 127 nm ITO film with 10 nm of various metal backings excited from a glass substrate at 65˚ incidence.

The ENZ mode absorption profiles at 55˚ for each metal are presented together for comparison in Figure 6.17(a) and the peak mode absorption is presented for each metal in Figure 6.17(b). Interestingly, while Pt provided the highest absorption when exciting the Ferrell – Berreman mode, in this case Pt provides one of the lowest absorption values of around 90%, and the greatest absorption is achieved by Pd with a value of about 96%. Metals that had lesser performance appear now to achieve much better performance when exciting the non-radiative ENZ mode. This may be due to the fact that the ENZ mode lies beyond the critical angle and that transmission through the metal backing layer cannot occur. To determine how the peak ENZ mode absorption relates to the optical constants of the various metal backings, the peak mode absorption was again plotted on a double y-scale graph against the imaginary component of the refractive index, κ and the real component of the permittivity, Re(ε) of the metals. These are presented in Figure 6.18(a) and (b) respectively. As with the Ferrell – Berreman mode, there again appears to be some correlation between the optical constants of the metals and the absorption achieved in the ITO – Metal multilayers. Setting aside the data for Cr, which has previously shown to have quite different optical behaviour to the other metals, there appears to be an inverse trend between the peak mode absorption and κ, with the mode absorption increasing as κ decreases.

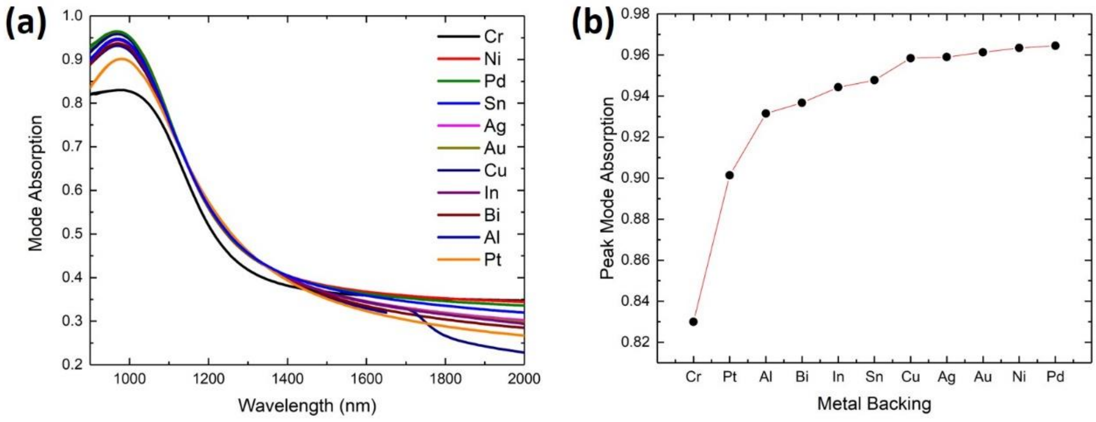

Figure 6.17 (a) Non-radiative ENZ mode absorption as a function of wavelength for a 127 nm ITO film with a 10 nm metal backing of various metals and (b) the peak mode absorption for each metal.

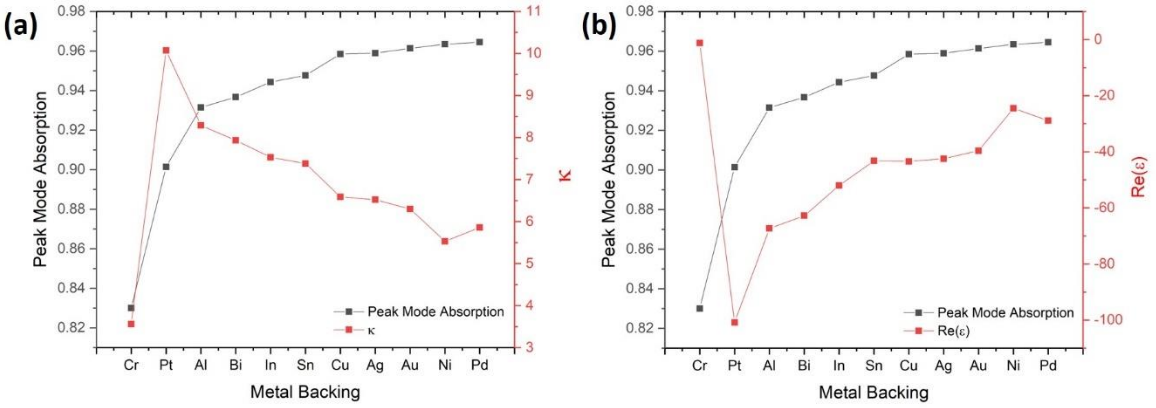

Figure 6.18 (a) Peak non-radiative ENZ mode absorption (black) compared to the imaginary component of the complex refractive index (red) at 980 nm for various metals and (b) compared to the real component of the dielectric permittivity at 980 nm.

The opposite trend is noted between the peak absorption and $\mathrm{Re}(\varepsilon)$, with the mode absorption increasing as the value of $\mathrm{Re}(\varepsilon)$ increases. Surprisingly, both these trends are the inverse to those observed for the peak Ferrell – Berreman mode absorption. While this suggests that Pt is not the ideal choice for achieving enhanced ENZ mode absorption, it remains the best candidate for our structure in achieving overall near-perfect absorption due to the fact that it achieves the highest Ferrell – Berreman mode absorption at lower angles which does not require prism coupling, and also because while achieving one of the lowest ENZ mode absorptions, it still achieves a theoretical value of around 90% which is an extremely large absorption by such thin films.

However, it is important to note that the point of maximum absorption for each ITO – Metal structure can actually be located along a locus of incident angle values depending on the metal backing used. Two approximate expressions to determine the incident angle of perfect absorption, θ_{PA} and the wavelength of perfect absorption, λ_{PA} were derived by Luk et al. who studied and experimentally demonstrated perfect absorption from Glass – ITO – Ag structures. These expressions were

$$\sqrt{\varepsilon_s}\sin\theta_{PA} = \sqrt{\frac{Re(\varepsilon_{ITO})^2 + Im(\varepsilon_{ITO})^2}{Re(\varepsilon_{ITO})}} \tag{6a}$$

$$\frac{2\pi d_{ITO}}{\lambda_{PA}} = \frac{Re(\varepsilon_{ITO})\cos\theta_{PA}}{\sqrt{\varepsilon_s}Im(\varepsilon_{ITO})} \tag{6b}$$

where ε_s is the permittivity of the ambient dielectric substrate and d_{ITO} is thickness of the ITO layer. By rewriting Equation 6a to find an expression for θ_{PA} in terms of the permittivities of the substrate and ITO layer, i.e.

$$\theta_{PA} = \sin^{-1}\left(\frac{1}{\sqrt{\varepsilon_s}}\sqrt{\frac{Re(\varepsilon_{ITO})^2 + Im(\varepsilon_{ITO})^2}{Re(\varepsilon_{ITO})}}\right) \tag{7}$$

the range of incident angles for which perfect absorption is possible could be determined for our ITO – Metal structures.

To calculate the angles at which perfect absorption can occur in our ITO – Metal structures, the permittivity of the superstrate was taken from published data for soda-lime glass [30] and the permittivity of ITO was defined using the Drude model using the same optical constants determined from spectroscopic ellipsometry measurements on the 127 nm 8 – 12 Ω sq^{-1} commercial film. The resulting data is plotted in Figure 6.19.

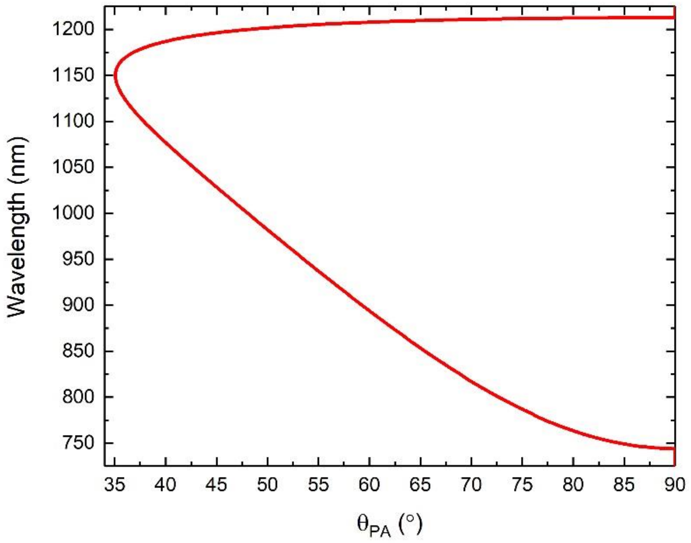

Figure 6.19 Wavelength vs angle of perfect absorption for a 127 nm ITO film with a soda-lime glass superstrate.

This plot shows the locus of incident angle values at which perfect absorption can occur for each wavelength of near-perfect absorption. For each sample, the point of highest absorption can occur anywhere along this locus. The data agrees very well with the simulations in Figure 6.14 and Figure 6.15, particularly the shift to shorter wavelengths of the NPA with increased incident angle. However, one drawback of this calculation is that the precise angle and wavelength at which perfect absorption occurs for a given sample cannot be determined with absolute precision as of yet, only this locus of potential values can be determined. While Luk et al. were able to determine their point of perfect absorption with precision for their Glass – ITO – Ag structures, they considered only a single metal backing of significantly larger thickness of 100 nm than considered in this work, whereas here we consider the effects of various metal backing of much thinner thickness of 10 nm. While we cannot determine with precision the exact point of highest absorption, the novelty in this research lies in the discovery that NPA of values greater than 90% according to simulation and greater than 85% experimentally can be achieved from practically any metal of just 10 nm.

For comparison with the absorption data from the ITO – Metal structures, T-Matrix simulations were also carried out for each of the metal films alone, excited from a glass substrate. The angle-resolved absorption for one these films alone, Pt is presented in Figure 6.21. The purpose of this simulation is to demonstrate that the absorption achieved by Pt is homogenous across the spectral range without any high absorbing features. All metals studied exhibited similar homogeneity of the absorption across the spectral range. An increase in absorption is noted, however about 80° as would be expected, but this absorption is again homogenous across the spectral range. This demonstrates clearly that the high absorption achieved from the ITO – Metal structures is not simply a result of the metal, but rather a coupling of the physics between metals and the ENZ behaviour of ITO. The absorption as a function of wavelength is presented for all metals at an incident angle of 39° and 55° respectively in Figure 6.22(a) and (b). As shown, the highest absorption is achieved by the metals with lowest κ-value and the absorption decreases progressively for metals with gradually increasing κ-value down to Al which has the highest. While this result at first seemed counterintuitive as it would be expected that the absorption from a metal film would increase linearly with κ-value consistent with the absorption coefficient, α of each metal which is given by

$$\alpha = \frac{4\pi\kappa}{\lambda} \tag{8}$$

where λ is the incident wavelength. However, in reality the absorption from a metal is also dependent on how much light is reflected at the initial superstrate – metal interface and the absorption coefficient then tells us how much of the light that isn't reflected will be absorbed. To examine how much light would be expected to be reflected from the surface of metals of various

κ-value we can consider a simple case of the Fresnel equation for normal incidence and an air superstrate. The resulting reflection can be calculated using the expression

$$R = \left|\frac{(n-1)^2 + \kappa^2}{(n+1)^2 + \kappa^2}\right| \tag{9}$$

where n and κ are the real and imaginary components of the complex refractive index of the hypothetical metal in question. The output of Equation 9 was thus plotted as a function of κ between 0 and 15 (consistent with the ranges of the actual metals considered in this work) and for values of n in the range 0 – 4 (again consistent with the ranges of the actual metals considered). The resulting plots are presented in Figure 6.20.

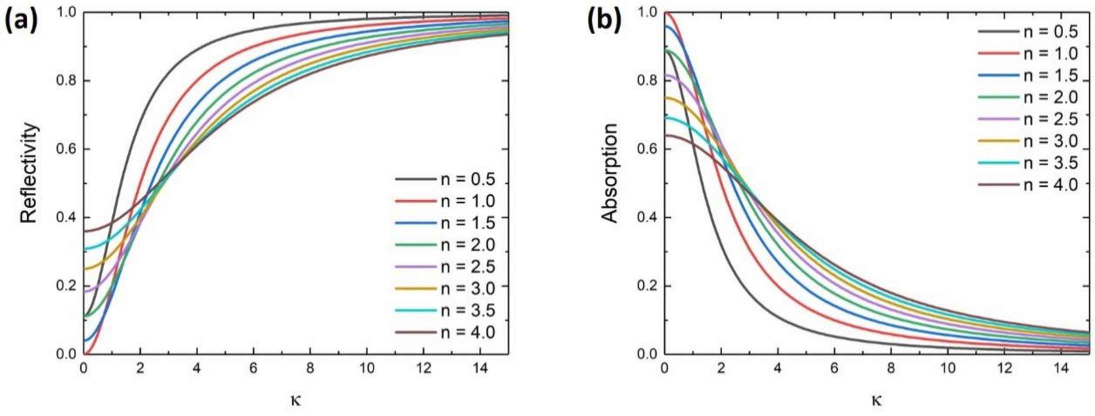

Figure 6.20 Reflectivity (a) calculated from Equation 9 for a range of κ-values and a range of n-values and absorption (b) calculated assuming there is no transmission and the absorption can be approximated as A = 1 – R.

As shown, the reflectivity increases as a function of κ-value and assuming that transmission is zero (as is the case for a sufficiently thick metal, the absorption also decreases as a function of κ.

This data demonstrates that the metals which achieve the highest free-standing absorption also exhibit the lowest reflectivity and hence exhibit the least absorption when coupled with an ITO film. This suggests that the metals with the highest κ-values, whilst having the highest absorption coefficients increase reflectivity back into the ITO layer of the ITO – Metal structures which leads to further absorption by exciting the Ferrell – Berreman and non-radiative ENZ modes once again.

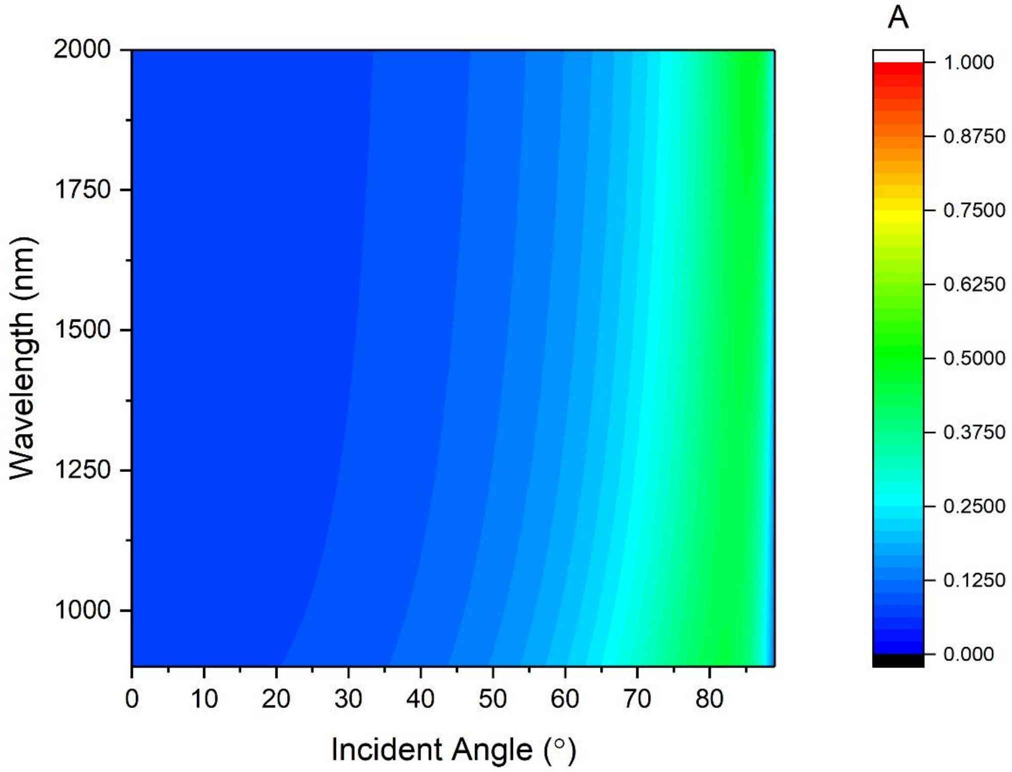

Figure 6.21 Broadspectrum angle-resolved absorption for 10 nm metal films Pt. This simulation was carried out for a semi-infinite glass superstrate and a semi-infinite air substrate.

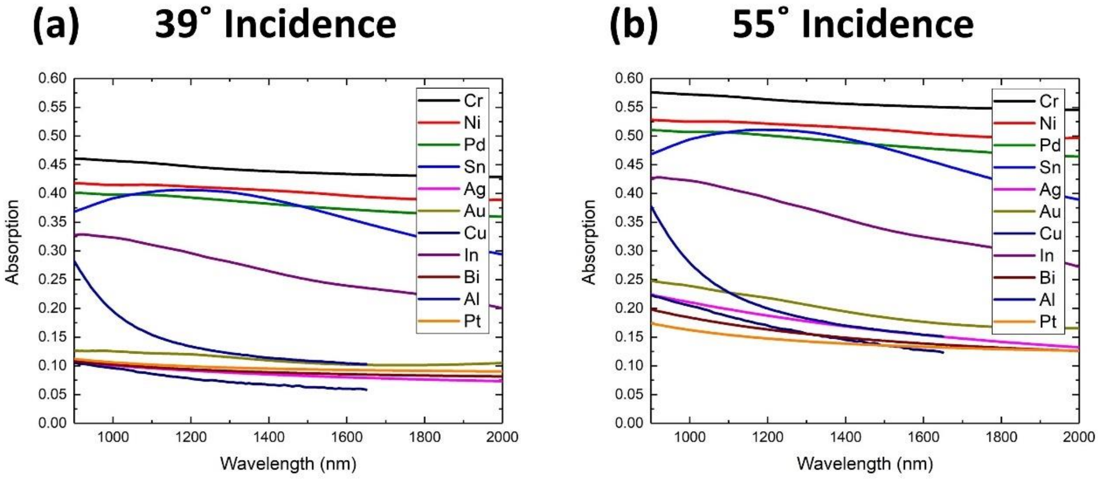

Figure 6.22 Absorption as a function of wavelength for various 10 nm metal films excited from glass at an incident angle of (a) 39˚ and (b) 55˚. These angles correspond to the angles of incidence used for the analysing the Ferrell – Berreman and ENZ modes respectively in the ITO – Metal structures.

6.3.4 Thickness Dependence of Metal Backing on Non-Radiative ENZ Mode Absorption

COMSOL FEM simulations were again carried out on the structure depicted in Figure 6.4, but this time at an incident angle of 55° and a wavelength of 1060 nm. The optical properties of the 127 nm ITO layer were again defined by a Drude model using the Drude parameters determined from spectroscopic ellipsometry and presented in Chapter 3 and the optical constants of the various metals were taken from the COMSOL library and originate from the publications cited in Section 6.3. A parametric sweep of the metal backing thickness was again carried out between 1 nm and 130 nm with increments of 1 nm. The peak mode absorption and reflection as a function of the metal backing thickness were calculated and are presented in Figure 6.24(a) and (b) respectively. Once again, an increase in mode absorption with increasing metal backing thickness is observed, however an interesting feature present in all profiles, except that of Cr, is the presence of an absorption peak at thicknesses below 20 nm. The presence of this peak is attributed to the excitation of an insulator – metal – insulator mode at the ITO – metal and metal – air interfaces. When light above the critical angle is incident on the boundary between the ITO and metal layers, a long-range surface plasmon polariton is excited at the boundary as shown represented in Figure 6.23 and an evanescent wave that decays exponentially with distance from the metal surface is setup in the metal. If the metal is sufficiently thin that the evanescent wave has not fully decayed across the thickness of the film, another surface wave can be induced at the lower metal – air boundary.

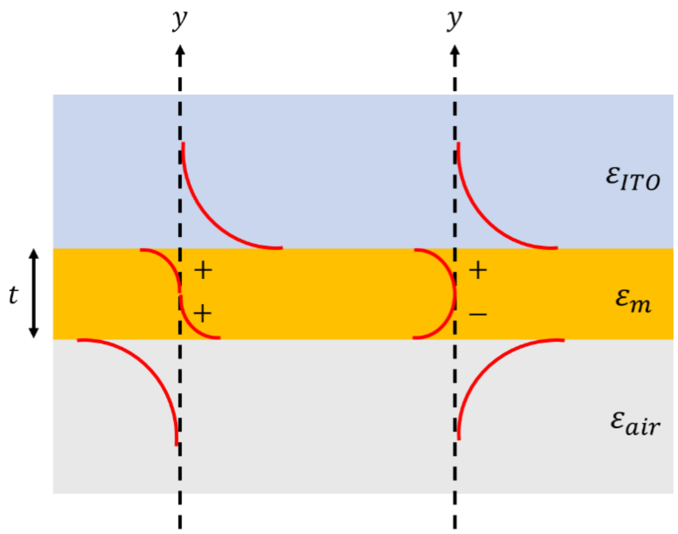

Figure 6.23 Schematic representation of the excitation of antisymmetric and symmetric bound surface plasmon polariton modes in an insulator – metal – insulator structure. [31]

If the metal layer is thin enough, these two surface waves can couple together with the ENZ mode of ITO to achieve sizeable enhancement of the absorption. Figure 6.24(c) presents a comparison of the peak mode absorption of each metal and the thickness at which the absorption maximum is achieved for each metal. There appears to be an interesting inverse correlation between the peak absorption and the thickness at which this absorption occurs. This is likely due to the fact that the surface waves on the upper and lower interfaces of the metal layer can couple to each other better in thinner metal films resulting in a greater current density in the film and hence absorption.

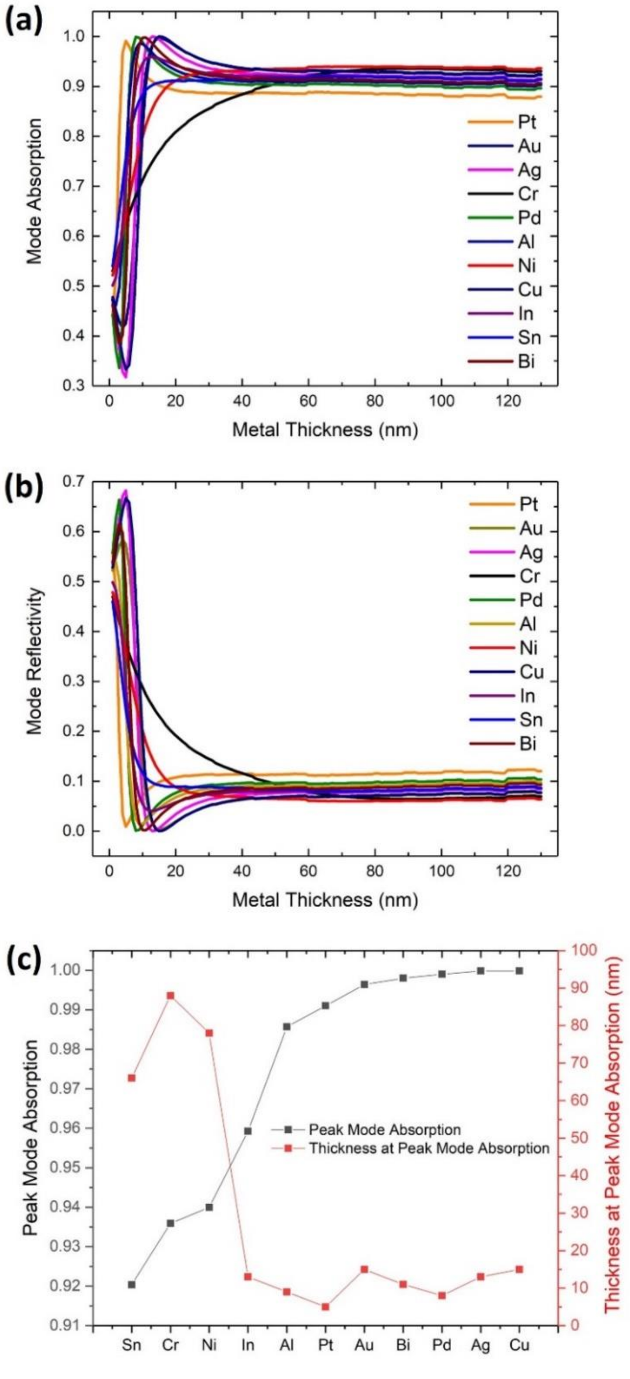

Figure 6.24 (a) Non-radiative ENZ mode absorption at 55˚ incidence and a wavelength of 1060 nm as a function of metal backing thickness for various metals, (b) the reflectivity corresponding thickness dependent reflectivity, and (c) a comparison of peak mode absorption (black) and the thickness at which the peak mode absorption is achieved (red) for each metal.

6.3.5 Insulator – Metal – Insulator Modes in ITO – Metal Multilayer Films

As mentioned in the previous section, if the metal layer in the ITO – metal multilayer structures is sufficiently thin that the evanescent wave in the metal does not fully decay across the thickness, a second surface wave, a long-range surface plasmon polariton, can be excited at the lower metal – air interface.

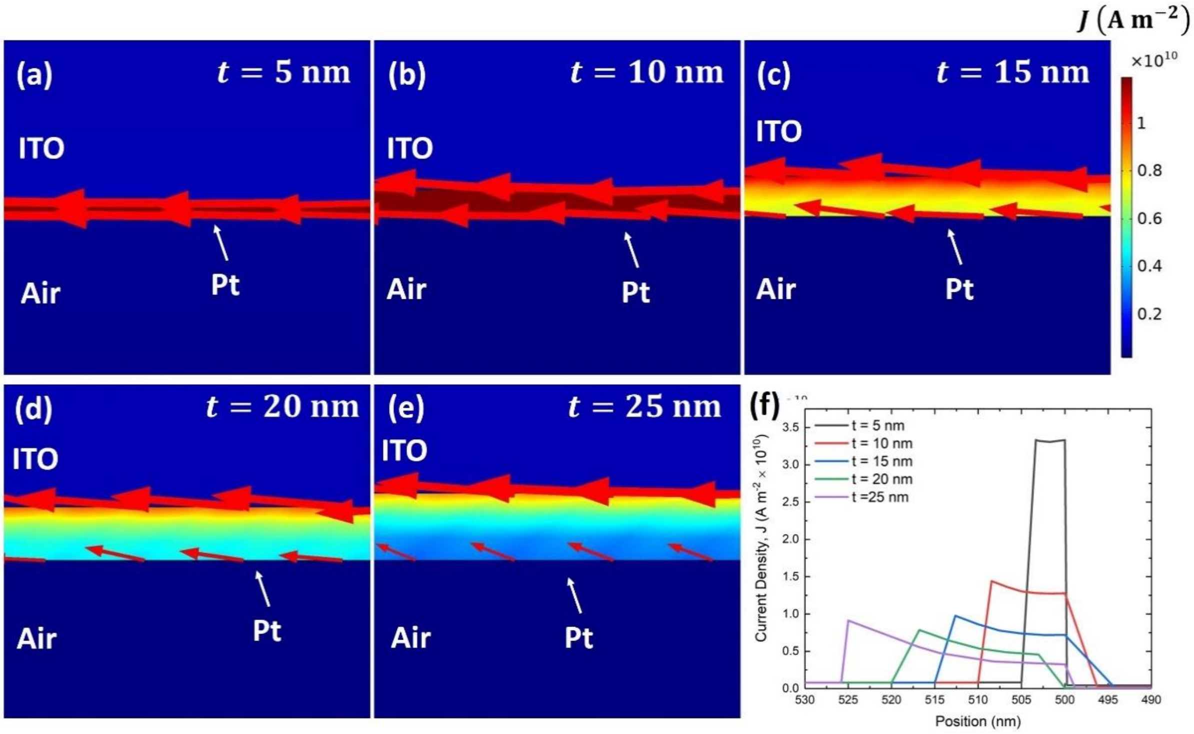

Figure 6.25 (a – e) 2D diagram displaying the norm of the current density in the Pt layer of an ITO – Pt multilayer film. The arrows on the upper and lower boundaries display the current density vector and (f) the current density as a function of position about the Pt layer of the ITO – Pt structure. These simulations were carried out at 1060 nm and 55° incidence.

If the metal layer is also sufficiently thin, these two surface waves can couple together, resulting in a large current density in the metal layer and at its boundaries. Figure 6.25(a – e) presents a 2D map of the COMSOL FEM simulations carried out to calculate the current density in the metal backing layer. As shown, when the metal is very thin (around 5 – 10 nm) as in (a) and (b), the norm of the current charge density, $\vec{\mathrm{J}} = \sqrt{\overrightarrow{\mathrm{J}_\mathrm{x}^2} + \overrightarrow{\mathrm{J}_\mathrm{y}^2}}$ where $\overrightarrow{\mathrm{J}_\mathrm{x}}$ and $\overrightarrow{\mathrm{J}_\mathrm{y}}$ are the x- and y-components of the current density, appears almost uniform across the Pt layer with a value above 1×10^{10} A m^{-2}. The red arrows at the upper and lower boundaries in each image represents the current density as a vector and the length and thickness of the arrows are proportional to the magnitude of the vector. As the Pt layer becomes thicker in (c – d), a gradient becomes apparent in the Pt layer. In the thinner Pt layers, the current density vector on both sides appear almost identical in magnitude, however as the film becomes thicker, the lower vector has a lower magnitude, consistent with the explanation than the thinner samples allow the light to more easily penetrate to the lower boundary and thus exciting a surface wave. This wave can then couple to the upper surface wave causing enhanced absorption. This is further evidenced by Figure 6.25(f) which presents the current density norm across the length of the ITO – Pt – Air structure about the Pt layer. As shown, the thinner Pt layers achieve a significantly higher current density than the thicker Pt films. Also, to be noted is the fact that the current density appears to decay slowly through the thickness of the Pt later. A further simulation was carried out for an ITO – Au film to give a fair comparison between metals and to further confirm the results of Figure 6.25. An identical set of simulations using Au are thus presented in Figure 6.26. As shown in Figure 6.26(a – c), the current again appears almost uniform across the thickness of Au films. The reason the current density is higher and more uniform across the 15 nm (c) film is a result of Au having a higher skin depth than Pt and a lower κ value. This allows the light to more easily penetrate to the lower Au – air boundary and excite a surface wave. This is also the reason that the absorption peak for Au in Figure 6.24(a) occurs at a larger value of thickness than for Pt. As the Au film becomes much thicker to between 20 nm – 25 nm in (d) and (e) respectively, a current density gradient is set up across the thickness of the Au layer, and this is further shown in (f) which again shows the magnitude of the current density across the length of the structure.

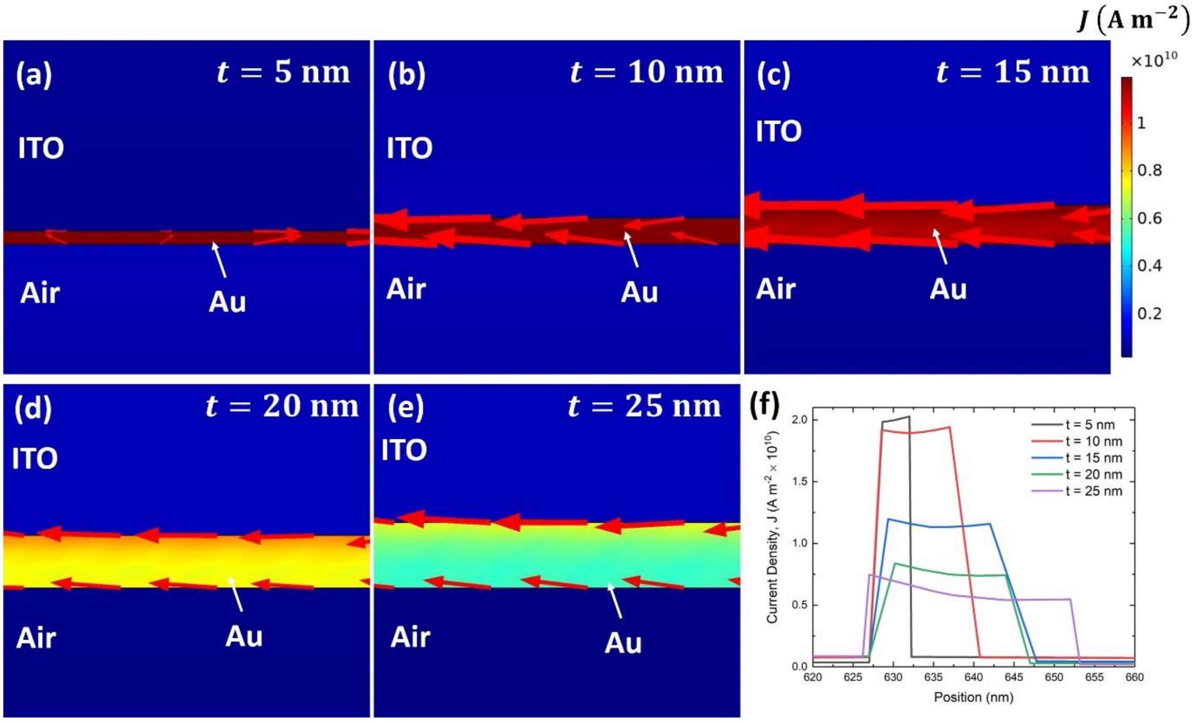

Figure 6.26 (a – e) 2D diagram displaying the norm of the current density in the Au layer of an ITO – Au multilayer film. The arrows on the upper and lower boundaries display the current density vector and (f) the current density as a function of position about the Au layer of the ITO – Au structure. These simulations were carried out 1060 nm and 55° incidence.

A further set of simulations of the current density was carried out for an ITO – Cr structure for comparison. As Cr exhibited the least absorption when exciting both the Ferrell – Berreman mode and non-radiative ENZ modes and had the greatest difference in its optical constants, this simulation was carried out to give further insight into the process behind the mode absorption and role of metals in these structures. Figure 6.27 presents these simulations using a Cr backing. We see in Figure 6.27(a) and (b) and we see that the thinner 5 nm and 10 nm Cr layers exhibit a larger current density than the larger layers of 15 nm – 25 nm in (c – e), however the current density is significantly lower than for a Pt or Au backing in Figure 6.25 and Figure 6.26. This is further demonstrated in Figure 6.27(f) which shows a significantly lower current density across all Cr layers than for Pt and Au and the red arrows representing the current density vector on the upper and lower interfaces of the Cr layer appear roughly the same size suggesting that the current density is almost equal in magnitude. This is consistent with the fact that Cr has a larger skin depth than most of the other metals examined in this chapter and that it has the lowest κ-value. These two parameters together explain why the current density is comparable in magnitude on the upper and lower interfaces as the light can penetrate significantly further into the Cr layer than the high κ-valued Pt and Au layers with smaller skin depths. As these surface waves induced on the metallic backing tend to be long-range in nature, i.e. extending over a large range of frequencies and k-vectors, these results also shine light on an a seemingly unusual result from Chapter 4. In Figure 4.22 of Chapter 4, at longer wavelengths away from the Ferrell – Berreman and ENZ mode resonances, there is an inverse relationship between metal backing thickness and absorption.

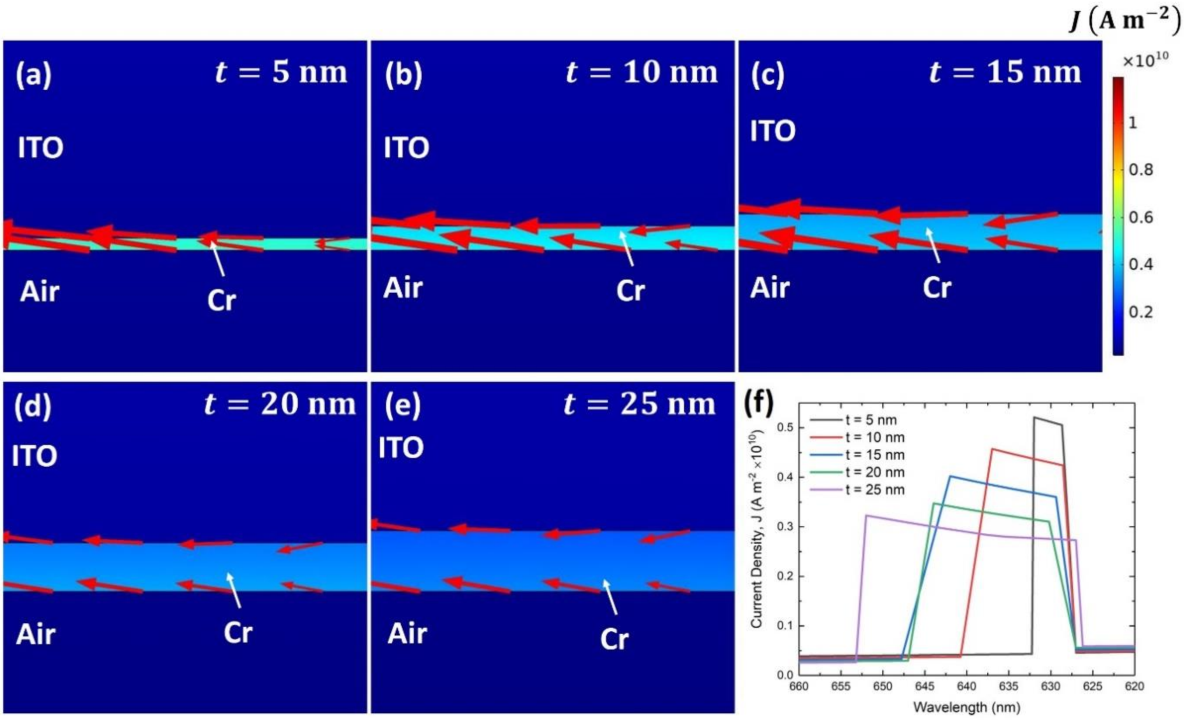

Figure 6.27 (a – e) 2D diagram displaying the norm of the current density in the Pt layer of an ITO – Cr multilayer film. The arrows on the upper and lower boundaries display the current density vector and (f) the current density as a function of position about the Cr layer of the ITO – Cr structure. These simulations were carried out 1060 nm and 55˚ incidence.

This can be attributed to the fact that there is better coupling, and hence better absorption between these surface waves when the metal layer is thinner. As the metal backing layer becomes thicker, the absorption in the off-resonance region decreases as a result of reduced coupling between the surface waves at the upper and lower interfaces as a result of the increased distance between them.

Figure 6.28, Figure 6.29, and Figure 6.30 present identical COMSOL FEM simulations of the current density norm of films of Pt, Au, and Cr respectively of thicknesses 5 nm – 25 nm excited from just a glass superstrate and without an ITO layer. In these cases, we again see a very high current density for thinner films of about 5 nm – 15 nm, and the presence of a current density gradient for thicker films of 20 nm – 25 nm. The red arrows again represent the current density vector and their thickness and length are proportional to the magnitude of the vector. For Pt and Au these vectors appear to have greater magnitude at the upper interface for the thicker samples, and for Cr they appear to have the same magnitude even at 25 nm. This is again a result of the skin depth and κ-value of the films as discussed above. Furthermore, the in part (f) of each figure, the current density is once again plotted along the vertical cross section of the multilayer structure and a clear and rapid increase of the current density is observed across the metal layer. This is attributed to the excitation of an IMI mode as before. However, when compared to their corresponding figures with the ITO layer included in Figure 6.25, Figure 6.26, and Figure 6.27, we can see that the current density in the metal layer is higher than when the ITO layer is included.

This is simply due to the absence of the 127 nm ITO layer which causes significant absorption of light, thus a great intensity of light is incident on the metal films in this case. This data clearly shows that the increased absorption as a result of the metal layer is not simply due to increased reflectivity back into the ITO layer of the ITO – Metal structures, but also due to the excitation of long-range surface plasmon polariton modes. The excitation of these IMI modes coupled with the Ferrell – Berreman and ENZ mode absorptions is what leads near-perfect absorption in these ITO – Metal structures.

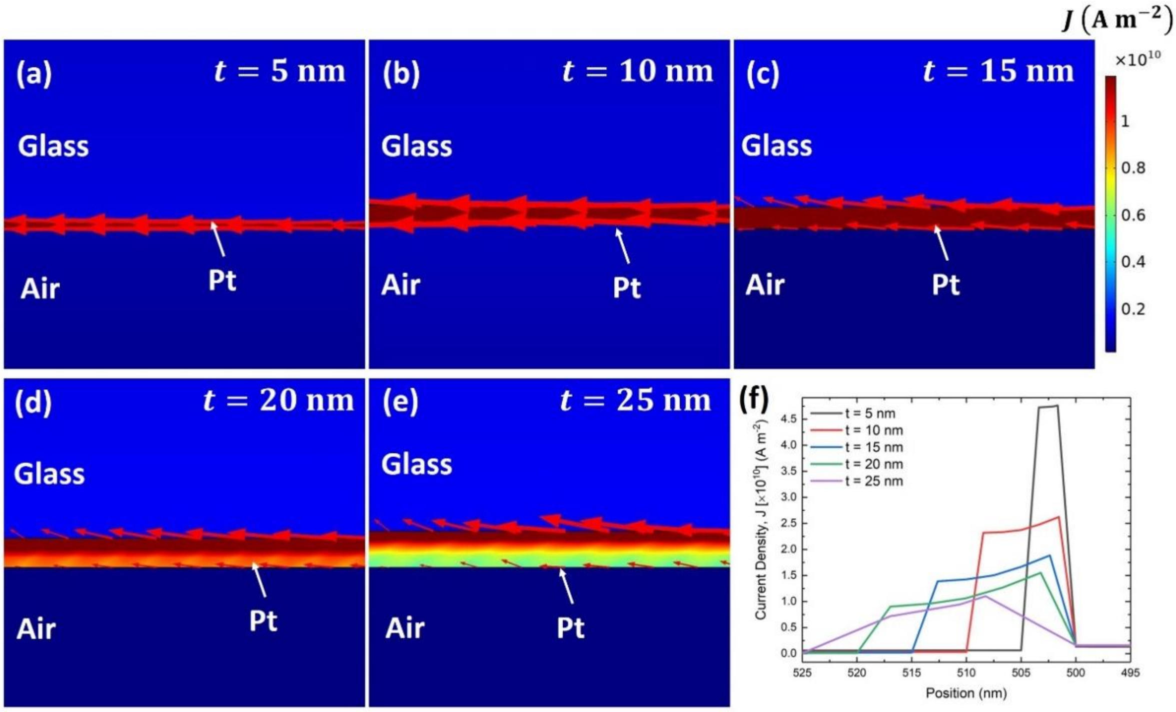

Figure 6.28 (a – e) 2D diagram displaying the norm of the current density in the Pt layer of a Glass – Pt multilayer film. The arrows on the upper and lower boundaries display the current density vector and (f) the current density as a function of position about the Pt layer of the Glass – Pt structure. These simulations were carried out 1060 nm and 55˚ incidence.

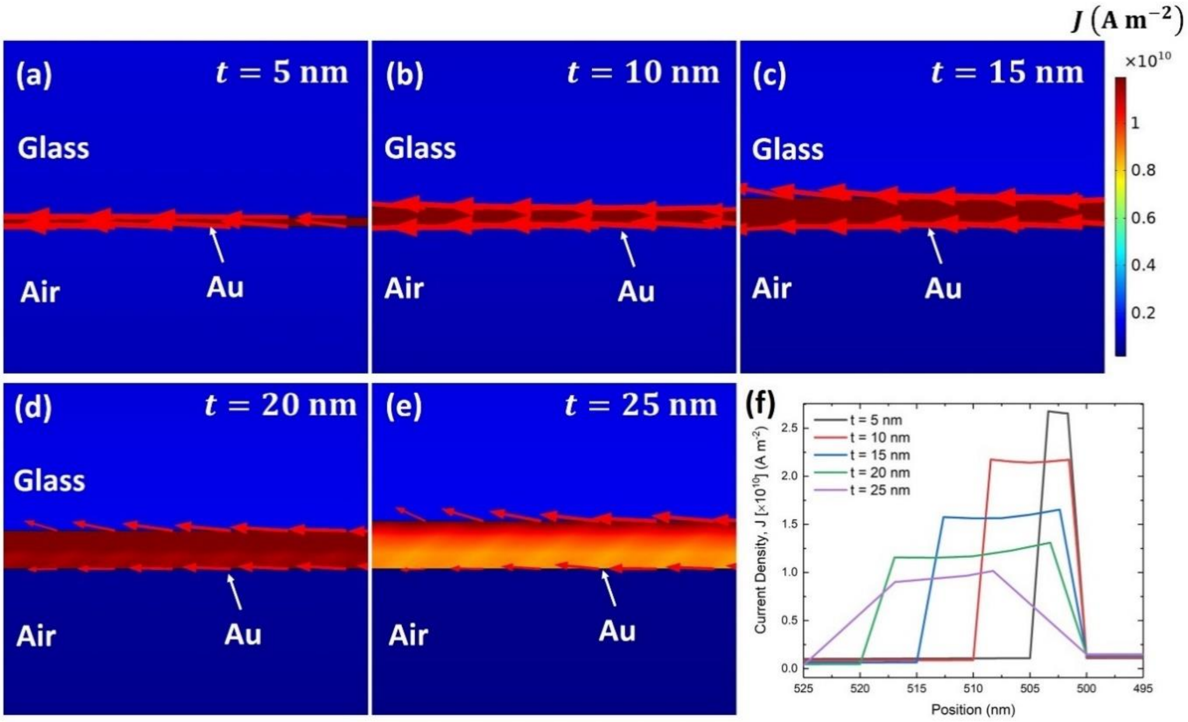

Figure 6.29 (a – e) 2D diagram displaying the norm of the current density in the Au layer of a Glass – Au multilayer film. The arrows on the upper and lower boundaries display the current density vector and (f) the current density as a function of position about the Au layer of the Glass – Au structure. These simulations were carried out 1060 nm and 55˚ incidence.

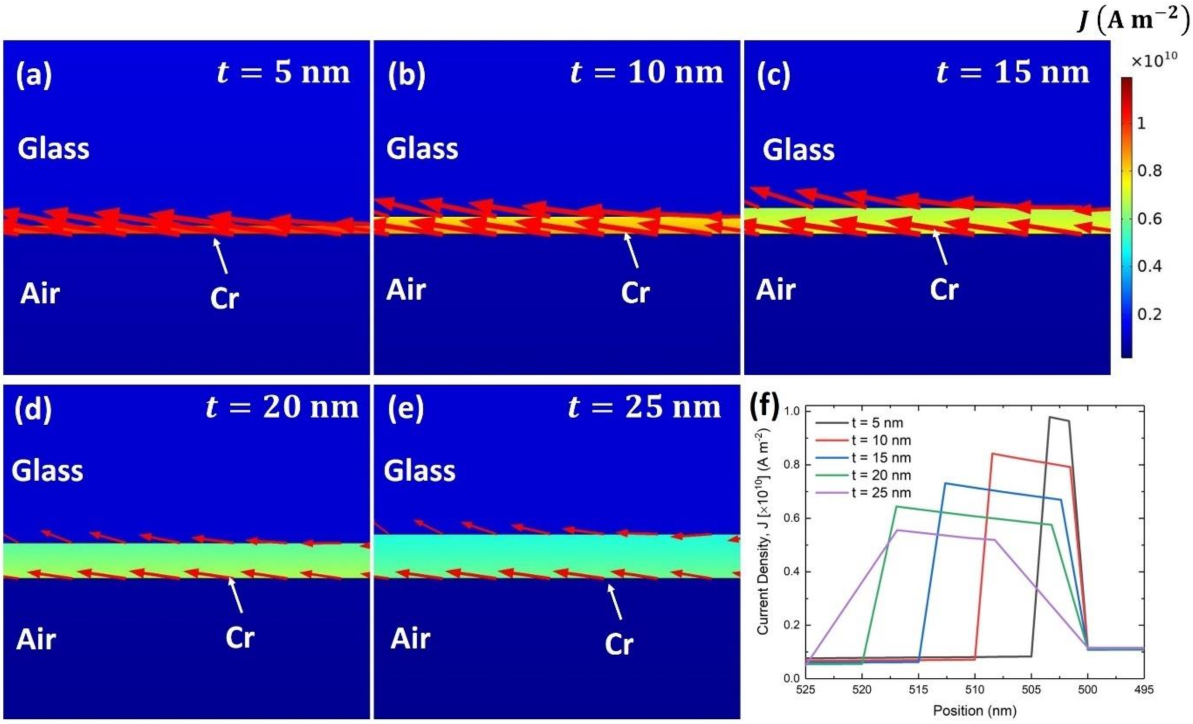

Figure 6.30 (a – e) 2D diagram displaying the norm of the current density in the Cr layer of a Glass – Cr multilayer film. The arrows on the upper and lower boundaries display the current density vector and (f) the current density as a function of position about the Cr layer of the Glass – Cr structure. These simulations were carried out 1060 nm and 55˚ incidence.

While ITO is sometimes described as having “metallic” behaviour above its ENZ wavelength, particularly its reflectivity, it is in reality very different from a metal and thus in these structures, and the IMI structures discussed in Chapter 6 it can be considered to behave more like an insulator relative to the metal. As shown in Figure 2.4 of Chapter 2, the condition to have a surface plasmon polariton at the boundary between a metal and insulator is $\varepsilon_m' < -\varepsilon_d'$, i.e. the real component of the permittivity of the metal must be less than that of the insulating dielectric and the frequency at which $\varepsilon_m' = -\varepsilon_d$ is the surface plasmon frequency. Figure 6.31 presents the parameter $-\varepsilon_{ITO}'$ for ITO, where the dash represents the real component, compared to the real component of the permittivity of Pt, ε_{Pt}'. As shown, the permittivity of Pt is significantly lower than $-\varepsilon_{ITO}'$, satisfying the necessary condition for a bound surface plasmon to exist at the interface between the two media. However, the wavelength at which $\varepsilon_{Pt}'(\lambda) = -\varepsilon_{ITO}(\lambda)$, i.e. the plasma wavelength lies outside the range of available data for ITO.

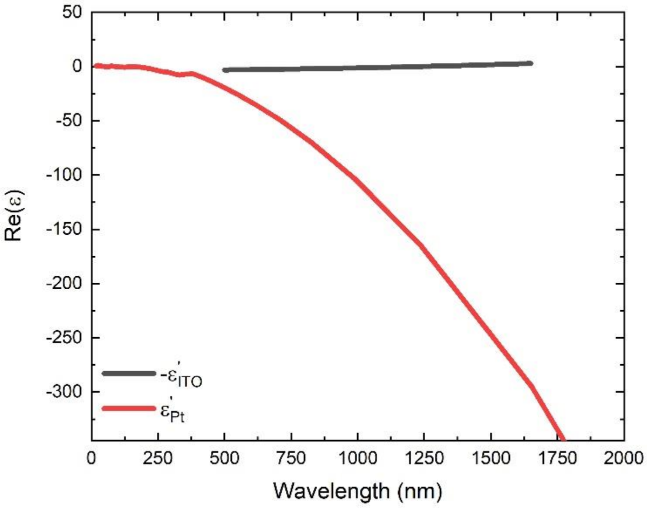

Figure 6.31 A comparison of the $-\varepsilon_{ITO}'$ (black) compared to ε_{Pt}' (red). The wavelength at which $\varepsilon_{Pt}' = -\varepsilon_{ITO}'$ is outside the range of available data for ITO.

6.4 Conclusion

In this chapter, we extended the work in achieving near-perfect absorption discussed in Chapter 4 by examining the role of the metal backing in the ITO – Metal ENZ structures. We theoretically, by means of T-Matrix simulations and COMSOL FEM simulations, provided the first study of the effects of various metal backings on the absorption of the Ferrell – Berreman and non-radiative ENZ modes. We determined that the highest absorption of the Ferrell – Berreman mode can be achieved by using Pt as the metal backing, and that the highest absorption of the ENZ mode could be achieved by using Pd. However, considering that the ENZ mode absorption achieved by Pt is 90%, we conclude that the best choice of metal backing overall is Pt due its extremely high absorption below the light line and its significantly large absorption above the light line also. As Au and Ag are typically chosen as metal backings for ITO and other ENZ materials, the discovery of Pt as a better backing is a significantly advantageous result for future studies of ENZ behaviour and perfect absorption. Furthermore, we provide the first study of the effects of the metal backing thickness for various metals in the ITO – Metal structure. It was found that the Ferrell – Berreman mode absorption increased asymptotically with increased thickness of the metal backing and that all metals achieved a plateau value of absorption above a certain thickness related to the skin depth and κ-values. Pt was shown to achieve its plateau value for much thinner values than all other metals, and that Cr, having a larger skin depth and lower κ-value achieved its plateau at much larger thicknesses. A somewhat similar trend was also noted for the ENZ mode absorption, as increased thickness lead to rapidly increasing absorption until finally the absorption reaches a plateau value. However, an absorption peak as a function of thickness was noted at values below 20 nm. In this case, the absorption peak at lower thicknesses was a result of exciting long-range surface plasmon polaritons on the upper and lower metal boundaries which could couple together if the metal layer was sufficiently thin. This was confirmed by calculating the current density norm as a function of thickness for the ITO – Metal structures. Finally, in both the Ferrell – Berreman mode and non-radiative ENZ modes the peak absorption at the NPA wavelength was found to correlate with the imaginary component of the refractive index, κ and the real component of the complex permittivity, Re(ε). By now understanding the role of the metallic backing in achieving NPA and the ability to locally fabricate ITO for ENZ applications (discussed in Chapter 5) many avenues of research have now been opened for future work. Particularly, structures composed of high-quality ITO and various metal layers can be produced. In Chapter 8, we will discuss the design of a simple Metal – ITO – Metal structure capable of achieving enhanced absorption throughout the near-infrared, with NPA about the ENZ region. Such structures would be ideal candidates for future solar-cell technology.

References

[1] T. Y. Kim, M. A. Badsha, J. Yoon, S. Y. Lee, Y. C. Jun, and C. K. Hwangbo, "General Strategy for Broadband Coherent Perfect Absorption and Multi-wavelength All-optical Switching Based on Epsilon-Near-Zero Multilayer Films," *Sci. Rep.*, vol. 6, 2016.

[2] J. Yoon, M. Zhou, M. A. Badsha, T. Y. Kim, Y. C. Jun, and C. K. Hwangbo, "Broadband Epsilon-Near-Zero Perfect Absorption in the Near-Infrared," *Sci. Rep.*, vol. 5, p. 12788, 2015.

[3] T. S. Luk *et al.*, "Directional perfect absorption using deep subwavelength low-permittivity films," *Phys. Rev. B - Condens. Matter Mater. Phys.*, vol. 90, no. 8, pp. 1–10, 2014.

[4] J. Park *et al.*, "Omnidirectional Near-Unity Absorption in an Ultrathin Planar Semiconductor Layer on a Metal Substrate," *ACS Photonics*, vol. 1, no. 9, 2014.

[5] J. R. Hendrickson *et al.*, "Coupling of Epsilon-Near-Zero Mode to Gap Plasmon Mode for Wideband Perfect Light Absorption," *ACS Photonics*, p. acsphotonics.7b01491,

2018.

[6] L. J. Krayer and J. Kim, “Near-perfect absorption throughout the visible using ultra-thin metal films on index-near-zero substrates,” vol. 9, no. 1, pp. 330–338, 2019.

[7] P. B. Johnson and R. W. Christy, “Optical constants of transition metals,” *Phys. Rev. B*, vol. 9, no. 12, pp. 5056–5070, 1974.

[8] W. S. M. Werner, K. Glantschnig, and C. Ambrosch-Draxl, “Optical constants and inelastic electron-scattering data for 17 elemental metals,” *J. Phys. Chem. Ref. Data*, vol. 38, no. 4, pp. 1013–1092, 2009.

[9] A. I. Golovashkin and G. P. Motulevich, “Optical and electrical properties of tin,” *Sov. Phys. JETP*, vol. 19, no. 2, pp. 310–317, 1964.

[10] K. M. McPeak *et al.*, “Plasmonic films can easily be better: Rules and recipes,” *ACS Photonics*, vol. 2, no. 3, pp. 326–333, 2015.

[11] L. Gao, F. Lemarchand, and M. Lequime, “Refractive index determination of SiO2 layer in the UV/Vis/NIR range: spectrophotometric reverse engineering on single and bi-layer designs,” *J. Eur. Opt. Soc. Publ.*, vol. 8, 2013.

[12] A. I. Golovashkin, I. S. Levchenko, G. P. Motulevich, and A. A. Shubin, “Optical properties of indium,” *Sov. Phys. JETP*, vol. 24, no. 6, pp. 1093–1100, 1967.

[13] S. Campione, I. Kim, D. De Ceglia, G. A. Keeler, and T. S. Luk, “Experimental verification of epsilon-near-zero plasmon polariton modes in degenerately doped semiconductor nanolayers,” *Opt. Express*, vol. 24, no. 16, pp. 18782–18789, 2016.

[14] D. Barchiesi and T. Grosges, “Fitting the optical constants of gold, silver, chromium, titanium, and aluminum in the visible bandwidth,” *J. Nanophotonics*, vol. 8, no. 1, pp. 1–17, Jan. 2014.

[15] N. C. Constantinou and M. G. Cottam, “Bulk and surface plasmon modes in a superlattice of alternating layered electron gases,” *J. Phys. C Solid State Phys.*, vol. 19, no. 5, p. 739, 1986.

[16] K.-D. Tsuei, E. W. Plummer, A. Liebsch, K. Kempa, and P. Bakshi, “Multipole plasmon modes at a metal surface,” *Phys. Rev. Lett.*, vol. 64, no. 1, p. 44, 1990.

[17] J. Nelayah *et al.*, “Mapping surface plasmons on a single metallic nanoparticle,” *Nat. Phys.*, vol. 3, no. 5, p. 348, 2007.

[18] F. Bello, A. F. Page, A. Pusch, J. M. Hamm, J. F. Donegan, and O. Hess, “Combining ε-Near-Zero Behavior and Stopped Light Energy Bands for Ultra-Low Reflection and Reduced Dispersion of Slow Light,” *Sci. Rep.*, vol. 7, no. 1, p. 8702, 2017.

[19] W. D. Newman, C. L. Cortes, J. Atkinson, S. Pramanik, R. G. DeCorby, and Z. Jacob, “Ferrell–Berreman Modes in Plasmonic Epsilon-near-Zero Media,” *ACS Photonics*, vol. 2, no. 1, pp. 2–7, 2015.

[20] R. Maas, J. Parsons, N. Engheta, and A. Polman, “Experimental realization of an epsilon-near-zero metamaterial at visible wavelengths,” *Nat Phot.*, vol. 7, no. 11, pp. 907–912, 2013.

[21] Y. Li *et al.*, “On-chip zero-index metamaterials,” *Nat Phot.*, vol. 9, no. 11, pp. 738–742, 2015.

[22] P. Moitra, Y. Yang, Z. Anderson, I. I. Kravchenko, D. P. Briggs, and J. Valentine, “Realization of an all-dielectric zero-index optical metamaterial,” *Nat Phot.*, vol. 7, no. 10, pp. 791–795, 2013.

[23] L. Brillouin, "*Wave propagation in periodic structures: electric filters and crystal lattices*," Courier Corporation, 2003.

[24] H. D. Young, R. A. Freedman, T. R. Sandin, and A. L. Ford, "*University Physics*," vol. 9. Addison-Wesley Reading, MA, 1996.

[25] S. Hrabar, I. Krois, I. Bonic, and A. Kiricenko, “Ultra-broadband simultaneous superluminal phase and group velocities in non-Foster epsilon-near-zero metamaterial,” *Appl. Phys. Lett.*, vol. 102, no. 5, p. 54108, 2013.

[26] S. Hrabar, I. Krois, I. Bonic, and A. Kiricenko, “Broadband superluminal effects in ENZ active metamaterial,” in *2011 IEEE International Symposium on Antennas and Propagation (APSURSI)*, 2011, pp. 661–664.

[27] A. Ciattoni, A. Marini, C. Rizza, M. Scalora, and F. Biancalana, “Polariton excitation in epsilon-near-zero slabs: Transient trapping of slow light,” *Phys. Rev. A*, vol. 87, no. 5, p. 53853, 2013.

[28] M. A. Swillam and A. S. Helmy, “Characteristics and applications of rectangular waveguide in sensing, slow light, and negative refraction,” in *Integrated Optics: Devices, Materials, and Technologies XV*, 2011, vol. 7941, p. 794110.

[29] A. Vander Vorst, A. Rosen, and Y. Kotsuka, "*RF/microwave interaction with biological tissues*," vol. 181. Wiley Online Library, 2006.

[30] M. Rubin, “Optical properties of soda lime silica glasses,” *Sol. Energy Mater.*, vol. 12, no. 4, pp. 275–288, 1985.

[31] C. Zhong *et al.*, “Mapping of surface plasmon dispersion in thin Ag–Au layered composite films,” *J. Opt. Soc. Am. B*, vol. 33, no. 4, p. 566, 2016.

Chapter 7: Single and Multiple Light Scattering from Turbid Suspensions of Two-Dimensional Hexagonal Boron Nitride Nanoflakes

7.1 Introduction

In previous chapters we demonstrated the achievement of near-perfect absorption in thin film ITO backed by Pt and other metals. However, a host of 2D materials can potentially be applied to ENZ materials, particularly 2D nanoflakes produced by liquid phase exfoliation (LPE). However, when deposited on solid films, they films tend to form rough and highly-scattering surfaces. Thus, in this this chapter we analyse the scattering of one such material as a potential candidate for coupling with our ITO. In recent years the popularity of two-dimensional nanomaterials has soared due to their unique optical, electronic, and mechanical properties. Graphene, one of the most widely studied 2D materials was first isolated in 2004 [1] and since then the range of 2D materials under investigation has grown dramatically to include transition metal dichalcogenides (TMDs) [2], transition metal oxides such as $TiTaO_5$ [3], MnO_2 [4] , and a myriad of others [5]. 2D materials of various forms have been demonstrated , including metallic [6], semiconducting [7], magnetic [8], semi-metallic [9], insulating [10] and even superconductor phases [11]. Tuneable bandgaps and Fermi levels (and hence absorption), strong light-matter interactions, surface passivity to enable integration in photonic devices and many other properties have made these materials very desirable avenues of investigation. 2D materials have been proposed for novel batteries [12], photodetectors [13], strong composite materials [14], medical devices [15], and photovoltaic cells [16]. Hexagonal boron nitride (h-BN), a semiconducting 2D material with a large bandgap [17] is often considered an isoelectronic analogue to graphene, as shown in the representative structure diagram in Figure 7.1(a).

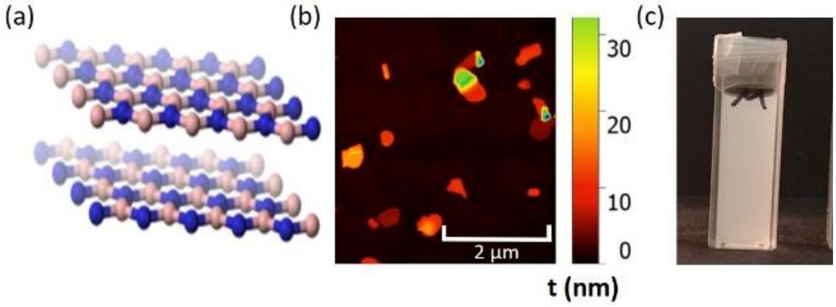

Figure 7.1 (a) Structure of a h-BN nanoflake, with blue atoms representing boron and pink ones representing nitrogen. (b) AFM image of BN nanoflakes before separation by centrifugation. Particles vary over a range of lateral dimensions <2 µm (black) and thicknesses <30 nm (green). The colourmap represents these thicknesses with the smallest thicknesses represented by dark black and red colours and the thickest particles represented by yellows and greens. (c) presents a representative aqueous 2D h-BN suspension of medium particle size particles (~388 nm) after centrifugation with mass concentration is fixed at 1.05 g/cm^3 for all samples showing strong visible light scattering.

h-BN exhibits high thermal and chemical stability and this has led to its frequent use in extreme temperature environments [18]. In industry, h-BN is widely-used as an industrial lubricant, due to its ability to withstand temperatures of up to 900°C and still maintain its lubricity in vacuum [19]. h-BN can be synthesised on mass scales using liquid phase exfoliation (LPE) outlined in Section 7.2.4, and this results in highly anisotropic dispersions of particles with lateral sizes in the 100 nm to 2 μm range and thickness ranging from 5 nm to 30 nm. A representative AFM image of h-BN flakes produced by LPE is presented in Figure 7.1(b). As a result of their extreme aspect ratio (up to 500), 2D nanomaterials are expected to have unique single particle light scattering properties, dependent on the polarisation of incident light and the particle orientation [20]. The particles are further separated by lateral size using a centrifugation technique [21]. It has been shown that this results in narrow size distributions. This presents an ideal opportunity to study single and multiple light scattering of these particles as a function of their size. The resulting dispersions display strong light scattering and turbidity characteristic of multiple light scattering with minimal absorption [22]. The strong light scattering, thermal, and chemical stability of 2D h-BN, suggest that it might be of use as a stable scattering agent for random lasing [23]. Gain in a standard laser occurs in a well-defined cavity at frequencies defined by the modes of the cavity [24]. In a random laser, a highly disordered multiple scattering medium acts as the gain medium in which light can be strongly amplified over a large optical path length [25][26]. These LPE particles are often used as additives in the described applications and their resultant properties are highly dependent on particle size, shape, and distribution. It is therefore essential to have an accurate and scalable method of sizing these particles and understanding how the particle size and shape affects these scattering properties. Light scattering is commonly used in industry as a method of sizing particles, however if the particle cannot be easily approximated as a sphere and are highly non-spherical, as is the case with 2D materials, the sizing results can be very inaccurate.

In this chapter, we study single and multiple light scattering in size selected dispersions of liquid phase exfoliated 2D h-BN and compare them to spherical polystyrene (PS) nanospheres as an ideal spherical reference. The angle and polarization dependence of scattering from the single particle to the multiple particle light scattering regimes were measured and compared with the PS nanospheres of similar sizes. From this we identify suitable theories to describe the scattering in the samples and to try and extract the particles size. Finally, it was demonstrated that 2D h-BN can be used as an effective scattering material for random lasing using Rhodamine B (RhB) as the active medium. However, in order to examine the scattering of light from such 2D materials, we must first understand light scattering theory in general.

7.2 Light Scattering Theory

When an electromagnetic wave is incident on a particle, the oscillating electric field generates an oscillating charge dipole which then radiates. The pattern and spatial distribution of the emitted radiation is heavily dependent on the shape, size, orientation (which is randomised in a dispersion) and refractive index contrast of the particle from the background material. Both static light scattering [27] (SLS) and dynamic light scattering [28] (DLS) are important analytical tools for particle rheology in physical, biological, and pharmaceutical sciences. In SLS the intensity of scattered light is measured as a function of scattering angle and compared with an appropriate model to determine mean particle size and variance. However, these models commonly assume spherical particles and can give inaccurate results for non-spherical particles, particularly those with high aspect ratio [29].

When the particles are well separated, such that they can be considered as a collection of isolated particles, they are said to be in the single particle scattering regime. Mie theory, developed by Gustav Mie in 1908, provides a complete description of the scattering from spherical particles in the single scattering regime which requires only three parameters, the size parameter $\alpha = \frac{2\pi r}{\lambda}$, where r is the diameter of a scattering sphere, λ which is the incident wavelength, and the refractive index contrast $m = \frac{n_p}{n_{bg}}$, where n_p is the refractive index of the particle and n_{bg} is the refractive index of the background medium [30][31]. However, for non-spherical particles, no simple general closed form solution exists, and the light scattering is dependent on particle shape, size, refractive index contrast, orientation and incident polarization [32]. For particles in dispersion, Brownian motion causes random rotation of the particles and the angle averaged scattering properties are often sufficient to determine particle size.

To describe light scattering in an aqueous dispersion of particles, the particle concentration, scattering cross section σ_s [m^2], which determines the magnitude of scattered light from each particle, and the scattering phase function $p(\theta)$ which is a function of scattering angle, θ and determines the angular distribution of the scattered light, must be known. For spherical particles, σ_s [m^2] and $p(\theta)$ have an analytical form as a sum over multipoles [33]. However, for a non-spherical or anisotropic particle these parameters have a complicated dependence on the shape, size, orientation and index contrast of the particle. The Henyey-Greenstein phase function is an approximate expression proposed by Henyey and Greenstein in 1941, which describes the angular distribution of scattered radiation with a single parameter, g, the asymmetry parameter [34].

$$p(\theta) = \frac{1}{4\pi}\frac{1-g^2}{[1+\ g^2+2g\cos\theta]^{\frac{3}{2}}} \tag{1}$$

where g is the weighted average over all scattering angles, $g = \langle\cos\theta\rangle$, $(-1 \leq g \leq 1)$ and describes the amount of forward scattering and backscattering. A value of $g = -1$ corresponds to complete backscattering, $g = 0$ corresponds to isotropic scattering, and $g = 1$ corresponds to entirely forward scattering [35]. The parameter g is tuned to match analytical, experimental measurements or numerical simulations of the real particle phase function.

For a large scattering cross section, or for a high particle concentration, multiple light scattering occurs. The scattering behaviour changes dramatically from the single scattering regime, and in the limit of high particle concentration the scattering is purely diffusive photon transport. A plethora of models and approximations exist to describe multiple scattering, all with their strengths and drawbacks, such as the diffusion approximation [36], the two-stream approximation [37], the four-stream approximation [38], and the scattering transfer matrix method [39]. In this work, the Monte Carlo approach of numerical modelling using the Henyey–Greenstein phase function to model the photon transport in the concentrated dispersions was used. Because the materials used in this work are comparable in size to the incident wavelength (λ = 632.8 nm), the scattering examined lies in the Mie scattering regime. While Mie scattering has been well understood for almost a century, scattering from non-spherical particles remains somewhat more difficult to analyse. However, to understand the latter, we must first examine the former.

7.2.1 Mie Scattering from a Homogenous Sphere

Mie scattering is a particular solution to Maxwell's equations which describes the scattering of electromagnetic plane waves from a homogeneous sphere. There are three main regimes of light scattering, the Rayleigh [40], Mie [41] and Geometric scattering [42] regimes. The three regimes of scattering are distinguished by the value of the size parameter, α which is given by $\frac{\pi D}{\lambda}$, where λ is the incident wavelength, and D is the diameter of the sphere off which the wave is scattering. The three regimes can be neatly categorised as follows:

$\alpha \ll 1$	Rayleigh Scattering Regime	Sphere is much smaller than the wavelength.
$\alpha \approx 1$	Mie Scattering Regime	Sphere approximately equal in size to wavelength.
$\alpha \gg 1$	Geometric Scattering Regime	Sphere is much larger than the wavelength.

In general, the Rayleigh regime, which applies for particles or spheres much smaller than the incident wavelength, breaks down when the diameter of the sphere/particle in question is larger than $\sim\frac{\lambda}{10}$ [43]. A very clear difference is present in the angular scattering profiles between the Rayleigh and Mie regimes. Figure 7.2 shows a representative diagram of this difference. As shown in the Rayleigh regime there is equal probability of forward-scattering and backscattering with a decrease in scattering probability around 90˚ to the incident wave. For the Mie regime, it can be noted that there is a significantly higher proportion of forward-scattering, which increases with increasing sphere diameter approaching the geometric scattering regime.

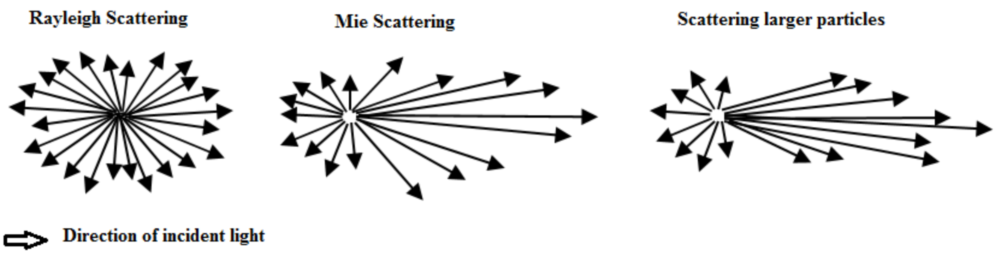

Figure 7.2 Scattering profiles for Rayleigh scattering, Mie scattering and geometrical scattering for larger particles. The arrow length corresponds to the probability of scattering in the given direction.

These scattering phenomena can be simply explained by considering how an electromagnetic wave interacts with particles. Consider a particle much smaller than the wavelength, if a linearly polarised incident plane wave propagating in the $+x$-direction is incident on the particle. Particles much smaller than the incident wavelength become entirely polarised by the incident wave and an oscillating dipole is set up in the direction of the electric field (y-direction), i.e. the wave exhibits constant phase over the entire particle and the particle oscillates in phase with the wave [44]. Since an oscillating dipole never emits in the plane of its oscillation [45], we would thus expect to see no emission in the y-direction. In the case of an unpolarised wave, this phenomenon manifests itself as a dip in the scattering in the y-direction. This phenomenon is regularly used in commercial particle size analysers. However, these commercial setups are only accurate for spherical particles as a sphere is the only three-dimensional shape which can be perfectly described by a single parameter, i.e. the radius. However, a non -spherical particle cannot be so simply described. When non-spherical particles are analysed in these machines, a technique known as the "equivalent sphere method" is used. This works by taking a size-dependent measurement of the particle and approximating the particle as a sphere having the very same property. Typically, the length is the property used but the inability to measure the width and thickness of the particle leads to inaccuracies, particularly for atomically thin two-dimensional materials such as graphene and hexagonal boron nitride (h-BN) nanoflakes. At present there are only two methods to accurately measure the aspect ratio of 2D nanoflakes, atomic force microscopy (AFM) and a technique devised by McCloskey and Coleman which requires access to a spectrophotometer with an integrating sphere [46]. As shown in Figure 7.2, the angular distribution of the scattered intensity is quite characteristic of the scattering regime, and hence should contain some information about the size and/or shape of the scattering particle. The angular distribution of scattered radiation can be understood in terms of a probability distribution function known as the scattering phase function [47]. If the distribution of scattered light is highly dependent on the size and shape of the particle, it follows that the distribution from non-spherical particles must be significantly different and this is what we examine in this chapter by comparing our highly scattering 2D h-BN nanoflakes to an ideal spherical reference of PS nanospheres.

7.2.2 Scattering Phase Functions for Aqueous Suspensions of Spherical Particles

To understand light scattering in aqueous suspensions of highly anisotropic particles it is first necessary to consider how light interacts with ensembles of spherical nanoparticles. Scattering can be broadly defined as the redirection of radiation from one path to another. Consider a single electromagnetic wave incident on a scattering particle which redirects the wave along a new path deviated from the original by a scattering angle, θ. Due to the quantum nature of electromagnetic radiation, the scattering angle of an individual EM wave cannot be pre-determined with absolute certainty; it can be scattered at any angle. We can only determine the probability that it's scattered at a given angle.

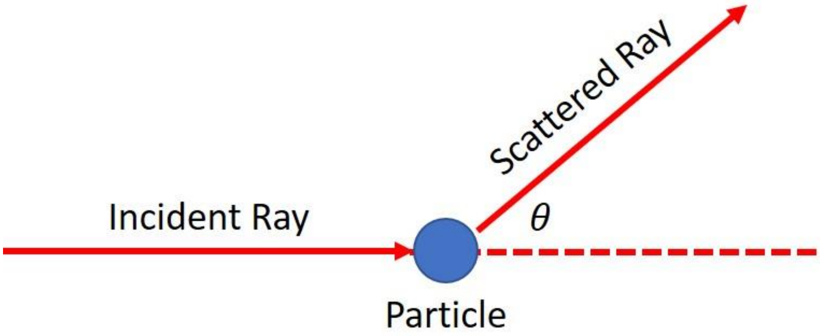

Figure 7.3 Representative diagram of a scattering event. An incident ray is scattered off a particle and redirected along a new path by a scattering angle, θ.

We define a parameter, $p(\theta)$ known as the scattering phase function which is in essence a probability density function which describes the chances of an EM wave being scattered by a particle in any particular direction. The phase function is defined as the radiance, F at a given scattering angle, θ relative to the normalised integral of the scattered intensity over all angles, i.e. [48]

$$p(\theta) = \frac{F(\theta)}{\int_0^{\pi} \sin\theta \, d\theta} \tag{2}$$

Since the phase function describes the scattering of light over all angles the normalisation condition of the phase function must be unity when integrated over a full sphere, i.e. [48]

$$\frac{1}{4\pi}\int_0^{2\pi}\int_0^{\pi} p(\cos\theta)\sin\theta \, d\theta d\varphi = 1 \tag{3}$$

where φ is the azimuthal co-ordinate which can be neglected when dealing with a spherical particle. Several variation and alternate expressions for the phase function exist. Two such variations are considered in this research, the first of which is an expression in terms of Legendre polynomials which are utilised in the models considered later. The phase function can be expressed in terms of Legendre polynomials [27] such that

$$p(\cos\theta) = \sum_{l=0}^{N-1} \beta_n P_n(\cos\theta) \tag{4}$$

where $P_n(\cos\theta)$ are the Legendre polynomials, and β_n are the moments of the phase function given by

$$\beta_n = \frac{2n+1}{2}\int_{-1}^{1} P_n(\cos\theta)p(\cos\theta)d\cos\theta\,. \tag{5}$$

Due to the normalisation condition, the zeroth moment of the phase β_0 will always be unity. Of particular interest, is the first moment of the phase function, β_1 which can be related to the asymmetry parameter, g of the Henyey-Greenstein phase function previously mentioned in Section 7.2.2. The Henyey-Greenstein phase function can also be expressed in terms of Legendre polynomials, i.e. [49]

$$P(\mu) = \sum_{n=1}^{\infty}(2n+1)g^n P_n(\mu) \tag{6}$$

where $\mu = \cos\theta$. The form of the phase function in equation 2 is not particularly useful for numerical calculations such as the Monte Carlo method described later in this work, and thus an accumulated distribution of this phase function is used instead.

$$p(\mu) = \frac{1}{2}\int_{-1}^{\mu}\frac{(1-g^2)d\mu}{[1+g^2-2g\mu]^{\frac{3}{2}}} = \frac{1-g^2}{2g}\left[(1+g^2-2g\mu)^{-\frac{1}{2}}-(1+g^2)^{-1}\right] \tag{7}$$

Given that $P(-1) = 0$ and $P(1) = 1$, the expression can be inverted to give μ as a function of the asymmetry parameter alone, thus allowing the phase function to be calculated.

$$\mu = \frac{1}{2g}\left[1+g^2-\left(\frac{1-g^2}{1+gc}\right)^2\right] \tag{8}$$

where c is defined as $c = 2P - 1$.

7.2.3 Asymmetry Parameter for Aqueous Suspensions of Spherical Particles

To theoretically calculate the scattering phase function of the PS nanosphere samples, a Matlab code based on the code originally published by Craig Bohren and Donald Huffman in the Appendix of their 1983 book "Absorption and Scattering of Light by Small Particles" was used to calculate the asymmetry parameter of the aqueous PS nanosphere suspensions. The code utilises the refractive index of the PS nanospheres (n = 1.61), the refractive index of the water in which they were dispersed (n = 1.33), the particle diameter, the mass concentration (c = 1.05 g cm^{-3}), and the incident wavelength (632.8 nm) to calculate the asymmetry parameter. Figure 7.4 shows the calculated asymmetry parameter for PS nanospheres as a function of nanosphere radius. This asymmetry parameter was then used to calculate the scattering phase function of these suspensions.

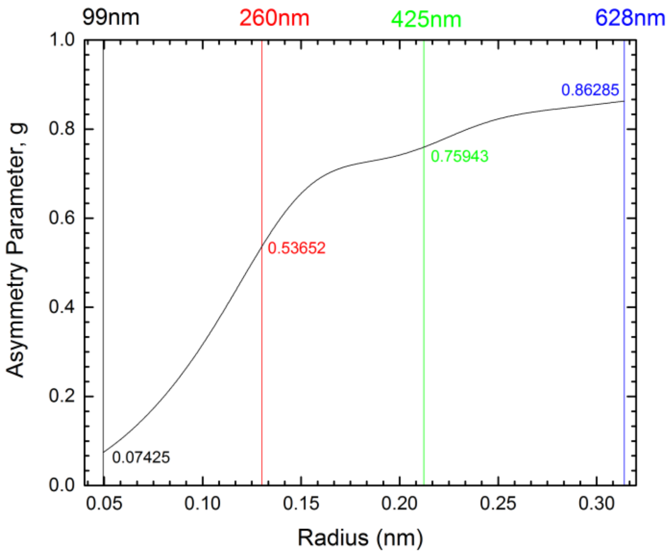

Figure 7.4 Asymmetry parameter of an ensemble of PS nanosphere (n = 1.61) of mass concentration 1.05 g cm^{-3} dispersed in water (n = 1.33) for an incident wavelength of 632.8 nm as a function of nanosphere radius. The coloured vertical lines and the marks values are the asymmetry parameters for each of the purchased PS nanosphere samples.

These scattering phase functions are presented in Figure 7.5 for nanosphere diameters of 99 nm (a), 260 nm (b), 425 nm (c), and 628 nm (d) for TE and TM incident polarisations at 632.8 nm. The trend is consistent with what would be expected of scattering from particles with increasing particle diameter. In Figure 7.5(a) the 99 nm diameter spheres are significantly smaller than the incident wavelength and thus behave more in line with what would be expected of Rayleigh scattering, particularly the lack of scattering for TM polarisation at 90˚ and 270˚. This is explained by the fact that the incident electric field sets up an oscillating electric dipole and an oscillating dipole never emits in the plane of its oscillation hence the lack of scattering at these angles for TM polarisation. As the particles progressively become bigger in Figure 7.5(b – c) and hence more comparable to the size of the wavelength of the incident light, the proportion of forward scattering greatly increases, with no backscattering expected. At larger diameters, the TE polarised light scatters forward over a reduced angular range. The graphs in Figure 7.5 are plotted to maximise the visibility of the scattering trends. To highlight the difference in the magnitude of the scattering phase functions with increasing particle diameter, the data is replotted in Figure 7.6

for (a) TE and (b) TM polarisation. The progressive increase in the proportion of forward scattering with increasing particle diameter becomes more apparent for both polarisations.

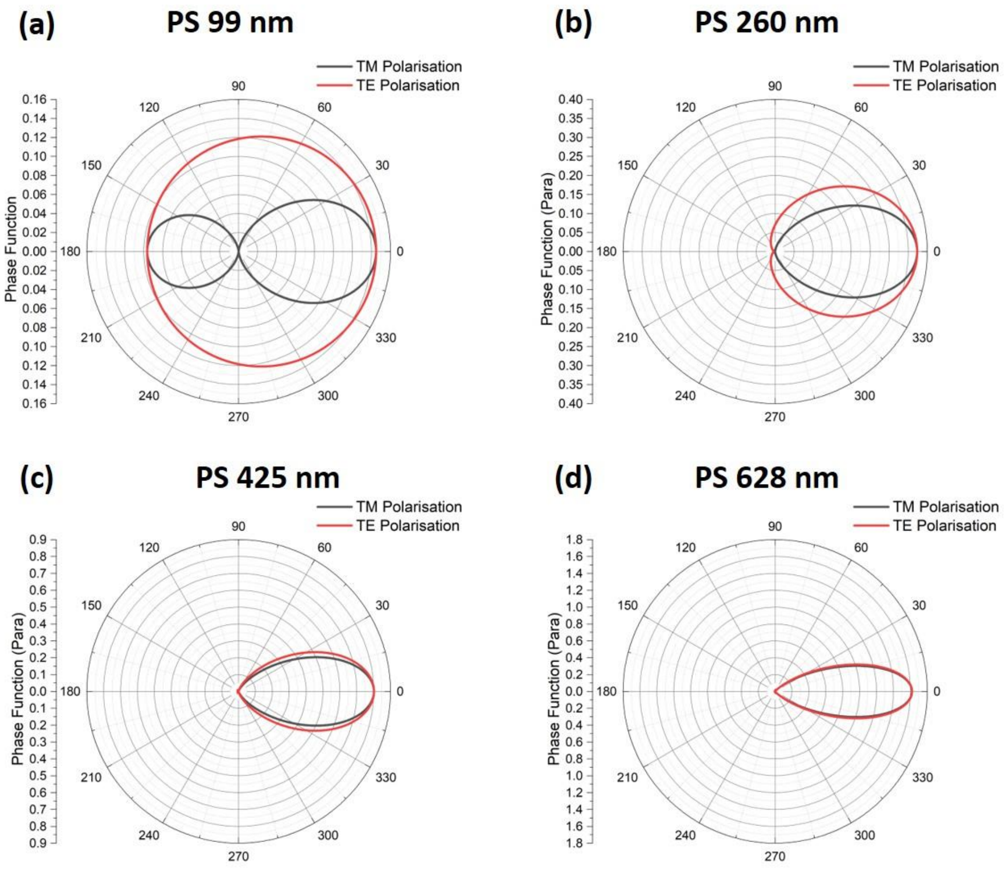

Figure 7.5 Calculated scattering phase functions for PS nanospheres in water (1.05 g cm^{-1}) of diameters (a) 99 nm, (b) 260 nm, (c) 425 nm, and (d) 628 nm for an incident wavelength of 632.8 nm.

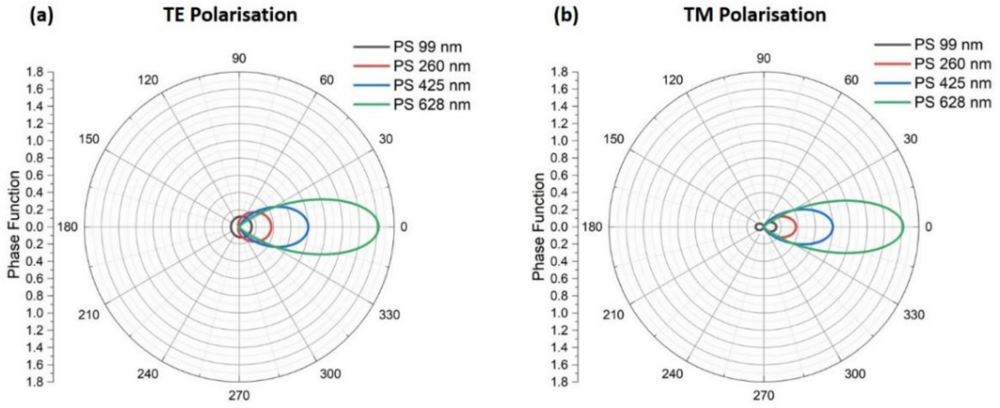

Figure 7.6 Calculated scattering phase functions for PS nanospheres in water (1.05 g cm^{-1}) of diameters 99 nm, 260 nm, 425 nm, and 628 nm for (a) TE and (b) TM polarised light with an incident wavelength of 632.8 nm.

From both Figure 7.5 and Figure 7.6, it is clear that there exists a diameter-dependent trend of the scattering phase function. However, while these are relatively easy to calculate for perfect spherical particles, it is a much more difficult task to calculate these for non-spherical particles, and particularly high-aspect 2D materials such as h-BN.

7.2.4 Liquid Phase Exfoliation of Hexagonal Boron Nitride Nanoflakes

2D hexagonal boron nitride (h-BN) nanoflakes were produced by liquid phase exfoliation (LPE) as outlined by Coleman *et al.* [5][23][22] The starting material was boron nitride powder which was pre-treated by sonication using a sonic tip for two hours in deionised water in order to remove any impurities in the powder. The dispersion was then centrifuged for one hour at 4.5 krpm (2150g) and the supernatant decanted. The remaining sediment was dried at 60˚C. This pre-treated boron nitride was then sonicated in a mixture of surfactant and deionised water (2 gL^{-1}) in an 80 mL metal cup using a flat head sonic tip (Sonics VX-750) at 60% amplitude and an on:off pulse ratio of 6:2 s. The temperature was maintained at 15˚C using water cooling around the metal cup. After sonication, the result was a dispersion of 2D h-BN nanoflakes of varying sizes. This dispersion was then centrifuged using a Hettich Mikro 220R centrifuge with a fixed-angle rotor. For this centrifuge, the g-force is related to the rate of revolution by the expression

$$RCF = 106.4f^2$$

where f is the rate of rotation in krpm. Liquid cascade centrifugation with subsequently increasing rates of rotation was used to size-select the h-BN nanoflakes. 80 mL of sonicated solution was centrifuged for 60 minutes at 0.5 krpm. The resulting sediment was discarded, and the supernatant was then centrifuged for 60 minutes at 1 krpm. The resulting sediment from this last centrifugation was redispersed in 25 mL of fresh surfactant (25 gL^{-1}) and placed in a sonication bath for 5 minutes. The result was the largest sample of h-BN nanoflakes. The supernatant remaining after the 1 krpm centrifugation was then centrifuged for 60 minutes at 2 krpm, redispersed in fresh surfactant solution as before thus producing the second largest size of h-BN nanoflakes. These were repeated thrice more at 3 krpm, 4 krpm, and 5 krpm. The end result was five aqueous dispersion of h-BN nanoflakes with lateral sizes of 163 nm, 243 nm, 388 nm, 475 nm, and 628 nm which were given the labels XS, S, M, L, and XL respectively. The stock dispersion, in order of smallest to largest, had a mass concentration of 3.14 g mL^{-1}, 3.62 g mL^{-1}, 5.90 g mL^{-1}, 8.78 g mL^{-1}, 4.50 g mL^{-1}. All samples were then diluted with Millipore water to a mass concentration of 1.05 g mL^{-1}. This concentration was chosen because these samples were used to measure multiple scattering of h-BN and this concentration was turbid sufficiently turbid to multiply scatter incident light but not so turbid as to cause complete attenuation of a laser beam passing through the sample.

Figure 7.7(a – e) presents transmission electron microscopy (TEM) images of the LPE produced h-BN nanoflakes and the corresponding histograms of the lateral nanoflake size distributions (f –

j). While the nanoflakes will be referred to throughout this thesis by their average lateral size, $\langle L \rangle$, it is important to note that the nanoflakes are not a monodisperse distribution of flake lengths, but in reality, a distribution of lateral sizes. Another set of h-BN nanoflakes were produced with an average lateral size of 400 nm. This sample was diluted to various concentrations of the stock dispersion (1% – 100% of stock solution) and used in angle-resolved scattering measurements.

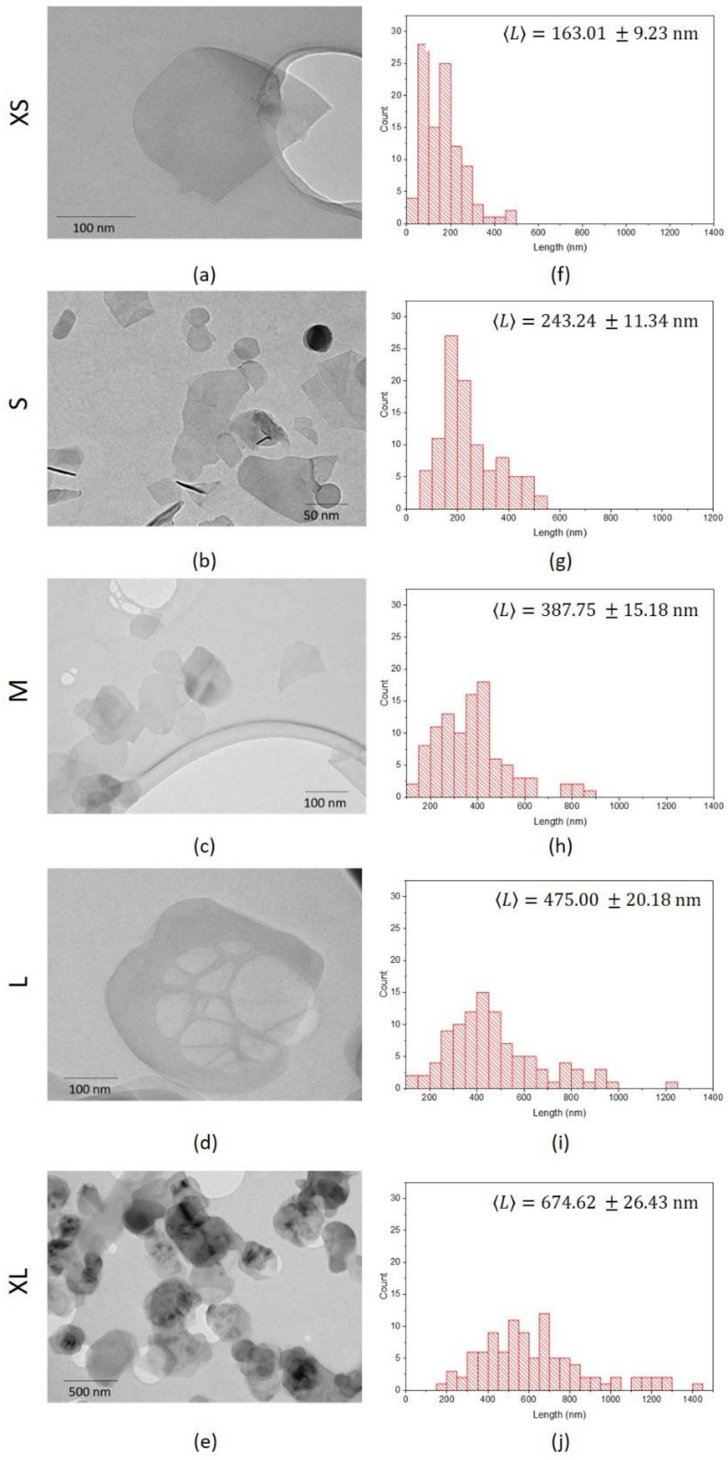

Figure 7.7 Transmission Electron Microscopy images (a – e) of h-BN nanoflakes and histogram showing the distribution of the nanoflake lateral sizes (f – j).

7.3 Multiple Light Scattering by Path – Length Resolved Scattering Profile Measurements

As mentioned in Section 7.2.4, the PS microsphere were diluted to a mass concentration of 1.05 g cm^{-3} with Millipore water. The h-BN samples were also diluted to this value. This concentration was chosen because it was sufficiently scattering to produce a strong diffuse scattered signal and sufficiently dilute to allow the beam to pass through the sample without complete attenuation. Measurements of the multiple scattering intensity profile of 632.8 nm laser beam were taken using a custom-built setup consisting of HeNe laser beam, linearly polarised using a Glan-Thomson polariser (LP) and collimated by means of two lenses (L1 and L2) and then incident on a PMMA cuvette containing an aqueous solution of multiply scattering particles. The diameter of the beam incident upon the cuvette was 2 mm. The polarisation could be changed between TE and EM input by means of a half wave plate (HWP) placed after the Glan-Thompson polariser. The stability of the laser was monitored by placing a beam splitter (BS) in the path of the laser, passing it through an optical chopper and incident on a photodiode (PD) connected to a Signal Recover lock-in amplifier. Any fluctuations in the laser output could be accounted for in post-processing of the data. The particles measured were 2D h-BN nanoflakes and polystyrene microspheres as a spherical reference. A Point Grey USB camera was place transversely to the direction of beam propagation through the solution and 100 images of the beam profile were taken. These images were averaged using an image averaging algorithm written in Python and then exported into Matlab as an image matrix. The intensity of the beam was then profiled across the path length of the cuvette. These measurements were carried out for five aqueous suspensions of h-BN nanoflakes with lateral sizes of 163 nm, 388 nm, 475 nm, and 628 nm. and were compared to four aqueous suspensions of PS microspheres of diameters 99 nm, 260 nm, 425 nm, and 628 nm. These samples were placed in a poly(methyl methacrylate) (PMMA) cuvette of 10 mm optical path-length. Figure 7.8 shows a photo of the setup and Figure 7.9 shows a schematic diagram of the setup.

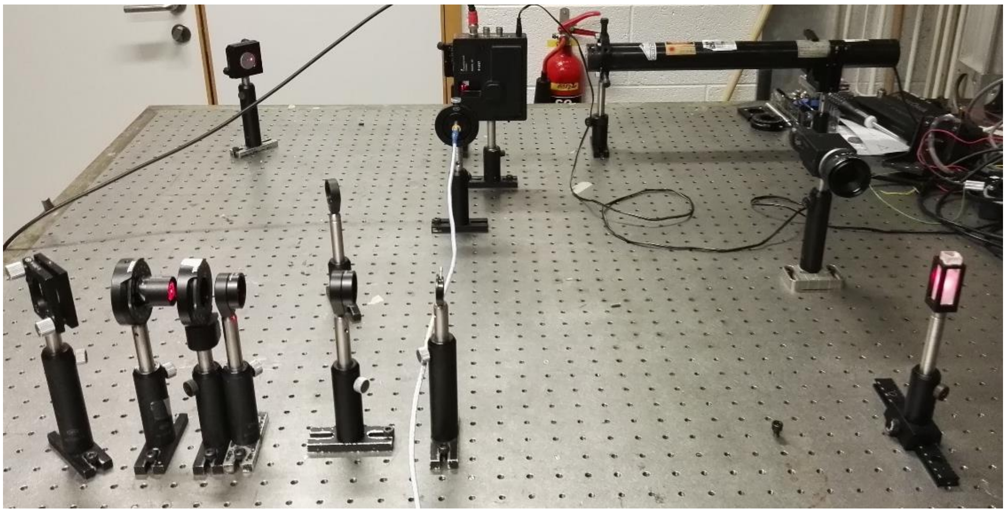

Figure 7.8 Photo of the path length resolved multiple scattering setup in operation.

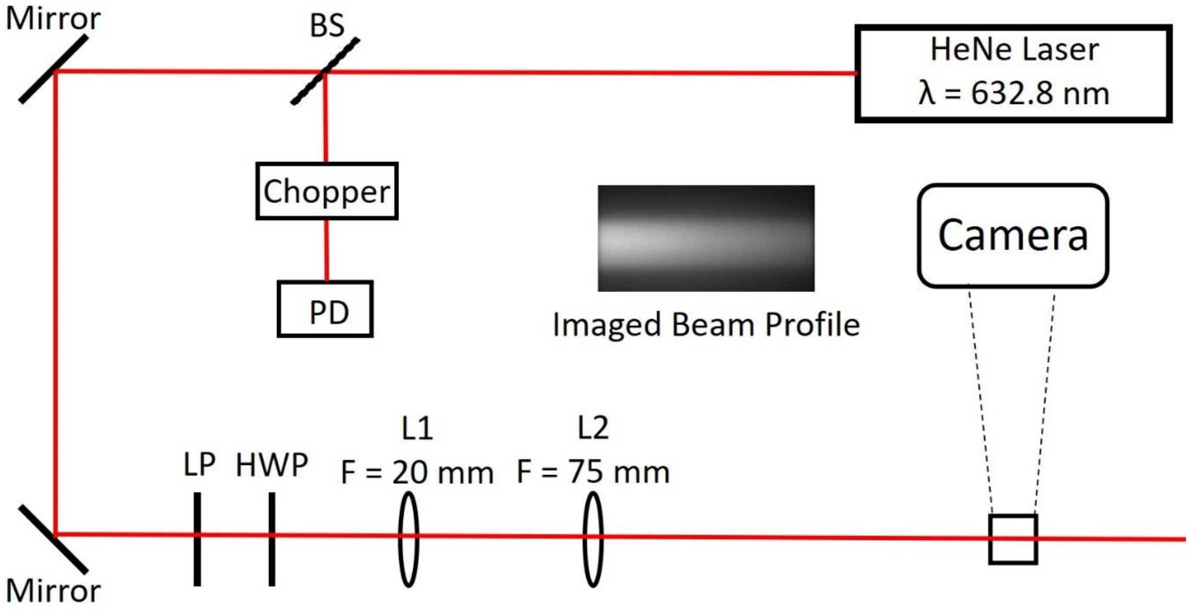

Figure 7.9 Representative schematic of the path length resolved multiple scattering setup.

7.4 Diffuse Multiple Light Scattering and Lateral Particle Size Estimation of Turbid Suspension of Aqueous h-BN Nanoflakes

Measurements of the diffuse multiple light scattering of the h-BN and PS nanosphere samples were carried out. The initial motive for these measurements were based on the Beer-Lambert Law

$$I(x) = I_0 e^{-N\sigma l} \tag{9}$$

which describes the attenuation of the intensity, $I(x)$ of a beam of light propagating through an attenuating medium as a function of distance. Here I_0 is the initial incident intensity, x is the distance travelled by the beam, and $\mu_{ext} = N\sigma l$ is the extinction/attenuation coefficient. The Beer-Lambert law breaks down for sufficiently high values of concentration, and thus an extension of the Beer-Lambert law is required. Initially it was hoped that an extension of the Beer-Lambert law could be determined which included information of the particle size, shape, and/or aspect ratio. However, after much research and experiment it became apparent that extracting the aspect ratio of non-spherical particles is no easy task with no clear analytical solution. The methods most commonly used to determine particle properties from multiple scattering are statistical and/or numerical methods requiring long and complex computation.

Figure 7.10 presents the diffuse scattering intensity profiles of aqueous suspensions of PS nanospheres as a function of the optical path length. Figure 7.10 (a – d) presents the profiles for TE polarised light, and (e – h) for TM polarisation. All samples were diluted to a mass concentration of 1.05 g cm^{-3} and incident wavelength was from a collimated 632.8 nm HeNe laser beam. There is a clear trend in the intensity with increasing particle diameter for both polarisations consistent with the trend in the scattering phase functions calculated in Figure 7.5. For TE polarisation the diffuse scattered intensity decreases with increasing particle size, consistent with their being greater scattering with increased sphere diameter. For TM polarisation, the reverse trend is observed; the diffuse scattered intensity increases with increasing sphere diameter. This again is consistent with Figure 7.5 as the beam profiles were photographed orthogonally to the direction of propagation of the beam, and these smaller particles, falling closer to the Rayleigh scattering regime scatter less orthogonally to this direction. As the particle diameter increases, the particles enter further into the Mie regime, becoming comparable in size to the wavelength of the incident light, and these then scatter more in the orthogonal direction.

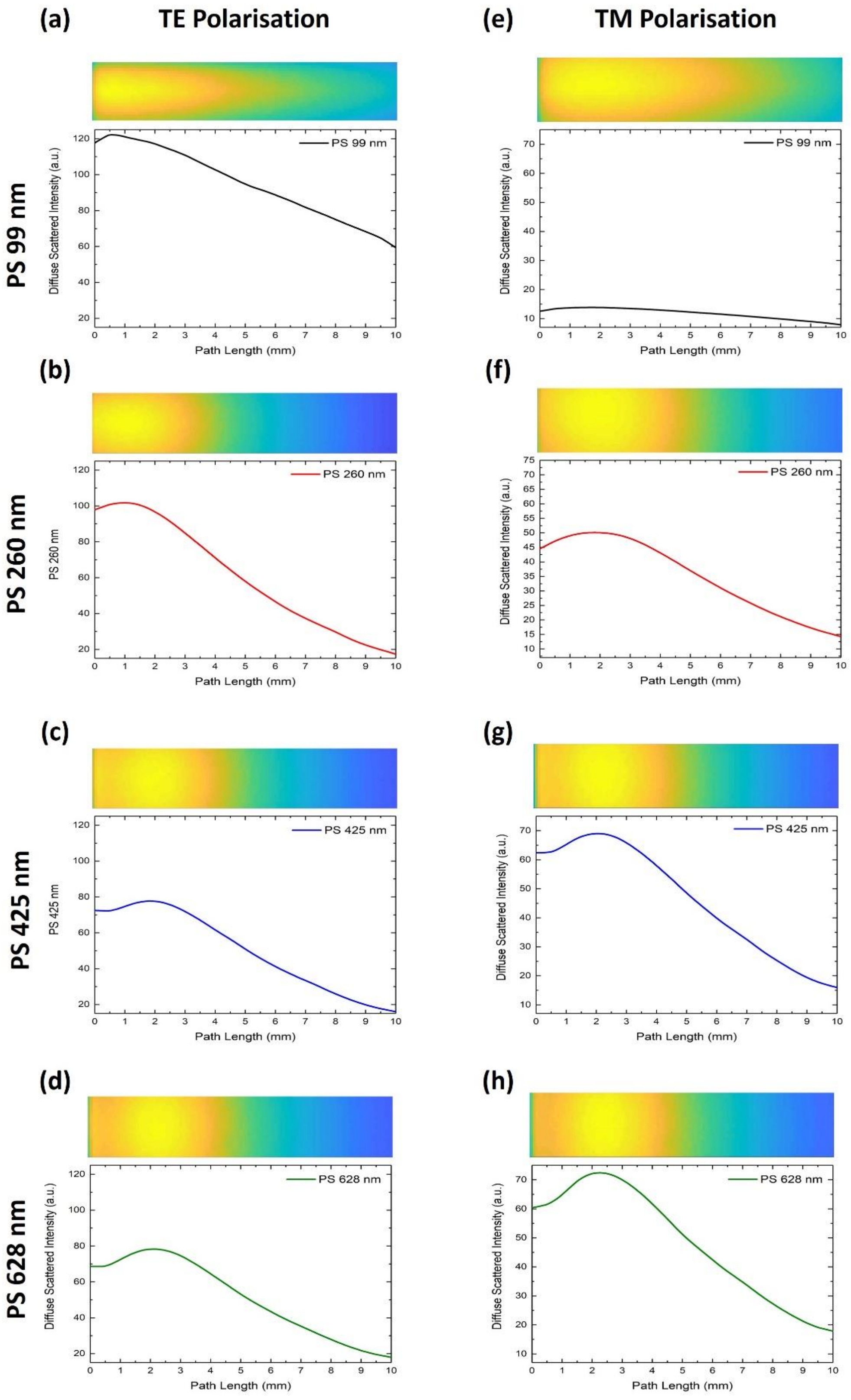

Figure 7.10 Diffuse scattering intensity profiles for aqueous suspensions of PS nanospheres with mean sphere diameters of 99 nm, 260 nm, 425 nm, and 628 nm. All samples were diluted to a mass concentration of 1.05 g cm^{-3}. The colour map represents the intensity of the laser beam with yellow being the most intense and dark blue being the least.

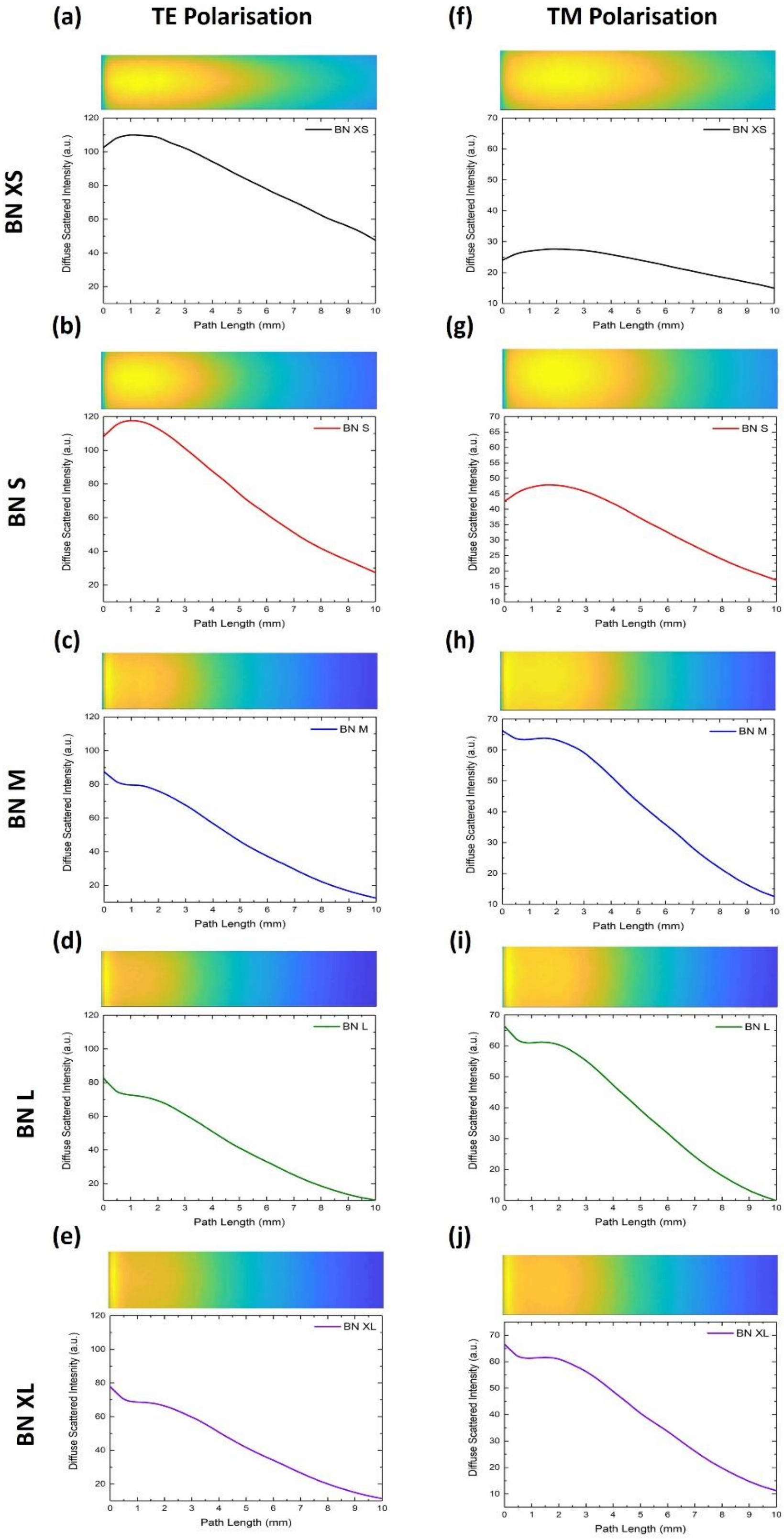

Figure 7.11 Diffuse scattering intensity profiles for aqueous suspensions of h-BN nanoflakes of mean lateral lengths of 163 nm (BN XS), 243 nm (BN S), 388 nm (BN M), 475 nm (NM L), and 674 nm (BN XL). All samples were diluted to a mass concentration of 1.05 g cm^{-3}. The colour map represents the intensity of the laser beam with yellow being the most intense and dark blue being the least.

Figure 7.11 presents the diffuse scattered intensity data for aqueous suspensions of the h-BN nanoflakes at a mass concentration of 1.05 g cm^{-3}, identical to that of the PS nanospheres. The incident wavelength was again 632.8 nm. The same trend is apparent in h-BN samples as in the PS nanospheres. The diffuse scattered intensity of TE polarised light (a – e) again decreases with increasing particle size and increases for TM polarisation (f – j). This is exactly what would be expected based on the trends in scattering phase functions in Figure 7.5 which show that as particle size increases, the proportion of scattered TM light normal to the direction of beam propagation (as was the geometry for these measurements) increases with increasing particle size and instead there is greater forward scattering. The opposite trend is also expected of TE polarised light, which for increasing particle size should show a decrease in the proportion of radiation scattered normal to the direction of propagation. For the BN M, BN L, and BN XL samples, there is an anomalous point of high intensity at the beginning of optical path through the cuvette. This may be explained by some light reflecting/guiding on the edges of the cuvette. Figure 7.12 presents the diffuse scattering profiles for both PS and h-BN samples for TE and TM polarisation in one figure for comparison.

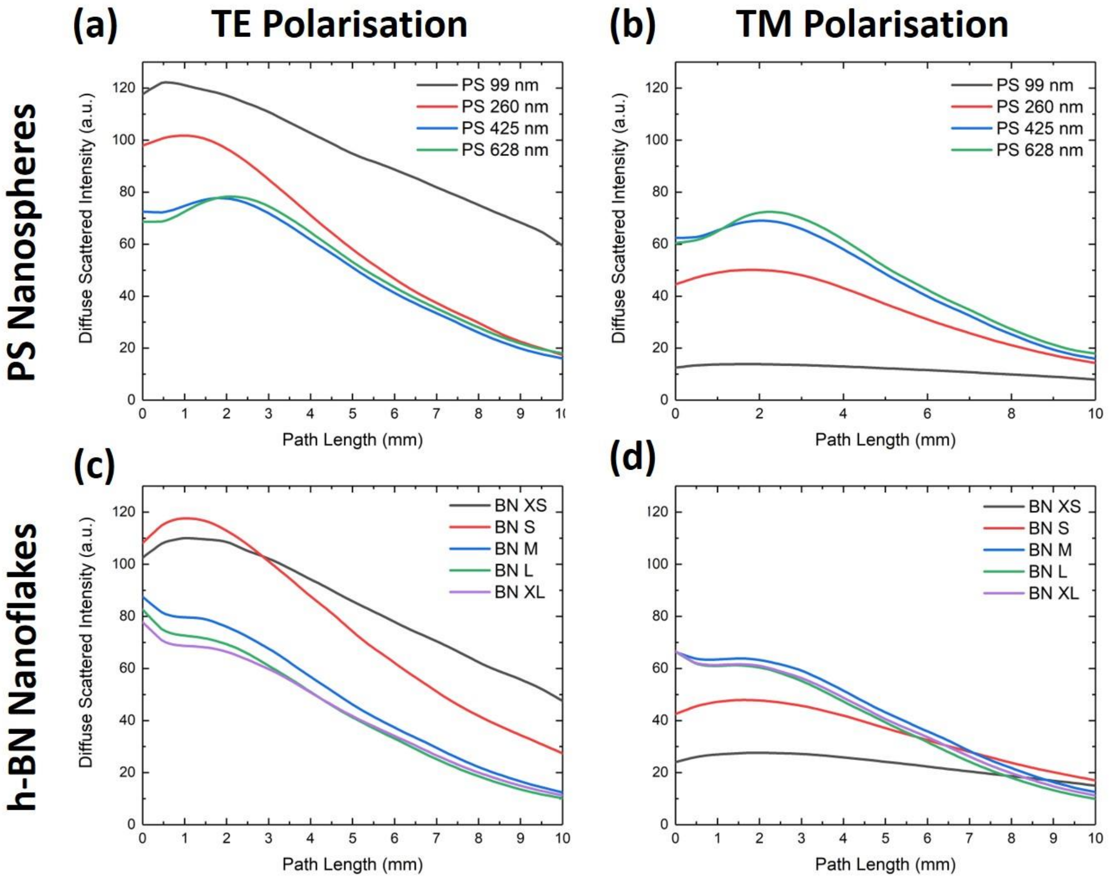

Figure 7.12 Diffuse scattered intensity as a function of optical path length for PS nanospheres with (a) TE and (b) TM polarisation, and h-BN nanoflakes with (c) TE and (d) TM polarisation at incident wavelength of 632.8 nm.

7.5 Modelling Multiple Light Scattering in Turbid Suspensions of Highly Scattering Nanoparticles: A Comparison of Simulation and Experiment

While single scattering from homogenous spheres can be easily modelled both analytically and numerically, multiple light scattering is a far more complex scenario. When the number density of particles is sufficiently high to cause significant multiple scattering, simple analytical models such as the Beer-Lambert extinction law break down and thus other more complex models must be considered. In this research, we consider and attempt to fit several alternatives models for multiple scattering to the experimentally measured data, with limited and varied success. Three models are considered, the Two-Stream Approximation (Section 7.5.1), Hartel Theory (Section7.5.2), and the numerical Monte Carlo Method (Section 7.5.3).

7.5.1 Two-Stream Approximation to the Radiative Transfer Equation

A simple method for estimating the size of nanoparticles was posited based on the aforementioned Lambert-Beer Law. According to this law, the intensity of an electromagnetic wave is attenuated by the process of absorption and scattering as it propagates through a medium of path length, l. The intensity as a function of the path length is given by [50]

$$I = I_0 e^{-N\sigma l} \tag{10}$$

where N is the number density of particles, $\sigma = \sigma_a + \sigma_s$ is the extinction cross section and I_0 is the incident intensity, σ_a and σ_s are the absorption and scattering cross-sections respectively. In the case of highly-scattering and non-absorbing particles such as the h-BN studied in this work, the absorption and hence the absorption cross-section are zero, i.e. $\sigma_a = 0$ and thus the attenuation cross-section is simply the scattering cross section. The problem with this particular law is that for sufficiently high values of N, the Lambert-Beer law is no-longer applicable as the medium is now in the multiple scattering regimes (i.e. a wave undergoes two or more scattering events before exiting the medium). In this regime, the attenuation and scattering can be more precisely described using the radiative transfer equation [51], i.e.

$$\frac{1}{c}\frac{\partial}{\partial x} I_v + \widehat{\Omega} \cdot \nabla I_v + \left(k_{v,s} + k_{v,a}\right) I_v = j_v + \frac{1}{4\pi} k_{v,s} \int_{\Omega} I_v \, d\Omega \tag{11}$$

This equation mathematically describes the propagation of electromagnetic radiation through a medium in which the propagation of radiation is affected by absorption, emission, and scattering. The first term of this on the left-hand side describes the variation in the spectral radiance, I_v as it propagates outward in all directions. The second term, the divergence of I_v over a solid angle $\widehat{\Omega}$ describes the volume density of spectral radiance propagating outwards over the solid angle. The third term describes the attenuation of the spectral radiance due to absorption and scattering which manifests itself mathematically as the scattering and absorption opacities, $k_{v,s}$ and $k_{v,a}$ respectively. On the right hand-side we can equate this to an emission coefficient, j_v plus an integral over the solid of I_ν. This second term essentially describes light that is scattered from all other directions back into the incident direction. The problem with this equation, however, is that there is no analytical solution without making approximations and assumptions to the model [52][53][54]. One such assumption is the two-stream approximation [55], where the scattering is assumed to only occur in one of two directions, forwards, or backwards through a medium with two flat parallel sides. Koh *et al.*[56] used this approximation to yield an expression for the diffuse intensity I_d (i.e. the light that is scattered multiple times) as a function of the optical depth, τ (a measure of how light is attenuated through a medium of a given path length) for the propagation of radio waves in falling snow. We start by considering the transmission of diffuse intensity through a plane-parallel medium [57]

$$\mu \frac{d}{d\tau} I_d(\tau,\mu,\varphi) = I_d(\tau,\mu,\varphi) - \frac{1}{4\pi}\int_{-1}^{1}\int_{0}^{2\pi} I_d(\tau,\mu',\varphi')\, P(\mu',\varphi';\mu,\varphi) d\varphi' d\mu' - I_0 e^{\frac{\tau}{\mu_0}}\, P(-\mu_0,\varphi_0;\mu,\varphi) \tag{12}$$

where $\mu = \cos\theta$ is the cosine of the angle from the axis normal parallel to the medium and $P(-\mu_0,\varphi_0;\mu,\varphi)$ is the scattering phase function describing a single scattering event from the direction (μ_0,φ_0) to (μ,φ). We now make two assumptions, we assume azimuthal independence over the forwards and backwards hemispheres, and we assume that scattering is constrained in only two directions, forwards $I_d^{\rightarrow}(\tau\,,+1)$ and backwards $I_d^{\leftarrow}(\tau\,,-1)$. Applying these two constraints to equation 11 we obtain

$$\frac{d}{dx} I_d^{\rightarrow} = -I_d^{\rightarrow}(\tau) + F(-1;+1) I_d^{\rightarrow}(\tau) + F(+1;+1) I_d^{\leftarrow}(\tau) + F(-1;+1) I_0 e^{-\tau} \tag{13a}$$

where $\mu = +1$, and

$$\frac{d}{dx} I_d^{\leftarrow} = -I_d^{\leftarrow}(\tau) + F(+1;-1) I_d^{\leftarrow}(\tau) + F(-1;-1) I_d^{\rightarrow}(\tau) + F(-1;-1) I_0 e^{-\tau} \tag{13b}$$

where $\mu = -1$ and $F(\mu',\mu)$ is the fraction of light incident on a particle from the direction μ' and scattered to the direction μ.

$$F(-1;+1) \approx \frac{1}{4\pi}\int_{-1}^{0}\int_{0}^{2\pi} P(\mu',\varphi';\mu,\varphi) d\varphi' d\mu \tag{14a}$$

$$F(+1;+1) \approx \frac{1}{4\pi}\int_{0}^{+1}\int_{0}^{2\pi} P(\mu',\varphi';\mu,\varphi) d\varphi' d\mu \tag{14b}$$

We now introduce a new parameter, the asymmetry factor, $g = \langle\cos\theta\rangle$. The asymmetry factor is the mean cosine of the scattering angle and is a number $-1 \leq g \leq +1$ that describes the proportion of scattering in the backwards ($g = -1$) and forwards ($g = +1$) directions [58]. In the case of isotropic scattering around 90˚, $g = 0$ such that $F(\mu',\mu)$ values are both one-half, i.e.

an equal proportion of scattering forwards and backwards. This parameter can be approximately applied as follows

$$F(+1;-1) = F(-1;+1) = \frac{\omega_0}{2}(1+g) \tag{15a}$$

$$F(+1;+1) = F(-1;-1) = \frac{\omega_0}{2}(1-g) \tag{15b}$$

where ω_0 is the single scattering albedo[59]. Substituting these into equations 13a and 13b

$$\frac{d}{d\tau} I_d^{\rightarrow}(\tau) = I_d^{\rightarrow}(\tau) + \omega_0 \frac{(1+g)}{2} I_d^{\rightarrow}(\tau) + \omega_0 \frac{(1-g)}{2} I_d^{\leftarrow}(\tau) + \omega_0 \frac{(1+g)}{2} I_0 e^{-\tau} \tag{16a}$$

$$\frac{d}{d\tau} I_d^{\leftarrow}(\tau) = I_d^{\leftarrow}(\tau) - \omega_0 \frac{(1+g)}{2} I_d^{\leftarrow}(\tau) - \omega_0 \frac{(1-g)}{2} I_d^{\rightarrow}(\tau) - \omega_0 \frac{(1-g)}{2} I_0 e^{-\tau} \tag{16b}$$

Applying the boundary conditions that $I_d^{\rightarrow}(\tau) = 0$ and $I_d^{\leftarrow}(\tau) = 0$, i.e. the diffuse intensity at the start and end of the optical path is zero the coupled differential equations can be solved. The result is an expression for the diffuse intensity as a function of the optical depth $\tau = \sigma_s N l$

$$I_d = \frac{I_0}{1 + \frac{(1-g)}{2}} \tau - I_0 e^{-\tau} \tag{17}$$

To account for the capabilities of the USB camera used in these measurements, a minor modification to Equation 17 was used to fit the experimental data to the Two-Stream Approximation to the radiative transfer equation. A constant parameter d was introduced to account for the background signal of the camera and the second I_0 parameter was replaced with a scattered intensity parameter I_1 to account for the variation in the diffuse scattered radiation. The fitting equation used was

$$\frac{I_0}{1 + \frac{1-g}{2}} cx - I_1 e^{-cx} + d \tag{18}$$

where $c = N\sigma_s$ is the attenuation coefficient and g is the previously described asymmetry parameter. The Two-Stream model fits for the normalised diffuse scattered intensity data are given in Figure 7.13. This model works reasonably well in predicting the behaviour of the scattered intensity, particularly in terms of the rate of change of intensity across the path length of the sample, however for larger diameters ((c) and (d)) the position of the peak is not precise, possibly due to the anomalous peak in scattered intensity at the beginning of the optical path.

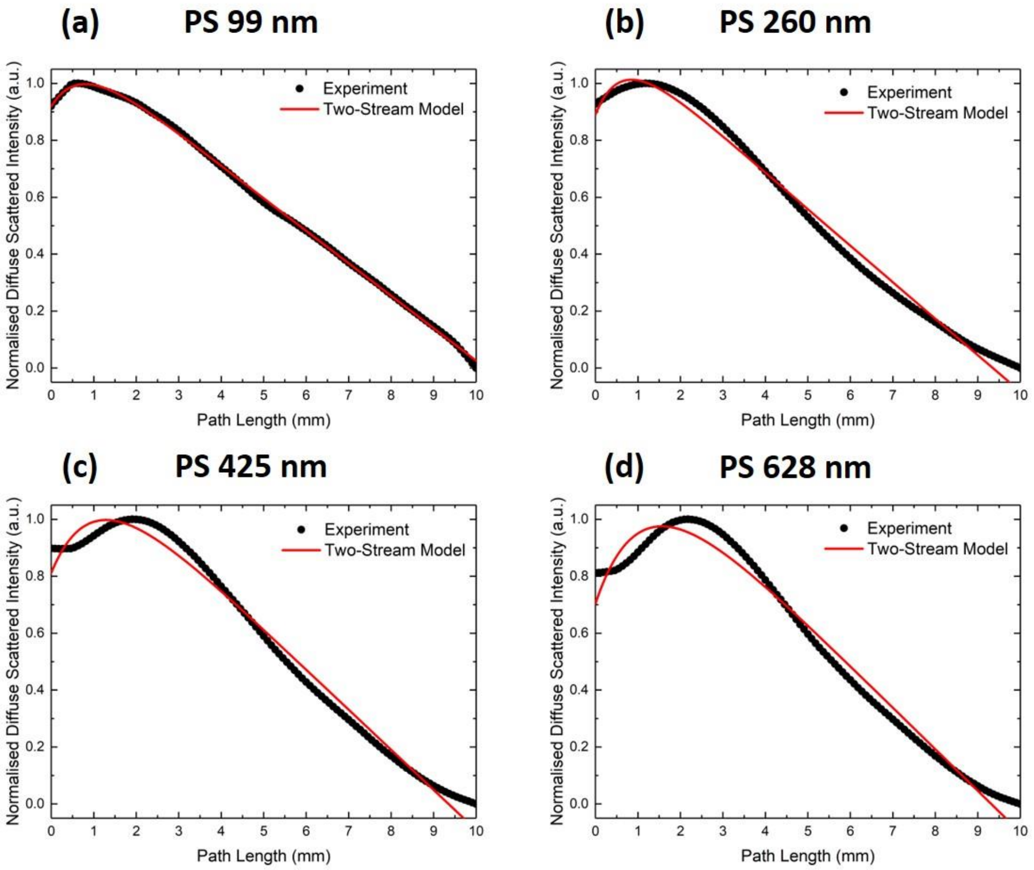

Figure 7.13 Normalised diffuse scattered intensity for multiply scattering PS nanosphere suspensions of (a) 99 nm, (b) 260 nm, (c) 425 nm, and (d) 628 nm fitted to the Two-Stream Approximation model for multiple scattering.

Similar agreement is observed for the h-BN nanoflakes samples also. The fits for these samples are provided in Figure 7.14. For both the BN XS and BN S samples, the fits match the data almost precisely.

For the larger, BN M, BN L, and BN XL samples, the fits match the trends in the data quite closely, however some disagreement is evident due to the high scattering feature at the beginning of the optical path length which is attributed to a reflection/guiding of the incident light along the walls of the PMMA cuvette. Despite this minor disagreement, all data fit the trend with a high correlation coefficient of greater than 0.95. The output of the fitted data is presented in Table 7.1. In the fits, the initial intensity, I_0 was fitted as a constant value of 170 a.u. across all samples and the asymmetry parameters for the PS nanosphere samples were specified. For the h-BN samples, the asymmetry parameters were allowed to be adjusted as another fitting variable due to the inability to calculate an asymmetry parameter for an irregularly shaped particle.

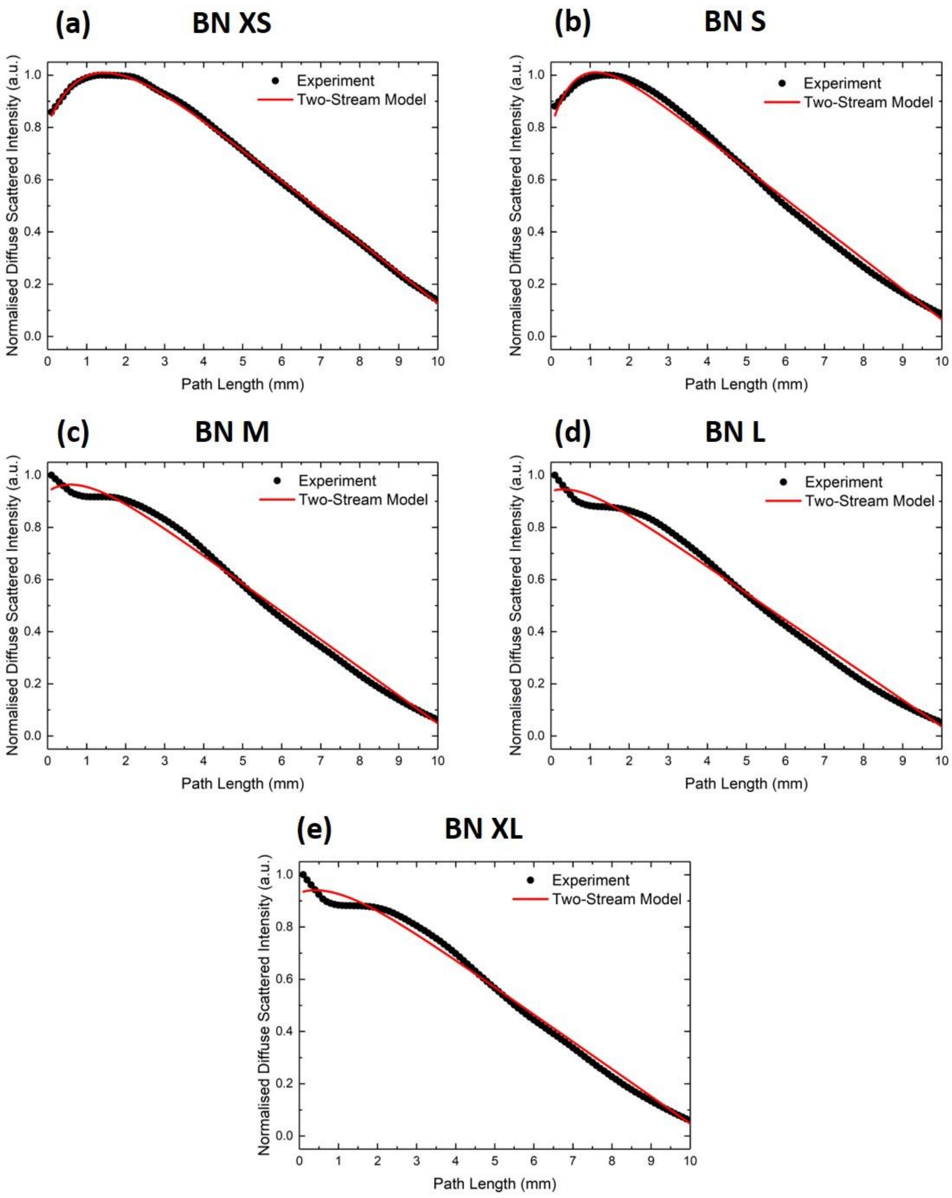

Figure 7.14 Normalised diffuse scattered intensity for multiply scattering h-BN nanoflake suspensions of sizes (a) XS, (b) S, (c) M, (d) L, and (e) XL.

Sample	**I_1 (a.u.)**	**c (mm^{-1})**	**g**
PS 99 nm	0.00520 ± 0.00059	1.40585 ± 0.05282	0.07425*
PS 260 nm	0.02304 ± 0.00107	1.59188 ± 0.20643	0.53652*
PS 425 nm	0.02418 ± 0.0048	0.98115 ± 0.09958	0.75943*
PS 628 nm	0.02904 ± 0.00209	0.89208 ± 0.08619	0.86285*
BN XS	0.49566 ± 0.00527	0.09417 ± 0.00205	0.99851 ± 0.00004
BN S	0.42325 ± 0.02264	0.14729 ± 0.01251	0.99907 ± 0.00008
BN M	0.18835 ± 0.02231	0.11103 ± 0.02239	0.99885 ± 0.00233
BN L	0.12434 ± 0.02562	0.12120 ± 0.03737	0.99900 ± 0.00305
BN XL	0.16618 ± 0.02031	0.09325 ± 0.02148	0.99867 ± 0.00311

Table 7.2 Fitted parameters of the Two-Stream Approximation. The starred parameters indicate that the values were specified prior to fitting.

All data fit the Two-Stream Approximation model with significantly large correlation coefficient. The fitted value of d was allowed to vary freely for all samples, however the consensus between fits at a value of around -169 suggests that this parameter is in fact correcting for a background intensity or noise present in the data. The values of I_1 vary substantially across all samples, however this would be expected as each sample has a different size and relative geometry.

7.5.2 Hartel Theory for Multiple Scattering of Light from Spherical Particles

Among the many models for multiple scattering of light in turbid media is Hartel Theory. In this model the angular distribution of the diffuse scattered radiation in the forward hemisphere of a turbid medium is considered as a superposition over all orders of multiple scattering. An order of scattering, n is the number of scattering events experiences buy an individual wave passing through a multiple scattering/turbid medium. In a such a medium, there are multiple orders of scattering as each individual wave has the potential to undergo a various number of scattering events. To consider this we examine a parameter known as the scattering phase function, $P_n(\cos\theta)$ which is the angular distribution of the relative scattered intensity, Q_0 of radiation scattered by an angle θ. This parameter can be represented in terms of scattering amplitudes (i.e. probability amplitudes for scattering), or more commonly expanded in terms of Legendre polynomials and is always a number between -1 and 1. In this theory, Hartel expresses the overall angular distribution of the scattered intensity as

$$f_k(\theta) = \frac{1}{4\pi}\sum_{n=0}^{N_t}(2n+1)B_n^k P_n(\cos\theta) \tag{19}$$

where N_t is the truncation number and is given in terms of the size parameter, $a = \frac{2\pi}{\lambda}r$, where r is the radius of the sphere, and $N_t = 4a^{\frac{1}{3}} + a + 2$ and B_n is a multiple scattering expansion coefficient in terms of Ricatti-Bessel functions, i.e.

$$B_n(x) = \frac{\xi_{n-1}(x)}{\xi_n(x)} \tag{20}$$

and is determined by the size parameter and the relative refractive index of the scattering medium. The very basis of Hartel Theory is that this angular distribution function, $f_k(\theta)$ is unity over all solid scattering angles, i.e.

$$\int_\Omega f_k(\theta)\, d\Omega = 1. \tag{21}$$

Hartel also derived an expression for the relative intensity of scattered radiation as

$$Q_k(x) = \frac{(\alpha x)^k}{k} e^{-(\alpha+\beta)x} \tag{22}$$

where α and β are proportional to the scattering and absorption cross-sections respectively. Combining all this, we arrive at an expression for the diffuse intensity of light scattered over multiple orders of scattering

$$I(x, \cos\theta) = \sum_{k=1}^{N_t} Q_k(x) f_k(\theta). \tag{23}$$

The index of the sum starts at $k = 1$ because for $k = 0$ is the straight-through, unscattered light position and does not contribute to the diffuse scattered intensity.

A comparison of the normalised experimental data to theoretically calculated values for the diffuse scattered intensity using Equation 22 are presented in Figure 7.16 for aqueous suspensions of PS nanospheres (a – d) and Figure 7.17 for h-BN nanoflakes. Equation 23 account for incident polarisation and the HeNe laser used in these experiments had a polarised output which was alternated between TE and TM polarisation by means of a half-wave plate, thus to approximate unpolarised light the diffuse scattered intensities for each sample were halved and then summed. In order to simulate the scattering using Hartel Theory, a custom Matlab code was written calculating the relative scattered intensity and the distribution function. Since the expression for the diffuse scattered intensity is the summation over all orders of scattering of the product of the relative scattered intensity and the distribution function, it was first necessary to determine how many orders of scattering had to be calculated. An initial calculation of the relative scattered intensity, Q_k was carried out as a function of the path length and scattering order. The result of this calculation in Figure 7.15 shows that five orders of scattering, i.e. k = 5, is sufficient as scattering at higher orders becomes negligible. In fact, the calculation appears to suggest that the majority of scattering, greater than 35% of the input intensity, is a result of single scattering events, with a smaller proportion being a result of two scattering events, an even smaller proportion a result of three scattering events, and so on. As a result of this, all further calculations of scattering in these suspensions were calculated up to a value of k = 5. While Hartel theory does not succeed in completely modelling the behaviour of our highly-scattering suspensions, the position of the diffuse scattering peak is predicted quite well for the PS nanospheres, and reasonably well for the h-BN nanoflakes. While the agreement appears less substantial in Figure 7.17(c – e), this is a result of the anomalous spike in intensity at the beginning of the path length, attributed to a reflection/guiding of the input light along the thickness of the cuvette. Neglecting this anomaly, it’s clear that the position of the diffuse peak is simulated quite well using this method. However, the failure of Hartel Theory to properly describe the behaviour of these samples is in the drop-off rate of the intensity as a function of path length, which for the Hartel

Theory plots is significantly greater than experimental values. This is possibly due to the fact that this theory assumes a monodisperse suspension of spheres when in reality the PS microspheres used in this work are a polydisperse suspension of spheres following a normal distribution of diameters with a mean value at the stated sphere diameter. Another possibility that cannot be ruled out is that the sensitivity of the camera to changes in intensity is not as accurate as desired.

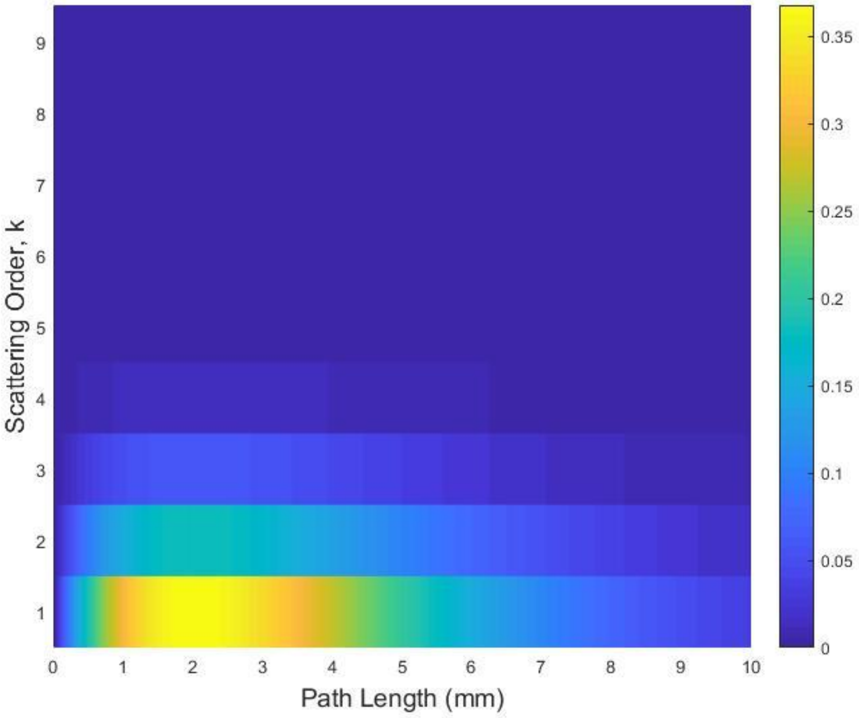

Figure 7.15 A calculation of the diffuse scattered intensity according to Hartel Theory as a function of path length and scattering order for a turbid suspension of PS nanospheres.

Various attempts were made at improving the fit by tuning the α and β values, however with little success, suggesting that while Hartel Theory correctly describes the position of the diffuse scattering peak, its predictive ability breaks down at larger path lengths. In an attempt to achieve a better model to describe this multiple scattering behaviour, a numerical method was thus chosen, the Monte Carlo Method for photon transport.

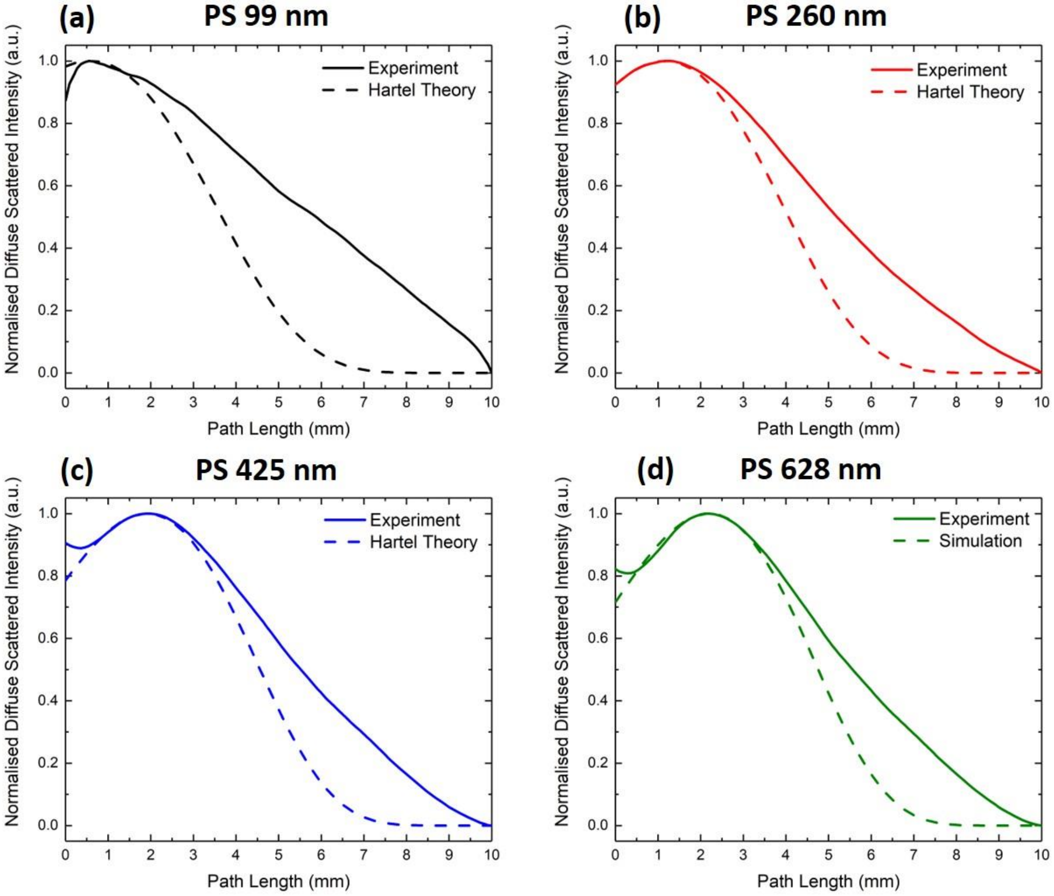

Figure 7.16 A comparison of experiment (solid lines) and Hartel Theory (dashed lines) for the normalised diffuse scattered intensity of aqueous suspensions of PS nanospheres of sizes (a) 99 nm, (b) 260 nm, (c) 425 nm, and (d) 628 nm.

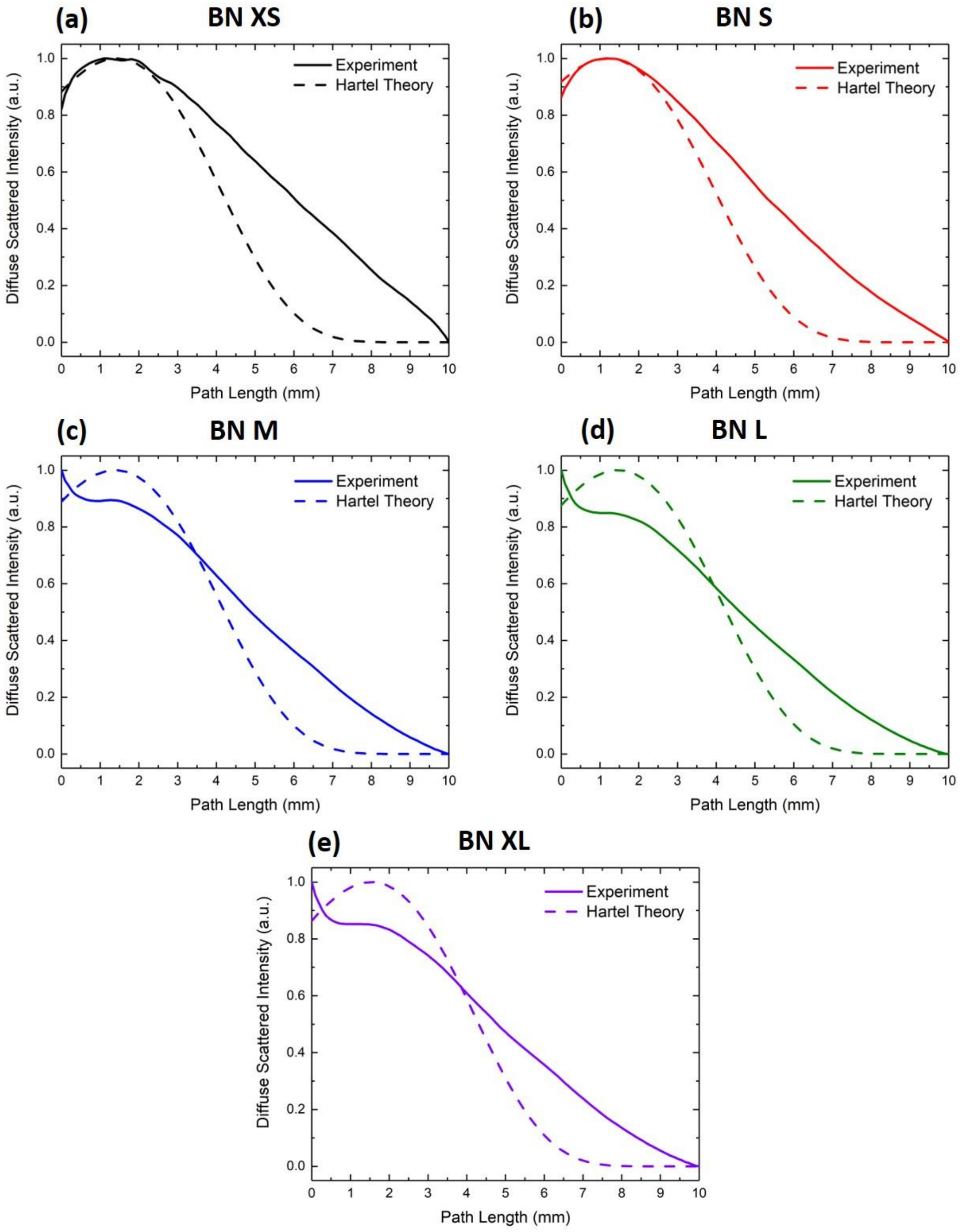

Figure 7.17 A comparison of experiment (solid lines) and Hartel Theory (dashed lines) for the normalised diffuse scattered intensity of aqueous suspensions of h-BN nanoflakes of sizes (a) XS, (b) S, (c) M, (d) L, and (e) XL.

7.5.3 Monte Carlo Method for Photon Transport

The Monte Carlo Method is a common technique used to model the propagation of photons through a turbid medium of absorbing and scattering particles. Photon transport can be modelled analytically using the radiative transfer equation in Equation 10 [60][35]. For some geometries, closed-form solutions to this equation are not possible and hence approximations need to be made, such as the diffusion approximation.[61] However, as with all approximations, in doing so inaccuracies are introduced into the model. As a solution to this, partially with the availability of modern computers, a more statistical and computationally intense model can be used, the Monte Carlo Method for Photon Transport. This method is widely used now, particularly in biomedical imaging [62][63], radiotherapy [46], and radiography [64][65][66]. This method works by expressing the rules of photon transport as probability distributions; it calculates the step-size for photon transport between sites of scattering and absorption and calculates the angle of deflection in a photon's trajectory upon scattering. The Monte Carlo Method, in basic terms, can be broken down into four easy steps [37][56][67].

Step 1: Launching the Photon Packet

A packet of 1000 photons is defined, and the initial position and direction of the photon packet are set in Cartesian co-ordinates as follows:

Position:

$$x = 0$$
$$y = 0$$
$$z = 0$$

Direction Cosines:

$$\cos\theta_x = 0$$
$$\cos\theta_y = 0$$
$$\cos\theta_z = 0$$

where θ_x , θ_y , and θ_z are the scattering angles in the x, y and z directions respectively.

Step 2: Setting the Step Size

The step size, d, is the distance travelled by the photon packet between absorption/scattering interactions and is defined as follows:

$$d = -\frac{\ln\xi}{\mu_{ext}} \tag{24}$$

where ξ is a random number and μ_{ext} is the total extinction coefficient, which gives the amount of light that is attenuated by the medium over a given unit distance. The photon packet then travels a distance d in the direction specified by the direction cosines and the co-ordinates are then updated, i.e.

$$x \rightarrow x + \cos\theta_x\, d$$
$$y \rightarrow y + \cos\theta_y\, d$$
$$z \rightarrow z + \cos\theta_z\, d$$

Step 3: Absorption & Scattering

Each photon in the simulation has a probability of surviving which we describe as a photon "weight". At each interaction site in the simulation, a fraction ΔW of the photon weight is absorbed. Essentially, this means that at each interaction site the probability of the photon surviving decreases.

$$\Delta W = \frac{\mu_a}{\mu_{ext}} W \tag{25}$$

where μ_a is the absorption coefficient. The photon weight is then updated.

$$W \rightarrow W - \Delta W \tag{26}$$

in the case of non-absorbing particles such as the polystyrene microspheres and hexagonal boron nitride used in this project, $\Delta W = 0$, $\mu_{ext} = \mu_s$ and only scattering occurs at interaction sites. The scattering must now be considered in terms of its isotropy/anisotropy. This is done in terms of a parameter known as the asymmetry parameter g which is the weighted average of the photon scattering angle, i.e. $g = \langle\cos\theta\rangle$. g is a number between -1 and 1 and determines the isotropy of scattering and general direction of scattering [50].

$g = -1$	Anisotropic:	Scattering entirely in the backwards direction.
$g = 0$	Isotropic:	Scattering equally in forwards and backwards directions
$g = +1$	Anisotropic:	Scattering entirely in forward direction.

The scattering phase function in terms of this parameter is then used to determine the new direction of scattering. The most commonly used phase function in Monte Carlo photon transport simulation is the Henyey-Greenstein phase function [68]

$$p(\theta) = \frac{1}{4\pi} \frac{(1 - g^2)}{[1 + g^2 - 2g\cos\theta]^{\frac{3}{2}}} \tag{27}$$

and the new direction cosine can be determined using the equation

$$\cos\theta = \frac{1}{2g}\left[1 + g^2 - \left(\frac{1 - g^2}{1 - g + 2g\xi}\right)^2\right] \tag{28}$$

and the azimuthal angle, φ is assumed to be uniformly distributed between 0 and 2π, thus $\varphi = 2\pi\xi$. The original direction cosines are then updated.

$$\cos\theta_x' = \frac{\sin\theta\left(\cos\theta_x\cos\theta_y - \cos\theta_y\sin\varphi\right)}{\sqrt{1-\cos^2\theta_x}} + \cos\theta_x\cos\theta$$

$$\cos\theta_y' = \frac{\sin\theta\left(\cos\theta_y\cos\theta_z - \cos\theta_z\sin\varphi\right)}{\sqrt{1-\cos^2\theta_x}} + \cos\theta_y\cos\theta$$

$$\cos{\theta_z}' = -\sqrt{1-\cos^2\theta_z}\sin\theta\cos\varphi + \cos\theta_z\cos\varphi$$

Step 4: Terminating the Photon Packet

When the weight of the photon packet has fallen below a specific threshold the simulation must terminate that photon packet. The technique commonly used for this is a Russian roulette technique whereby a roulette constant m is employed to determine whether or not a photon packet below the threshold will survive. This gives the photon packet a $\frac{1}{m}$ chance of survival. If the packet survives its new weight becomes $m * W$, otherwise the weight is 0 which terminated the packet. Photon packets that cross the boundaries of the simulated cuvette are also given a weight of 0 and hence they terminate. Once the weight of all photons packets has become 0 the simulation terminates. For the simulations carried out in this research, the threshold value used was 1×10^{-4} and the roulette parameter was chosen to be $m = 10$ which gives photon packets below the threshold a 0.1 chance of survival. Whether an individual photon packet survives or terminates is determined by a random number generator. If the generated random number is lower than $\frac{1}{m}$ the photon packet terminates. While this is a simplified explanation it is the basis and underlying idea of all Monte Carlo simulations for photon transport. A plethora of Monte Carlo photon transport codes exist with varying degrees of complexity, from simple cases of scattering from spherical particles to more advanced biomedical scattering simulations of the human brain. The flowchart in Figure 7.18 shows the steps of the simulation.

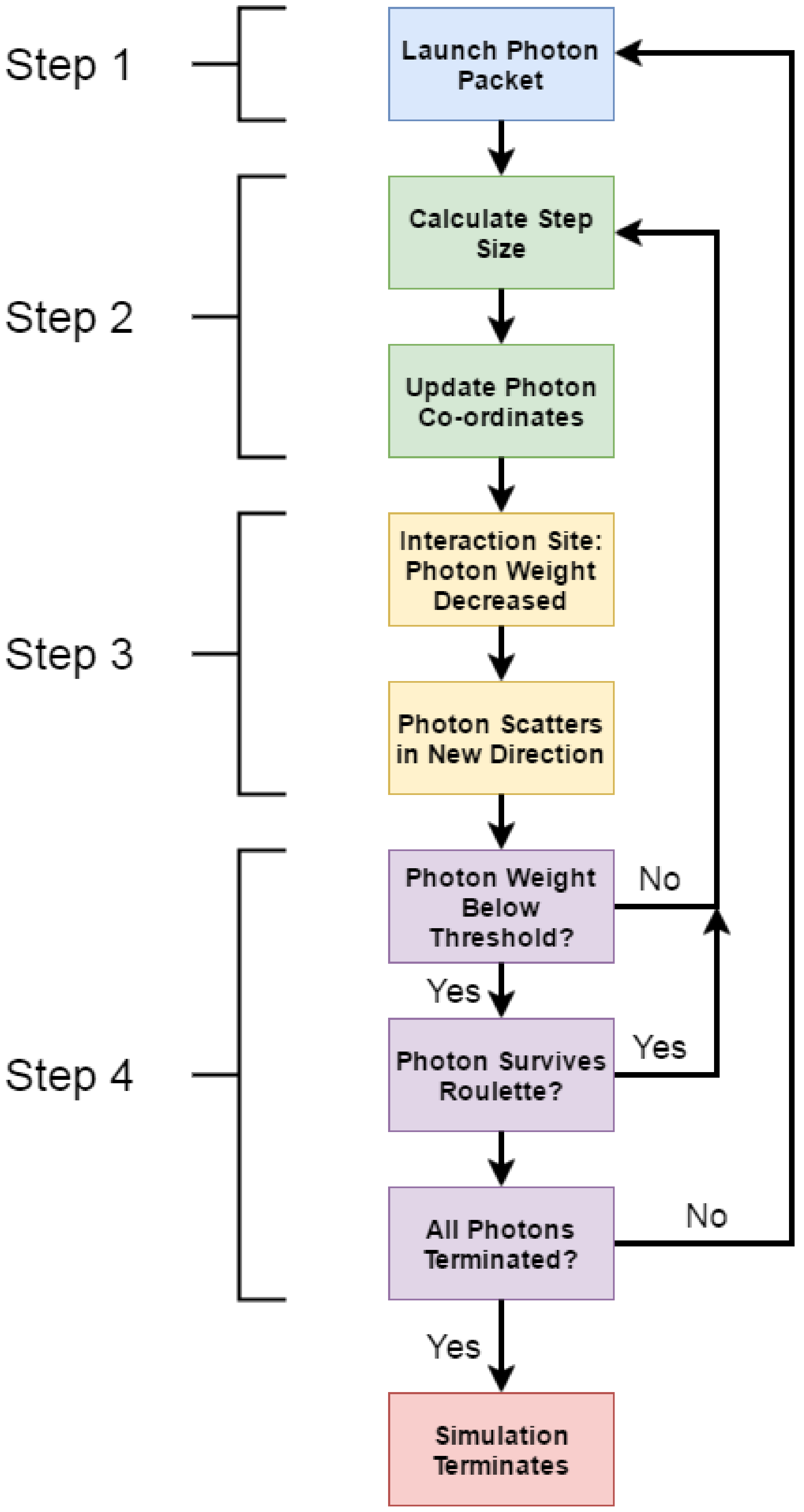

Figure 7.18 Flowchart depicting the steps of the Monte Carlo photon transport simulation.

A Monte Carlo method code was used to simulate the scattering of light through an ensemble of PS nanospheres dispersed in water. The code uses the refractive index of the nanospheres (n_{PS} = 1.61), its diameter, the refractive index of the surrounding medium, which was water (n_w = 1.33), the incident wavelength of 632.8 nm, the mass concentration of the nanospheres (c = 1.05 g cm^{-3}) and the asymmetry parameter calculated in Figure 7.4 to calculate the attenuating and scattering properties of the medium. This simulation again does not account for input polarisation and thus during comparison unpolarised light was approximated by averaging the TE and TM contributions of the experimental data.

Figure 7.19 shows surface maps presenting spatial distributions of the calculated fluence rate for light propagating through the simulated multiple scattering medium for various particle sizes (a-d). The diffuse scattered intensity was extracted from these plots by taking a profile of the scattered intensity at the edge of the simulated medium. Figure 7.19(e – h) presents a comparison of the normalised experimental (solid lines) diffuse scattered intensity as a function of path length compared to the simulated values (dashed lines). As shown, there is substantial agreement between simulation and experiment for this method at larger diameters, with the 260 nm – 628 nm samples agreeing well in both positioning of the diffuse scattering peak as well as comparatively better agreement in the drop-off rate of intensity across the path-length. The PS 99 nm sample however disagrees with the simulation suggesting that this technique works better away from the Rayleigh regime and further into the Mie scattering regime. While the Monte Carlo method provides fair agreement between experiment and simulation, this unfortunately do not help with determining the particle size and/or aspect ratio. However, it does give an important insight into the statistically random nature of multiple scattering given the fair agreement between experiment and these statistically random simulations.

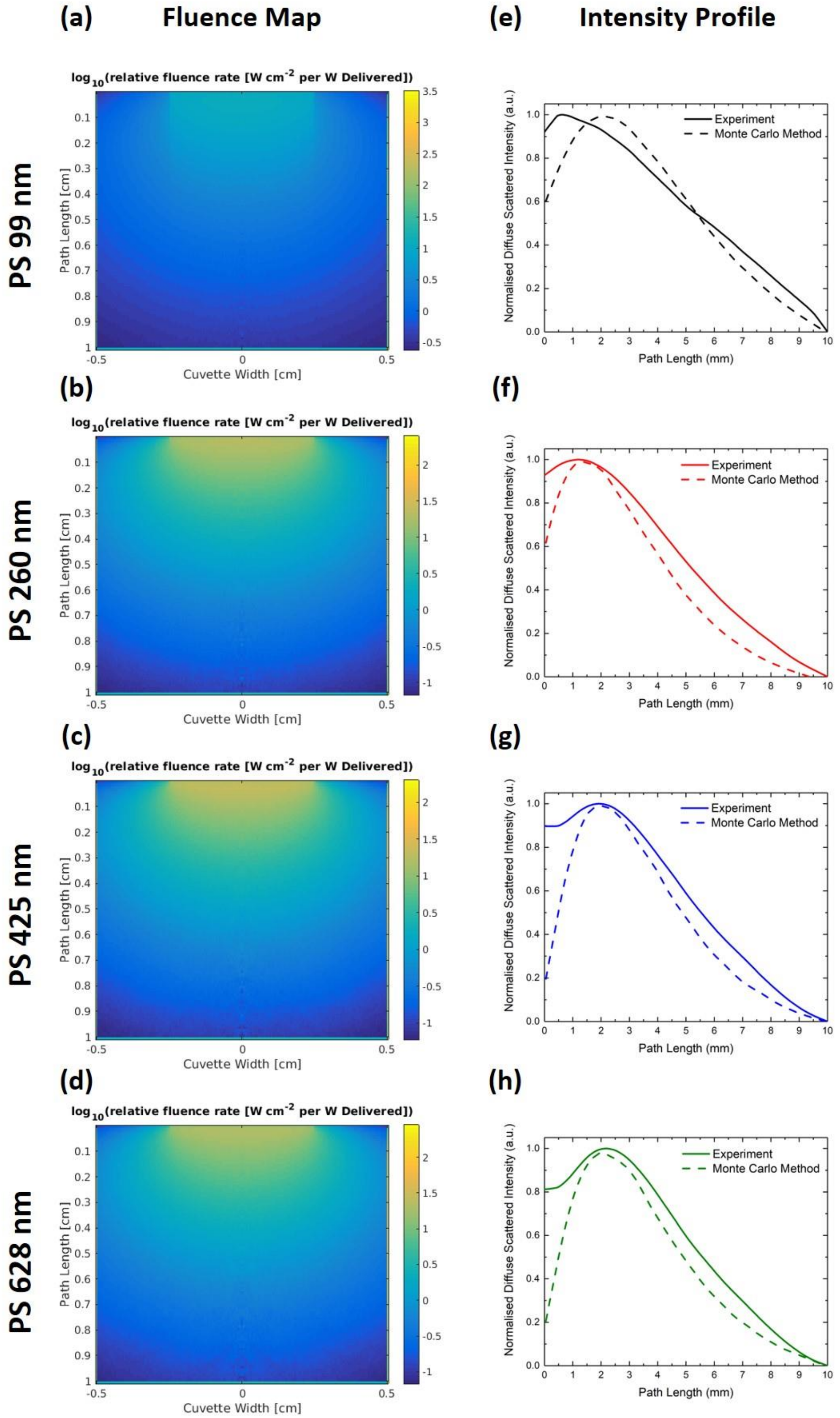

Figure 7.19 (a – d) Monte Carlo method simulations for light scattering through turbid suspensions of PS microspheres of various diameters and (e – h) experimental (solid lines) and simulated (dashed lines) normalised diffuse scattered intensities as a function of path length for the various PS nanosphere suspensions.

7.6 Measuring Angle Resolved Single Light Scattering

Samples of h-BN nanoflakes with an approximate lateral size of 400 nm and PS microspheres of diameter 425 nm were diluted to various concentrations ranging from 0.01 – 1 of the stock solutions. These were placed in a borosilicate glass vial and fixed stationary in the centre of a rotating stage. A HeNe laser beam was chopped at a frequency of 1123 Hz, linearly polarised using a Glan-Thompson polariser (LP), focused and collimated with two lenses (L1 and L2) onto the sample vial. The scattered light in all directions was measured as a function of angle by means of a photodiode mounted on a rotating stage. Another Glan-Thompson polariser (LP) was placed in front of the photodiode (PD) to allow the measurement of co-polarised and cross polarised signal. The rotation of the stage was controlled using a custom-written LabView code. The input polarisation was switched between TE and TM polarisation using a half-wave plate (HWP) positioned after the first polariser. The stability of the laser was monitored by redirecting a portion of the beam intensity onto a second photodiode connected to a Signal Recovery lock-in amplifier by means of a beam splitter (BS). Any fluctuations in the laser output were accounted for as part of the code by taking the ratio of the detected scattered signal to the input reference signal. The data obtained was output as a .csv file and post-processed in Origin. Figure 7.20 shows a schematic diagram of this setup.

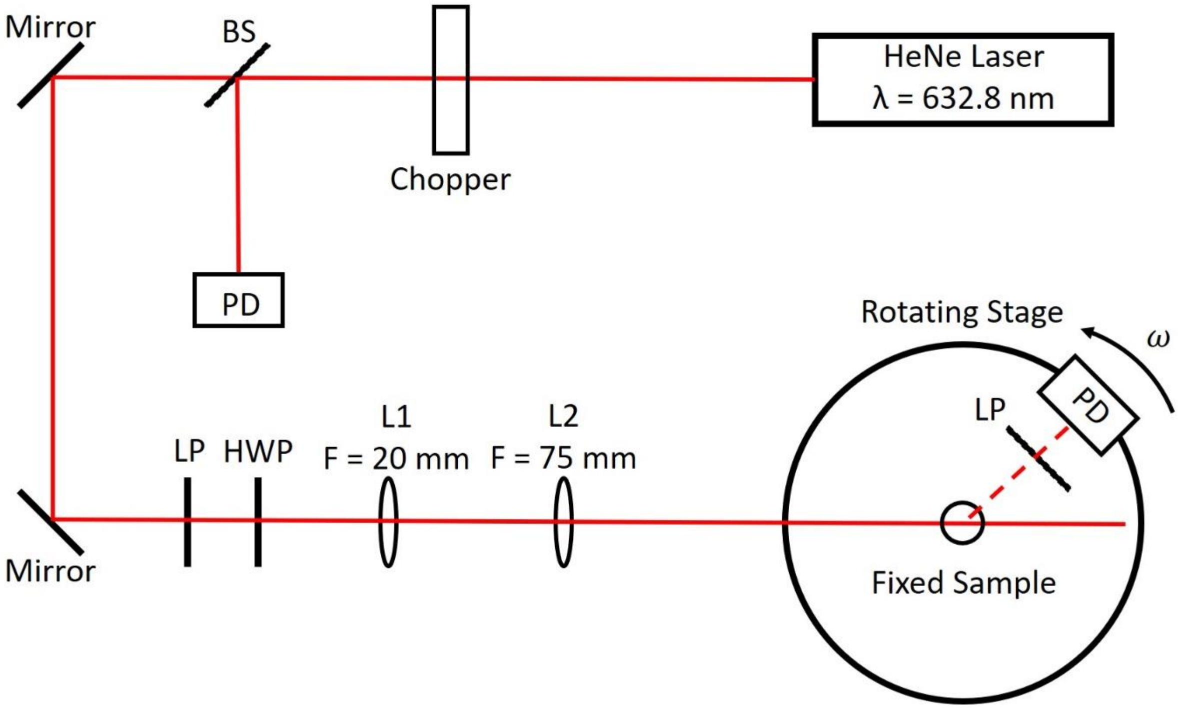

Figure 7.20 Schematic diagram of the angle-resolved single scattering setup.

7.7 Angle Resolved Single Light Scattering of Aqueous Suspensions of h-BN

Figure 7.21 (a) and (b) show a comparison of the co-polarised angle resolved single scattering for 2D h-BN and PS microspheres, respectively, for a range of concentrations of the original stock solution of which the mass concentration was unknown in the angular range 5˚ – 145˚.

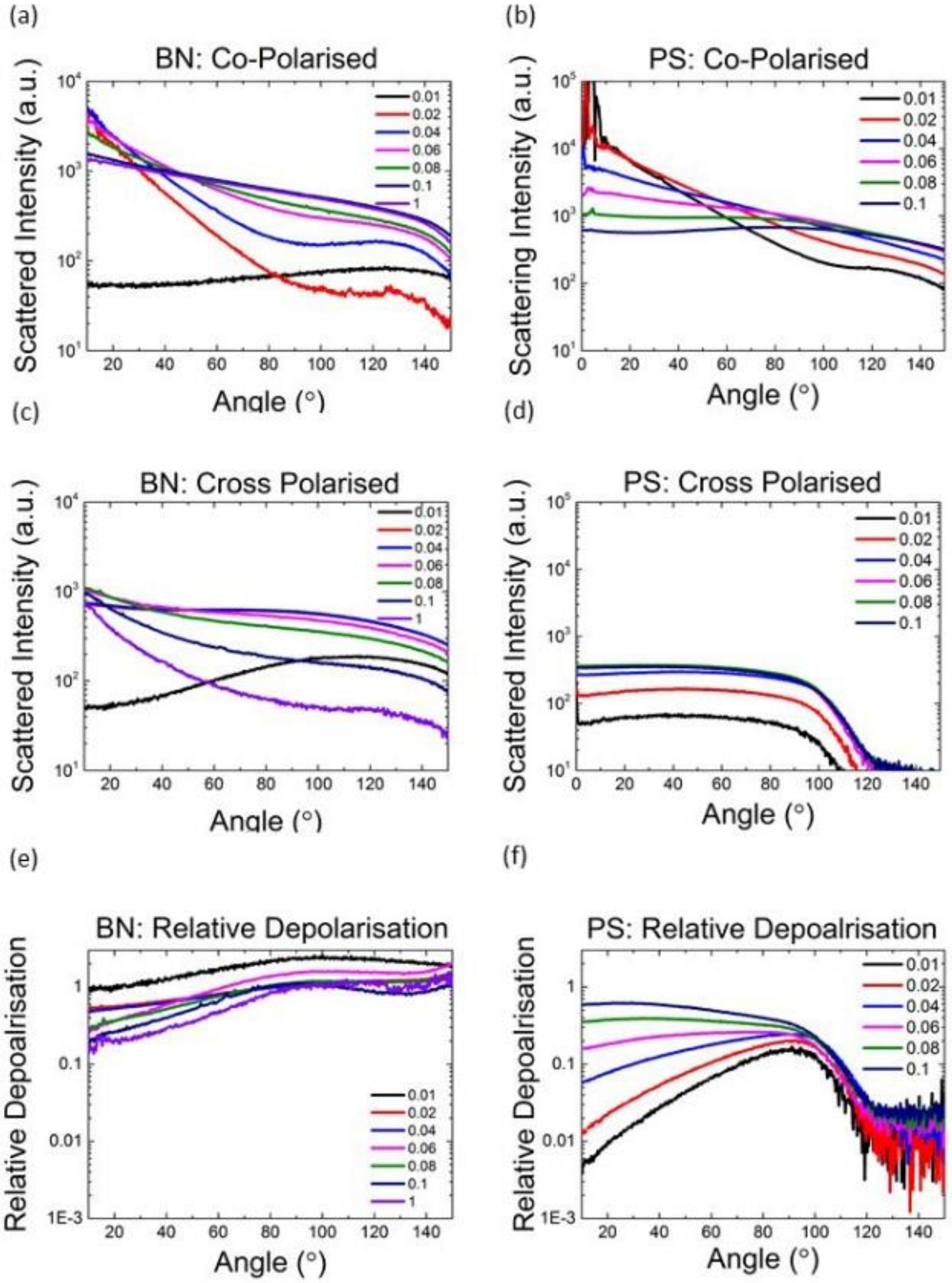

Figure 7.21 Scattered light intensity as a function of angle for (a) h-BN nanoflakes and (b) PS nanospheres of diameter 400 nm for co-polarized incidence and collection, h-BN nanoflakes (c) and 400 nm PS nanospheres (d) for cross polarized incidence and collection, and relative depolarisation for h-BN (e) and PS nanospheres (f). The specified concentrations are multiples of the initial stock concentration which was unknown.

There is a variation in the magnitude of scattered light of over 3 orders in this range. The trends of decreasing light scattering at larger angles for both materials are quite similar, however, the h-BN exhibits a stronger fall-off than similarly dilute concentrations of PS nanospheres. The angular scattering properties in the multiple scattering regime of both samples become similar, however the particle shape has an important contribution to the scattering at lower concentrations. This is shown in Figure 7.21(c) and (d) which compares the cross-polarised scattered light intensity from the h-BN and PS samples respectively. The h-BN shows a much larger cross-polarised scattering intensity than the PS nanospheres due to the strong depolarising properties of the highly anisotropic 2D h-BN particles. The relative depolarisation, which is the ratio of the cross-polarised signal to the co-polarised signal, is presented in Figure 7.21(e) and (f) to highlight the depolarising properties of the h-BN flakes. These figures show that the depolarisation is more uniform for the h-BN particles than for the PS nanospheres and that the depolarisation is not as dependent on particle concentration. A distinct difference between scattering from 2D and 3D particles becomes clear for scattering at higher angles and for cross-polarised incident light.

7.8 Random Lasing in Aqueous Suspensions of h-BN

Random lasing can be observed in multiple scattering media. Any highly scattering medium with a mean free path, l, much smaller than the scattering medium that also amplifies light via stimulated emission can be considered a random laser. Commonly, random lasers are made of a gain-exhibiting dye in a suspension of highly scattering spherical colloidal particles [69][70]. Initial spontaneous emission followed by subsequent stimulated emission leads to amplification. Random lasers operate in three main scattering regimes: the localisation regime, where the scattering mean free path, $l_S \leq \lambda$ [71], the diffuse scattering regime, $\lambda \leq l_S \leq L$ [72], and the weak scattering regime $l_S \geq L$ [73]. Here, L is the length of the sample and l_S is the scattering mean free path, $l_S = \frac{1}{\mu_S}$, where μ_S is the scattering coefficient which is the number of scattering interactions per unit distance. When $l_s \geq l_g$, where l_g is the gain length, random lasing occurs. Unlike cavity-based lasers, random lasers output radiation over the entire solid angle of 4π, making them ideal for use in displays. Potential applications of these lasers include remote temperature sensing in hostile environments by probing the emission spectra of a piece of random lasing material, unique security tags on documents such as bank notes and identification tags on military vehicles [74]. More recently, random lasers have even shown great promise in medical diagnostics for distinguishing cancerous tissue from healthy tissue [62]. The large scattering cross section and low intrinsic absorption of 2D h-BN makes it an ideal candidate material for use in random lasers. By tuning the size and concentration of this material, lasers with highly tuneable mode volumes could be produced.

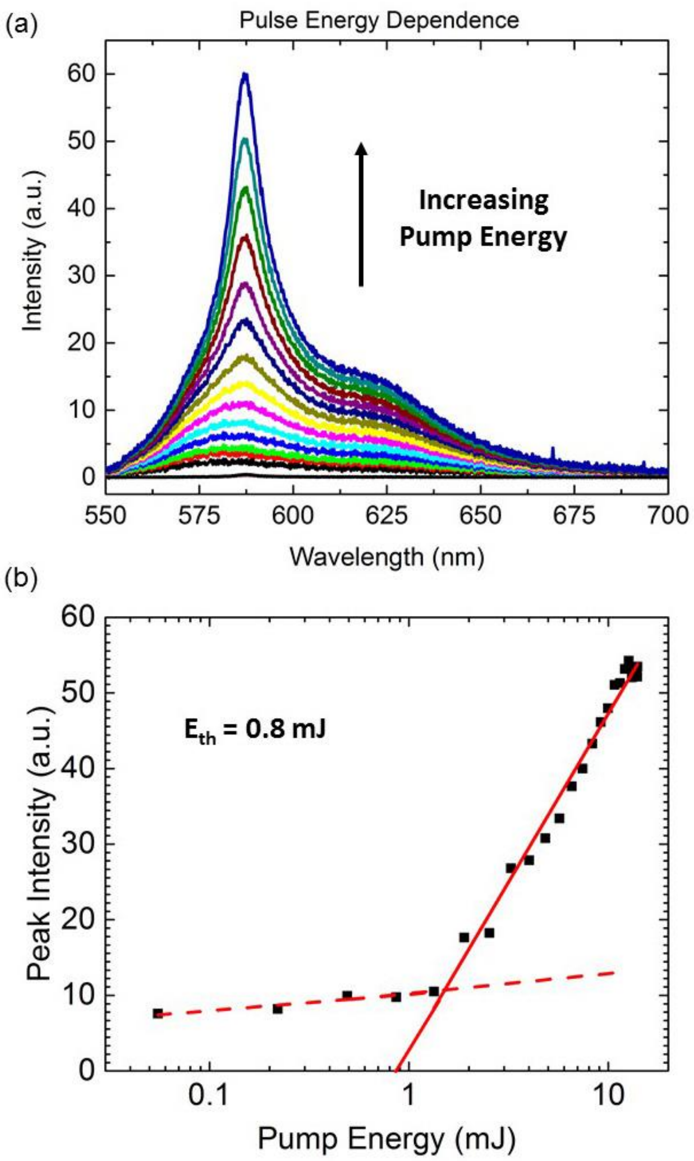

Figure 7.22 (a) PL spectrum for increasing incident pump energy. Peak forming at 587nm (b) Light-Light curve showing onset of lasing with threshold at pump energy of 0.8 mJ.

Figure 7.22(a) presents the PL spectrum for a highly multiply scattering suspension of h-BN nanoflakes with Rhodamine B dye. The data was taken using a green pump laser of 532 nm wavelength with variable power output. As the incident power of the pump laser increased a clear narrowing peak about 587 nm is observed. Figure 7.22(b) presents the peaking intensity at 587 nm as a function of the pump laser intensity in mJ. The data points fitted with a solid red line shows the onset of lasing which when extrapolated back onto the abscissa gives a lasing threshold energy of 0.8 mJ.

7.9 Conclusion

While light scattering by homogenous spheres of all sizes has been well understood and easily modelled for quite some time, the light scattering from extremely non-spherical particles, particularly atomically thin 2D particles still remains difficult to approach analytically. In this chapter, we examined the angle-resolved single scattering of non-absorbing h-BN nanoflakes of various lateral sizes compared to spherical PS nanosphere references of comparable diameters. We have demonstrated that 2D h-BN nanoflakes exhibit greater randomisation of polarisation and depolarisation than a spherical reference of comparable size. We also observed random lasing in a highly scattering suspension of h-BN nanoflakes acting as a scattering medium with Rhodamine B as the optical gain medium. As well as this, we studied in depth the path-length dependent variation in intensity of 632.8 nm HeNe laser beam passing through a turbid suspension of these h-BN nanoflake and PS nanosphere samples. Several analytical and numerical models were considered to theoretically explain this behaviour. While each model had its drawbacks, the analytical Two-Stream Approximation model achieved the greatest match between theory and experiment, followed closely by the numerical Monte Carlo method. Hartel Theory however only had partial success in explaining this multiple scattering behaviour. In the multiple scattering regime, very little qualitative difference was noted between the h-BN nanoflakes compared to the PS nanospheres. Thus, we conclude that these highly scattering 2D nanoflakes qualitatively behave like spheres of equivalent diameter to their lateral size. Furthermore, we point out that this path-length – intensity variation technique can be used to estimate the lateral size of such flakes by comparing them to spheres of similar diameter, However, the accuracy of this technique is highly dependent on the range of PS nanospheres available to act as a size reference. While determining exact particle size / aspect ratio is greatly desired, we have concluded that such a measurement is not possible with any of the techniques examined in this research. In fact, such a feat may be impossible, leading several research teams to study the application of multiple scattering media as a potential method of producing un-hackable statistically random encryption keys [75].

References

[1] K. S. Novoselov *et al.*, “Electric Field Effect in Atomically Thin Carbon Films,” *Science*, vol. 306, no. 5696, pp. 666 LP – 669, Oct. 2004.

[2] M. Chhowalla, H. S. Shin, G. Eda, L.-J. Li, K. P. Loh, and H. Zhang, “The chemistry of two-dimensional layered transition metal dichalcogenide nanosheets,” *Nat. Chem.*, vol. 5, p. 263, Mar. 2013.

[3] A. Takagaki *et al.*, “Titanium Niobate and Titanium Tantalate Nanosheets as Strong Solid Acid Catalysts,” *J. Phys. Chem. B*, vol. 108, no. 31, pp. 11549–11555, Aug. 2004.

[4] L. Peng, X. Peng, B. Liu, C. Wu, Y. Xie, and G. Yu, “Ultrathin Two-Dimensional MnO_2/Graphene Hybrid Nanostructures for High-Performance, Flexible Planar Supercapacitors,” *Nano Lett.*, vol. 13, no. 5, pp. 2151–2157, May 2013.

[5] V. Nicolosi, M. Chhowalla, M. G Kanatzidis, M. S Strano, and J. Coleman, "*Liquid Exfoliation of Layered Materials*," vol. 340. 2013.

[6] J. F. Annett, “Metals in flatland,” *Nat. Phys.*, vol. 8, p. 8, Dec. 2011.

[7] H. Liu *et al.*, “Phosphorene: An Unexplored 2D Semiconductor with a High Hole Mobility,” *ACS Nano*, vol. 8, no. 4, pp. 4033–4041, Apr. 2014.

[8] Y. Ma, Y. Dai, M. Guo, C. Niu, Y. Zhu, and B. Huang, “Evidence of the Existence of Magnetism in Pristine VX2 Monolayers (X = S, Se) and Their Strain-Induced Tunable Magnetic Properties,” *ACS Nano*, vol. 6, no. 2, pp. 1695–1701, Feb. 2012.

[9] M. O’Brien, N. McEvoy, D. Hanlon, T. Hallam, J. N. Coleman, and G. S. Duesberg, “Mapping of Low-Frequency Raman Modes in CVD-Grown Transition Metal Dichalcogenides: Layer Number, Stacking Orientation and Resonant Effects,” *Sci. Rep.*, vol. 6, 2016.

[10] J.-G. Kho, K.-T. Moon, J.-H. Kim, and D.-P. Kim, “Properties of Boron Nitride (B_xN_y) Films Produced by the Spin-Coating Process of Polyborazine,” *J. Am. Ceram. Soc.*, vol. 83, no. 11, pp. 2681–2683, Nov. 2000.

[11] N. Mason and A. Kapitulnik, “Dissipation Effects on the Superconductor-Insulator Transition in 2D Superconductors,” *Phys. Rev. Lett.*, vol. 82, no. 26, pp. 5341–5344, Jun. 1999.

[12] Y. Jing, Z. Zhou, C. R. Cabrera, and Z. Chen, “Metallic VS2 Monolayer: A Promising 2D Anode Material for Lithium Ion Batteries,” *J. Phys. Chem. C*, vol. 117, no. 48, pp. 25409–25413, Dec. 2013.

[13] N. H. Al-Hardan, M. J. Abdullah, N. M. Ahmed, F. K. Yam, and A. Abdul Aziz, “UV photodetector behavior of 2D ZnO plates prepared by electrochemical deposition,” *Superlattices Microstruct.*, vol. 51, no. 6, pp. 765–771, 2012.

[14] Y. Xu, W. Hong, H. Bai, C. Li, and G. Shi, “Strong and ductile poly(vinyl alcohol)/graphene oxide composite films with a layered structure,” *Carbon N. Y.*, vol. 47, no. 15, pp. 3538–3543, 2009.

[15] E. K. Wujcik and C. N. Monty, “Nanotechnology for implantable sensors: carbon nanotubes and graphene in medicine,” *Wiley Interdiscip. Rev. Nanomedicine Nanobiotechnology*, vol. 5, no. 3, pp. 233–249, May 2013.

[16] S. Das, D. Pandey, J. Thomas, and T. Roy, “The Role of Graphene and Other 2D Materials in Solar Photovoltaics,” *Adv. Mater.*, vol. 31, no. 1, p. 1802722, 2019.

[17] C. Oshima and A. Nagashima, “Ultra-thin epitaxial films of graphite and hexagonal boron nitride on solid surfaces,” *J. Phys. Condens. Matter*, vol. 9, no. 1, pp. 1–20, 1997.

[18] S. Sarkar, “The Fabrication Of Polymer-derived Sicn/sibcn Ceramic Nanostructures And Investigation Of Their Structure-property Relationship,” *Ph.D.*, 2010.

[19] J. Eichler and C. Lesniak, "*Boron Nitride (BN) and BN Composites for High-Temperature Applications*," vol. 28. 2008.

[20] J. Y. Lu *et al.*, “Atomically thin optical lenses and gratings,” *Light Sci. Appl.*, vol. 5, no. 3, 2016.

[21] C. Backes *et al.*, “Production of Highly Monolayer Enriched Dispersions of Liquid-Exfoliated Nanosheets by Liquid Cascade Centrifugation,” *ACS Nano*, vol. 10, no. 1, pp. 1589–1601, Jan. 2016.

[22] J. N. Coleman *et al.*, “Two-Dimensional Nanosheets Produced by Liquid Exfoliation of Layered Materials,” *Science (80-.).*, vol. 331, no. 6017, pp. 568 LP – 571, Feb. 2011.

[23] S. A. O’Brien, A. Harvey, A. Griffin, T. Donnelly, D. Mulcahy, J. N. Coleman, J. F. Donegan and D McCloskey, “Light scattering and random lasing in aqueous suspensions of hexagonal boron nitride nanoflakes,” *Nanotechnology*, vol. 28, no. 47, p. 47LT02,

2017.

[24] L. E. Hargrove, R. L. Fork, and M. A. Pollack, “Locking of He–Ne Laser Modes Induced by Synchronous Intracavity Modulation,” *Appl. Phys. Lett.*, vol. 5, no. 1, pp. 4–5, Jul. 1964.

[25] S. John, “Electromagnetic Absorption in a Disordered Medium near a Photon Mobility Edge,” *Phys. Rev. Lett.*, vol. 53, no. 22, pp. 2169–2172, Nov. 1984.

[26] H. Cao, Y. G. Zhao, S. T. Ho, E. W. Seelig, Q. H. Wang, and R. P. H. Chang, “Random Laser Action in Semiconductor Powder,” *Phys. Rev. Lett.*, vol. 82, no. 11, pp. 2278–2281, Mar. 1999.

[27] H. Schnablegger and O. Glatter, “Sizing of colloidal particles with light scattering: corrections for beginning multiple scattering,” *Appl Opt*, vol. 34, no. 18, pp. 3489–3501, 1995.

[28] B. J. Berne and R. Pecora, "*Dynamic Light Scattering: With Applications to Chemistry, Biology, and Physics*," Dover Publications, 2013.

[29] K. R. Paton *et al.*, “Scalable production of large quantities of defect-free few-layer graphene by shear exfoliation in liquids,” *Nat Mater*, vol. 13, no. 6, pp. 624–630, 2014.

[30] H. C. Hulst and H. C. van de Hulst, "*Light Scattering by Small Particles*," Dover Publications, 1981.

[31] C. F. Bohren and D. R. Huffman, "*Absorption and Scattering of Light by Small Particles*," Wiley, 2008.

[32] T. A. Germer, “Light scattering by slightly nonspherical particles on surfaces,” *Opt. Lett.*, vol. 27, no. 13, p. 1159, 2007.

[33] A. B. Evlyukhin, C. Reinhardt, E. Evlyukhin, and B. N. Chichkov, “Multipole analysis of light scattering by arbitrary-shaped nanoparticles on a plane surface,” *J. Opt. Soc. Am. B*, vol. 30, no. 10, pp. 2589–2598, 2013.

[34] L. G. Henyey and J. L. Greenstein, "*Diffuse radiation in the Galaxy*," vol. 3. 1941.

[35] V. I. Haltrin, “One-parameter two-term Henyey-Greenstein phase function for light scattering in seawater,” *Appl. Opt.*, vol. 41, no. 6, pp. 1022–1028, 2002.

[36] J. Stam, “Multiple scattering as a diffusion process BT - Rendering Techniques ’95,” 1995, pp. 41–50.

[37] J. A. Coakley and P. Chylek, “The Two-Stream Approximation in Radiative Transfer: Including the Angle of the Incident Radiation,” *J. Atmos. Sci.*, vol. 32, no. 2, pp. 409–418, Feb. 1975.

[38] Q. Fu, K. N. Liou, M. C. Cribb, T. P. Charlock, and A. Grossman, “Multiple Scattering Parameterization in Thermal Infrared Radiative Transfer,” *J. Atmos. Sci.*, vol. 54, no. 24, pp. 2799–2812, Dec. 1997.

[39] J. J. Rehr and R. C. Albers, “Scattering-matrix formulation of curved-wave multiple-scattering theory: Application to x-ray-absorption fine structure,” *Phys. Rev. B*, vol. 41, no. 12, pp. 8139–8149, Apr. 1990.

[40] X. H. Wu, A. Yamilov, H. Noh, H. Cao, E. W. Seelig, and R. P. H. Chang, “Random lasing in closely packed resonant scatterers,” *J. Opt. Soc. Am. B*, vol. 21, no. 1, pp. 159–167, 2004.

[41] E. Berrocal, D. L. Sedarsky, M. E. Paciaroni, I. V Meglinski, and M. A. Linne, “Laser

light scattering in turbid media Part I: Experimental and simulated results for the spatial intensity distribution,” *Opt Express*, vol. 15, no. 17, pp. 10649–10665, 2007.

[42] S. Stramigioli, A. van der Schaft, B. Maschke, and C. Melchiorri, “Geometric scattering in robotic telemanipulation,” *IEEE Trans. Robot. Autom.*, vol. 18, no. 4, pp. 588–596, 2002.

[43] H. Moosmüller and W. P. Arnott, “Particle Optics in the Rayleigh Regime,” *J. Air Waste Manage. Assoc.*, vol. 59, no. 9, pp. 1028–1031, Sep. 2009.

[44] J. P. B. Mueller and F. Capasso, “Asymmetric surface plasmon polariton emission by a dipole emitter near a metal surface,” *Phys. Rev. B*, vol. 88, no. 12, p. 121410, Sep. 2013.

[45] S. V Lobanov, T. Weiss, D. Dregely, H. Giessen, N. A. Gippius, and S. G. Tikhodeev, “Emission properties of an oscillating point dipole from a gold Yagi-Uda nanoantenna array,” *Phys. Rev. B*, vol. 85, no. 15, p. 155137, Apr. 2012.

[46] C. Backes *et al.*, “Edge and confinement effects allow in situ measurement of size and thickness of liquid-exfoliated nanosheets,” *Nat Commun*, vol. 5, 2014.

[47] E. Berrocal, D. L. Sedarsky, M. E. Paciaroni, I. V Meglinski, and M. A. Linne, “Laser light scattering in turbid media Part II: Spatial and temporal analysis of individual scattering orders via Monte Carlo simulation,” *Opt Express*, vol. 17, no. 16, pp. 13792–13809, 2009.

[48] G. W. Petty, "*A first course in atmospheric radiation*," Madison, Wis.: Sundog Pub., 2006.

[49] D. Toublanc, “Henyey–Greenstein and Mie phase functions in Monte Carlo radiative transfer computations,” *Appl. Opt.*, vol. 35, no. 18, pp. 3270–3274, 1996.

[50] W. E. Vargas and G. A. Niklasson, “Intensity of diffuse radiation in particulate media,” *J. Opt. Soc. Am. A*, vol. 14, no. 9, pp. 2253–2262, 1997.

[51] W. L. Smith, “Iterative solution of the radiative transfer equation for the temperature and absorbing gas profile of an atmosphere,” *Appl. Opt.*, vol. 9, no. 9, pp. 1993–1999, 1970.

[52] G. Becker, J.-U. Grooß, D. S. McKenna, and R. Müller, “Stratospheric photolysis frequencies: Impact of an improved numerical solution of the radiative transfer equation,” *J. Atmos. Chem.*, vol. 37, no. 3, pp. 217–229, 2000.

[53] I. P. Grant and G. E. Hunt, “Solution of radiative transfer problems using the invariant S n method,” *Mon. Not. R. Astron. Soc.*, vol. 141, no. 1, pp. 27–41, 1968.

[54] M. I. Chahine, “A general relaxation method for inverse solution of the full radiative transfer equation,” *J. Atmos. Sci.*, vol. 29, no. 4, pp. 741–747, 1972.

[55] N. Kryzhevoi, G. V Efimov, and R. Wehrse, “Radiative Transfer Equation: Analytical Solution in the Two-stream Approximation,” in *Astronomische Gesellschaft Meeting Abstracts*, 2000, vol. 17.

[56] G. Koh, “Radiative transfer in falling snow: A two-stream approximation,” *US Army Corps of Engineers, CRREL, Report 89-6*, 1989.

[57] K. Stamnes, “The theory of multiple scattering of radiation in plane parallel atmospheres,” *Rev. Geophys.*, vol. 24, no. 2, pp. 299–310, 1986.

[58] Q. Fu, “A new parameterization of an asymmetry factor of cirrus clouds for climate models,” *J. Atmos. Sci.*, vol. 64, no. 11, pp. 4140–4150, 2007.

[59] J. Heintzenberg *et al.*, “Measurements and modelling of aerosol single-scattering albedo: Progress, problems and prospects,” *Contrib. to Atmos. Phys.*, vol. 70, no. 4, pp. 249–263,

1997.

[60] M. M. R. Williams, “The transport and diffusion theory of a line source in an infinite half-space with internal reflection,” *Ann. Nucl. Energy*, vol. 34, no. 11, pp. 910–921, 2007.

[61] Y. Gu and K. N. Liou, “Radiation parameterization for three-dimensional inhomogeneous cirrus clouds: Application to climate models,” *J. Clim.*, vol. 14, no. 11, pp. 2443–2457, 2001.

[62] R. C. Polson and Z. V. Vardeny, “Random lasing in human tissues,” *Appl. Phys. Lett.*, vol. 85, no. 7, pp. 1289–1291, 2004.

[63] H. K. Paul, “Spatial light-scattering analysis as a means of characterizing and classifying non-spherical particles,” *Meas. Sci. Technol.*, vol. 9, no. 2, p. 141, 1998.

[64] D. Calloway, “Beer-Lambert Law,” *J. Chem. Educ.*, vol. 74, no. 7, p. 744, 2009.

[65] J. Mellqvist and A. Rosfin, “DOAS for flue gas monitoring—II. Deviations from the Beer-Lambert law for the U.V./visible absorption spectra of NO, NO_2, SO_2 and NH_3,” vol. 56, no. 2, pp. 209–224, 1996.

[66] S. Chandrasekhar, "*Radiative Transfer*," Dover Publications, 1960.

[67] C.-M. Chu and S. W. Churchill, “Representation of the Angular Distribution of Radiation Scattered by a Spherical Particle,” *J. Opt. Soc. Am.*, vol. 45, no. 11, pp. 958–962, 1955.

[68] E. V. William and A. N. Gunnar, “Forward-scattering ratios and average pathlength parameter in radiative transfer models,” *J. Phys. Condens. Matter*, vol. 9, no. 42, p. 9083, 1997.

[69] V. M. Shalaev, *Optical Properties of Nanostructured Random Media*. Springer Berlin Heidelberg, 2002.

[70] F. Luan, B. Gu, A. S. L. Gomes, K.-T. Yong, S. Wen, and P. N. Prasad, “Lasing in nanocomposite random media,” *Nano Today*, vol. 10, no. 2, pp. 168–192, 2015.

[71] P. Sebbah and C. Vanneste, “Random laser in the localized regime,” *Phys. Rev. B*, vol. 66, no. 14, p. 144202, Oct. 2002.

[72] D. S. Wiersma and A. Lagendijk, “Light diffusion with gain and random lasers,” *Phys. Rev. E*, vol. 54, no. 4, pp. 4256–4265, Oct. 1996.

[73] R. C. Polson and Z. V Vardeny, “Organic random lasers in the weak-scattering regime,” *Phys. Rev. B*, vol. 71, no. 4, p. 45205, Jan. 2005.

[74] D. S. Wiersma, “The physics and applications of random lasers,” *Nat Phys*, vol. 4, no. 5, pp. 359–367, 2008.

[75] R. Uppu *et al.*, “Asymmetric cryptography with physical unclonable keys,” *arXiv Prepr. arXiv1802.07573*, 2018.

Chapter 8: Future Work

8.1 Introduction

In Chapter 4, we demonstrated the achievement of near-perfect absorption in commercial ITO films via the application of a 10 nm Pt backing. In Chapter 5, we discussed the development of a technique and recipe for the deposition of high-quality thin film ITO with ENZ behaviour, and in Chapter 6 we discussed the role of the metal backing in these ITO – Metal structures. In this work, we demonstrated significant enhancement of absorption from ITO films by exciting the Ferrell – Berreman and non-radiative ENZ mode in both commercial and locally fabricated ITO thin films and demonstrated the achievement of near-perfect absorption from the excitation of these modes by applying a 10 nm Pt backing. Furthermore, we demonstrated theoretically that NPA is achievable by most common metals and analysed the effects of metal backing thickness on this absorption. We found that any metal can achieve this NPA, however the maximum absorption and the thickness at which this maximum value is achieved is dependent on the refractive index of the metal used and its skin depth at the measured NPA wavelength. The combination of all this research has left us with a myriad of possibilities and avenues of research to explore with ITO and various metals. Particularly, the ability to locally fabricate our own ITO films allows the ability to produce various different geometries and combinations of ITO and other materials. In this chapter we will discuss and provide theoretical and simulated data for some of the possible structurers considered for future work.

8.2 Broadband Absorption from a Cr – ITO – Pt Multilayer Structure

In Chapter 6, we found that Cr achieved the worst performance for enhancing Ferrell – Berreman and ENZ mode absorption as a result of its relatively low κ-value and the small difference between the real and imaginary components of the complex refractive index in the region near 1100 nm as shown in Figure 6.1(a) of Chapter 6. However, this metal, having a particularly large skin depth can be used to our advantage in improving absorption from ITO – Metal multilayers. T-Matrix simulations were carried out for a Cr (10 nm) – ITO (127 nm) – Pt (10 nm) multilayer structure as depicted in Figure 8.1. As before, the optical constants for the ITO layer were specified by the Drude model using parameters obtained from spectroscopic ellipsometry on the 127 nm 8 – 12 Ω sq^{-1} commercial films, and the optical constants for Cr [1] and Pt [2] were obtained from the literature.

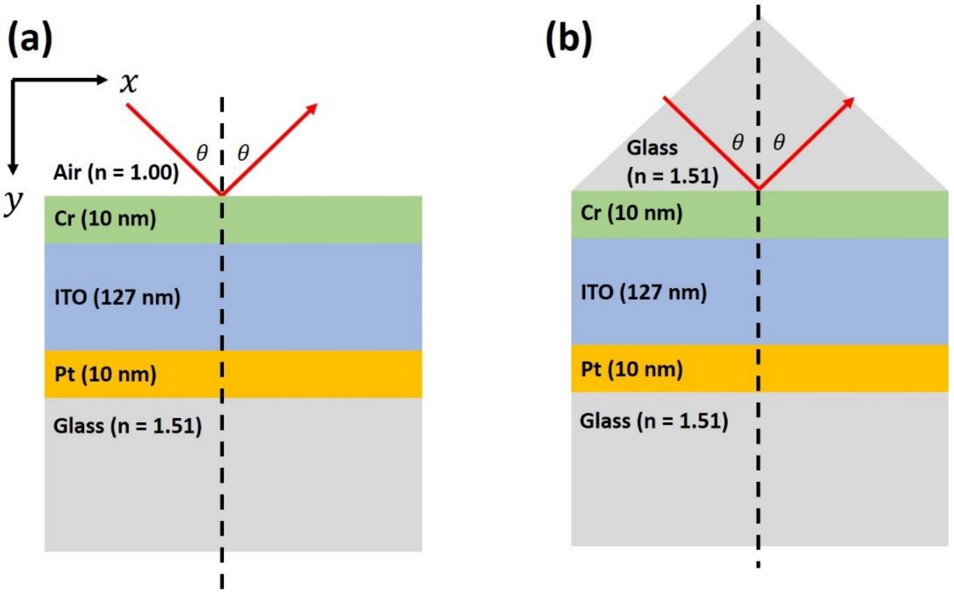

Figure 8.1 2D schematic of the Cr – ITO – Pt multilayer structure. Absorption from the structure was considered in the case of an air superstrate (a) and a glass superstrate (b).

As shown, the simulations were carried in two cases, excitation from an air superstrate in Figure 8.1(a) and from a glass superstrate in Figure 8.1(b). The reasoning for the addition of the 10 nm Cr layer on top was to increase absorption in non-resonant regions while allowing the light to still penetrate through to the ITO layer wherein the Ferrell – Berreman and non-radiative ENZ mode can be excited, as well as the IMI mode in the Pt layer. Several metals were considered as the capping layer, however only Cr exhibited a large enough skin depth and a low enough κ-value to not cause too much reflection of light. The simulated broadspectrum angle-resolved absorption is presented in Figure 8.2. As shown, in both cases the addition of the 10 nm Cr capping layer to the ITO – Pt structure causes significant broadband absorption that even extends into the upper wavelength limits of the visible range. The choice of substrate appears to cause a shift in the high-absorption feature to lower incident angles allowing easier excitation. However, a particularly useful feature of this structure is the existence of the high absorption features at normal incidence.

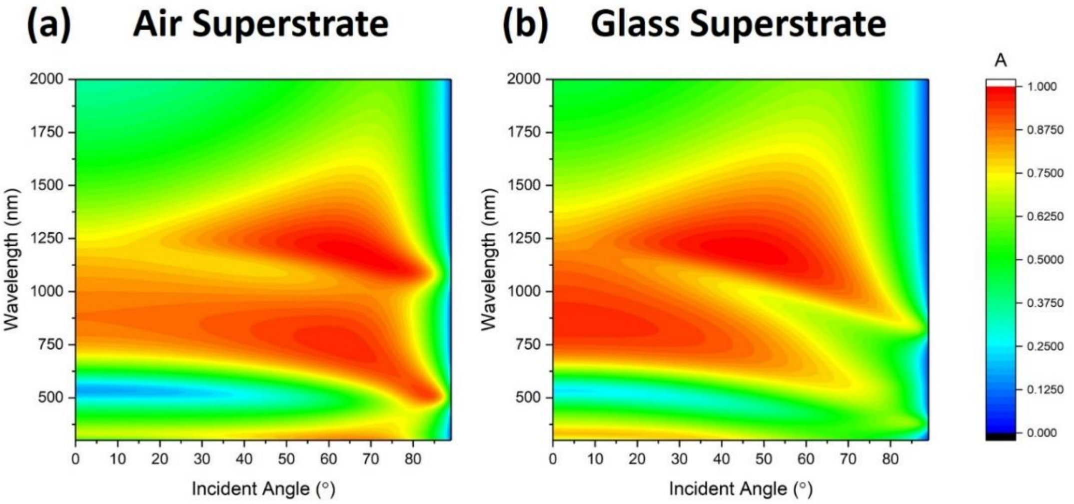

Figure 8.2 Broad spectrum angle-resolved absorption from a Cr (10 nm) – ITO (127 nm) – Pt (10 nm) multilayer structure excited from (a) an air superstrate and (b) a glass superstrate.

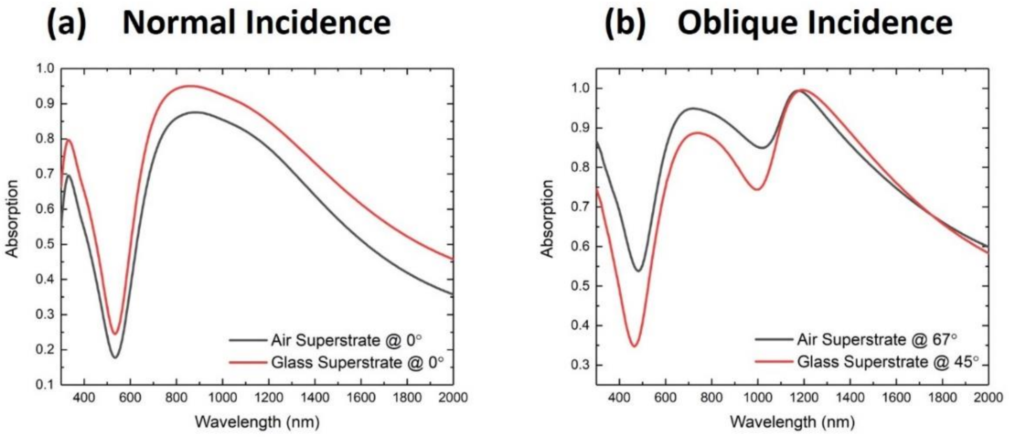

Figure 8.3 Absorption profile as a function of wavelength from a Cr (10 nm) – ITO (127 nm) – Pt (10 nm) multilayer structure at normal incidence (a) and oblique incidence (b).

As shown in Figure 8.3(a) significant absorption above 80% is achieved at normal incidence in the 800 nm – 1000 nm range and above 90% when excited from a glass superstrate. Figure 8.3(b) presents the absorption as a function of wavelength at the oblique angle of highest absorption when excited from both an air and glass superstrate. The profile when excited from air was taken at 67˚ incidence, and at 45˚ when excited from glass. As shown significant absorption is achieved in the 650 nm – 1200 nm range of great than 85%, and another high absorption region about 1200 nm, which is attributed to the ENZ behaviour of the ITO film. While significant broadspectrum and broad angular range absorption are achieved from this structure, not all of that absorption is due to the ITO layer itself. In fact, the high absorption in this structure is a combination of two different physical processes. While of course the absorption around 1200 nm is due to excitation of the Ferrell – Berreman and ENZ modes, the added absorption closer to the visible range is a result of exciting metal – insulator – metal (MIM) modes. Extensive research has previously been carried out on such MIM structures and the subsequent absorption from them [3][4][5][6]. For comparison, a further set of simulations were carried out replacing the ITO films with glass, i.e. a Cr – Glass – Pt structure. The resulting broadspectrum angle resolved absorption maps are presented in Figure 8.4 with the structure excited from an air superstrate (a) and a glass superstrate (b). Again, in both sets of simulations we see a high absorption feature extending across the 750 nm – 1500 nm spectral range. By exciting from a glass superstrate, we see a shift in the absorption feature to lower incident angle. Particularly, when exciting from air, the point of highest absorption is at about 60˚ and 900 nm, which gets pushed to normal incidence and spread over a larger wavelength range.

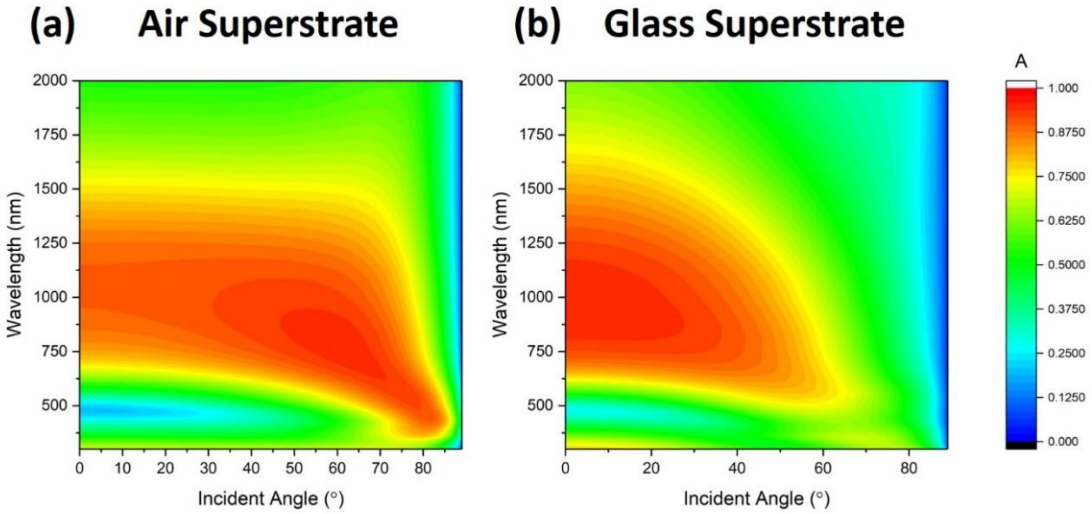

Figure 8.4 Broad spectrum angle-resolved absorption from a Cr (10 nm) – Glass (127 nm) – Pt (10 nm) multilayer structure excited from (a) an air superstrate and (b) a glass superstrate.

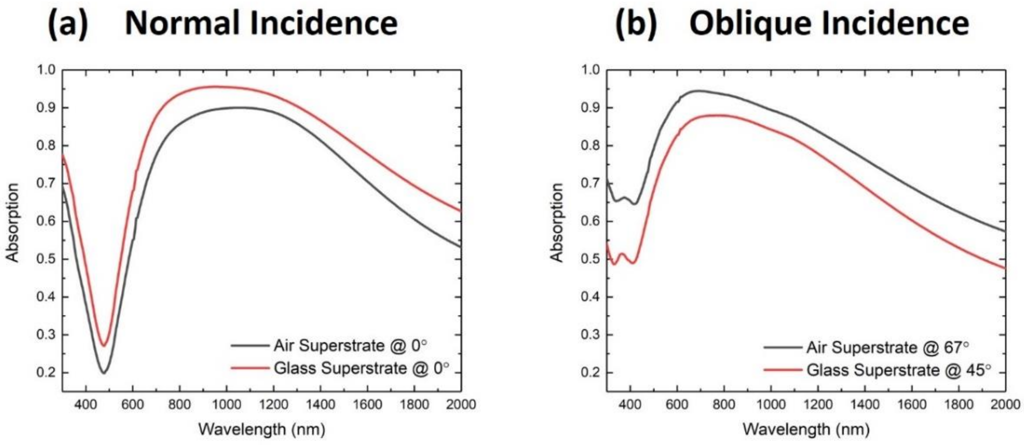

Figure 8.5 Absorption profile as a function of wavelength from a Cr (10 nm) – Glass (127 nm) – Pt (10 nm) multilayer structure at normal incidence (a) and oblique incidence (b).

Figure 8.5(a) and (b) present the absorption profiles as a function of wavelength at normal incidence and at the oblique angle of highest absorption for the Cr – Glass – Pt structure excited from air and glass. As shown, absorption of greater than 85% is achieved when exciting the structure from air, and above 90% when exciting from glass. For oblique incidence, we again see significant absorption of greater than 85% when exciting from glass and greater than 90% when exciting from air. For normal incidence, we can see that the absorption remains above 85% across the entirety of the 700 nm – 1500 nm spectral range, and across the 500 nm – 1300 nm spectral range at oblique incidence. However, most noticeable is the absence of the ENZ related absorption. This demonstrates that the broadspectrum and broad angular absorption from the Cr – ITO – Pt structure is a combination of ENZ related absorption and the high absorption achievable by MIM structures. The resulting combined structure offers great promise as a broadband absorber in the visible and NIR ranges and could potentially be considered for use in solar cell technology [7][8][9]. Given the outcome of the research in previous chapters, particularly the ability to now locally deposit ITO of various thicknesses, the production of this structure is now possible.

8.3 ENZ Induced Near Perfect Absorption at Visible Wavelengths

Initially upon starting this research into ENZ materials and the subsequent near-perfect absorption attainable from such materials, the goal was to attempt to shift the ENZ wavelength of the ITO films into the visible range. However, after much research it was discovered that achieving carrier concentrations sufficiently high to obtain near-zero permittivity in visible is very difficult by simply doping via the generation of oxygen vacancies and ion activation. Typically, ITO can hold carrier concentrations in the range 10^{19} – 10^{21} cm^{-3} [10]. To obtain an estimate of the carrier concentration that would be needed to achieve an ENZ wavelength in the visible range, an estimate was made using the expression

$$N = \left(\frac{4\pi^2 c^2}{\lambda_{ENZ}^2} + \gamma^2\right) m^* \varepsilon_0 \varepsilon_\infty \qquad (1)$$

where all parameters are the standard Drude parameters previously discussed in other chapters, N is the carrier concentration in [m^{-3}], e is the charge of an electron, γ is the scattering rate, and ε_0 and ε_∞ respectively are the permittivity of free space and the high frequency permittivity of ITO. m^* is the reduced mass of an electron and was taken to be $0.35m_0$ where m_0 is the rest mass of an electron. For this calculation, the values of the Drude parameters used for the ITO layer were those of the 127 nm 8 – 12 Ω sq^{-1} commercial ITO sample characterised in Chapter 3. The values used were, $\varepsilon_\infty = 3.6596$, $\gamma = 0.1893$, and λ_{ENZ} was allowed to vary across the 600 nm – 2000 nm range. The resulting data is plotted in Figure 8.6. As shown, a significantly higher carrier concentration is required to achieve ITO with an ENZ wavelength in the visible range. Such a material has yet to be demonstrated. However, there is an alternative route to achieving an ENZ wavelength in the visible range. Research carried out by Feigenbaum et al. (2010) [11] and published in Nano Letters experimentally demonstrates that by applying a voltage across a structure composed of a 350 nm Au layer, a 300 nm ITO layer, a 100 nm SiO_2 insulating layer, and a 20 nm Au layer as depicted in Figure 8.7, a 5 nm depletion layer with a higher localised carrier concertation, and hence short ENZ wavelength is achieved. This depletion layer is localised at the ITO – SiO_2 interface.

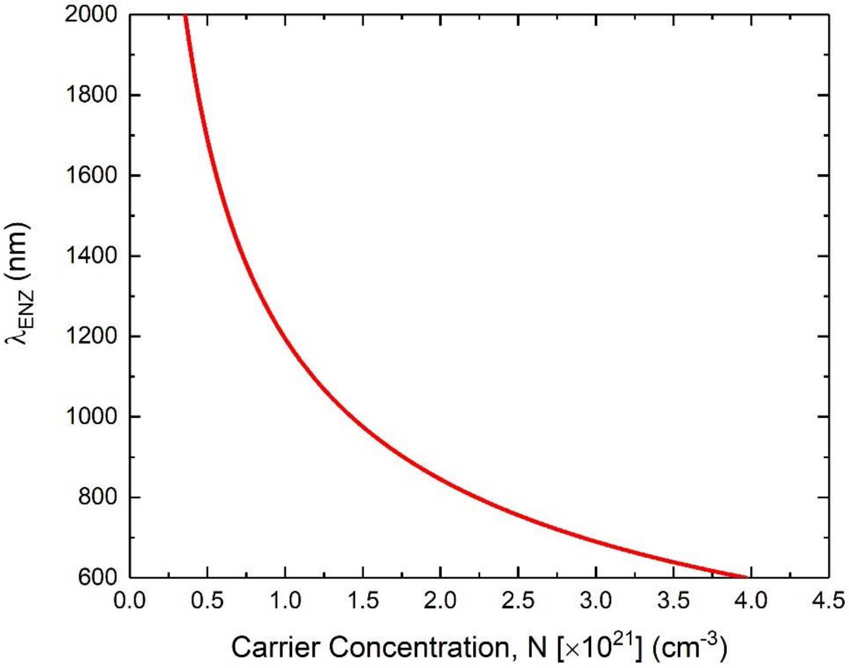

Figure 8.6 An estimation of the required carrier concentration needed to achieve an ENZ wavelength in the 600 nm – 2000 nm spectral range.

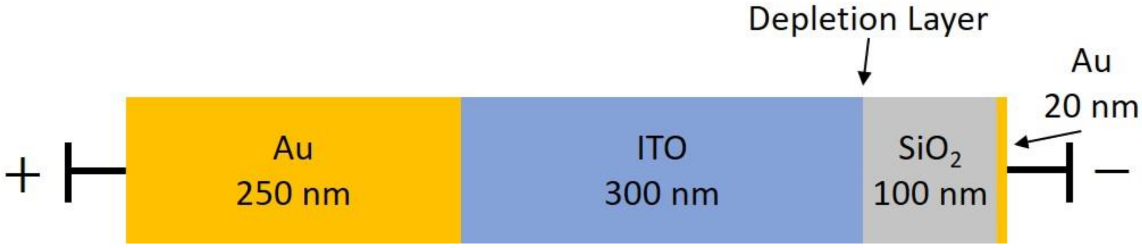

Figure 8.7 2D schematic of the structure studied by Feigenbaum *et al.* for the generation of ITO with an ENZ wavelength at visible frequencies. By applying an applied voltage in the 0 – 2.5 V range, significant concentration of charge carriers could be setup in the depletion layer leading to an increased localised carrier concentration and a visible range ENZ wavelength [11].

Feigenbaum et al. found that by applying a bias voltage between 0 – 2.5 V the localised carrier concentration in the depletion region could increase by an order of magnitude. The resulting large increase in carrier concentration shifts the ENZ region of the depletion layer to visible wavelengths. Figure 8.8 presents two graphs plotted using the data from the work of Feigenbaum et al. The localised carrier concentration in the depletion region as a function of applied voltage is presented in Figure 8.8(a) and the corresponding plasma frequency and ENZ wavelength in the same region are presented in (b).

As shown, by applying a bias voltage across the structure, the localised carrier concentration can be increased by an order of magnitude and the ENZ wavelength can be pushed close to the visible range to wavelengths as low as 800 nm.

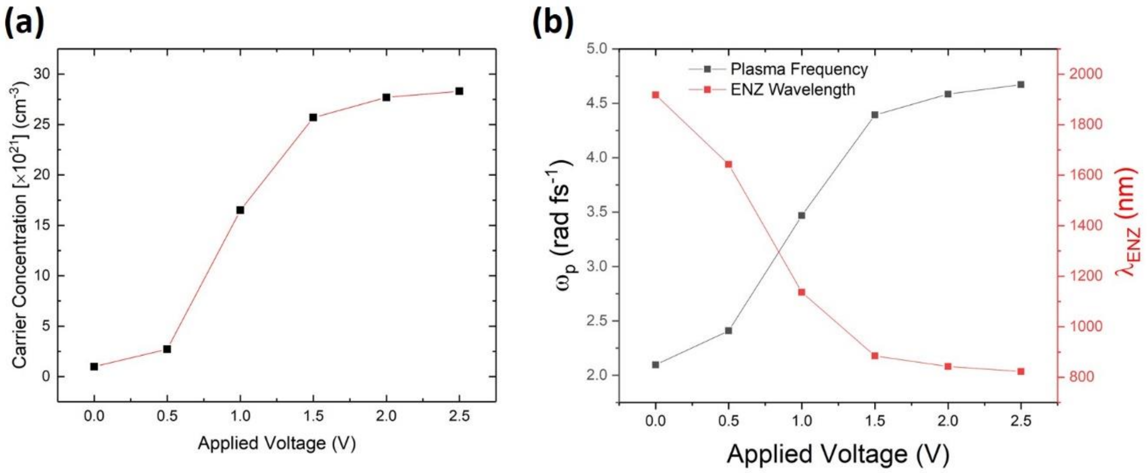

Figure 8.8 (a) Carrier concentration as a function of applied voltage for the depletion layer of the Au – ITO – SiO_2 – Au structure studied by Feigenbaum et al. and (b) the resulting plasma frequency (black) and ENZ wavelength (red) for the depletion region.

While depositing ITO with ENZ behaviour in the visible range may not be possible, this work demonstrates that achieving ENZ behaviour in the visible range is possible from ITO by applying a voltage, and thus it may be possible to also achieve near-perfect absorption in ITO at visible wavelengths by utilising this or a similar technique. Thus, a set of T-Matrix simulations were carried out to theoretically determine the absorption that such a structure would exhibit. In these simulations, presented in Figure 8.9, the previous Drude parameter values were used and the plasma frequency was chosen was $\omega_p = 6.00$ rad fs^{-1}, corresponding to an ENZ wavelength of $\lambda_{ENZ} = 600$ nm. Figure 8.9(a) presents the broadspectrum angle-resolved absorption from a 127 nm ITO with the aforementioned plasma frequency. As shown, a very clear absorption feature is noted just below 600 nm. The same absorption feature is again noted in Figure 8.9(b), however the addition of the 10 nm Pt backing has caused an enhancement of the absorption as in previous cases in the near-infrared range. In both graphs, the Ferrell – Berreman mode is located below the critical angle of 41˚ and the ENZ mode is located above 41˚ and extends to lower wavelengths.

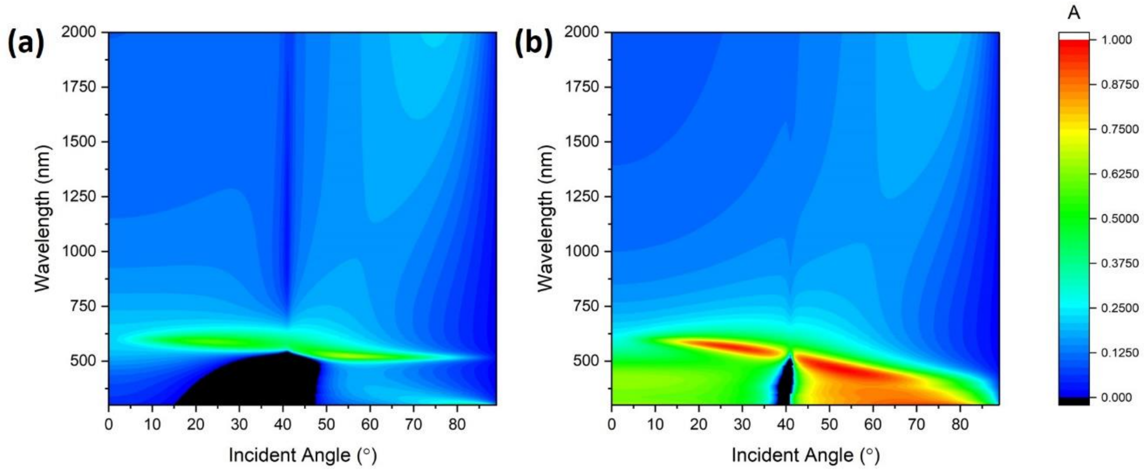

Figure 8.9 Broadspectrum angle-resolved absorption for (a) a 127 nm ITO with a plasma frequency, $\omega_p = 6.00$ rad fs^{-1}, and (b) a 127 nm ITO with a plasma frequency, $\omega_p = 6.00$ rad fs^{-1} and a 10 nm Pt backing. Both the Ferrell – Berreman mode, below 41° and the non-radiative ENZ mode, above 41° are clearly visible below 600 nm.

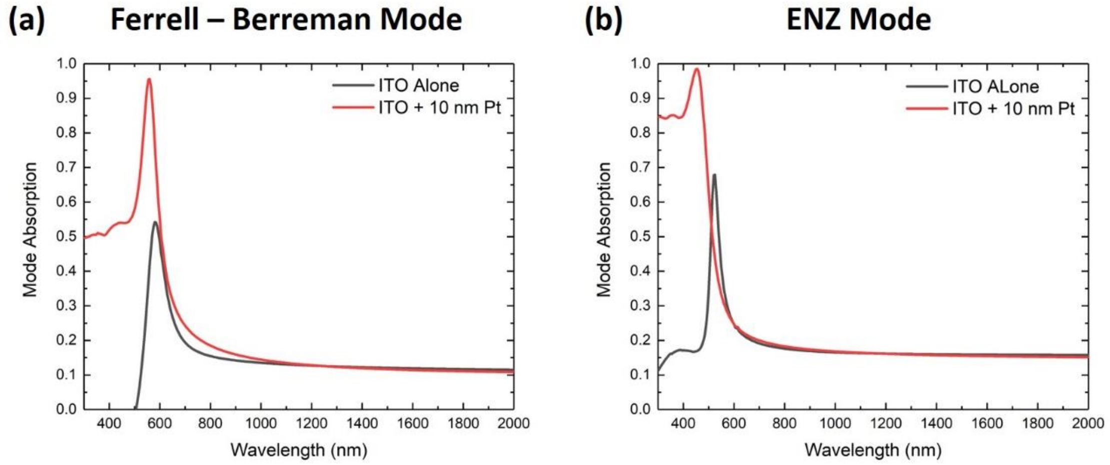

Figure 8.10 A comparison of (a) the Ferrell – Berreman mode absorption and (b) the non-radiative ENZ mode absorption from a 127 nm ITO with a plasma frequency, $\omega_p = 6.00$ rad fs^{-1} with (red) and without (black) a 10 nm Pt backing layer.

The Ferrell – Berreman and non-radiative ENZ mode profiles as a function of wavelength at 39° and 55° incidence respectfully are presented for the 127 nm ITO film with (red) and without (black) the 10 nm Pt backing layer. For the ITO film alone, the maximum simulated Ferrell – Berreman mode absorption was found to be just above 50%, and just above 65% for the non-radiative ENZ mode. However, the addition of just 10 nm of Pt on the back causes a significant enhancement of the absorption to values greater than 95% for the Ferrell – Berreman mode, and to values just below 100% for the ENZ mode. The results of Feigenbaum et al. and of these simulations suggest that the achievement of near-perfect absorption may be achievable from such structures as those considered in this thesis in the future. These results indeed open up a fascinating avenue of research for future work into this field.

8.4 Purcell – Factor Enhancement of Quantum Emitters by Coupling to ENZ Materials

Significant theoretical work has previously been carried out on the spontaneous emission lifetime of quantum emitters couples to an ENZ material. Fleury and Alù [12] and Chebykin et al[13]. both theoretically demonstrated the possibility of achieving Purcell Factor enhancements and Dicke superradiance from quantum emitters embedded in an ENZ environment.

The Purcell Effect is the enhancement of the spontaneous emission rate of a quantum system due to its environment. It was first discovered and published by Edward Purcell in 1946 [14] by measuring the spontaneous emission rate of atoms in a resonant cavity. The magnitude of this enhancement is given by the Purcell Factor,

$$F_p = \frac{3}{4\pi^2}\left(\frac{\lambda_0}{n}\right)^3\left(\frac{Q}{V}\right) \qquad (2)$$

where λ_0 is the free-space wavelength, n is the refractive index of the cavity environment, Q is the quality factor or 'Q-Factor', and V is the mode volume. The Q-Factor [15] is a dimensionless parameter that described the damping of a resonator and is given by

$$Q = \frac{f_r}{\Delta f} \qquad (3)$$

where f_r is the resonant frequency and Δf is the bandwidth and the mode volume, V is the volume number of bound modes that the cavity can support [16]. In the past it was believed that spontaneous emission was simply an intrinsic property of atoms, however Purcell's work was the first demonstration that the spontaneous emission rate actually depends on the environment of the emitter. Modern applications of this phenomenon include fluorescence microscopy, Surface Enhanced Raman Spectroscopy (SERS) [17], DNA sequencing, and single molecule detection. However, the drawback of this phenomenon is that to gain enhancement of the spontaneous emission rate, precise control over the position of the quantum emitter is necessary to position it in the region of the environment with the highest density of states. However, another mechanism by which the spontaneous emission rate can be enhanced is by placing a multiple, N of identical quantum emitters in close proximity to each other in the environment which results in a phenomenon known as superradiance. This phenomenon was studied, and the subsequent work published by Robert Dicke in 1954 [18] in which he discovered that if these N quantum emitters are confined within a deeply subwavelength volume that there is a collective emission from them. The resulting emission intensity is proportional to the square of the number of emitters, N^2 and the decay time is proportional N^{-1}. However, the downside of this phenomenon is that the quantum emitters have to be packed very close together to achieve Dicke superradiace. Fleury and Alù examined these effects theoretically by considering quantum emitters embedded in an ENZ environment composed of a narrow plasmonic channel operating at its cut-off frequency. They demonstrated that a quantum emitter embedded in such an ENZ channel should exhibit significant enhancements of the Purcell Factor and Dicke superradiance as well as an increased density of states independent of the position in the channel. Further work by Chebykin et al. theoretically studying quantum emitters in ENZ ultra-anisotropic uniaxial metamaterials. This designed structure consisted of a periodic metal – dielectric multilayer nanostructure with a complex unit cell containing two different metallic layers which had an effective zero-permittivity at the operating frequency. They report the possibility of achieving strong Purcell enhancement of the spontaneous emission rate and significant far-field emission power in the studied structure. Engheta et al. [19] also carried out numerical simulations for the coupling of two quantum emitters in a linear waveguide and in two identical waveguides separated by an ε-μ-near zero (EMNZ) material as depicted in Figure 8.11.

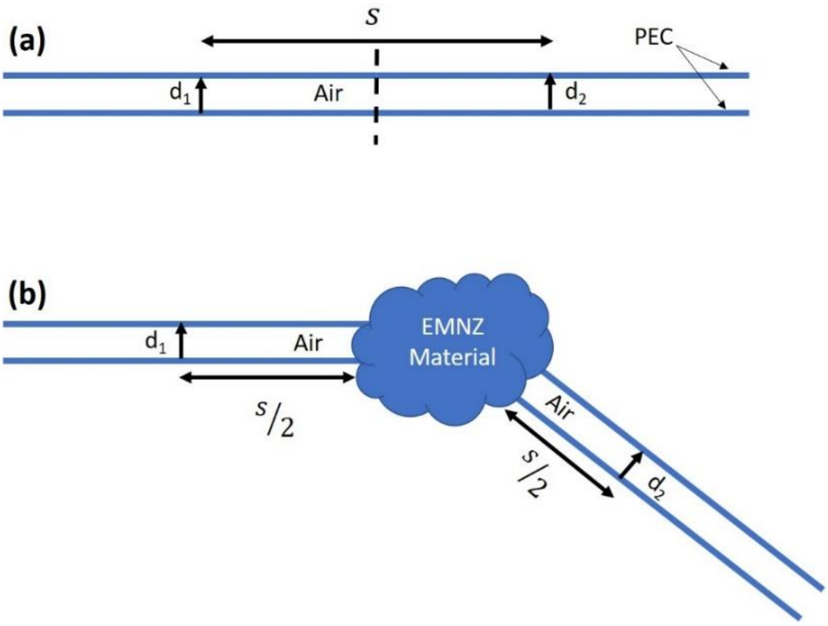

Figure 8.11 Schematic of the waveguide structure considered by Engheta et al. demonstrating the coupling between two dipoles in (a) a standard linear waveguide, and (b) two waveguides separated by an EMNZ material. This figure was redrawn based on that published by Engheta et al. [19].

Typically, dipole – dipole coupling between two quantum emitters requires very precise positioning of the emitters. However, as previously mentioned, by embedding quantum emitters in an ENZ material this need for precise positioning is no longer necessary. This is a result of the ENZ ‘supercoupling’ effect which is the tunnelling like zero phase advance / decay of light at the ENZ wavelength as it passes through the material as well as the spatially static electric field in the ENZ material. However, Engheta et al. found that by separating two identical waveguides with an EMNZ material and placing two quantum emitters a distance of $^{s}/_{2}$ from the EMNZ material boundary on either waveguide results in identical coupling to placing two quantum emitters a distance *s* apart in a linear waveguide. This effect is independent of the shape, size and geometry of the EMNZ material separating the waveguides and is even independent of the angle between the two waveguides.

As shown, there is significant evidence to suggest that coupling ENZ or EMNZ materials with quantum emitters can lead to these Purcell enhancements and Dicke superradiance effects. However, to date very few experimental demonstrations of such an effect have been reported, possibly due to the unavailability of quantum emitters with an emission wavelength that overlaps with the ENZ wavelength of the ENZ material in question. Although, in recent years PbS core quantum have been produced which can have emission wavelengths in the 1000 – 1600 nm spectral range. For future work, we hope to couple such quantum dots to our ITO films or to embed them in locally fabricated ITO and to measure their resulting emission lifetimes using the techniques of Fluorescence Lifetime Imaging Microscopy (FLIM) or photoluminescent spectroscopy.

8.5 Potential Application in Heat Assisted Memory Recording (HAMR)

HAMR is a memory writing process for storing binary magnetic data to hard drives. It works by applying thermal energy to individual bits of a bit-writing medium until the electrons in the bit are above the Curie temperature and thus become paramagnetic. The spins of these electrons can thus be aligned either "up" corresponding to a "1" or "down" corresponding to a "0" via the application of an external magnetic field. Once the electron spins in the bit are aligned, the bit is quickly cooled down to lock the electrons in their spin configuration. By repeating this process across several bits and aligning the electron spins binary data can thus be physically stored in the medium. This process is schematically demonstrated in Figure 8.12 [72].

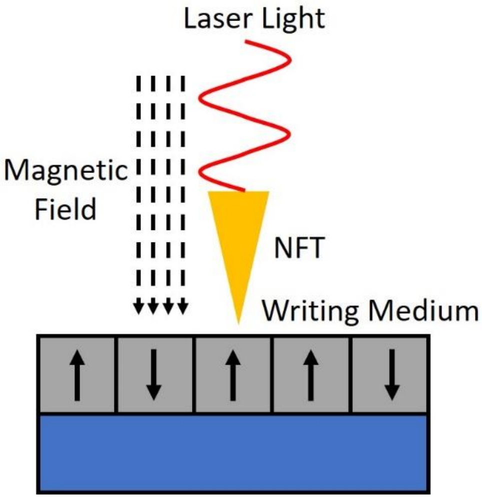

Figure 8.12 Representative schematic demonstrating the principle process of heat assisted magnetic recording (HAMR).

However, in order to apply energy to the bit writing medium, a device called a near-field transducer (NFT) is used to harness the energy from a laser and the energy is then non-radiatively transferred to the medium. Currently, many NFTs are made of plasmonic gold tapers which harness the optical energy of the laser in form of surface plasmons which are then confined to the tip of the taper. However, the issue with using gold for such applications is that gold is not particularly thermally stable. Significant research by Abbot et al. has demonstrated the dewetting of gold films as a result of laser induced thermal energy [73][74]. If perfect absorption can be achieved from ITO in the correct wavelength range, the plasmonic and ENZ behaviour of ITO could harness the incident optical laser energy and operate in a similar fashion to gold tapers, the result would be a highly thermally stable NFT that is resistant to dewetting and thermal degradation as ITO can withstand temperature between 1100˚C - 1600˚C depending on the ambient atmosphere. In this work, we demonstrated near-perfect absorption (NPA) in ITO thin films coupled with a Pt backing and also demonstrated that it is possible using a whole range of different metal backings with thicknesses as low as 10 nm. However, the suitability of such ENZ materials for use in this process relies heavily on the wavelength at which perfect absorption can be achieved. Currently, HAMR operated in the near-infrared 700 – 900 nm range [75]. Numerical simulation in Chapter 6 shows that when a metal backing is applied to thin film ITO and excited from glass, the NPA achieved extends to this 700 – 900 nm spectral range, however only at oblique incidence. This is a promising result and could lead to significant advancements in improving NFTs for HAMR. However, significant further research is required.

8.6 Conclusion

ENZ materials, particularly ITO show great promise for a host of novel physical phenomena and has been readily demonstrated in this work to exhibit perfect absorption. As outlined in this chapter, a whole host of possibilities for the continuation of this work exist, from broadspectrum and broad-angle perfect absorption, Purcell factor enhancements, Dicke superradiance, and even the possibility of perfect absorption in the visible range. A plethora of avenues of further exploration into ITO and ENZ materials in general exists.

In this work, we demonstrated and studied in depth the excitation of ENZ modes in ITO and demonstrated the achievement of near-perfect absorption on Pt-backed ITO thin films. We have shown that absorption values of > 95% are possible from ITO on metal backings much thinner than previously considered (< 25 nm) and that the peak absorption increases asymptotically with Pt thickness. This is a highly advantageous discovery as it demonstrates that these materials can be implemented in devices with considerable size restrictions, such as in HAMR. Furthermore, we provide the first study of this behaviour for various different metal backings by T-Matrix and FEM simulations. We demonstrate for the first time that the achievement of NPA is possible from most common metals, however, the value of the maximum absorption and the thickness at which that maximum is achieved is dependent on the refractive indices, wave impedances, and skin depths of the metals. We conclude that the best backing for ITO films to achieve maximum absorption about their ENZ region is one with a low real component of the refractive index and a very large imaginary component. Furthermore, we experimentally demonstrated that thinner metal backings result in higher non-radiative ENZ mode absorption as a result of exciting IMI modes in the ITO – Metal structures.

Finally, we considered the potential of coupling high refractive index, 2D, boron nitride nanoflakes to ENZ materials but demonstrated that the dominance of scattering in the optical response makes them unsuitable for such applications. However, we provide a detailed study of the scattering form such nanoflakes in both the single and multiple scattering regimes. We demonstrate that the high aspect ratio nanoflakes cause significant depolarisation of light compared to a polystyrene nanosphere reference. We also show that the lateral size of these particles can be estimated using a path length dependent, diffuse scattered, light intensity technique by direct comparison to polystyrene nanospheres of similar diameter. We also examined various models to describe this diffuse scattering from these nanoflakes in the multiple scattering regime and demonstrate that the Two-Stream Approximation to the radiative transfer equation is the best model to describe this phenomenon. However, extraction of the particle width and thickness of the 2D nanoflakes was not demonstrated to be possible using this technique. This may suggest that dynamic light scattering in general is insensitive to the aspect ratio of such particles and is dependent on the lateral dimension of the nanoflakes which when randomly oriented could result in successive scattering events that approximate the response of a sphere of similar diameter.

References

[1] D. Barchiesi and T. Grosges, “Fitting the optical constants of gold, silver, chromium, titanium, and aluminum in the visible bandwidth,” *J. Nanophotonics*, vol. 8, no. 1, pp. 1–17, Jan. 2014.

[2] W. S. M. Werner, K. Glantschnig, and C. Ambrosch-Draxl, “Optical constants and inelastic electron-scattering data for 17 elemental metals,” *J. Phys. Chem. Ref. Data*, vol. 38, no. 4, pp. 1013–1092, 2009.

[3] C. Zhong *et al.*, “Mapping of surface plasmon dispersion in thin Ag–Au layered composite films,” *J. Opt. Soc. Am. B*, vol. 33, no. 4, p. 566, 2016.

[4] M. J. Preiner, K. T. Shimizu, J. S. White, and N. A. Melosh, “Efficient optical coupling into metal-insulator-metal plasmon modes with subwavelength diffraction gratings,” *Appl. Phys. Lett.*, vol. 92, no. 11, p. 113109, 2008.

[5] J. Chen, G. A. Smolyakov, S. R. J. Brueck, and K. J. Malloy, “Surface plasmon modes of finite, planar, metal-insulator-metal plasmonic waveguides,” *Opt. Express*, vol. 16, no. 19, pp. 14902–14909, 2008.

[6] H.-J. Li, L.-L. Wang, and X. Zhai, “Plasmonically induced absorption and transparency

based on MIM waveguides with concentric nanorings," *IEEE Photonics Technol. Lett.*, vol. 28, no. 13, pp. 1454–1457, 2016.

[7] A. J. Labelle *et al.*, "Broadband Epsilon-near-Zero Reflectors Enhance the Quantum Efficiency of Thin Solar Cells at Visible and Infrared Wavelengths," *ACS Appl. Mater. Interfaces*, vol. 9, no. 6, pp. 5536–5565, 2017.

[8] S. Molesky, C. J. Dewalt, and Z. Jacob, "High temperature epsilon-near-zero and epsilon-near-pole metamaterial emitters for thermophotovoltaics," *Opt. Express*, vol. 21, no. 101, pp. A96–A110, 2013.

[9] C. Hägglund and S. P. Apell, "Plasmonic near-field absorbers for ultrathin solar cells," *J. Phys. Chem. Lett.*, vol. 3, no. 10, pp. 1275–1285, 2012.

[10] J. J. Lin and Z. Q. Li, "Electronic conduction properties of indium tin oxide: Single-particle and many-body transport," *J. Phys. Condens. Matter*, vol. 26, no. 34, pp. 1–39, 2014.

[11] E. Feigenbaum, K. Diest, and H. A. Atwater, "Unity-order index change in transparent conducting oxides at visible frequencies," *Nano Lett.*, vol. 10, no. 6, pp. 2111–2116, 2010.

[12] R. Fleury and A. Alù, "Enhanced superradiance in epsilon-near-zero plasmonic channels," *Phys. Rev. B*, vol. 87, no. 20, p. 201101, 2013.

[13] A. V. Chebykin, A. A. Orlov, A. S. Shalin, A. N. Poddubny, and P. A. Belov, "Strong Purcell effect in anisotropic ε-near-zero metamaterials," *Phys. Rev. B - Condens. Matter Mater. Phys.*, vol. 91, no. 20, pp. 1–6, 2015.

[14] E. M. Purcell, "Spontaneous emission probabilities at radio frequencies," *Confined electrons and photons*, Springer, 1995, p. 839.

[15] J. H. Harlow, "Electric power transformer engineering-Book Review," *IEEE Electr. Insul. Mag.*, vol. 20, no. 3, p. 64, 2004.

[16] K. Srinivasan, M. Borselli, O. Painter, A. Stintz, and S. Krishna, "Cavity Q, mode volume, and lasing threshold in small diameter AlGaAs microdisks with embedded quantum dots," *Opt. Express*, vol. 14, no. 3, pp. 1094–1105, 2006.

[17] Y. Gu *et al.*, "Surface-Plasmon-Induced Modification on the Spontaneous Emission Spectrum via Subwavelength-Confined Anisotropic Purcell Factor," *Nano Lett.*, vol. 12, no. 5, pp. 2488–2493, 2012.

[18] R. H. Dicke, "Coherence in spontaneous radiation processes," *Phys. Rev.*, vol. 93, no. 1, p. 99, 1954.

[19] A. M. Mahmoud, I. Liberal, and N. Engheta, "Dipole-dipole interactions mediated by epsilon-and-mu-near-zero waveguide supercoupling," *Opt. Mater. Express*, vol. 7, no. 2, p. 415, 2017.